Simuler la plasticité phénotypique des Poacées comme propriété émergente de processus locaux : Un modèle structure-fonction couplant la morphogénèse et le métabolisme du carbone et de l'azote

Marion Gauthier

Thèse de doctorat

NNT : 2021UPASB005

université PARIS-SACLAY

Simuler la plasticité phénotypique des Poacées comme propriété émergente de processus locaux : Un modèle structure-fonction couplant la morphogénèse et le métabolisme du carbone et de l'azote

Thèse de doctorat de l'université Paris-Saclay

École doctorale n°581 : agriculture, alimentation, biologie, environnement et santé (ABIES)
Spécialité de doctorat : Sciences végétales
Unité de recherche : Université Paris-Saclay, INRAE, AgroParisTech, UMR ECOSYS, 78850, Thiverval-Grignon, France
Référent : AgroParisTech

Thèse présentée et soutenue à Paris-Saclay, le 23/02/2021, par

Marion GAUTHIER

Composition du Jury

Alexandre PERY ICPEF (assimilé PR), AgroParisTech	Président
Hélène GAUTIER Directrice de recherche, INRAE – Centre Provence-Alpes-Côte d'Azur	Rapporteur & Examinatrice
Christophe GODIN Directeur de recherche, Inria – Centre Grenoble - Rhône-Alpes	Rapporteur & Examinateur
Jessica BERTHELOOT Chargée de recherche, INRAE – Centre Pays de la Loire	Examinatrice

Direction de la thèse

Bruno ANDRIEU Directeur de recherche, INRAE – Centre IdF-Versailles-Grignon	Directeur de thèse
Romain BARILLOT Chargé de recherche, INRAE – Centre Nouvelle-Aquitaine Poitiers	Co-Encadrant & Examinateur
Christian FOURNIER Ingénieur de recherche, INRAE – Centre Occitanie-Montpellier	Co-Encadrant & Invité
Amélie PINET Docteure, entreprise ITK	Tutrice en Entreprise & Invitée

Remerciements

Ce travail a été financé par l'entreprise montpelliéraine ITK par le biais du dispositif Cifre de l'Association Nationale Recherche et Technologie (ANRT).

Je remercie tout d'abord mon directeur de thèse, Bruno Andrieu, ainsi que mon principal co-encadrant, Romain Barillot, pour leur accompagnement sans faille tout au long de mon parcours de thèse, pour leur disponibilité et pour leur sympathie. Je n'aurai pas osé rêver meilleur duo d'encadrement ! Merci Bruno d'avoir essayé de me transmettre sans relâche ta vision de la modélisation, ta rigueur et ton souci du détail. J'espère avoir réussi à en intégrer suffisamment ! Merci Romain d'avoir régulièrement insufflé du pragmatisme à mon travail, et, merci de m'avoir enseigné l'implémentation de modèle complexe et épaulée dans l'utilisation d'OpenAlea. Par avance, je suis désolée pour les bugs de code que tu pourras trouver dans le futur !

Merci à mes deux soutiens côté ITK, Amélie Pinet et Vianney Houlès, de m'avoir intégrée dans l'entreprise et de m'avoir régulièrement aiguillée dans mon travail de recherche scientifique ainsi que dans mes recherches professionnelles. Je remercie aussi Christian Founier de m'avoir éclairée sur ADEL-Wheat avec autant de bonne humeur, et Camille Chambon de m'avoir initiée à Python.

Je remercie les membres de mon jury d'avoir accepté d'évaluer ce travail, et en particulier les deux rapporteurs, Hélène Gautier et Christophe Godin, dont les rapports d'évaluation m'ont permis de prendre encore d'avantage de recul par rapport à mon travail. Je remercie également les membres de mon comité de thèse, Delphine Luquet, Pierre Martre, Jean-Louis Drouet et Jacques Le Gouis, pour les discussions constructives et pour leur bienveillance. Merci à Alexandre Pery, directeur de l'école doctorale, pour son enthousiasme communicatif, toujours bienvenu au cours du parcours de thèse.

Un immense merci à Josiane Jean-Jacques, Fabrice Duhamel, Maxime Marques, Christelle Franchet et Nicolas Boulard pour le travail technique colossal réalisé pour la mise en œuvre des expérimentations. C'était, pour moi, un véritable plaisir de réaliser chaque nouveau prélèvement grâce à votre bonne humeur. Je remercie tout particulièrement Josiane d'avoir continué d'arrachepied toutes les analyses biochimiques pendant mon congé maternité. Je remercie vivement Pierre Bancal de m'avoir aidée à la conception de mon expérimentation et d'avoir consacré du temps pour la définition des protocoles d'analyses biochimiques puis pour l'analyse des résultats. Je remercie aussi Florence Lafouge pour ces multiples « coups de main » au labo.

Je remercie chaleureusement tous les collègues d'EcoSys pour leur fabuleux accueil, leur soutien quotidien, leurs discussions enrichissantes et leurs conseils avisés. L'ambiance familiale régnant au labo a significativement contribué à la réussite de ce travail. Un grand merci à Frédéric Rees, Tiphaine Vidal, Céline Richard-Molard et Andrée Tuzet et aux chercheurs de l'UR P3F pour leurs conseils lors des répétitions de ma soutenance.

Je remercie les différents amis et collègues qui, au cours de mon parcours précédent, m'ont insistée à faire une thèse : Jean-Charles, Alban, Alice, Juan, Morgane, Séverin, François, c'était effectivement une bonne idée !

Enfin, je remercie ma famille et mes amis de m'avoir épaulée, et tout particulièrement Xavier.

Table des matières

Introduction générale

Les changements récents et futurs du climat sont marqués par une augmentation de la concentration en CO_2 de l'atmosphère et une modification conjointe des températures, des pluies et des disponibilités en eaux. Dans le même temps, la société revendique une transition vers des pratiques agroécologiques qui visent à être plus respectueuses de l'environnement et de la santé. Le recourt à des couverts mixtes est par exemple proposé pour augmenter la durabilité et la résilience des cultures (Altieri *et al.*, 2015; Raseduzzaman and Jensen, 2017). Le contexte du changement climatique et de l'agroécologie crée, pour les plantes, des conditions de croissance inédites et en perpétuelle évolution. Il est alors crucial d'anticiper leurs impacts sur la réponse des plantes, et *in fine* sur la production. Les modèles permettent d'intégrer le rôle de différents facteurs environnementaux sur un ensemble de processus écophysiologiques (acquisition des ressources, respiration, croissance, mise en place du rendement...). Les modèles sont alors des outils utiles dans la mesure où ils permettent d'explorer, rapidement et à moindre coût, une large gamme de scenarii de conduite de culture sous les climats actuels et futurs.

La **plasticité phénotypique** – la capacité d'un génotype à adapter son phénotype à ses conditions de croissance - est un aspect essentiel des interactions plante-environnement. La croissance et le développement de l'appareil foliaire est un processus morphogénétique important dont la plasticité phénotypique se traduit par des variations de vitesse et de durée de croissance, de dimensions finales du limbe et de la gaine et de composition biochimique. Les caractéristiques des feuilles déterminent notamment la surface photosynthétique du couvert et donc la mise en place du rendement de la culture (Monteith, 1977; Gallagher, 1979). Les feuilles jouent aussi un rôle dans les épidémies foliaires de par leur vitesse de croissance, leur géométrie (Garin et al., 2016) et leur composition biochimique (Mitchell et al., 2002). On peut aussi citer le rôle des feuilles dans l'équilibre hydrique de la plante, comme principales surfaces de transpiration. Ces exemples illustrent les enjeux de la modélisation de la croissance foliaire, aussi bien au niveau d'une feuille individuelle qu'à l'échelle de la plante entière. Aussi, de nombreux modèles ont été développés pour prédire la croissance foliaire en fonction des conditions de croissance.

Développés depuis les années 1960, les modèles de cultures permettent de simuler la croissance du peuplement végétal en fonction des conditions climatiques, édaphiques et des pratiques culturales (Boote et al., 2013). Ils représentent le peuplement végétal comme un système homogène. Ils considèrent l'effet sur la croissance d'une large variété de facteurs environnementaux tels que la lumière, la fertilisation azotée, l'eau, la température, le CO2, la profondeur et le type de sol, les pratiques de désherbage, *etc.* (Muller and Martre, 2019). Le nombre élevé de facteurs pris en compte permet également d'utiliser les modèles de culture à des échelles spatiotemporelles larges, par exemple, pour prévoir l'effet des pratiques sur l'émission de gaz à effets de serre sur une exploitation agricole (Drouet *et al.*, 2008) ou pour réaliser une étude économique de filières de production (Basso *et al.*, 2012). La contrepartie de la diversité des facteurs pris en compte est une description très simplifiée (i) de la plante et (ii) des processus physiologiques impliqués dans la plasticité. Ils ne permettent pas de simuler finement les caractéristiques des plantes.

Parallèlement aux modèles de culture, la **modélisation structure-fonction** (Functional-Structural Plant Models, FSPM) s'est développée (Godin and Sinoquet, 2005; Vos *et al.*, 2010; DeJong *et al.*, 2011; Louarn and Song, 2020).

Les FSPM sont des modèles individu-centré qui reposent sur une description 3D botaniquement réaliste de l'architecture (aérienne et/ou souterraine) de la plante du point de vue de la topologie des organes, de leurs dimensions et de leur géométrie. Les premiers FSPM étaient purement descriptifs de l'architecture des plantes. Par exemple, ADEL-Wheat simule l'évolution dans le temps de l'architecture aérienne du blé en rendant compte de coordinations observées dans les dynamiques de mise en place des phytomères et des axes (Fournier *et al.*, 2003; Abichou *et al.*, 2013). Couplés à des modèles de distribution de la lumière, les modèles FSPM permettent alors d'avoir accès à la lumière interceptée et à la température de chaque organe (phylloclimat, Chelle and Andrieu, 1998). Des modèles décrivant le fonctionnement de la plante en lien avec le phylloclimat ont ensuite été développés. On constate que ces FSPM « trophiques » reposent sur un ensemble de formalismes empiriques (développés dans le chapitre suivant) qui limitent la prise en compte des rétroactions entre l'architecture de la plante et son environnement et donc *in fine* la simulation de la plasticité phénotypique (Poorter *et al.*, 2013). Pour le moment, aucun modèle de plante entière ne permet de simuler la plasticité phénotypique comme une propriété émergeant des interactions entre la croissance, le phylloclimat et les relations source-puit au niveau de chaque organe.

La thèse soutenue est qu'il est possible de construire un tel modèle. Le manuscrit présente les travaux réalisés pour construire le modèle et évaluer sa capacité à simuler la plasticité phénotypique dans des conditions de croissance contrastées. De nombreux facteurs influencent la morphogénèse, en particulier, les disponibilités en carbone, en azote et en eau, la température, les hormones et les signaux lumineux. Dans le cadre du travail présenté, nous nous intéressons aux effets du carbone et de l'azote qui sont les principaux facteurs limitant la croissance des plantes, et les principaux constituant de la biomasse sèche (McIntyre, 2001). Les voies métaboliques du carbone et de l'azote sont intimement liées ce qui implique de nombreuses rétroactions. Un enjeu est de comprendre, de façon intégrée, comment le métabolisme carbone – azote interagit avec la morphogénèse au cours du cycle de la plante. L'espèce étudiée dans le travail présenté est le blé d'hiver (*Triticum aestivum* L.) (i) pour son fort intérêt agronomique, et (ii) car il s'agit d'une plante modèle en écophysiologie et donc son fonctionnement a été très étudié et de nombreuses données s'y rapportant sont disponibles dans la littérature. Toutefois, l'objectif de ce travail est de développer plus largement un modèle de morphogénèse qui soit générique aux Poacées.

Le modèle développé s'appuie sur le modèle structure-fonction CN-Wheat préalablement développé (Barillot *et al.*, 2016*a*,*b*). CN-Wheat simule le métabolisme du carbone et de l'azote dans chaque organe pour la période de post-floraison *i.e.* une architecture statique. L'objectif de ce travail est donc d'étendre CN-Wheat aux stades pré-floraison.

Analyse bibliographique

et objectifs de l'étude

Ce chapitre est composé de cinq parties, dont les objectifs sont exposés ci-dessous :

1. La première partie présente l'état des connaissances générales sur l'architecture aérienne du blé afin d'introduire la structure de la plante et de situer les phases de développement de la plante qui sont traités au cours de l'étude.
2. La seconde partie expose des caractéristiques marquantes des feuilles et leur plasticité en réponse à des conditions de croissance contrastées en lumière et en azote. Cette partie détermine les phénomènes remarquables que notre modèle de morphogénèse aérienne doit simuler.
3. La troisième partie est une revue des modèles de morphogénèse aérienne du blé. Nous montrons que ces modèles sont limités pour simuler la plasticité phénotypique de la plante dans certaines conditions de croissance. En alternative, nous proposons de développer un modèle structure-fonction qui explicite les mécanismes à l'origine des traits foliaires et de plante, et de leur plasticité.
4. La quatrième partie dresse un bilan des connaissances et des zones d'ombre sur les mécanismes de croissance foliaire des Poacées. Nous en dégageons des processus clés qui seront utilisés comme moteurs dans notre modèle de croissance foliaire (hypothèses de modélisation).
5. La cinquième partie expose les objectifs de l'étude.

1 - Généralités sur l'architecture aérienne du blé

Structure de l'architecture aérienne du blé

L'appareil aérien des Poacées est constitué d'un ensemble d'axes (les talles) de structure similaire ; le brin-maître correspond au premier axe issu de la germination de la graine. Chaque axe est composé d'un empilement de **phytomères** qui sont des unités émises successivement par le méristème apical caulinaire et qui se développent puis sénescent généralement par ordre d'émission. Les premiers phytomères émis par le méristème apical caulinaire sont des phytomères végétatifs (constitués de feuilles et d'entre-nœuds) et les suivants sont des phytomères floraux (constitués d'épillets) ; le nombre final de phytomère végétatifs est fixé par le moment de la transition florale du méristème apical caulinaire (He *et al.*, 2011) qui est synchrone approximativement pour le maître-brin et les premières talles (Ljutovac, 2002). Chaque phytomère végétatif regroupe une feuille, un entre-nœud, un nœud et un bourgeon axillaire pouvant donner naissance à une talle. Les feuilles matures de blé sont constituées d'une **gaine** tubulaire entourant la tige et d'un **limbe** libre et plat, les deux étant séparés par une membrane appelée **ligule**.

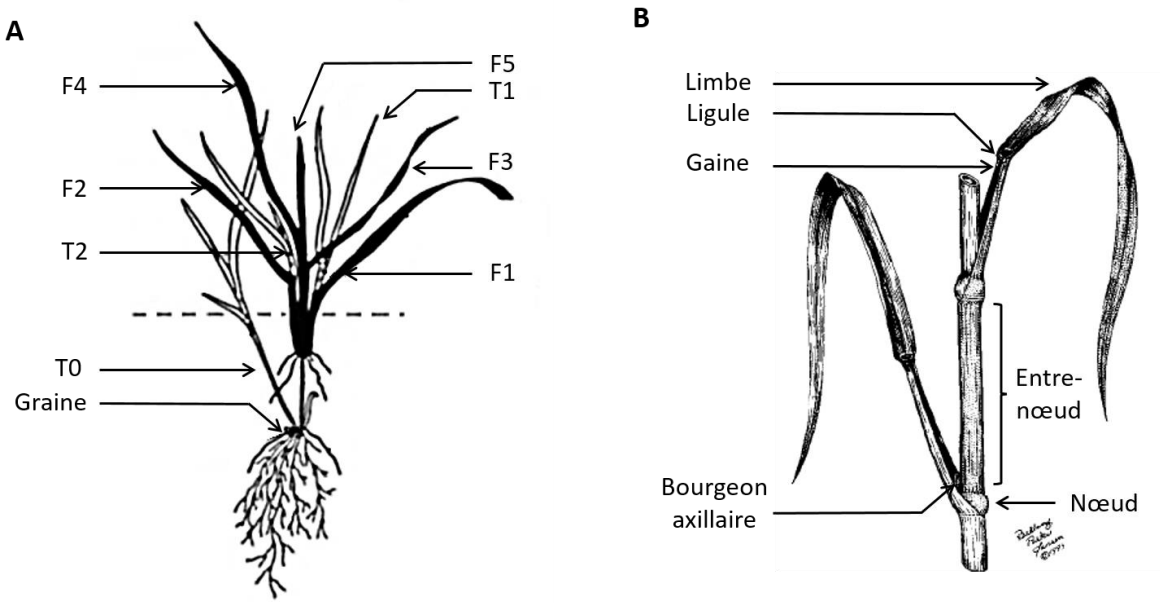

Figure 1 - Structure des Poacées. A : plantule de blé au stade 5 feuilles (F). Le brin-maître est coloré en noir et les talles primaires (T) sont présentées en blanc. Figure adaptée de (Klepper *et al.*, 1983) B : phytomère mature de blé avec entre-nœud long. Figure adaptée de (Moore and Moser, 1995)

Cycle de développement du blé

Le grain de blé contient un embryon de plante et des réserves. L'embryon est une ébauche du brin-maître. Son appareil aérien comporte trois ébauches de feuille et le méristème apical caulinaire (Williams, 1974). Après la germination, le méristème apical caulinaire émet de nouveaux phytomères. Les premiers phytomères se développent successivement avec des entre-nœuds courts : c'est la phase de croissance végétative (Figure 2). Au cours de cette phase, les talles successives émergent. Dans des conditions de culture usuelles, la première

talle émerge à l'aisselle de la feuille 1 au moment de l'émergence de la feuille 4 (Kirby *et al.*, 1985; Abichou *et al.*, 2018). Le début et la fin du tallage sont régulées par les conditions de croissance, principalement la disponibilité en azote et la densité du couvert (Longnecker *et al.*, 1993; Nelson, 2000). Après un délai suivant la transition florale du méristème apical caulinaire, les entre-nœuds des phytomères en croissance s'allongent : c'est la montaison (Kirby and Faris, 1970; Malvoisin, 1984*a*; Kirby *et al.*, 1994). Les talles les moins développées sénescent au cours de cette phase (Abichou *et al.*, 2018), les autres donneront des épis. A la floraison de l'épi, les feuilles et les entre-nœuds de tous les phytomères et le pédoncule floral ont atteint leurs dimensions finales. L'architecture aérienne de la plante est alors fixée. Tout au long du développement du blé, les feuilles meurent une à une. Les métabolites sont continuellement remobilisés depuis les tissus les plus anciens vers les plus jeunes et, après floraison, vers les grains.

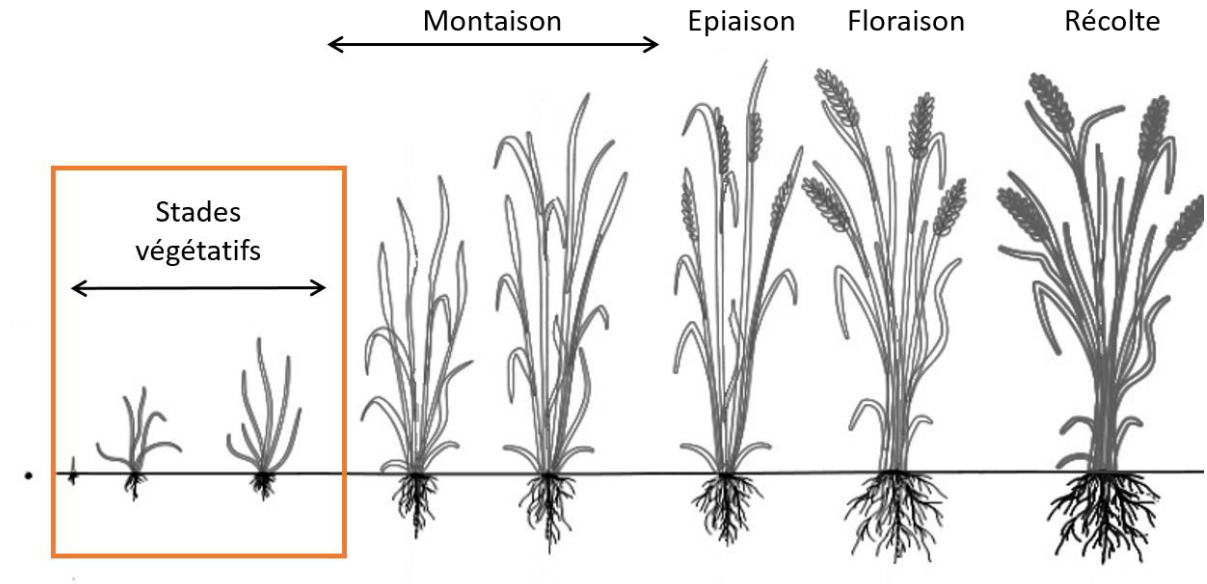

Figure 2 – Cycle de développement du blé. Le modèle développé au cours de l'étude couvre les stades végétatifs qui s'étendent de la levée jusqu'à l'allongement du premier entre-nœud.

Le modèle développé au cours de l'étude se limite aux stades végétatifs de croissance du blé, c'est-à-dire avant l'allongement de la tige. Aussi, la suite de ce chapitre se focalise sur la croissance foliaire.

2 - Caractéristiques des feuilles et leur plasticité

Les Poacées sont caractérisées par un ensemble de caractéristiques morphologiques de l'architecture aérienne, qui sont relativement conservées pour différentes conditions de croissance. Nous présentons les caractéristiques morphologiques bien connues du brin-maître d'une plante de blé en précisant les réponses des feuilles à des conditions contrastées en lumière et en azote. Les similarités entre axes sont brièvement abordées. Il est attendu que le modèle développé simule, comme propriétés émergentes, ces caractéristiques morphologiques et leur plasticité phénotypique.

Le phyllochrone

Le phyllochrone est la durée entre l'émergence de deux feuilles successives. Il dépend principalement de la température. Lorsque exprimé en temps thermique, le phyllochrone est approximativement constant au cours du développement du blé (Gallagher, 1979; Klepper *et al.*, 1982; Malvoisin, 1984*a*; Kirby *et al.*, 1985). Toutefois, il a été montré qu'il peut changer au cours du développement (Abichou, 2016). Une diminution du phyllochrone a, en effet, été observée dans certains cas au moment de la transition florale du méristème apical (Boone *et al.*, 1990) ou de l'initiation de la feuille drapeau (Abichou *et al.*, 2018).

Pour un même génotype, le phyllochrone est plus faible pour un nombre final de feuilles plus élevé (Malvoisin, 1984*a*; Abichou *et al.*, 2018) et varie alors avec la date de semis (Kirby *et al.*, 1985; Baccar, 2011). Le phyllochrone est faiblement sensible aux stress abiotiques. Il augmente en cas de carences marquées en eau ou en azote (Cutforth *et al.*, 1992; Longnecker *et al.*, 1993; McMaster, 2005). Il a, de plus, été montré que le phyllochrone était corrélé négativement au quotient photothermique (Baumont *et al.*, 2019) qui renseigne sur la disponibilité en produits de la photosynthèse (Nix, 1976).

Profil de dimensions finale des feuilles successives

La longueur finale des limbes augmente le long de l'axe, sauf pour le ou les derniers limbes qui sont souvent plus petits que les précédents (Williams, 1960; Gallagher, 1979; Ljutovac, 2002; Andrieu *et al.*, 2006; Dornbusch *et al.*, 2011; Abichou, 2016). L'incrément de longueur entre les premiers limbes, émis avant la phase de montaison (limbes juvéniles), est faible et devient bien plus important pour les limbes portés par des phytomères à entre-nœud long (limbes adultes). La largeur maximale des limbes augmente le long de l'axe, même dans des cas où la longueur est plus faible pour les derniers limbes (Gallagher, 1979; Ljutovac, 2002). La longueur finale des gaines est quasiment identique pour les premières feuilles, puis augmente le long de l'axe (Dornbusch *et al.*, 2011). Les profils de dimensions sont donc fortement marqués par (i) la distinction feuille juvéniles/adultes, (ii) la diminution de longueur du ou des derniers limbes. Aussi, les profils de dimensions sont souvent comparés entre axes ou entre conditions de croissance relativement à la feuille drapeau, *i.e.* en alignant les axes par rapport à la dernière feuille.

Les conditions de croissances modulent les dimensions des feuilles. Les profils de dimensions sont cependant relativement bien conservés pour différentes conditions de croissance (Dornbusch *et al.*, 2011; Abichou *et al.*, 2018). Dornbusch *et al.* (2011) ont observé que la densité de semis augmentait la longueur des feuilles juvéniles mais diminuait celle des feuilles adultes. La quantité de lumière a peu d'influence sur la longueur des feuilles, sauf dans les cas de très faibles rayonnements où leur longueur augmente (Friend *et al.*, 1962). La densité de semis et l'intensité du rayonnement impactent également la largeur des limbes (Friend *et al.*, 1962; Bos and Neuteboom, 1998; Dornbusch *et al.*, 2011). La fertilisation azotée augmente la longueur des feuilles et la largeur des limbes (Wilman and Mohamed, 1980; Fricke *et al.*, 1997; Dornbusch *et al.*, 2011).

Similarités de rythme d'émergence et de dimensions des feuilles entre axes

Le phyllochrone est souvent considéré comme identique pour tous les axes d'une même plante de blé (Evers *et al.*, 2005) ; toutefois, des différences entre axes ont été observées (Kirby *et al.*, 1985; Abichou *et al.*, 2018).

Lorsque les axes sont comparés relativement à la feuille drapeau, les profils de longueur foliaire sont relativement similaires sur le maître-brin et les talles, surtout pour les feuilles adultes (Figure 3). Les feuilles juvéniles sont souvent plus courtes sur les talles par rapport au brin-maître (Dornbusch *et al.*, 2011; Abichou, 2016). Suivant les génotypes, les limbes des talles sont parfois beaucoup plus étroits que le brin-maître, surtout pour les feuilles juvéniles (Dornbusch *et al.*, 2011).

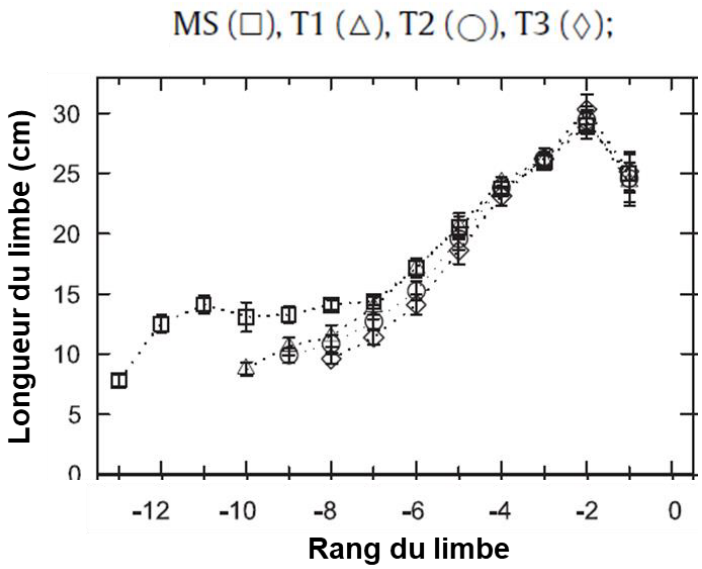

Figure 3 - Longueur des limbes successifs de blé de quatre axes : le brin-maître (MS) et trois talles primaires (T1, T2 et T3). Les axes sont comparés relativement à la feuille drapeau. Figure adaptée de (Dornbusch *et al.*, 2011).

Profils verticaux de masse et de composition biochimique

Il existe des gradients verticaux de masse surfacique des limbes, de teneur en azote (pourcentage d'azote de la matière sèche) et de teneur en azote par unité de surface (Specific Leaf Nitrogen, SLN) : à chaque instant, le dernier limbe ligulé est le plus épais, avec une teneur en azote et un SLN plus élevée (Rawson *et al.*, 1987; Dreccer *et al.*, 2000). Plusieurs facteurs déterminent le gradient vertical de SLN ; l'acclimatation des tissus à la lumière est un facteur prédominant (Bertheloot, 2009). Cette répartition préférentielle de l'azote au sein du couvert conduit à une augmentation de la photosynthèse de la plante par rapport à une répartition homogène de l'azote (Grindlay, 1997). Dreccer *et al.* (2000) ont montré que le gradient vertical des SLN au sein de couverts de blé est plus marqué après montaison.

Les conditions environnementales modulent la masse et la composition biochimique des feuilles. La masse surfacique augmente avec le rayonnement et diminue avec la densité de plante (Friend *et al.*, 1962; Tardieu *et al.*, 1999; Poorter *et al.*, 2019). La littérature rapporte des effets opposés de la fertilisation azotée sur la masse surfacique des Poacées (Robson and Parsons, 1978; Wilman and Mohamed, 1980; Fricke *et al.*, 1997; Dreccer *et al.*, 2000). Evans (1983, 1989) et Dreccer *et al.* (2000) ont montré que le SLN augmente avec le rayonnement et la fertilisation azotée et diminue avec la densité de plante.

Les feuilles de blé ont un ensemble de schémas morphologiques relativement bien conservées pour différentes conditions de croissance. Le phyllochrone exprimé en temps thermique est relativement constant. L'évolution des longueurs finales de limbe et de gaine et des largeurs maximales de limbe est progressive le long de l'axe. A chaque instant, il existe des gradients verticaux de masse surfacique et des SLN des limbes ligulés.

Le modèle développé au cours de l'étude doit simuler ces schémas morphologiques à partir des conditions environnementales.

3 - Les modèles actuels de morphogénèse et leurs limites pour simuler la plasticité phénotypique

Dans le cadre du changement climatique et des nouvelles pratiques culturales, les plantes sont soumises à une modification conjointe de facteurs environnementaux. Les formalismes utilisés dans les modèles doivent donc être en mesure de simuler correctement la croissance des plantes dans de telles conditions. Dans le cas de formalismes empiriques, ceux-ci doivent être établis expérimentalement, ce qui est extrêmement difficile du fait du grand nombre de combinaisons à tester et de l'incertitude sur les scenarii futurs. Afin de simuler la morphogénèse dans une large gamme de conditions, il est donc nécessaire que les modèles simulent, de façon suffisamment mécaniste, les variables et processus clés de la morphogénèse. Dans cette section, nous

présentons les variables et processus, simulés de façon empirique dans la plupart des modèles trophiques, qui nous semblent les plus limitants pour la simulation de la plasticité phénotypique.

L'acquisition de la biomasse (ou du carbone) et de l'azote

Biomasse

Le gain de biomasse sèche chez les plantes est le bilan entre la photosynthèse et les pertes qui sont principalement dues à la sénescence des tissues, la respiration et l'exsudation racinaire. Il a été largement montré que le cumul de rayonnement intercepté par la culture est corrélé à la production de biomasse (Duncan *et al.*, 1973; Monteith, 1977; Gallagher and Biscoe, 1978). Aussi, la plupart des modèles calculent la production journalière de biomasse à partir du rayonnement intercepté et de l'efficacité d'utilisation du rayonnement (Radiation Use Efficiency, RUE). La popularité de ce type de formalisme repose sur sa robustesse, sa simplicité (pas d'explicitation de la photosynthèse, respiration et autres pertes) et sur sa praticité (simulations possibles à partir de grands pas de temps). Cette relation est ainsi utilisée dans la plupart des modèles de culture (voir Asseng *et al.*, 2015 pour revue) et dans certains FSPM, *e.g.* Virtual Grass Land (Louarn and Faverjon, 2018), EcoMeristem (Luquet *et al.*, 2006). Dans ces modèles, la RUE est soit fixe, soit une fonction empirique d'un ou plusieurs facteurs suivants : le statut hydrique de la plante, son statut azoté, la part de rayonnement diffus. Cependant, bien que ces facteurs soient les principaux facteurs environnementaux régulant la RUE, il a été montré que la RUE varie aussi avec la concentration en CO_2 atmosphérique (Manderscheid *et al.*, 2003) par exemple, et au cours de la croissance de la plante (Calderini *et al.*, 1997; Cai *et al.*, 2016).

Azote

Lemaire et Salette (1984) ont montré que la dynamique de teneur en azote des parties aériennes d'une prairie dans plusieurs conditions de croissance est bien décrite par une unique fonction allométrique de la biomasse, introduisant alors le concept de courbe de dilution de l'azote. Ils ont, de plus, défini une courbe de dilution critique de l'azote qui décrit la teneur en azote minimale de la biomasse pour laquelle la production de biomasse est maximale. Ainsi, la plupart des modèles de culture pilotent l'absorption d'azote et régulent l'acquisition de biomasse à partir de la courbe de dilution critique de l'azote (voir Zhao *et al.*, 2014 pour revue). Dans les rares cas de FSPM qui considèrent l'azote, cette approche est aussi parfois utilisée (Louarn and Faverjon, 2018). Cette approche conduit cependant à de larges écarts (>100 %) entre les teneurs en azote simulées et les résultats expérimentaux (Stockle and Debaeke, 1997; Coucheney *et al.*, 2015; Faverjon *et al.*, 2019).

Ainsi, dans la plupart des modèles, les voies métaboliques du carbone et de l'azote ne sont pas entièrement explicites. De telles simplifications ne permettent pas de prendre en compte finement les interactions entre le métabolisme du carbone et celui de l'azote. Les modèles utilisant la RUE et/ou la courbe de dilution de l'azote comme moteurs sont limités dans leur capacité à simuler l'acquisition de biomasse et le prélèvement d'azote.

La répartition de la biomasse dans la plante

La grande majorité des modèles de culture et des FSPM reposent sur un rapport entre l'offre et la demande : le potentiel de croissance d'un organe (demande) est atteint seulement si l'offre (biomasse ou nutriments) est suffisante à l'échelle de la plante entière (*e.g.* Evers *et al.*, 2007; Kang *et al.*, 2008) ou à l'échelle de l'organe (*e.g.* Drouet and Pagès, 2007). Les ressources sont ensuite distribuées aux puits suivant des règles formalisant l'hypothèse de priorités ou de force de puit. Dans cette approche, les forces de puits et les priorités sont empiriques, et sont en général indépendantes des conditions de croissance. Nous notons l'originalité du FSPM de riz EcoMeristem (Luquet *et al.*, 2006) qui repose sur une approche offre-demande et considère une rétroaction des sources sur le potentiel de croissance des organes (puits).

Les modèles reposant sur l'approche offre – demande n'explicitent pas les processus physiologiques à l'origine de la répartition de la biomasse au sein de plante. Cette approche implique de quantifier la demande des puits et leur priorité. La capacité des modèles basée sur l'approche offre – demande à simuler la répartition de la biomasse pour de nouvelles conditions de croissance semble donc limitée.

Contrairement à la plupart des modèles, le modèle développé au cours de ce travail ne repose pas sur l'approche offre – demande. Le rapport massique aérien/racines, et la masse des différentes feuilles devra résulter des processus locaux gouvernant la répartition de la biomasse.

Les traits foliaires

Parmi les traits foliaires qui sont mal ou ne sont pas simulés par la plupart des modèles, nous présentons le phyllochrone et la masse surfacique. On pourrait toutefois en citer d'autres tels que la durée de vie des feuilles.

Le phyllochrone

Nous l'avons vu, chez le blé comme chez de nombreuses Poacées, le phyllochrone est relativement constant en temps thermique au cours du cycle de développement (Kirby *et al.*, 1985; Rickman and Klepper, 1995; McMaster, 2005). Ainsi, les modèles de cultures utilisent classiquement le phyllochrone comme un paramètre d'entrée qui pilote l'émergence des feuilles successives, conduisant ainsi à un calendrier de stades fixes en temps thermique (Muller and Martre, 2019). Cette approche est purement empirique et simule la croissance des feuilles uniquement à partir de leur émergence. En réalité, c'est le phyllochrone qui résulte de l'allongement des feuilles successives, et non l'inverse. De plus, le phyllochrone est sensible à d'autres facteurs environnementaux comme la durée du jour, le déficit hydrique et la nutrition azotée (Cutforth *et al.*, 1992; Longnecker *et al.*, 1993; McMaster, 2005; Baumont *et al.*, 2019), et peut varier au cours de l'ontogénie (Jamieson *et al.*, 2008; Abichou *et al.*, 2018). Une alternative plus mécaniste serait donc de simuler la croissance des feuilles dès leur initiation, pour simuler la stabilité du phyllochrone et sa plasticité comme propriétés émergentes.

La masse surfacique

Dans la grande majorité des modèles, les disponibilités en nutriments pilotent l'augmentation de la surface foliaire et l'épaisseur des tissus est considérée comme indépendante des conditions de croissance. Parfois, la masse surfacique n'est pas explicitement formalisée. Le gain de biomasse est alors converti en surface foliaire par une fonction dépendante du temps thermique. C'est le cas par exemple des différentes versions du modèle de culture Sirius (Jamieson *et al.*, 1995, 1998; Martre *et al.*, 2006). Lorsque la masse surfacique est explicite, elle est en général uniquement dépendante du rang foliaire ou du temps thermique (Ratjen *et al.*, 2018). Dans ce cas, on peut citer le FSPM de riz EcoMeristem (Luquet *et al.*, 2006), le FSPM de maïs GRAAL-CN (Drouet and Pagès, 2007), GreenLab (De Reffye and Hu, 2003; Kang *et al.*, 2008). En réalité, la masse surfacique est sensible aux conditions de croissance telles que la lumière (Friend *et al.*, 1962; Rawson *et al.*, 1987; Poorter *et al.*, 2009) et la fertilisation azotée (Robson and Parsons, 1978; Wilman and Mohamed, 1980; Fricke *et al.*, 1997; Dreccer *et al.*, 2000). Cette plasticité n'est donc pas simulée par la plupart des modèles.

Afin de rendre compte de la plasticité des principaux traits foliaires, les formalismes impliqués dans notre modèle seront plus mécanistes que ceux proposés dans les modèles actuels simulant la morphogénèse de la plante entière. Une originalité marquante de notre modèle concerne le rythme d'émergence des feuilles qui n'est pas considéré comme constant dans notre modèle. Il devra résulter des processus gouvernant l'allongement des feuilles successives.

Bilan : Vers plus d'explicitation des mécanismes

Nous l'avons vu, les modèles actuels reposent sur plusieurs formalismes empiriques pour simuler des variables clé de la morphogénèse. Les modèles sont alors limités pour simuler de la plasticité phénotypique des plantes notamment dans les cas de multi-stress et en cas de stress extrêmes (Muller and Martre, 2019).

La modélisation FSPM décrit plus finement que les modèles de culture la perception de l'environnement par la plante grâce à des modèles de phylloclimat. Toutefois, les FSPM existants de morphogénèse reposent eux-aussi sur des formalismes empiriques pour simuler des variables clé, et parmi eux, peu considèrent l'azote.

Aussi, il est nécessaire de prendre en compte dans les modèles les mécanismes qui sont à l'origine de la construction de ces variables clé. Nous les présentons dans la partie suivante.

4 - Les mécanismes de la mise en place de la série foliaire des Poacées

Les principaux mécanismes de la mise en place de la série foliaire sont génériques à la plupart Poacées. La longueur des feuilles et leur vitesse d'allongement a fait l'objet de nombreuses recherches alors que les mécanismes de mise en place de la surface et de la masse surfacique ont été moins étudiés.

Histogénèse de la feuille en croissance

Les feuilles sont émises successivement par le méristème apical caulinaire à l'intérieur de la **pseudo-tige** (Figure 4 ; Figure 5) formée par les gaines matures des feuilles précédentes (Schnyder *et al.*, 1987). Le primordium foliaire forme d'abord un renflement qui s'étend autour du méristème apical caulinaire puis le surplombe. Les cellules se divisent périclinalement, puis s'allongent principalement longitudinalement de sorte qu'elles s'éloignent de leur origine créant alors un flux de cellules depuis la base de la feuille vers la pointe. On distingue trois zones cellulaires spatialement distinctes de la base à la pointe (Skinner and Nelson, 1994) : (i) la zone de division cellulaire où le rythme de division et d'allongement des cellules est tel que leur dimension est en moyenne constante, (ii) la zone de pur allongement des cellules existantes où il n'y a pas de nouvelle division, (iii) la zone mature où les cellules ont atteint leur longueur maximale et se différencient (Figure 6). La **zone de croissance** désigne les zones de division et d'allongement cellulaire ; elle est située au sein de la pseudo-tige (Schnyder *et al.*, 1987). La gaine et le limbe sont mis en place au niveau de la même zone de croissance, et se séparent dès la formation de la ligule au sein de la zone de croissance (Schnyder *et al.*, 1990). Aussi, le limbe s'allonge et devient mature avant la gaine.

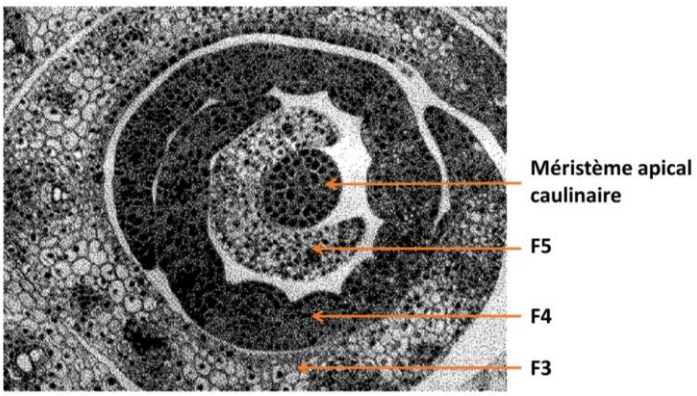

Figure 4 - Coupe transversale de la pseudo-tige d'une plantule de blé à l'émergence de la feuille 3 (F3) hors de la pseudo-tige. Les feuilles successives sont enroulées dans la pseudo-tige.

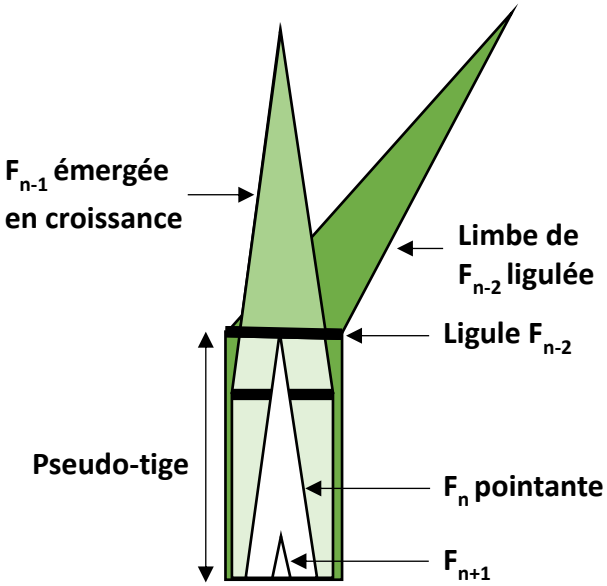

Figure 5 - Talle de blé en phase de croissance végétative (entre-nœuds non allongés). Les rapports de longueur ne sont pas respectés. La feuille F_{n+1} termine sa phase d'allongement exponentiel à l'émergence de la feuille précédente F_n. F_n et F_{n-1} sont en phase d'allongement linéaire. Fn-2 a terminé sa croissance.

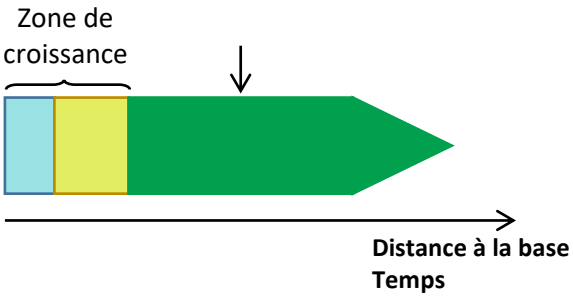

Figure 6 - Les trois zones cellulaires de la feuille en croissance. La zone de divisions cellulaires (bleu) et la zone de pure allongement cellulaire (jaune) forment la zone de croissance de la feuille. Une partie de la zone mature (vert) se trouve à l'intérieur de la pseudo-tige, dont la limite supérieure est indiquée par la flèche noire. Les cellules migrent depuis la base vers la pointe de feuille.

L'augmentation de la largeur de la feuille s'effectue par une augmentation du nombre de files cellulaires et par une augmentation de la largeur des cellules (Beemster and Masle, 1996). Le nombre de files cellulaires est établi par divisions anticlines à proximité du point d'insertion de la feuille (Silvy, 1982). La croissance en largeur des cellules s'étend plus loin de la base de la feuille que la zone d'allongement cellulaire (Fricke and Flowers, 1998; Macadam and Nelson, 2002).

L'augmentation de la masse surfacique de la feuille au cours de sa croissance est liée à la maturation des tissus (Lemaire and Millard, 1999). Dans le cas de la fétuque élevée (*Festuca arundinacea Schreb.*), il a été montré que la masse surfacique est plus faible dans la zone d'allongement cellulaire que dans la zone de division cellulaire dû à une diminution de la densité des parois. Elle augmente alors pour les cellules matures suite à la formation de la paroi secondaire (Macadam and Nelson, 2002).

Dans ce manuscrit, nous distinguons les termes suivant pour définir la mise en place des feuilles :

- **Allongement** : augmentation de la longueur
- **Extension** : augmentation de la surface
- **Croissance** : augmentation de la surface et de la biomasse

La mise en place de la surface photosynthétique correspond pour les stades végétatifs à l'extension des feuilles, qui principalement déterminée par leur allongement. Aussi, dans notre modèle de morphogénèse, il semble prioritaire de décrire finement les mécanismes de l'allongement foliaire, en comparaison de l'augmentation en largeur et en masse.

Cinétique d'allongement des feuilles

La longueur de la feuille en fonction du temps thermique suit une sigmoïde. La vitesse d'allongement, absolue ou relative, exprimée en fonction du temps thermique est communément utilisée pour suivre la vitesse d'allongement des feuilles. Plusieurs auteurs ont identifié quatre phases dans la vitesse d'allongement des feuilles (Williams, 1960; Ljutovac, 2002) qui sont générées par l'évolution dans le temps de la longueur des trois zones cellulaires (Skinner and Nelson, 1995; Durand *et al.*, 1999; Fournier *et al.*, 2005) :

1. La première phase est une première phase d'allongement exponentiel pendant laquelle la feuille est composée uniquement de la zone de division cellulaire qui se met en place.
2. La seconde phase est une seconde phase d'allongement exponentiel avec une vitesse d'allongement relatif plus élevée. A la fin de cette phase, la vitesse d'allongement de la feuille est maximale. Cette phase correspond à la mise en place de la zone d'allongement cellulaire.
3. La troisième phase est une phase d'allongement linéaire. Au cours de cette phase, la plus grande partie de la feuille se met en place. Les zones de division et d'allongement cellulaire atteignent leurs longueurs maximales et la plupart des cellules deviennent matures.
4. La quatrième phase correspond au ralentissement de la vitesse d'allongement de la feuille. Les zones de division et d'allongement cellulaire régressent.

La Figure 7 schématise les relations entre la vitesse d'allongement de la feuille et son ontogénie.

Durant les deux premières phases d'allongement exponentiel, la feuille est entièrement cachée au sein de la pseudo-tige. Au cours de la phase d'allongement linéaire, la feuille **émerge** de la pseudo-tige (Figure 7), c'est-à-dire que sa pointe devient plus haute que la plus haute ligule (feuille F_n sur la Figure 5).

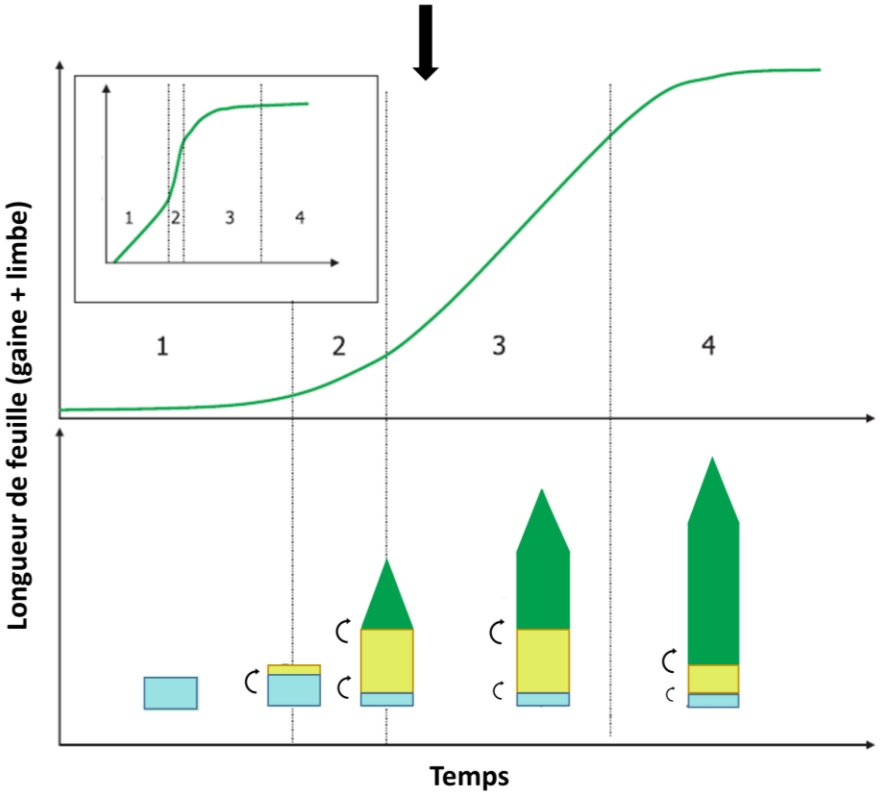

Figure 7 – Cinétique d'allongement de la feuille (gaine + limbe) en lien avec la longueur des trois zones cellulaires : la zone de divisions cellulaires (bleu), la zone de pure allongement cellulaire (jaune) et la zone mature (vert). L'insert montre la cinétique avec une échelle logarithmique pour la longueur de la feuille. La cinétique d'allongement est découpée en quatre phases : deux phases successives d'allongement exponentiel (1 et 2), une phase d'allongement linéaire (3) et une phase d'allongement ralentie (4). La flèche noire en haut du schéma indique le moment de l'émergence de la feuille hors da la pseudo-tige. Figure adaptée de (Fournier *et al.*, 2005).

Des coordinations dans l'allongement des phytomères successifs qui pourraient être médiées par la pseudo-tige

La longueur de la pseudo-tige détermine la longueur finale des feuilles

Une corrélation entre la longueur des feuilles et celle des gaines précédentes a été montrée sur plusieurs espèces de Poacées telles que le dactyle (Yu *et al.*, 1975), le blé (Ljutovac, 2002; Evers *et al.*, 2005) et le maïs (Fournier, 2000; Andrieu *et al.*, 2006), le ray-grass (Verdenal, 2009). Plus précisément, il a été démontré que la longueur de la pseudo-tige détermine la longueur finale des feuilles en croissance. En effet, une réduction de la longueur du cornet par défoliation réduit la taille du limbe et de la gaine des feuilles « cachées », et inversement en cas d'augmentation artificielle de sa taille (Wilson and Laidlaw 1985 sur ray gras). La réduction de la taille de la pseudo-tige a, en particulier, un impact sur l'histogénèse du primordium foliaire : la zone de croissance est plus courte (Kemp 1980 sur blé), les cellules sont moins nombreuses, de plus petite taille et se différencient plus précocement en gaine (Casey *et al.* 1999 sur ray gras).

Des synchronismes entre l'émergence d'organes hors de la pseudo-tige et le changement de vitesse d'allongement des feuilles

Parallèlement à cet effet de la longueur du pseudo-tige sur l'histogénèse, plusieurs synchronismes ont été relevés entre le changement de vitesse d'allongement foliaire et l'émergence d'organe (pointe de feuille ou ligule) hors de la pseudo-tige chez de nombreuses espèces de Poacées telles que la fétuque (Skinner and Nelson, 1995), le ray-grass (Verdenal, 2009), l'orge (Tesařová *et al.*, 1992) et le maïs (Fournier, 2000). Chez le blé, Ljutovac (2002) rapporte, pour des maîtres-brins et secondes talles de blé, que le passage de la première à la seconde phase d'allongement exponentiel de la feuille F_n correspond environ à l'émergence de la gaine F_{n-3}. Plusieurs auteurs ont trouvé que l'entrée dans la phase d'allongement linéaire est concomitante avec l'émergence de la pointe du limbe F_{n-1} (Williams, 1975; Malvoisin, 1984*a*). Cependant, Ljutovac (2002) montre un délai variable entre ces deux évènements, et obtient une meilleure corrélation avec l'émergence de la gaine F_{n-2}. L'entrée dans la dernière phase d'arrêt d'extension correspond à l'émergence du collet F_n (Williams, 1975). Notons cependant que plusieurs auteurs nuancent le synchronisme « parfait » de l'émergence de la feuille et du changement de phase d'allongement (Skinner and Nelson, 1994; Ljutovac, 2002). Expérimentalement, il est de plus difficile d'attribuer une date précise à l'émergence et aux transitions de phase d'allongement.

Fournier *et al.* (2005) montrent que toutes les feuilles (limbe + gaine) suivent une cinétique d'allongement commune lorsque le temps est exprimé en unités relatives à l'émergence des feuilles successives (**temps phyllochronique**). Ils notent cependant que les cinétiques des deux dernières feuilles se superposent moins bien les feuilles précédentes.

La date d'émergence hors de la pseudo-tige dépend de la date d'initiation, de la vitesse d'allongement au sein de la pseudo-tige et de la longueur de la pseudo-tige. L'existence de synchronismes entre l'émergence d'un organe hors de la pseudo-tige et le changement de vitesse d'allongement d'une feuille (du même ou d'un autre phytomère) renforce donc le rôle de la pseudo-tige dans l'allongement des feuilles successives. Les feuilles successives sont interdépendantes. La pseudo-tige joue un rôle dans cette interdépendance mais les mécanismes précis à l'origine de l'interdépendance des feuilles sont inconnus.

Ces observations ont conduit plusieurs auteurs à faire l'hypothèse que l'émergence d'un organe hors de la pseudo-tige représente un signal qui détermine les modifications de l'histogénèse de la feuille croissance (Begg and Wright, 1962; Malvoisin, 1984b; Wilson and Laidlaw, 1985; Fournier et al., 2005). Notre modèle repose sur cette hypothèse.

La pseudo-tige pourrait être impliquée dans l'effet prolongé d'un stress

Louarn *et al.* (2010) ont étudié l'impact d'une vague de froid précoce et transitoire sur la cinétique d'allongement des feuilles de maïs et leurs dimensions finales. La vague précoce de froid conduit à une réduction de longueur des feuilles, y compris de feuilles non initiées au moment du stress. La pseudo-tige des plantes soumises à la vague de froid était donc plus courte. Ils montrent que le stress a eu un impact direct sur les feuilles cachée dans la pseudo-tige au moment su stress, en réduisant la durée de leur phase d'allongement exponentiel (qui termine à l'émergence de la feuille hors de la pseudo-tige) tout en conservant la même vitesse relative d'allongement. Cette diminution de durée de la phase exponentielle s'est propagée aux phytomères suivants. Les auteurs ont fait l'hypothèse que la propagation de la réduction de la phase d'allongement exponentielle est causée (au moins en partie) par une réduction de la longueur de la pseudo-tige.

Il semble nécessaire de considérer le rôle de la pseudo-tige pour simuler correctement l'effet d'un stress précoce sur la construction de la série foliaire.

Des modèles reposant sur des règles de coordination entre les phytomères successifs

Afin de tenir compte de l'interdépendance observée entre les phytomères successifs, quelques modèles de morphogénèse aérienne reposant sur des **règles de coordination** ont été développé pour plusieurs espèces de Poacées. Ces modèles simulent la croissance des phytomères depuis leur initiation et donc même quand ils sont encore cachés au sein de la pseudo-tige. Dans ces modèles, l'émergence d'un organe déclenche un évènement dans la croissance du même ou d'un autre phytomère.

Verdenal *et al.* (2008) ont développé un modèle de ray-grass dans lequel la longueur de la pseudo-tige détermine la vitesse d'allongement et la longueur finale de la feuille. Ce modèle a permis de simuler la stabilité du phyllochrone comme propriété émergente du modèle, ainsi que l'effet du fauchage et du pâturage sur l'architecture des talles.

Chez le maïs, Zhu *et al.* (2014) ont développé un modèle de maïs dans lequel l'émergence des feuilles et des ligules pilote l'allongement des limbes, des gaines et des entre-nœuds. Ce modèle a été ensuite amélioré (Vidal and Andrieu, 2020) et a permis de simuler les profils de longueurs des organes matures d'un ensemble de génotypes aux phénotypes contrastés.

Ainsi, ces modèles reposant sur des règles de coordination ne considèrent pas de calendrier de stades fixes en temps thermique. Le développement de la plante résulte au contraire de l'allongement des organes successifs. Une telle approche permet donc de simuler plus de flexibilité dans le développement de la plante par rapport aux approches classiques. Parmi ces modèles, aucun ne module la morphogénèse par le carbone et l'azote.

Les rôles du carbone et de l'azote dans la croissance foliaire

Le carbone et l'azote sont les deux principales ressources, avec l'eau, qui limitent la croissance (Gastal *et al.*, 1992; McIntyre, 2001; Dornbusch *et al.*, 2011). Dans une première partie, nous présentons les différentes formes de carbone et d'azote dans la plante. Puis, nous présentons le rôle du carbone et de l'azote dans la croissance foliaire. Enfin, nous montrons qu'il existe de nombreuses interactions entre le métabolisme du carbone et de l'azote dans la plante.

Le carbone et l'azote dans la plante

La matière sèche de la plante est en majorité composée de carbone et d'azote, soit au sein de la structure des cellules (principalement les parois cellulaires), soit dans des métabolites. Parmi les principaux métabolites primaires, les sucres (glucose, fructose, saccharose, fructanes et amidon) sont composés à ~40 % de carbone, et les acides aminés (AA) et les protéines sont composés à ~40 % de carbone et ~15% d'azote (Penning de Vries *et al.*, 1989). Glucose, fructose, saccharose et AA sont des molécules mobiles dans la plante qui sont impliquées dans la mise en place des structures. Les fructanes, l'amidon et les protéines sont des molécules de stockage (Penning de Vries *et al.*, 1989; Lawlor *et al.*, 2001).

Le carbone et l'azote dans la feuille en croissance

Le carbone nécessaire est importé vers zone de croissance sous forme de saccharose (Schnyder and Nelson, 1987) et dégradé en hexoses utilisés pour la formation des parois (Williams and Rijven, 1965). Il a été montré par marquage isotopique sur l'orge que le carbone nécessaire à la division et l'allongement cellulaire est fourni dans un premier temps par les feuilles précédentes les plus photosynthétiquement actives. Le limbe différencié approvisionne ensuite progressivement en carbone la feuille (Anderson and Dale, 1983). (Schnyder and Nelson, 1987, 1989; Spollen and Nelson, 1988) ont montré que le carbone est accumulé dans la zone d'allongement cellulaire sous forme de fructanes, qui sont utilisés, lorsque les cellules atteignent la zone de maturation, pour synthétiser la seconde paroi cellulaire.

La quantité totale d'azote et son rythme de dépôt sont particulièrement élevés à la base de la zone de croissance alors qu'ils sont minimums et stables au niveau de la zone de maturation. L'azote est importé sous forme d'acides aminés dans la zone de croissance qui n'a pas de nitrate réductase active (Gastal and Nelson, 1994) ; il est principalement utilisé pour les mitoses. Les travaux de Gastal et Nelson (1994) suggèrent que l'azote nécessaire à la synthèse de l'appareil photosynthétique ne provient pas de nouveaux imports mais principalement d'une « réorganisation » des molécules déjà présentes. Une fois mature, la feuille assimile alors le nitrate et synthétise des acides aminés.

Liens entre les teneurs en carbone et azote de la feuille et la croissance foliaire

Sur blé de printemps, Kemp (1980) a étudié la vitesse relative d'allongement des zones de croissance de plusieurs étages foliaires de plantes cultivées à quatre fertilisations azotées. Celle-ci diminue significativement avec le rang foliaire pour tous les traitements azotés d'une part, et augmente avec la fertilisation azotée d'autre part. Il

montre que la vitesse relative d'allongement augmente avec la teneur en protéines de la zone de croissance, et diminue avec la teneur en hexose. De plus, il montre qu'une même relation entre la vitesse relative d'allongement et les teneurs permet de bien décrire les différences de vitesse entre étages foliaires et fertilisation (Figure 8). Ces observations ont conduit l'auteur à faire l'hypothèse que les protéines de la zone de croissance pilotent la vitesse d'allongement de la feuille.

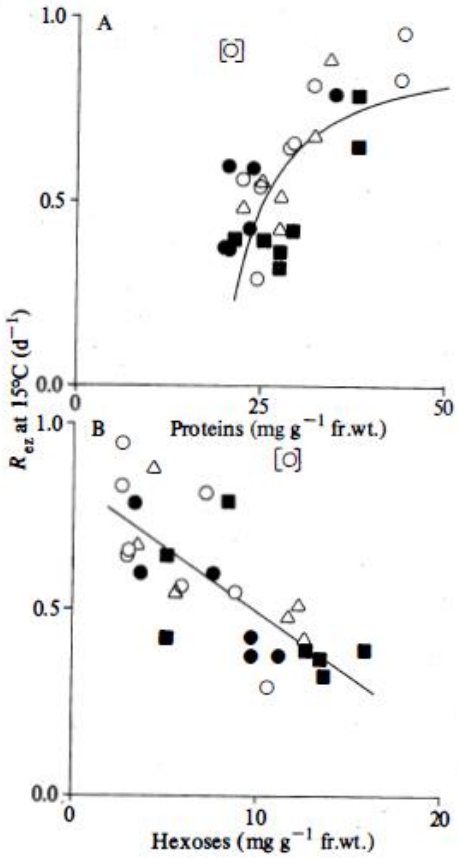

Figure 8 – Vitesse relative d'allongement des feuilles à 15°C en fonction de la teneur en protéines de la zone de croissance (A) et de la teneur en hexoses de la zone de croissance. Les symboles correspondent aux traitements azotés. Chaque point correspond à un étage foliaire. Figure tirée de (Kemp, 1980)

Sur fétuque, des expérimentations avec deux niveaux de fertilisation azotée ont montré qu'une vitesse d'allongement foliaire plus élevée était reliée à une teneur en protéines solubles et des imports nets en azote de la zone de croissance plus élevés, et à une teneur en fructanes plus faible (Volenec and Nelson, 1984; Gastal and Nelson, 1994).

De plus, des plantes de fétuque cultivées à faible éclairement ont eu un allongement foliaire plus rapide avec des feuilles plus étroites et plus fines par rapport aux plantes cultivées à un éclairement plus élevé (Schnyder and Nelson, 1989). A faible éclairement, les teneurs en sucres solubles des zones de croissance étaient moins élevées, en particulier les teneurs en fructanes.

La littérature rapporte des liens entre les teneurs en métabolites carbonés et azotés de la zone de croissance des feuilles et la croissance foliaire, principalement la vitesse d'allongement.

Dans notre modèle, nous faisons l'hypothèse que les concentrations en métabolites sous forme mobiles pilotent la croissance foliaire. Toutefois, une telle relation de causalité n'a pas été démontrée, et les potentielles lois de réponse sont inconnues. Une telle hypothèse de modélisation implique de simuler les concentrations en métabolites mobiles dans les zones de croissance.

Les interactions entre carbone et azote dans la plante

Le carbone de la plante provient du CO_2 atmosphérique fixé par la plante grâce à la photosynthèse. L'azote est assimilé par les racines depuis le sol. Les voies métaboliques du carbone et de l'azote dans la plante sont intimement liées (Hellebust and Bidwell, 1963; Atkin *et al.*, 2000; Foyer *et al.*, 2000; Chang and Zhu, 2017). Nous illustrons ci-dessous ces interactions par deux aspects majeurs d'interactions entre le carbone et l'azote dans la plante : la photosynthèse et l'absorption de l'azote.

De nombreuses protéines sont impliquées dans les différentes étapes de la photosynthèse : les protéines thylakoïdes (dont la chlorophylle) qui sont impliquées dans la collecte des photons, et les protéines solubles dans le stroma chloroplastique (dont la RubisCo) qui sont impliquées dans la fixation du CO_2. Les protéines photosynthétiques représentent une grande proportion de l'azote foliaire total : dans le blé, les protéines thylakoïdes et RubisCo représentent ensemble environ 50 % de l'azote foliaire total (Evans, 1989). Aussi, la fixation du carbone est dépendante de la teneur en azote foliaire (Braune *et al.*, 2009).

L'azote est absorbé principalement sous forme de nitrates par des transporteurs actifs *i.e.* qui nécessitent de l'énergie (Doddema and Telkamp, 1979; Pace and McClure, 1986; Siddiqi *et al.*, 1989). Il a été montré que la vitesse d'absorption des nitrates varie avec la teneur en sucre des racines (*e.g.* Delhon *et al.*, 1996).

Il existe de nombreuses boucles de rétroactions entre le carbone et l'azote au sein de la plante. Aussi, il est nécessaire de considérer un modèle du métabolisme du carbone et de l'azote à l'échelle de la plante entière pour simuler correctement les teneurs en métabolites carbonés et azotés dans chaque organe. Pour cela, le modèle développé au cours de l'étude s'appuie sur le modèle CN-Wheat (Barillot *et al.*, 2016*a*,*b*) développé préalablement. Ce dernier est présenté dans la partie suivante.

5 - Le modèle CN-Wheat initial

Le modèle CN-Wheat initial a été développé pour les stades post-floraison du blé, *i.e.* pour une architecture statique. CN-Wheat simule le métabolisme simplifié du carbone et de l'azote pour une talle individuelle. La talle est représentée comme un ensemble de compartiments botaniques (Figure 9 A) : plusieurs phytomères composés d'un entre-nœud, une gaine et un limbe, un compartiment pour les glumes de l'épi, un compartiment grains, un compartiment racines. Pour chaque organe photosynthétique, le modèle distingue les parties visibles et cachées qui ont des environnements lumineux différents. Chaque compartiment est caractérisé par une masse structurale (principalement les parois cellulaires), des concentrations en métabolites mobiles et de stockage et des dimensions. Le modèle considère aussi un pool commun de métabolites, le *phloème,* interconnecté à tous les compartiments botaniques et sans représentation spatialement explicite.

Les principaux aspects du métabolisme du carbone et de l'azote sont simulés pour chaque compartiment. Le modèle fournit alors l'évolution cours du temps des concentrations en métabolites dans chaque compartiment (Figure 9 B). Par soucis de parcimonie, le modèle ne considère que les principaux métabolites carbonés et azotés et les principaux processus du métabolisme carbone et azote. Un objectif de CN-Wheat est de simuler un bilan complet du carbone et de l'azote dans la plante. Pour cela, le modèle simule les processus d'acquisition de ressources et la respiration, la sénescence des tissus et la remobilisation des métabolites qui en résulte, et la synthèse, dégradation et le transport des métabolites (Figure 10). Les processus physiologiques dans chaque organe sont pilotés par l'environnement local, à savoir le phylloclimat et les concentrations en métabolites carbonés et azotés de l'organe. Le phylloclimat est simulé à partir d'une représentation 3D du couvert (Fournier *et al.*, 2003) et un modèle de répartition de la lumière (Chelle and Andrieu, 1998).

L'extension de la version initiale de CN-Wheat aux stades végétatifs, et donc pour une architecture dynamique (Figure 10), nécessite de définir, implémenter et calibrer principalement les processus suivants :

- Les lois de réponse de la croissance en masse et en dimensions des feuilles aux concentrations en métabolites simulées par le modèle
- Les coûts métaboliques associés à la croissance

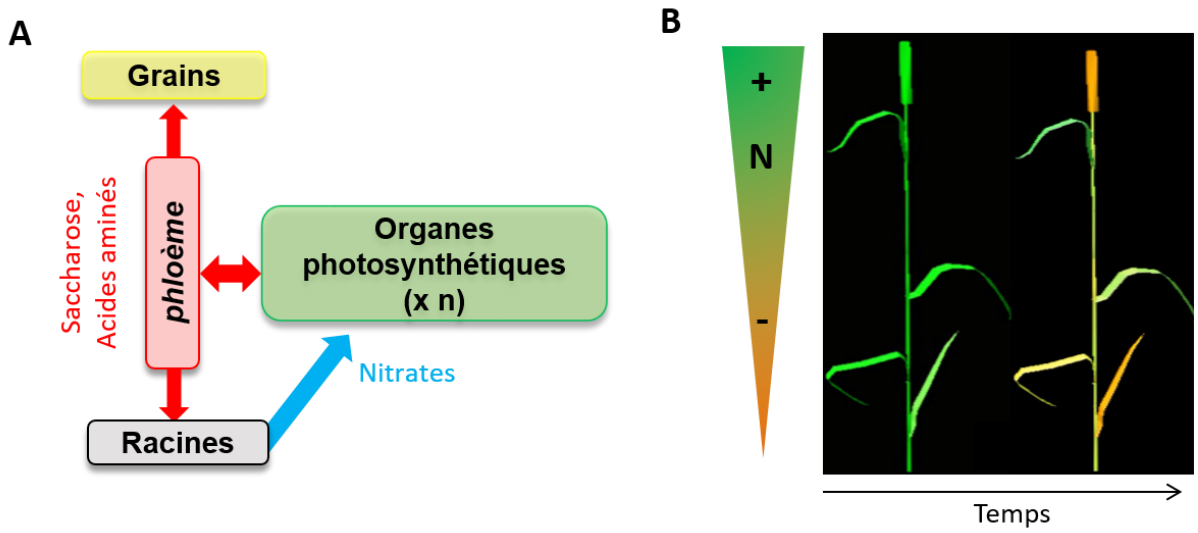

Figure 9 – Représentation de la plante dans la version initiale de CN-Wheat (Barillot *et al.*, 2016*a,b*). A : Représentation de la plante comme un ensemble de compartiments botaniques. B : Représentation 3D de la plante à deux dates. Les couleurs représentent les teneurs en azote simulées par le modèle à l'échelle de chaque compartiment botanique.

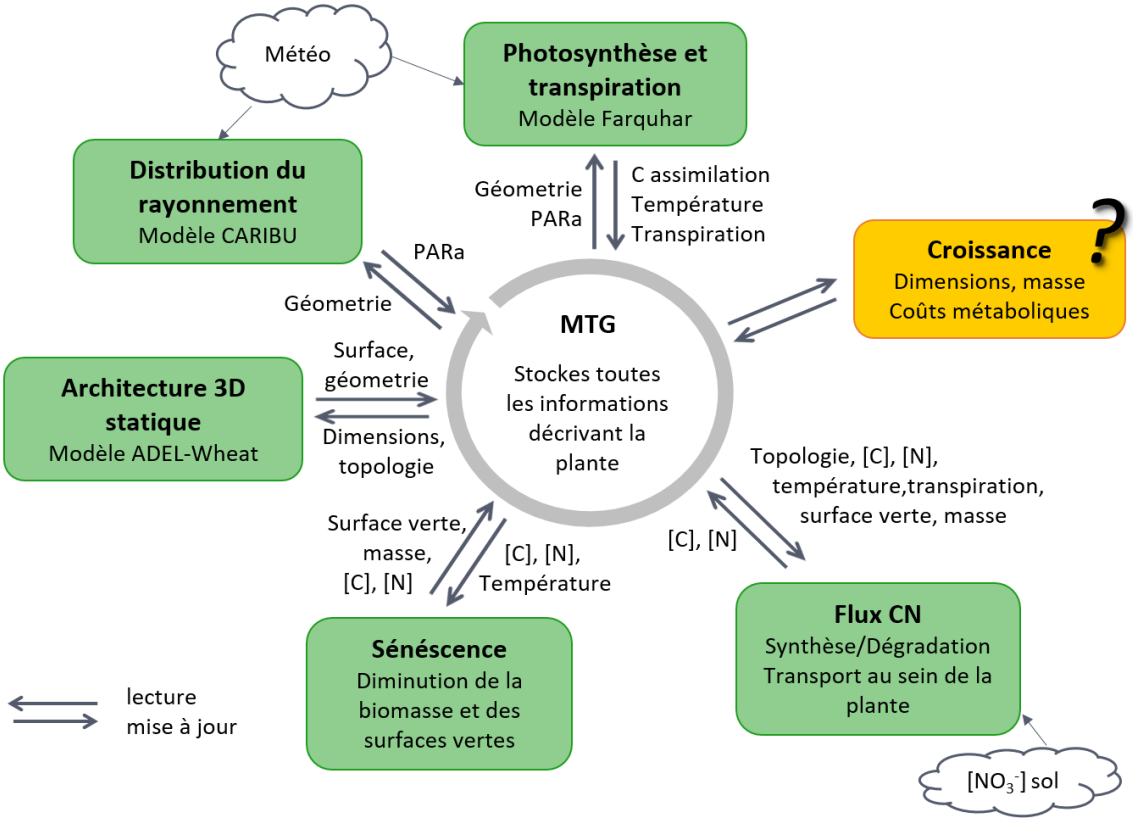

Figure 10 – Structure du modèle CN-Wheat initial (Barillot *et al.*, 2016*a,b*) développé préalablement pour une architecture statique (boîtes vertes) et développements à réaliser dans le cadre de l'étude (boîte organe + adaptation des boîtes vertes). Le modèle initial est le couplage d'un ensemble de sous-modèles qui échangent des informations via une structure centralisée de données, le MTG (Multiscale Tree Graph).

6 - Objectifs et étapes de l'étude

La plasticité phénotypique des plantes est le résultat d'une adaptation du fonctionnement de la plante aux conditions de croissance. Nous avons vu que les modèles existants traitant du couplage entre la disponibilité des ressources et la croissance sont limités pour simuler le fonctionnement de la plante dans des conditions de croissance contrastées car ils reposent largement sur des formalismes empiriques.

L'objectif de la présente étude est de proposer un modèle reposant sur un degré de mécanisme plus élevé que les modèles actuels. Nous avons adopté une approche « Bottom-Up », dans laquelle le comportement de la plante entière émerge des comportements locaux (*e.g.* Kroon et al., 2005; Poorter et al., 2013; Chang and Zhu, 2017). La plasticité phénotypique y résulte donc de l'intégration de la réponse individuelle de chaque organe de la plante (Kroon *et al.*, 2005). Plus spécifiquement, **ce travail vise à construire un FSPM de morphogenèse aérienne de Poacées qui considère le fonctionnement de la plante entière et qui simule l'acquisition de traits de feuille et de plante comme propriétés résultant des interactions entre la morphogenèse, les facteurs environnementaux et les activités source-puits au sein de la plante**.

Parmi de nombreux facteurs influençant la morphogénèse des plantes, l'étude se limite aux effets du carbone et de l'azote qui sont (avec l'eau) les principaux facteurs limitant la croissance (McIntyre, 2001). Les sous-objectifs de ce travail ont été (i) d'identifier des lois de réponse de la morphogénèse aux concentrations en métabolites carbonés et azotés, (ii) d'intégrer les interactions entre le métabolisme du carbone et de l'azote à l'échelle de la plante entière, et (iii) de proposer un bilan complet du carbone et de l'azote de la plante en croissance.

L'étude des mécanismes de la mise en place de la série foliaire a permis de dégager nos deux principales hypothèses de modélisation :

- les concentrations locales en métabolites carbonées et azotées pilotent les vitesses d'allongement des feuilles et certains traits foliaires majeurs
- des règles de coordination entre les feuilles successives marquent la durée d'allongement des feuilles et les moments où sont définis certains traits foliaires majeurs.

La thèse soutenue est qu'une telle approche de modélisation permet de simuler, de façon réaliste, la morphogénèse pour une large gamme de conditions de croissance contrastées en lumière et en azote.

Afin de tester cette hypothèse scientifique, le modèle a été développé, implémenté, calibré et évalué. Parallèlement au développement et à l'implémentation du modèle, une expérimentation a été menée. Les différentes étapes du travail sont exposées dans le paragraphe suivant.

La base bibliographique et expérimentale de notre étude concerne principalement le blé, toutefois une composante centrale de notre travail est d'avoir développé un modèle qui soit largement **générique et représentatif** de la plupart des Poacées.

Organisation du manuscrit de thèse

Le **chapitre 1** est dédié à la présentation du modèle et à l'évaluation de sa capacité à simuler de façon réaliste les traits foliaires et les traits de plante dans des conditions croissance usuelles au champ.

Le **chapitre 2** est consacré à l'évaluation de la capacité du modèle à simuler la plasticité phénotypique de la plante. Deux expérimentations virtuelles ont été réalisées. La première est un ensemble de simulations dans des conditions contrastées de densité de plante, de rayonnement et de fertilisation azotée. La seconde correspond à des simulations avec différents états initiaux de plante, dans plusieurs conditions de croissance. Ces deux expérimentations virtuelles ont conduit à certaines adaptations du modèle par rapport à la version présentée chapitre 1.

Le **chapitre 3** présente les résultats d'une expérimentation qui a été réalisée au cours de l'étude. Cette expérimentation avait deux objectifs. Le premier objectif était de caractériser les conséquences d'un stress précoce transitoire sur la croissance de blé pour ensuite discuter la capacité de CN-Wheat à simuler cet impact en comparant les résultats expérimentaux aux simulations du chapitre 2 pour différents états initiaux de plante. Le second objectif était de recueillir des données sur la composition biochimique des organes. Ces données sont nécessaires à la définition du modèle et à son évaluation. Les données recueillies ont été en partie utilisées pour la définition du modèle au chapitre 1.

La discussion générale synthétise les principaux résultats du travail et discute la fiabilité, les limites et les contraintes des principales hypothèses du modèle. Enfin, cette partie présente des perspectives possibles à court, moyen et plus long termes.

Les chapitres sont présentés sous forme d'articles scientifiques. Le chapitre 1 est publié dans la revue *Journal of Experimental Botany*. Les chapitres 2 et 3 seront adaptés en vue de leur publication prochaine. A la fin de chaque chapitre, un paragraphe résume en français les principaux résultats du chapitre et la façon dont il s'articule avec la suite du manuscrit.

Chapter 1 - Model description and evaluation for usual field conditions

1.1 - Introduction

Reconciling productivity and sustainability in the context of global change is a critical challenge that agriculture has to face. Mechanistic models can explore plant behaviour in present and future climates, thus allowing investigation of the benefits and drawbacks of novel crop management as well as the identification of plant traits that can be potential targets for plant breeding. For this purpose, models should provide a holistic view of whole-plant functioning by integrating the interactions between environmental factors, morphogenesis, and source-sink activities within the plant. Functional-structural plant models (FSPMs) have opened up possibilities to account for these plant-environment interactions through a realistic description of individual plant architecture (Prusinkiewicz, 1998; Godin and Sinoquet, 2005). Using an explicit representation of the individual variability and heterogeneity of resource availability, this approach provides a framework for understanding and integrating the mechanisms of plant competition and growth in a large range of agronomic situations (Vos *et al.*, 2010; DeJong *et al.*, 2011; Sievänen *et al.*, 2014; Barillot *et al.*, 2014; Gaudio *et al.*, 2019). FSPMs are based on a broad diversity of paradigms, ranging from empirical descriptions of growth to process-based approaches accounting for the trophic status of plants. Among the latter, most crop FSPMs consider only carbon (C) and are based on a supply:demand approach, in which resource allocation among organs is driven by sink priorities defined from empirical relations. Only a few models address the question of supply feedbacks on demand size (Luquet *et al.*, 2006), and key nutrients such as nitrogen (N) and water are rarely considered (Bertheloot *et al.*, 2011; Lobet *et al.*, 2014; Coussement *et al.*, 2018). For the sake of simplicity, existing models use as inputs key traits, which are actually emerging properties of plant functioning and vary with growth conditions. For example, since the rate of shoot development is relatively stable in thermal time (McMaster, 2005), most models have a phyllochron parameter to drive the duration of leaf elongation, while it has been shown that phyllochron may increase with C, N, or water stresses (Cutforth *et al.*, 1992; Longnecker *et al.*, 1993; Muller and Martre, 2019). From a mechanistic point of view, leaf extension drives the phyllochron rather than the opposite. Another example is the relationship between leaf mass and dimension, commonly included in models by using a constant specific leaf area (SLA), while SLA may in fact strongly vary between environments (Rawson *et al.*, 1987; Tardieu *et al.*, 1999; Poorter *et al.*, 2009). Such approximations can lead to large errors in the predictions of plant surface or biomass production. Finally, as pointed out in the review of Poorter *et al.* (2013), we still lack mechanistic modelling approaches simulating whole-plant functioning and trait acquisition as properties arising from the feedbacks between morphogenesis, environmental factors, and source-sink activities within the plant.

For grasses, leaf growth has been extensively studied in terms of (i) histology, (ii) coordination between the elongation of successive leaves, and (iii) regulation by the trophic status. The growth zone is located at the leaf base, inside the pseudostem made of previous sheaths (Begg and Wright, 1962), where cells move through division, elongation-only, and mature zones (Williams, 1975; Skinner and Nelson, 1995; Durand *et al.*, 1999). The length of the zone hidden in the pseudostem strongly influences the elongation of the growing leaf and also impacts the following leaves. Synchronies between emergence events out of the pseudostem and major changes

in the kinetics of leaf elongation have been repeatedly documented and formalized as coordination rules in models to account for a self-regulation of plant architecture (Durand *et al.*, 1998; Fournier *et al.*, 2005; Verdenal *et al.*, 2008; Zhu *et al.*, 2014; Vidal and Andrieu, 2020). Finally, a large number of studies have demonstrated the plasticity of leaf dimensions and the correlation of this plasticity with C and N content in the growth zone through an effect on the rate of cell division and/or elongation (Kemp, 1980*a*, page 1980; Volenec and Nelson, 1984; Schnyder and Nelson, 1987; Gastal and Nelson, 1994; Fricke, 2002).

The present paper describes a model of whole-plant functioning of grass based on a mechanistic representation of leaf growth. The main challenge was to identify a generic frame based on the existing knowledge of leaf growth integrating the effects of environmental conditions. The model relies on an explicit description of plant architecture and two core hypotheses. First, leaf elongation rate and key leaf traits are regulated by the concentrations of C and N metabolites in the growth zone. Second, the transition between successive phases of elongation is triggered according to coordination within and between phytomers. Recently, we have developed CN-Wheat, an FSPM simulating C and N metabolism during the post-flowering stages in wheat, that is, for a static shoot architecture (Barillot *et al.*, 2016a). For the present work, we focused on the implementation of a leaf growth model in CN-Wheat. The description of the metabolism was thus extended to the growth zone of leaves. Interactions of plants with environmental factors were calculated from a dynamic representation of leaf geometry. We evaluated the model's ability to simulate leaf growth and key traits at leaf and plant scale. Finally, we explored the sink-source relations in a growing plant.

1.2 - Materials and methods

Model description

The present work describes a generic frame to simulate the source-sink relations in interaction with the development of plant architecture and local environmental factors. The present implementation focuses on the early stages of development of winter wheat (*Triticum aestivum*) from the exhaustion of grain reserves to the beginning of stem elongation, that is, when leaf and root growth are the main morphogenetic processes. Later stages are not simulated because this would require accounting for tiller regression, which was beyond the scope of this work. The following sections provide an overview of the whole-plant model before focusing on the main assumptions related to leaf growth and metabolism. Finally, we describe the calibration and evaluation of the model. Detailed equations and parameters are available in Supplementary Protocol S1.1.1. The terms used in this paper to describe the morphology and development of grasses and model components are defined in Supplementary Data S1.3.

Overview of the model

Botanical structure of the model

The model can simulate an individual plant or a canopy, described as a collection of plants. A plant is composed of one or more tillers. As a provisional choice, all tillers share a single root compartment and a single metabolite pool without explicit spatial representation (hereafter called *phloem*; this does not intend to spatially represent the phloem tube of the living plant but instead mimics the functioning of this organ) allowing fluxes of mobile metabolites among organs. Each tiller has several growing and mature phytomers, each consisting of a leaf (consisting of a lamina and a sheath) and an internode. The number of phytomers increases during the simulation as new phytomers are initiated. In a growing phytomer, the growth zone, located inside the pseudostem, is represented by one single compartment, denoted *hz* (for hidden growth zone). Each type of mature tissue produced by the growth zones (lamina, sheath, or internode) is represented by one or two compartment(s) because we distinguish between the enclosed and exposed tissues to account for their contrasting light regimes.

Morphogenesis

In our approach, leaf growth is driven by (i) local metabolite concentrations, which depend on the source-sink relations and the environmental conditions, and (ii) coordination rules between successive leaves: that is, leaf elongation follows a two-phase kinetics and the emergence of a leaf outside the pseudostem triggers the phase transition for the following leaf. Although internode extension is limited for the stages addressed here, their growth has been implemented and partially calibrated (Supplementary Protocol S1.1.1). Briefly, the modelling of internode elongation follows the same principles as for leaves, except that for internodes the phase transition is triggered by leaf ligulation. Additionally, an empirical sub-model of tillering was implemented (Supplementary Protocol S1.1.1) to account for self-shading between tillers and tiller growth costs (Williams, 1964). Tiller emergence is coordinated with the emergence of leaves on the main stem (MS), and their botanical organization, metabolism, and growth dynamics were approximated from that of the MS.

Metabolism

The model accounts for different groups of state variables for each organ: dimensions (length, maximum width), structural mass, which is the dry mass 'immobilized' mainly in the cell wall compounds, and concentrations of mobile metabolites [sucrose, nitrates, amino acids (AA)] and storage metabolites (starch, fructans, proteins). Metabolite dynamics are described by differential equations reflecting the physiological activities occurring in the shoot (*e.g.* photosynthesis, C and N synthesis/degradation, *phloem* loading, growth, tissue death) and roots (*e.g.* N uptake, *phloem* unloading, transport of nitrates to the shoot, exudation, growth, tissue death). Both metabolite concentrations and the physical environment of each organ drive these activities. Compared with the initial version of CN-Wheat, new metabolic regulations by temperature were implemented for *phloem* conductivity and the rates of synthesis and degradation of metabolites (see Supplementary Protocol S1.1.2).

Implementation

Based on a modular composition described in Barillot *et al.* (2019), the current model is composed of (Figure 1.1): (i) sub-models of leaf, internode, and root growth; (ii) a dynamic representation of the three-dimensional (3D) geometry of plants, which extends the ADEL-Wheat model (Fournier *et al.*, 2003; Supplementary Protocol S1.1.3); (iii) a sub-model of light distribution within 3D canopies (Chelle and Andrieu, 1998); and (iv) sub-models simulating photosynthesis, N acquisition, synthesis and allocation of C and N metabolites, and senescence at the organ level, which extends the initial version of CN-Wheat (Barillot *et al.*, 2016a). Model inputs are hourly climatic conditions (temperature, light, humidity, CO2, wind), initial soil NO3-, and initial dimensions, mass, and metabolic composition of individual organs at the seedling stage. The whole composition is implemented in the OpenAlea platform (Pradal *et al.*, 2008, 2015) as a set of modular sub-models communicating via a central data structure, the multiscale tree graph (MTG) (Fournier *et al.*, 2010; Garin *et al.*, 2014; Albasha *et al.*, 2019; Barillot *et al.*, 2019; Reyes *et al.*, 2020). The code is open source, available on GitHub (https://github.com/openalea-incubator/WheatFspm), and released under a CecILL-C license. The archive of the code used to generate the present results is available at http://doi.org/10.5281/zenodo.3759714.

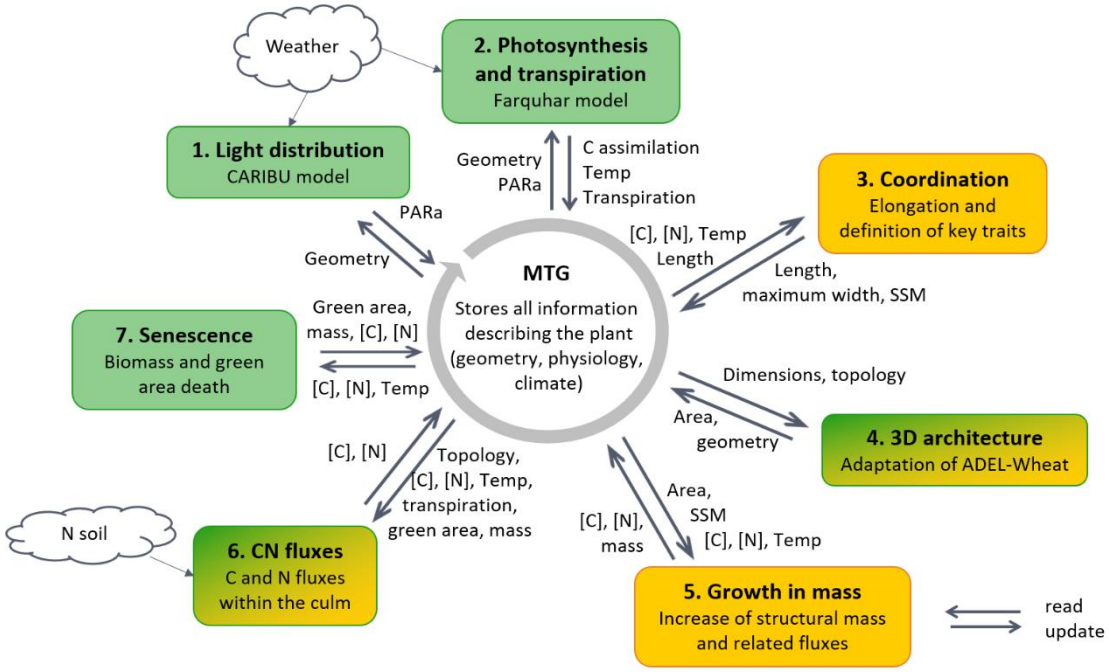

Figure 1.1 - Coupling of several sub-models using the multiscale tree graph (MTG) formalism as a central data structure. Green boxes 7 are sub-models that already existed (Barillot *et al.*, 2016a), yellow boxes are newly developed sub-models to integrate plant growth in dimensions and mass, and two-colour boxes are former sub-models that were adapted to model a growing plant. The numbering refers to the order in which the sub-models are called for the simulations. Briefly, the light distribution sub-model calculates the fraction, *f*PAR, of incident photosynthetically active radiation (PAR) absorbed by each phytoelement of the plant, from the 3D architecture of the plant and the light sources. The absolute absorbed PAR (PARa) is then calculated from the incident PAR and *f*PAR. The photosynthesis and transpiration sub-model calculates C acquisition, transpiration rate, and organ temperature (Temp). The coordination sub-model calculates the elongation (increase in length) of the leaves and internodes, as well as other key traits [maximum leaf width, specific structural mass (SSM)] based on the current status of the organs in term, of length, metabolite concentrations ([C], [N]), and Temp. The sub-module ADEL then updates the 3D architecture, which results in an increase in area. The increase in structural mass of the shoot organs is calculated from their increase in area and SSM. Based on the above-mentioned calculations, a solver of ordinary differential equations computes N acquisition, reactions of synthesis and degradation, and C and N fluxes. Finally, the senescence is calculated from the protein concentration and the age of each organ.

Detailed assumptions of the leaf growth sub-models

Leaf primordia are initiated according to a constant rate modulated by temperature. The plastochron and the final number of leaves are model parameters, as are the initial length, structural mass, and composition of a primordium.

Structure of the growing leaf

Before emergence, the leaf is represented only by a *hz* compartment (Figure 1.2). After emergence, the growing leaf is represented by a *hz*, an emerged lamina and, later, by an emerged sheath compartment. At the end of leaf elongation, the *hz* compartment is superseded by an enclosed mature sheath compartment, created with the same dimensions, structural mass, and metabolites as the former *hz*.

For the sake of simplicity, the growing zone was identified as the hidden part of the growing leaf, and thus was represented by the *hz* compartment. This is a simplified representation of the reality, as the hidden part of a growing leaf actually encompasses a dividing and an elongating zone, plus some mature tissues. Moreover, no distinction was made between lamina and sheath. We assumed that the *hz* is supplied with C and N by the *phloem* and by emerged leaf tissues if any are present (Figure 1.3). The *hz* is attributed a structural mass variable (including structural N), as well as mobile (sucrose and AA) and storage (fructans and proteins) metabolites. The metabolism of the emerged lamina and sheath tissues is the same as that of mature photosynthetic organs, except that the former export C and N towards their own *hz*.

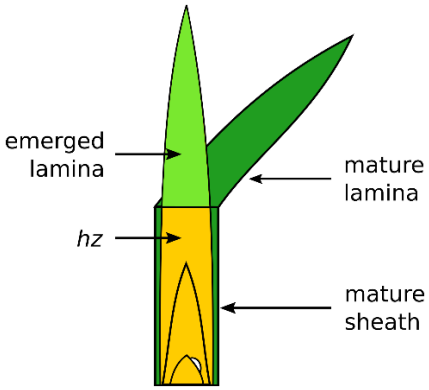

Figure 1.2 - Structure of a vegetative culm. Three types of compartments are considered: mature photosynthetic organs, the emerged part of the growing organ, and the hidden part of the growing leaf (*hz*).

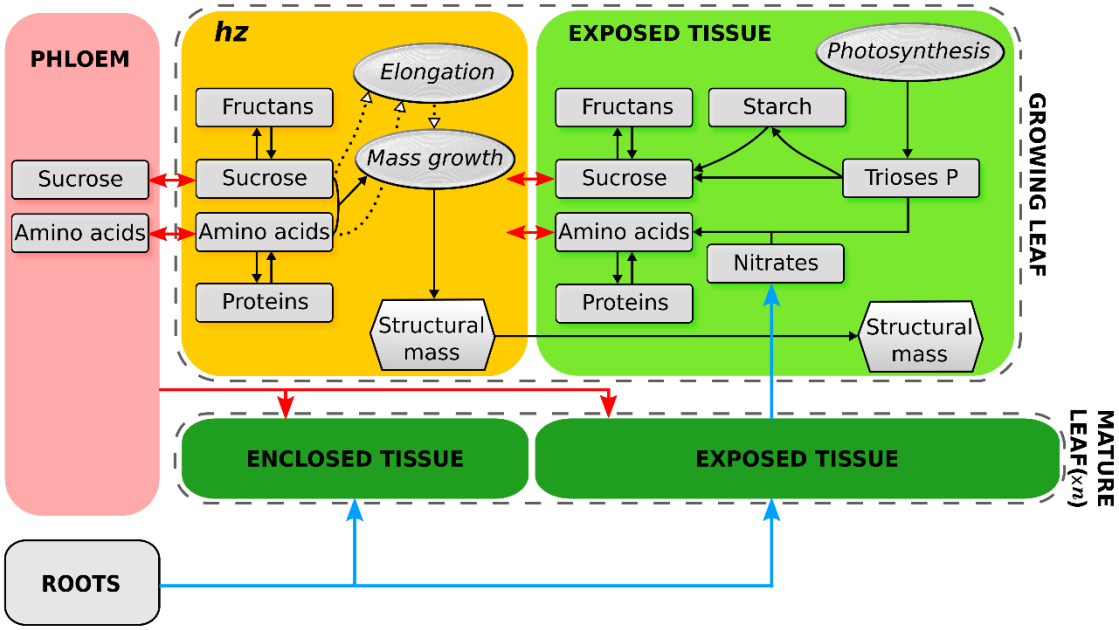

Figure 1.3 - Representation of the growing leaf and its connections with other plant compartments. The leaf is described as a set of botanical compartments (coloured large rectangles) with structural masses (hexagons) and metabolite concentrations (rectangles). Leaf elongation and mass growth processes (ovals) take place in the hidden growth zone (*hz*, orange) and are regulated (dotted arrows) by local metabolite concentrations. Mature tissues are in green. Only exposed tissues are photosynthetic. Fluxes of sucrose and amino acids between compartments are represented by red arrows. Imports of nitrates and amino acids from the root compartment are represented by blue arrows.

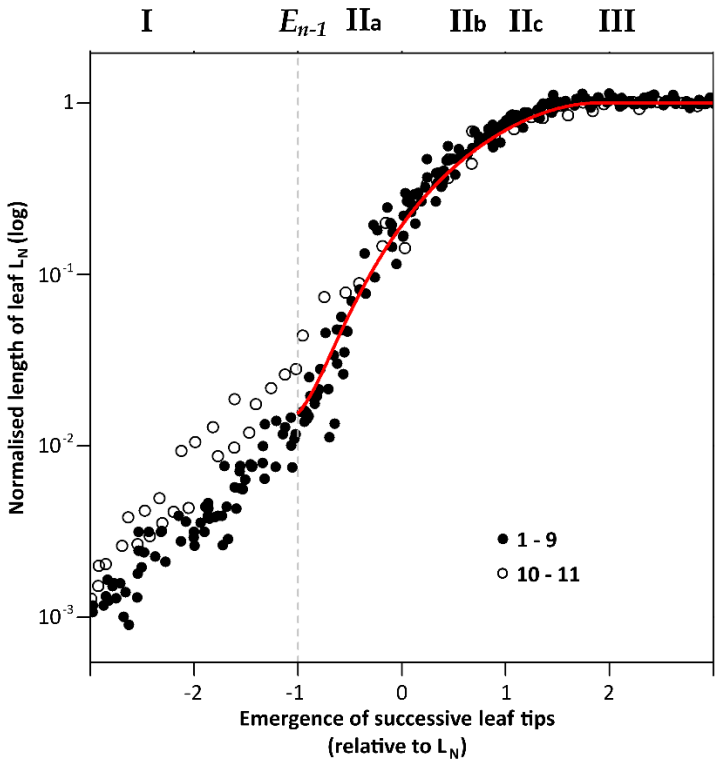

Figure 1.4 - Normalized length (logarithmic scale) of main stem leaves versus the phyllochronic time relative to leaf emergence (based on Fournier *et al.*, 2005; Supplementary Data S1.3 for definitions of terms). Symbols are phytomer rank (11=flag leaf). Each point is the median of 5-10 observations. Numbers above the plot show the main phases of leaf growth, described in the main text and Figure 1.5. The dashed line is the emergence of the previous leaf (E_{n-1}), which triggers the transition from an exponential-like elongation (phase I) to a sigmoidal elongation (phase II, solid curve).

Regulation of leaf growth in mass and dimensions by C and N metabolism and coordination rules

Fournier *et al.* (2005) reported that, starting from one phyllochron before its emergence, the normalized length of wheat leaves increases according to a common pattern for all phytomers when expressed in phyllochronic time, that is, thermal time normalized by the rate of leaf emergence (Figure 1.4). We also observed this property on two supplementary datasets (Malvoisin, 1984; Ljutovac, 2002; data not shown). Based on these observations, we modelled leaf elongation kinetics as two successive phases, with the transition between the phases being coordinated with the emergence of the previous leaf. The emergence of leaf n will be denoted E_n hereafter. The model is briefly described below (see Supplementary Protocol S1.1.1 for details of the equations describing leaf growth).

Throughout the first phase (Figure 1.5, phase I), which mainly encompasses the formation of the cell division zone, leaf length follows an exponential-like function whose relative elongation rate (RER) is driven by (i) the concentrations of sucrose and AA in the *hz*, (ii) temperature, and (iii) leaf rank, which determines the maximum RER. The increase in leaf structural mass is estimated from an empirical relationship with leaf length, fitted from anatomical observations (Williams and Rijven, 1965). As the leaf grows, it will emerge from the pseudostem formed by previous leaves. This event is central in our approach, since E_{n-1} triggers the transition from the first to the second elongation phase of leaf n (Figure 1.5).

Throughout the second phase (Figure 1.5, phases IIa-IIc), leaf elongation follows a sigmoidal function of leaf physiological age modulated by air temperature (Supplementary Protocol S1.1.2). The sigmoidal function is identical for all leaves and scaled according to leaf length at E_{n-1}. From E_{n-1} to leaf maturity, the leaf length kinetics are almost predefined and only slightly modulated by the concentrations of sucrose and AA in the *hz*. We therefore assumed that the trophic status does not impact on the time required to reach the final length but, rather, the elongation rate has such an effect. The final length of laminae and sheaths are calculated according to an ontogenic sheath:lamina ratio (Dornbusch *et al.*, 2011; Abichou, 2016). Leaf width and SLA are important traits that vary with growth conditions, in particular light availability (Friend, 1965; Kemp, 1981, page 1981; Schnyder and Nelson, 1989; Fournier *et al.*, 2001). We hypothesized that the variability reported in response to light conditions originated from a response to local C availability (Bertin and Gary, 1998). We also considered that variations in SLA partly originated from variations in specific structural masses (SSMs) of laminae (g m^{-2}) and sheaths (g m^{-1}). In order to simply account for this plasticity, the maximal leaf width and the SSMs of laminae and sheaths are calculated at E_n according to the sucrose concentration in the *hz* averaged over the previous two phyllochrons. The structural masses of the emerged laminae and sheaths are then dynamically calculated from their respective SSMs and dimensions. Lamina shape and area are calculated according to lamina length, maximal width, and rank (Dornbusch and Andrieu, 2010). Once the leaf is fully mature (Figure 1.5, phase III), the former *hz* is considered as the mature hidden part of the sheath.

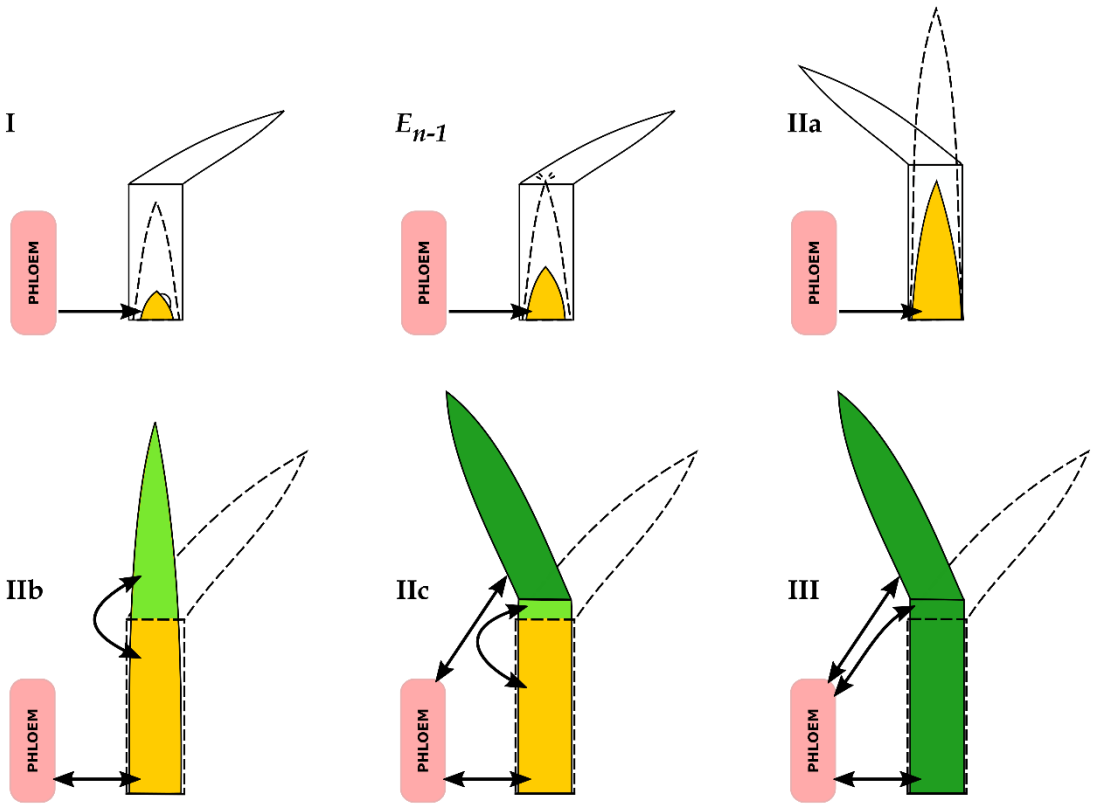

Figure 1.5 - Illustration of the elongation of leaf n (shaded) as represented in the model. See Figures 1.2 and 1.3 for identification of the compartments of leaf n. The dashed leaf is leaf n-1. Only the mature leaf that defines the pseudostem is represented, which is leaf n-3 in I and E_{n-1}, leaf n-2 in IIa, and leaf n in IIb, IIc, and III. For simplicity, internodes are not shown. I: From the initiation of leaf n to the emergence of the previous leaf (E_{n-1}), leaf n is a primordium surrounding the shoot apical meristem. Leaf n is represented as a homogenous hidden growth zone (*hz*), which imports metabolites from the *phloem* and follows an exponential-like growth. At E_{n-1} several key variables of leaf n are set and sigmoidal elongation starts. IIa: Leaf n is fully hidden inside the pseudostem and elongates according to its predefined sigmoidal function. IIb: The emerged lamina exchanges metabolites exclusively with the *hz*. IIc: The lamina is mature and now connected to the *phloem*. The sheath is still growing; its emerged part exclusively exchanges metabolites with the *hz*. III: The leaf is fully mature. The former *hz* is now the mature hidden part of the sheath.

Carbon and nitrogen metabolism of the growing leaf

The model of leaf elongation requires an explicit description of metabolite distribution at organ scale in order to provide the local concentrations of sucrose and AA that regulate the elongation rate and the key traits described in the previous section. In turn, we assume that the growth area and SSMs drive the structural mass synthesis and subsequent consumption of *hz* metabolites. The cost is calculated by assuming a constant fraction of C and N in the structural mass. Growth respiration also consumes sucrose according to a constant yield (Thornley and Cannell, 2000). Fluxes of sucrose and AA between the *phloem* and the *hz* follow diffusion laws, with conductance depending on the *hz* structural mass and temperature. After leaf emergence, we considered that the emerged tissues export sucrose and AA to their related *hz*. At maturity, the sheath and lamina directly load sucrose and AA into the *phloem* according to the transport formalism described in Barillot *et al.* (2016a).

Storage pools of C (fructans) and N (proteins) have also been attributed to *hz* (Schnyder *et al.*, 2000). As for photosynthetic tissues, the synthesis and degradation of fructans depend on their local concentration and the sucrose concentration (Barillot *et al.*, 2016a). The rate of protein synthesis is calculated from a Michaelis-Menten function of AA concentration. Since Gastal and Nelson (1994) noted that protein deposition mainly occurred in the division zone of growing tall fescue leaves, we introduced a dependency of the maximal rate of protein synthesis to a length ratio representing the size of the division zone in the *hz*.

The mature leaf

Once growth is complete, the leaf consists of a mature lamina and sheath, whose metabolisms are described in Barillot *et al.* (2016a). The model also accounts for tissue death (Supplementary Protocol S1.1.1). At each time step, a constant fraction of green area is lost if (i) protein concentration decreases below a fraction of the maximum protein concentration reached after leaf ligulation (Barillot *et al.*, 2016a) or (ii) the physiological age is higher than a fitted threshold (which applies only to laminae). The structural mass of the remaining green tissues is reduced proportionally to the green area, while a fraction of storage metabolites is remobilized towards the green tissue as sucrose and AA.

Model evaluation procedure

The whole-plant model was run to simulate a wheat plant from the emergence of leaf 4 to the beginning of stem elongation (2500 h). The model was run with an hourly time step, except for the 3D representation of the canopy, which was updated every 4 h. This means that the absorbed PAR was calculated from hourly values of incident PAR, applied to a structure updated every 4 h, to limit the computational cost of the calculation of the distribution of light between phytoelements.

Simulations were compared with three complementary experimental datasets (Exp1-Exp3; Supplementary Protocol S1.1.5) representative of optimal field conditions in north-western Europe. Detailed experimental data allowing comparisons with model outputs for identical conditions were available only for a few traits; the other traits were evaluated qualitatively, using data collected for various stages of development, grass species, or growth conditions. The whole model gathers approximately 160 parameters, some of which were set in the post-flowering version of CN-Wheat (Barillot *et al.*, 2016b), while new parameters were pragmatically calibrated or taken from the literature (Supplementary Table S1.1.2). Plant density was set to 250 plants m^{-2} and soil NO3-was initialized at 6 g m^{-2}. To simulate fertilization of Exp1, soil NO3-was increased by 5 g m^{-2} at t=2016 h. We used hourly weather data (temperature, incident PAR, humidity, and wind speed) from Exp1 (Supplementary Figure S1.2.1); atmospheric CO2 concentration was set at 360 ppm. Initialization of the state variables for each organ was performed from data of Exp1-Exp3. The detailed procedures for parameter calibration and model evaluation are presented in Supplementary Protocol S1.1.5.

1.3 - Results

Figure 1.6 illustrates the simulated growth of a plant from E_4 to ~E_9. First, we assessed the ability of the model to simulate some major leaf traits and realistic dynamics of shoot development. Second, we evaluated whether agronomic traits, usually observed at canopy level, emerge from the integration of the local processes simulated at organ scale. Finally, we investigated the sink-source relations within the plant, with a particular focus on C.

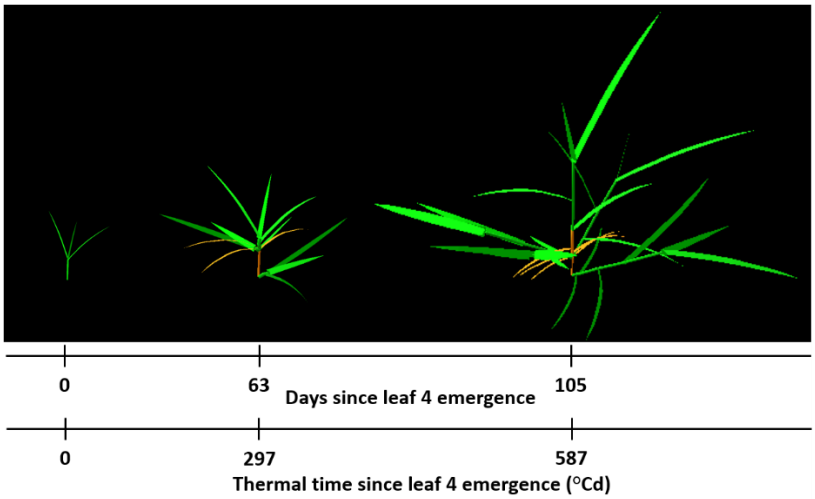

Figure 1.6 - 3D shoot architecture of a plant at three simulation steps. At day 63 and day 105, three and five leaves of the main-stem were fully senescent, respectively. Brown colour represents dead tissues.

Dynamics of shoot development

The model accurately predicted the increase in the final length of leaves and sheaths with foliar rank observed in Exp1 (Figure 1.7A). In the model, variations of final leaf length with the metabolic status and environmental conditions are generated by variations of the duration of the exponential growth prior to E_{n-1} (phase I) and of the elongation rate (mainly during phase I). Leaf RER observed in Exp1 markedly decreased with leaf rank (Figure 1.7B), which is in line with studies reporting that multiple primordia of wheat leaves elongate synchronously with different RERs (Williams, 1975; Malvoisin, 1984; Ljutovac, 2002). Simulated RERs, which depend on metabolite concentrations in the *hz*, temperature, and leaf rank, were aligned with these observations, ranging from 1.5 to 2.8×10^{-6} s^{-1} (see Supplementary Protocol S1.2.1 for calculations). The model simulates maximal lamina widths from their final length and sucrose concentration in the *hz* (Eqn. 7 in Supplementary Table S1.1.1), which predicted the increase in maximum lamina width with leaf rank, ranging from 0.4 to 1.2 cm (Figure 1.7C).

Overall, the simulated SSMs of laminae and sheaths showed a positive gradient with leaf rank (Figure 1.7D), which arose from the dynamics of sucrose concentration in the *hz* and an ontogenic parameter for sheaths. Simulations of metabolic content and structural masses allowed the prediction of specific leaf nitrogen (SLN; Figure 1.8) and SLA (Supplementary Figure S1.2.2B) as an emerging property of the model. SLN varied between

0.8 and 1.5 g m^{-2}, showing at any time a vertical gradient from the lower to the upper leaves. For leaves that emerged after model initiation, the vertical range of SLN increased from ~0.1 g m^{-2} at 200 °Cd to ~0.5 g m^{-2} at 500 °Cd. This is in line with data from the literature; for example, for spring wheat with optimal N fertilization, Dreccer *et al.* (2000) reported a vertical range of SLN of 0.7 g m^{-2} before canopy closure. The SLA of individual leaves increased from emergence to ligulation and was maximal for leaf 4 (~40 m^2 kg^{-1}) and then decreased for the following leaves (leaf 9, ~27 m^2 kg^{-1}).

In our simulations, leaves emerged at relatively stable thermal time intervals (Figure 1.7E). On average for all leaves, phyllochron (see Supplementary Protocol S1.2.1 for calculation) was 104 °Cd (95% confidence interval 99-109 °Cd), which is reasonably close to the observations (111 °Cd ±0.7). Phyllochron stability is a major property of the model emerging from coordination rules and the modulation of elongation rates by metabolic concentrations.

The dynamics of the decimal green leaf number (GLN) of the MS (Eqn. S1.2.1 in Supplementary Protocol S1.2.1) were compared with four independent datasets representing three winter wheat cultivars (Abichou, 2016). Experimental data followed typical kinetics (Figure 1.9A): GLN first increased up to the ligulation of leaf 5, then senescence began and GLN declined until the ligulation of the fourth leaf from the top (leaf 7 in our simulation). The overall trend of GLN was well captured by the model, although the model anticipated the senescence of leaf 1, which resulted in a transitory underestimation of GLN by one leaf. The senescence of this leaf was triggered by a low N content in the model, meaning that either the N dynamics were not well simulated or the rule for triggering senescence is not adapted to young leaves, or possibly both. Since leaf 1 is small, the photosynthetic area was underestimated by only 12% at that time (Supplementary Figure S1.2.2A).

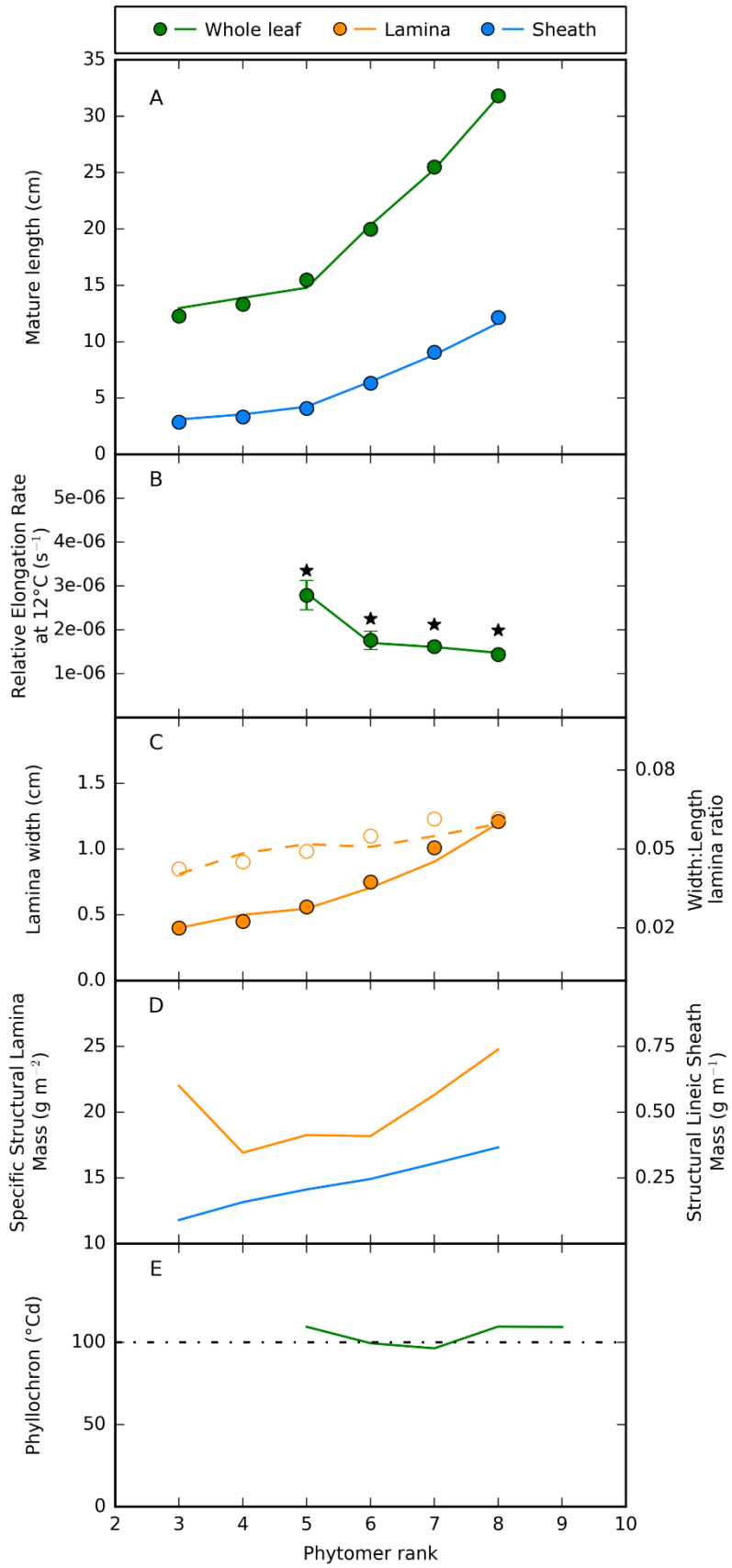

Figure 1.7 - Leaf traits on the main stem. (A) Final length of the whole leaf and of the sheath. Simulations are represented by solid lines and experimental data (Exp1) are represented by dots (confidence intervals of observed lengths are smaller than symbols). (B) Average RER of leaves during the first elongation phase, calculated from simulations (solid curve) and experimental data (Exp1, dots). Vertical bars represent the 95% confidence intervals. Confidence intervals for simulated RER are not shown (<1e-8). Asterisks indicate the maximal RER (see Supplementary Table S1.1.2 for model parameters). (C) Maximal lamina width simulated (solid line) and observed (filled circles); the dotted line and open circles are the simulated and observed ratio between lamina maximal width and final length (no confidence interval is available for width observations). (D) Specific structural lamina mass and structural lineic sheath mass simulated by the model. (E) Simulated interval (°Cd) leaf emergence dates. At the end of the simulation, leaf 10 is still hidden in the pseudostem.

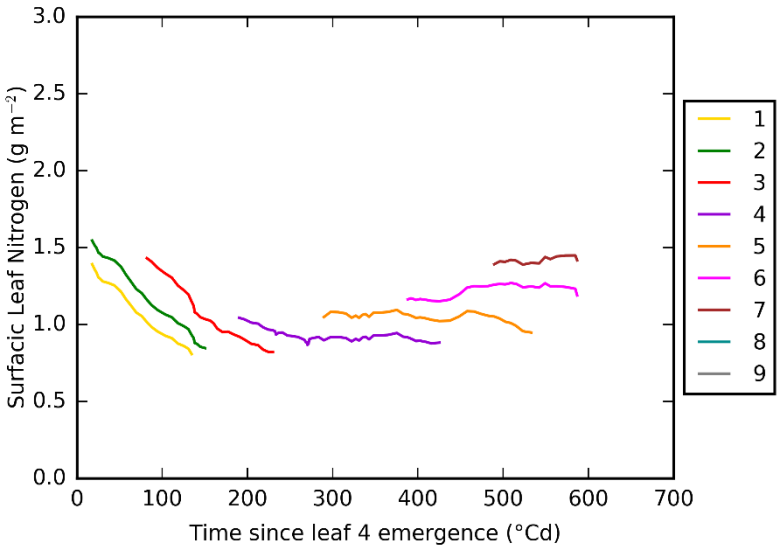

Figure 1.8 - Specific leaf nitrogen of laminae from leaf ligulation to the start of senescence. Colours represent the individual phytomers (see right panel for identification).

The simulation of the green area index (GAI; Eqn. S1.2.2 in Supplementary Protocol S1.2.1) followed an exponential dynamics (Figure 1.9B) aligned with observations for *cv.* Soissons and Caphorn. Increases in GAI in the model resulted from the development of leaves on the MS and the tillers. In the present simulation, four primary tillers have emerged following the concept of cohorts. At the end of the simulation, the canopy reached a GAI of 3 and ground cover, represented by the fraction of incident PAR absorbed by the canopy, was above 0.8, indicating canopy closure (Figure 1.9C). The close agreement between observed and simulated GAIs means that the estimates of absorbed PAR were calculated from realistic canopies. The PAR absorbed per unit surface of green tissues (Figure 1.9D) showed large daily oscillations but no clear trend during the simulated period (mean ~3.5 mol m^{-2} d^{-1}). Altogether, these results show that the canopy completely changed from a population of isolated plants to a closed canopy with self-shading of the lower leaves (Figure 1.9B, C), while mean light availability per unit surface of green tissue did not decrease because of the seasonal increase in light intensity (see Supplementary Figure S1.2.1B).

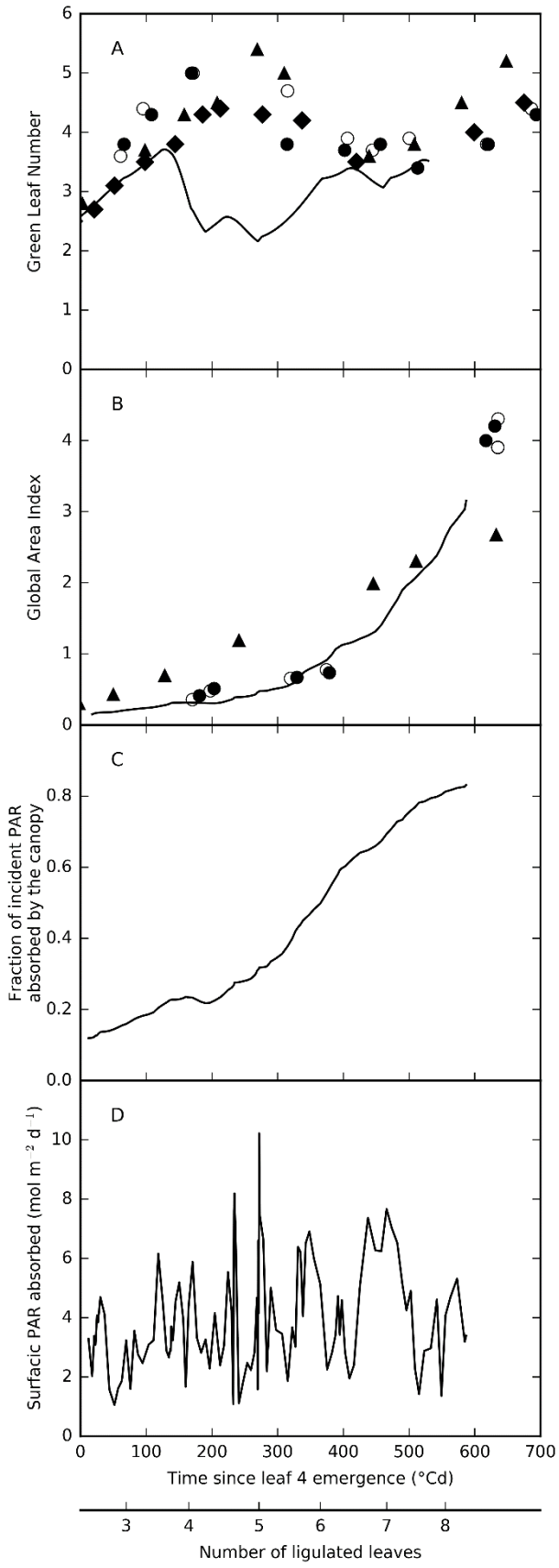

Figure 1.9 - Dynamics of canopy traits. (A) Green leaf number of the main stem. The solid line shows the simulation. Dots show observations from field experiments (Abichou, 2016) that were conducted with similar agronomic conditions and at the same location as Exp1–Exp3 [filled circles, *cv.* Soissons 2004/2005 (Exp2); open circles, *cv.* Caphorn 2004/2005; diamonds, *cv.* Maxwell 2010/2011; triangles, *cv.* Caphorn 2013/2014]. (B) Global area index of the whole plant. The solid line shows the simulation. Dots show observations from field experiments (Abichou, 2016), which were conducted with similar agronomic conditions and at the same location as Exp1–Exp3 (filled circles, *cv.* Soissons 2012/2013; open circles, *cv.* Caphorn 2012/2013; diamonds, *cv.* Maxwell 2010/2011). (C) Simulation of the fraction of incident PAR absorbed by green phytoelements. (D) Simulation of the daily PAR absorbed per area of green phytoelement.

Agronomic traits emerged from the integration of local processes at plant scale

The shoot:root ratio is an important agronomic trait that is strongly determined by gene × environment interactions. Simulated shoot and root biomasses increased exponentially over time (Figure 1.10) and the shoot:root ratio increased from ~0.8 at E_4 to ~1.5 at E_9. An increase in the shoot:root ratio during the tillering period is widely acknowledged but lacks accurate quantification. The few studies that have attempted to quantify the whole root system during early growth stages in field conditions (Siddiqi *et al.*, 1990; Kätterer *et al.*, 1993) reported a shoot:root ratio below 1 at the beginning of tillering and then an increase, which is qualitatively in line with our simulations.

Root N fraction decreased from 1.1% at E_4 to 0.7% at E_9, while shoot N fraction was stable at ~4%; these results are reasonably close to the experimental data (Figure 1.11), except for the latest date. The overestimate of shoot N at ~550 °Cd is explained by the single N fertilization of 5 g m^{-2} that was applied at ~410 °Cd in the model (as in Exp1), whereas the experimental data shown in the figure are from Exp3, in which only 4 g m^{-2} N were supplied at ~275 °Cd. When expressed as a function of the shoot biomass (Figure 1.11, inset), the shoot N fraction was relatively stable.

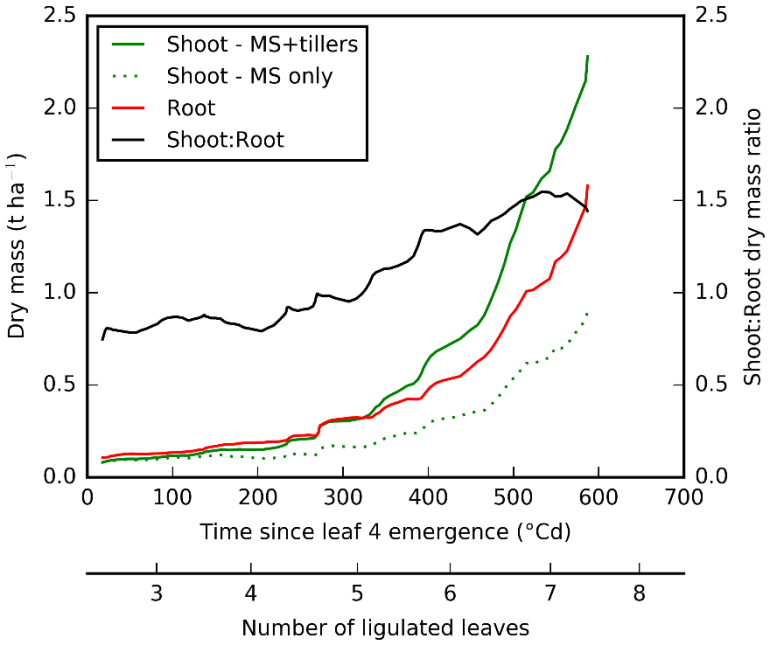

Figure 1.10 - Simulated dry mass and shoot:root dry mass ratio.

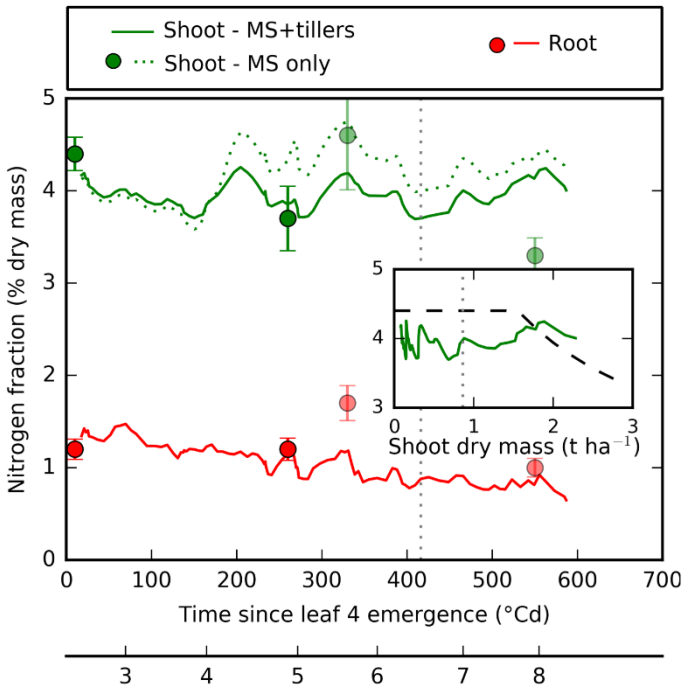

Figure 1.11 - N fraction of the main stem, whole shoot (main stem+tillers), and roots as a percentage of the dry mass of the compartments. Dots are N fractions of the main stem shoot and large roots as measured in Exp3. Vertical bars represent the 95% confidence interval. The last two (shaded) dots correspond to the measurements performed after 4 g m–2 N were applied at 275 °Cd in Exp3 (see Supplementary Protocol S1.1.5) whereas the simulation mimicked Exp1, in which 5 g m–2 N were applied at ~410 °Cd (vertical dotted line). The inset shows the whole shoot N fraction together with the critical N dilution curve for winter wheat (dashed line) as calculated by Justes *et al.* (1994). The critical N dilution curve has not been experimentally validated for biomasses <1.5 t ha–1.

Over the whole period, the radiation use efficiency (RUE), calculated as the ratio of shoot dry mass to the cumulative PAR absorbed by green tissues, was 1.6 g MJ^{-1}. The literature lacks accurate estimates of RUE for juvenile stages, and experimental studies generally refer to intercepted global radiation estimated from leaf area index using the Beer-Lambert law. Using this method, Calderini *et al*. (1997) reported an average RUE of 1.12 g MJ^{-1} (range 0.98-1.25 g MJ-1) for several cultivars from the double-ridge stage to anthesis. When we precisely reproduced this method, the RUE calculated from our virtual canopy was 1.1 g MJ^{-1}, which is in the middle of the reported range. However, simulated plant and shoot dry masses did not evolve linearly with the cumulative absorbed radiation (Figure 1.12A), and the weekly average of RUE varied between 0.1 and 2.2 g MJ^{-1} (Figure 1.12B) and was correlated with the photothermal quotient (PTQ) (see Supplementary Figure S1.2.4; R2=0.49, $P=9.10^{-7}$). Variations in shoot:root ratio, respiration, and exudation played minor roles in the increase in RUE simulated from E_4. In our simulation, this trend resulted from an increase in photosynthesis efficiency originating from higher leaf temperature and N content.

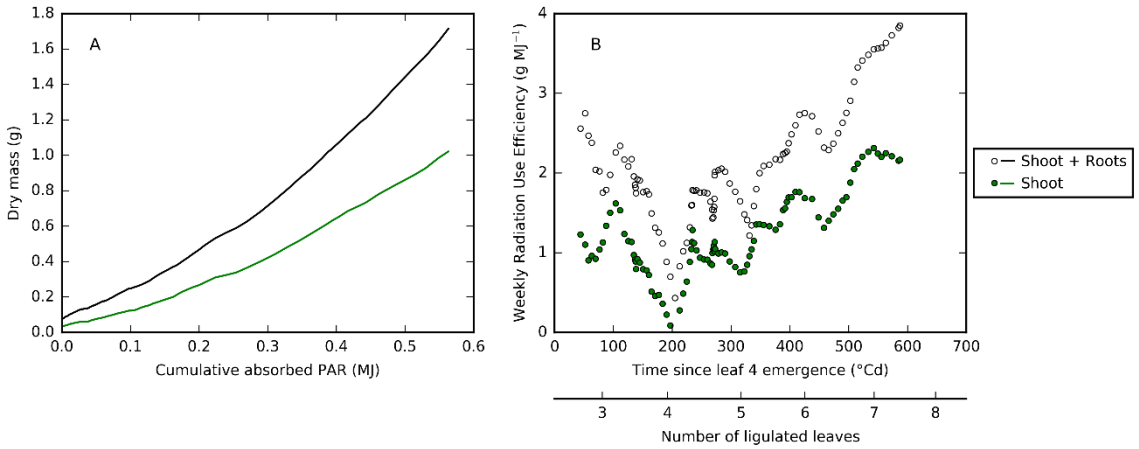

Figure 1.12 - Radiation use efficiency (RUE) computed from absorbed photosynthetically active radiation (PARa) of the plant. (A) Hourly dynamics of whole-plant dry mass (black) and shoot dry mass (green) as a function of the PARa accumulated from model initialization. (B) Dynamics of weekly integrated RUE.

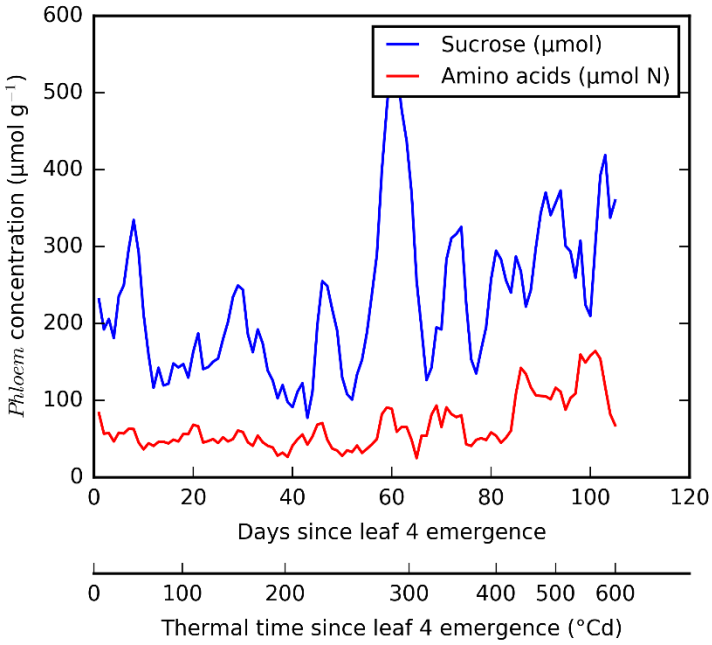

Figure 1.13 - *Phloem* and hidden growth zone (*hz*) concentrations of sucrose and amino acids. *Phloem* concentrations are calculated as the amount of metabolites of the *phloem* divided by the structural mass of the whole plant.

Investigating growth costs with respect to plant trophic status

Plant trophic status

The concentrations of sucrose and AA in the *phloem* represent the amounts of mobile C and N that can flow between sources (mainly mature leaves) and sinks (mainly roots and growing leaves). Due to low flux resistance, sucrose and AA concentrations in growing leaves (*i.e.* the *hz*) were at equilibrium with those in the *phloem*, ranging from ~100 to 550 µmol g^{-1} for sucrose and ~50 to 180 µmol g^{-1} for AA (Figure 1.13). The sucrose concentration showed large variations over periods of a few days, which could be associated with changes in the PTQ (Supplementary Figure S1.2.1C). This reflects that short-term changes in light and temperature markedly affected the source-sink balance and the availability of metabolites in the plant. Over the whole simulation period, however, PTQ explained 46% of variations in sucrose concentration ($P=10^{-7}$). Overall, *phloem* concentrations did not show a clear trend during the first 80 days, then sucrose presented an upward trend, which coincided with the increase in RUE (Figure 1.12). AA showed a transient rise associated with N fertilization (Supplementary Figure S1.2.1E).

From leaf heterotrophy to leaf autotrophy

The sink-source balance during leaf ontogeny is illustrated (Figure 1.14) for leaf 5, which was held on a short internode, and leaf 8, which was twice as long and twice as wide and held on an internode that will elongate later. When leaves were still hidden inside the pseudostem, they imported small amounts of mobile metabolites from the *phloem* (<2 µmol day-1 for sucrose; Figure 1.14A, B). The daily imports were larger for leaf 8 than leaf 5, in relation with their respective daily extension (Figure 1.14E, F). Leaves 5 and 8 switched from heterotrophy to autotrophy for C respectively 20 and 10 days after emergence, that is, once they had reached ~50% of the final lamina area (Figure 1.14E, F). These transition times are consistent with estimates for barley (Dale, 1985) and tall fescue (Bregard and Allard, 1999). The cumulative C consumption for leaf structural growth was 1.6 mmol for leaf 5 versus 11.9 mmol for leaf 8 (Figure 1.14C, D). At the end of its life, leaf 5 had produced five times as much C as it had consumed for its structural growth (Figure 1.14C). Both leaves reached the point of return on C investment when they were 95% of their final length, which corresponded to the full lamina emergence (Figure 14E, F).

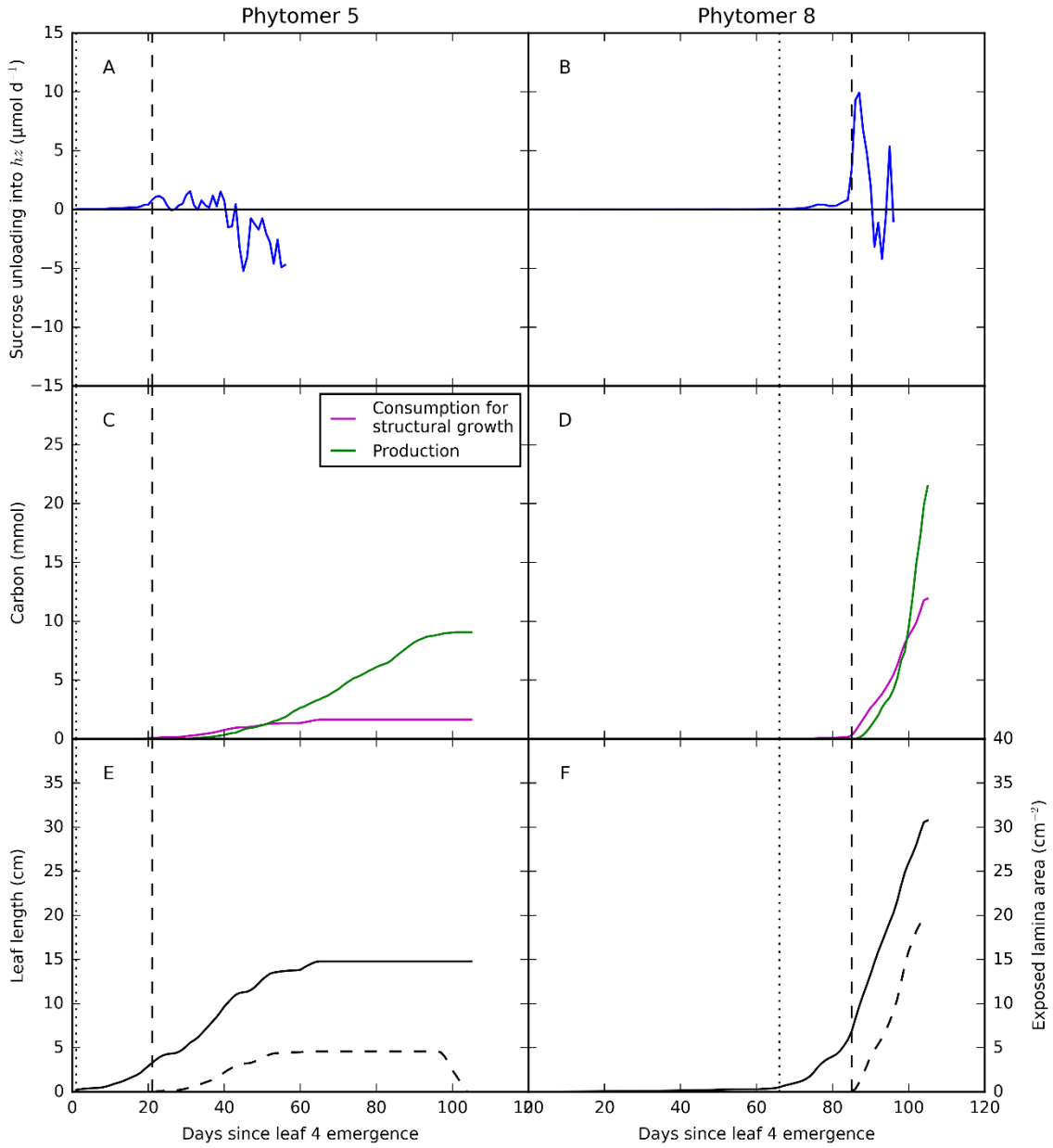

Figure 1.14 - C metabolism of phytomers 5 and 8 in relation to their growth. For the sake of clarity, daily values are shown from the hourly outputs provided by the model. (A, B) Daily fluxes of sucrose from the *phloem* to the hidden part of the growing phytomers (*i.e.* the *hz*) of the main stem. Positive values indicate unloading of the *phloem* into the *hz*, while negative fluxes represent exports from the *hz* to the *phloem*. The curve is shown as long as the impact of internode growth on *hz* fluxes is insignificant. (C, D) Comparison of C assimilation by the leaf (green) and consumption for structural growth (purple). (E, F) Dynamics of leaf length (solid line) and exposed green area of the laminae (dashed line). The vertical dashed and dotted lines show the time of leaf emergence and previous leaf emergence, respectively.

Carbon usage and growth costs

Over the simulated period, 40% of the assimilated C remained in the shoot (25% for structural growth and 15% in mobile and storage metabolites), 25% was allocated to roots, 27% was lost by respiration, and 8% was lost by exudation (Figure 1.15A). The fraction of C allocated to shoot structural growth tended to increase with time, in accordance with the dynamics of the shoot:root ratio (Figure 1.10). The simulated trend of C allocation is aligned with experiments on wheat based on 14C pulse-labelling, which reported an increasing fraction of net assimilated C allocated to the shoot over the growing season (reviewed in Swinnen *et al.*, 1995). During our simulation, 60% of the C allocated to the roots remained in the biomass, while 40% was lost through respiration and exudation. Experiments on wheat during tillering reported up to 60-75% of losses through these processes (Keith *et al.*, 1986; Swinnen *et al.*, 1995), which indicates that our model may underestimate root respiration and exudation, perhaps because it does not consider root turnover for the vegetative stages. Daily, growing leaves (MS+tillers) imported on average 20% of the C available in the *phloem* (Figure 1.15B), which also represented 20% of daily photosynthesis (Figure 1.15C). Roots were a major sink, daily importing ~40% of the C from the *phloem* (Figure 1.15B). On average, sinks consumed 70% of the C from the *phloem* each day, but photosynthesis maintained a high C content in the *phloem* (Figure 1.13), indicating a high C turnover. The source-sink relations were relatively stable over the simulated period, despite marked changes in the canopy structure (Figure 1.9) and climatic conditions. The strong daily variations observed in Figure 1.15B,C resulted from variations both in fluxes and in *phloem* sucrose concentrations. Over the simulated period, C influxes became higher than effluxes (Figure 1.15C), which resulted in an increase in non-structural C in both shoot and roots (Figure 1.15A).

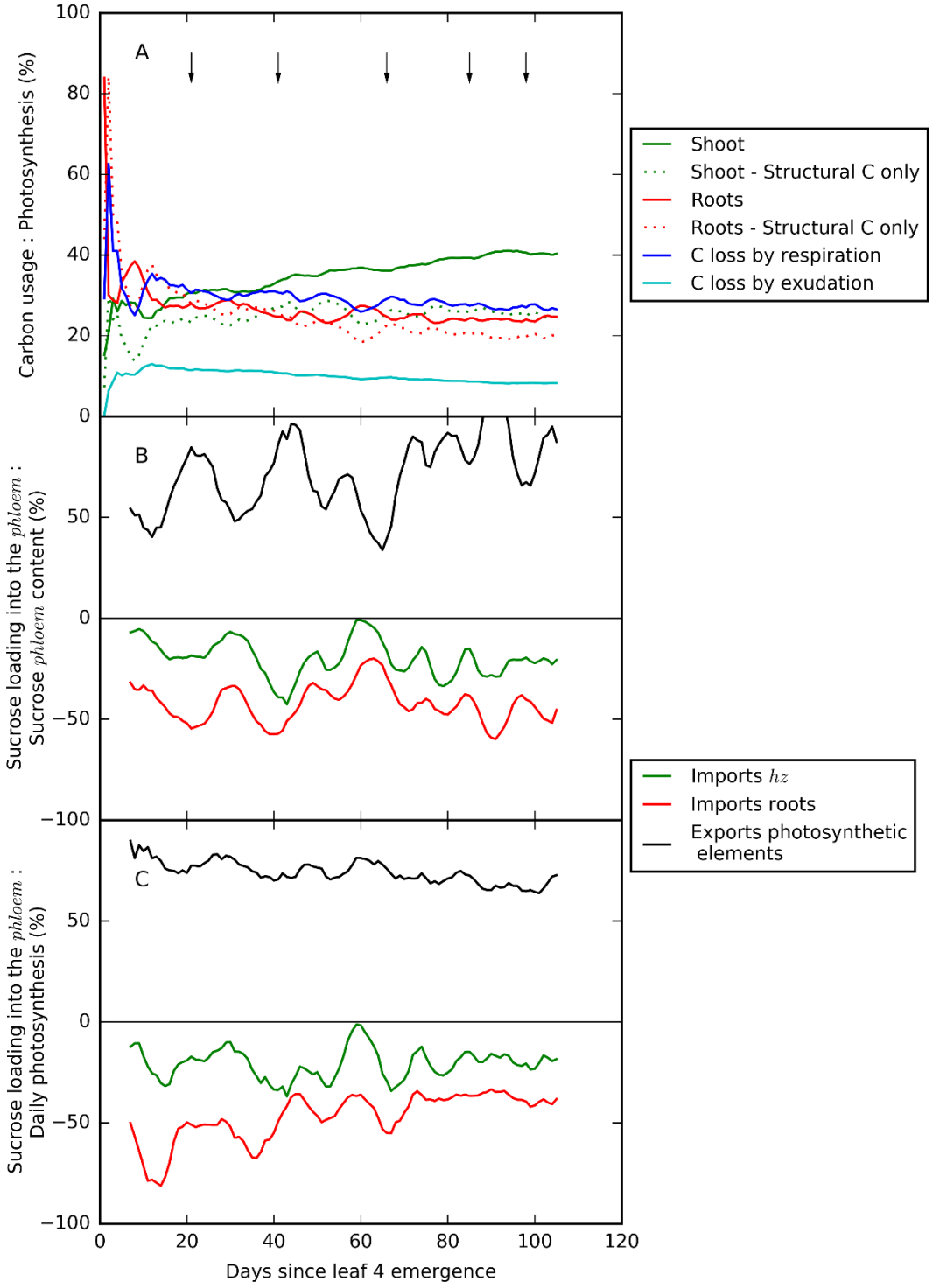

Figure 1.15 - C source–sink relations of the whole plant. (A) Cumulative C usage as compared with the cumulative C absorbed by photosynthesis. (B, C) Daily fluxes of sucrose into the *phloem* as compared with the sucrose *phloem* content (B) and the C absorbed by photosynthesis daily (C). Values are smoothed as the rolling mean of the previous 7 days. The green curves show the imports of the hidden part of the growing phytomer (*hz*) relate to its heterotrophic stage only. Arrows indicate leaf emergence.

1.4 - Discussion

Current models largely integrate predefined behaviours based on observations that may not be representative of novel situations (Poorter *et al.*, 2013). Mechanistic approaches may predict these behaviours as emerging properties and therefore account for their flexibility. This has recently motivated a large body of literature calling for the building of models closer to biological knowledge (Boote *et al.*, 2013; Muller and Martre, 2019) while maintaining a sufficient level of parsimony (Hammer *et al.*, 2019). With this in mind, we developed an individual-based model integrating shoot morphogenesis with C and N metabolism at the organ level.

We used metabolite concentrations to drive the behaviour of growth zones, which expresses the view that only local variables drive the local behaviour. This implied accounting for all activities affecting the metabolic budget and transfers within the plant. This also required a whole-plant model explicitly accounting for major metabolic costs including respiration and exudation. The expression of growth response to local concentrations, the growth-related costs in metabolites, and the response to temperature are novel features compared with the initial version of CN-Wheat. The regulation of leaf growth timing by coordination rules is another essential assumption, which expresses the idea that the mechanics of the whole plant body builds, rather than follows, rhythmic patterns. Such a view has been previously supported by both experimental and modelling papers (Casey *et al.*, 1999; Fournier *et al.*, 2005; Andrieu *et al.*, 2006; Verdenal *et al.*, 2008; Zhu *et al.*, 2014; Vidal and Andrieu, 2019). However, this is the first time such coordinations have been considered jointly with growth costs and modulations of extension rates by the plant status. We demonstrated the concept by simulating the early stages of wheat growth.

The model simulated as emerging properties plant traits that are usually model inputs

Coordination rules in which the emergence of a leaf triggers the rapid extension of the next growing leaf resulted in a regular rate of leaf appearance (Figure 1.7E). This mechanism played a pivotal role in predicting the increase in size between successive leaves (Figure 1.7A).

In our model, RUE is an emerging property of C (and N) budget, based on the balance between the acquisition of C by photosynthesis and loss by respiration and exudation. The average RUE calculated over the simulation period almost exactly matched experimental values reported for similar conditions. RUE is known to vary markedly with ontogeny, temperature, light conditions, and crop nutrition, and is considered a major target for raising yield potential (Parry *et al.*, 2011; Slattery and Ort, 2015). Some RUE-based models include part of these dependencies (Boote *et al.*, 2013) but experimental assessment is difficult to achieve because increases in biomass can be accurately measured only over long periods of time. When considering weekly intervals, simulated RUEs varied from 0.10 to 2.2 g MJ^{-1} (Figure 1.12B) and showed large short-term changes correlated with photosynthesis efficiency (Supplementary Figure S1.2.4), which was regulated by leaf temperature and N content. CN-Wheat appears to be a tool to disentangle the variability of RUE as a function of plant parameters, ontogeny, and growth conditions.

Over the simulated period, the simulated shoot:root ratio increased from 0.8 to ~1.5 (Figure 1.10), which is in line with the few data published for comparable situations (Lupton *et al.*, 1974; Siddiqi *et al.*, 1990). There are large ontogenetic trends in shoot:root ratio, together with substantial genotypic and environmental variability (Friedli *et al.*, 2019): this variability combined with experimental difficulties makes the shoot:root ratio a major unknown in our understanding of C economy in plants and the C cycle in terrestrial ecosystems. With a mechanistic approach to simulate shoot:root ratio and a conservative stoichiometric budget, our approach represents a further step forward to address these questions.

The N:C ratio is a key variable in plant models. Most crop models (*e.g.* STICS, APSIM, CERES; reviewed in Zhao *et al.* 2014) and some FSPMs (Louarn and Faverjon, 2018) regulate morphogenesis and N acquisition by comparing the current value of N:C in the plant shoot to a reference value, the critical N concentration. Experimental assessments, however, showed large errors (>100%) in N:C estimated with these models (Coucheney *et al.*, 2015; Faverjon *et al.*, 2019). Plant N consists of diverse compounds that have contrasting dynamics and are involved in different processes, so limitations should arise from aggregating them in a single driving variable. Identifying this complex set of processes in our model resulted in plausible dynamics of N:C (Figure 1.11), which emerged from our model, whereas teleonomic approaches use them as a target to drive plant growth.

The model allowed exploration of the functioning of growing grass

The 3D modelling of plant architecture has provided novel insights into the environment perceived by plant tissues, allowing a better understanding of plant functioning (Chelle, 2005). In this work, the simulation of metabolite availability at organ scale marks a further step by providing highlights on internal conditions during the early stages of growth. On the one hand, the model showed substantial changes in metabolite availability over short periods in response to meteorological variations (Figure 1.13). On the other hand, over the whole period, the general trend was a moderate increase in sugar availability, despite the increasing plant-plant competition, as GAI was close to 3 at the end of our simulation (Figure 1.9B). We could not find bibliographic data for the changes of metabolites during grass development but the trend of increasing C availability is consistent with the fact that the period simulated corresponds to active tillering. C availability is expected to decrease drastically shortly afterwards because of an increasing C demand for stem elongation without an increase in light capture.

The model allowed us to explore the feedback loops between sink and source activities and metabolite availability. Michaelis-Menten responses used in the model mean that when metabolite concentrations are low, this affects all sinks, independently of their size, but, depending on their affinity for substrate, small sinks are affected even when their growth requires extremely low amounts of metabolites. When metabolite concentrations are high, sink activity is regulated by their maximum rate. This implies that sink hierarchy changes depending on substrate availability, which showed considerable change over relatively short periods of time in response to the photothermal ratio. There was a high turnover of mobile metabolites in the plant; photosynthesis provided daily an amount of C representing ~60% (range 30-100%) of the C available in the *phloem* (Figure 1.15B), while sinks consumed very slightly less, resulting in increasing C availability. Roots imported daily ~40% of *phloem*

C, while leaf growth zones imported daily only ~10% of *phloem* C (Figure 1.15B). Leaves were very small sinks before their emergence, and after half the lamina had emerged, their costs were provided by their exposed tissues (Figure 1.14).

The model paves the way for improved process description and integration over the whole plant cycle

Our approach provides a new frame to combine morphogenesis with C and N metabolism, and demonstrates its ability to simulate a growing plant. However, the model requires further validation and several components will likely benefit from refinements. The ability of the model to simulate contrasting conditions with a unique set of parameters obviously deserves further investigation. We used a pragmatic approach for parameter fitting; parameters already existing for the post-flowering period were unchanged, except a few for which we made sure that changes did not affect the simulations of the post-flowering period (Supplementary Protocol S1.1.4). Given the large difference in growth conditions between the early-stage and post-flowering periods, correctly simulating both cases is the first evidence of robustness. Further developments are needed to simulate the whole plant life cycle, including tiller dynamics and floral transition.

While having a mechanistic structure, the model assembles a large number of sub-models (Figure 1.1), each being a simplified representation of the plant structure and functioning. The present level of detail is a transitory choice, to be refined based on further model assessment and needs. In particular, the root sub-model could be improved by a better description of the root architecture and the root-soil interactions, as well as root growth and senescence, which were empirically calibrated. Another example is the representation of the *hz* as a single compartment, while it actually includes cell division and elongation zones plus some mature tissues. Distinguishing these zones may be necessary to more faithfully represent the processes leading to the definition of leaf width and SLA, at the price of more complexity. In addition, the present implementation uses a predefined ontogenetic trend to simulate the sheath:lamina ratio (Eqn. 6B in Supplementary Table S1.1.1), rather than incorporating knowledge about ligule formation and cessation of sheath extension (*e.g.* Vidal and Andrieu, 2019). This choice may be revised in future versions. Another example is the use of an ontogenetic trend in the maximum RER of leaves during their exponential growth ($RER_{leaf,n}^{max}$) (Supplementary Table S1.1.2), while it would have been satisfactory to define a leaf model whose parameters are all independent of leaf rank. Why successive leaves in grasses elongate simultaneously with different RERs has been specifically questioned for a long time (Williams and Williams, 1968; Rogan and Smith, 1975). Our simulation showed no trend of a decrease in the availability in C or N during the simulated period, which excludes the possibility that differences in RER could simply originate from competition between an increasing number of sinks. The hierarchy between successive primordia seems to still lack a clear explanation, and that is what motivated the description through an ontogenetic trend in our model.

The present implementation is intended as a frame to be complemented to simulate the full pre-flowering period. The first step would be implementing an explicit description of tillers, similar to that taken for the MS. The behaviour of grass tillers, especially factors controlling their emergence and senescence, is a crucial aspect

of crop production, but this is only partly understood. Our approach will open opportunities to explore these processes in relation to C and N availability. The model structure (Figure 1.1) allows the implementation of new modules; for example, a module for apical meristem would allow simulation of the rate of initiation, the initial properties of phytomers, and the change from vegetative to reproductive phase. Finally, the focus here on C and N does not mean that we assume these variables are sufficient to provide all necessary information in a plant model. However, primary metabolites are obviously key variables that were missing in current models, so we believe the present work is a significant step towards a mechanistic approach of plant modelling.

Acknowledgements

The authors gratefully acknowledge Josiane Jean-Jacques and Christelle Franchet for their excellent technical assistance. The PhD of Marion Gauthier was funded by a CIFRE convention between ITK and ANRT. The authors acknowledge ITK and Amélie Pinet for supporting the present work and for discussions.

List of Supplementary Data

Supplementary Data S1.1 – Model description

Protocol S1.1.1: Detailed description of the growth sub-models

This protocol provides a detailed description of the assumptions and equations related to the morphogenetic processes implemented in the model. The sub-model of leaf growth and its metabolism are first described, then we provide details about the sub-models of internode growth and tillering.

Leaf growth in dimensions and mass

The above description follows the chronology of leaf growth, from initiation to maturity (see Figure 5 in the main text); equations and parameters are given in Table S1.1.1 and Table S1.1.2, respectively.

From leaf initiation to the emergence of the previous leaf (Phase I)

During the first phase, no tissues have emerged out of the pseudostem, the whole leaf is therefore only represented by a hidden growth zone (*hz*) compartment (Figure 5I). The elongation rate of leaf n (Table S1.1.1 Eqn. 1) is described by an exponential-like function. The relative elongation rate (RER) is calculated at each time step according to (i) concentrations of sucrose and amino acids (AA) in the *hz*, (ii) temperature and (iii) leaf rank, which determines the maximum RER, $RER_{leaf,n}^{max}$ (Table S1.1.1 Eqn. 2). The increase in leaf structural mass (Table S1.1.1 Eqn. 3) is estimated from an empirical relation with leaf length, fitted from the anatomical observations published by Williams & Rijven (1965) on wheat seedlings. The structural N mass is derived from the structural mass, assuming a constant N fraction.

Leaf emergence

Leaf emergence is a key event of the present model since it triggers the transition from the exponential to the sigmoidal phase of the following leaf. A leaf is considered to emerge when its tip is higher than the pseudostem in which it grows (Figure 5 E_n). For each growing leaf, a pseudostem length is dynamically calculated as the difference in height between the highest ligule of the mature leaves and the bottom of the *hz* (Figure S1.1.1). This calculation accounts for the effect of stem elongation on the pseudostem length, although internodes remain short for the stages considered here.

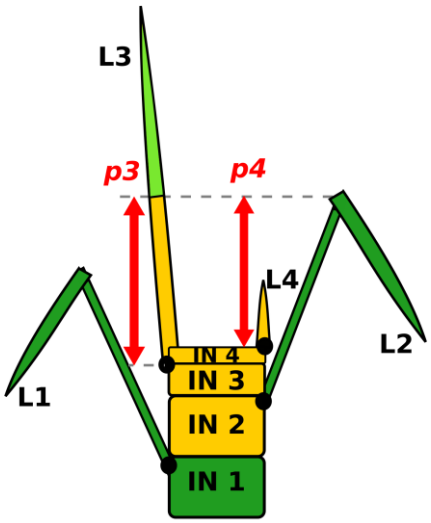

Figure S1.1.1 - Schematic representation of the pseudostem of growing leaves: p3 and p4 are the pseudostems associated to leaf 2 and leaf 3, respectively (denoted L3 and L4). The length of the pseudostem of leaf n is calculated at each time step as the difference between the height of the highest ligule (sheath of L2 here) and the cumulated length of the internodes (IN) bearing leaf n.

From previous leaf emergence to leaf emergence (Phase IIa)

During this phase, the growing leaf is still represented by a single *hz* compartment since no tissues have emerged (Figure 5IIa). However, the rate of leaf *n* elongation (Table S1.1.1 Eqn 4a) now follows a sigmoidal kinetics described by a normalised Beta function of leaf physiological age (Table S1.1.1 Eqn. 4b). Leaf physiological age is cumulated from previous leaf emergence (E_{n-1}) according to a non-linear response to temperature (Table S1.1.1 Eqn 4c; Protocol S1.1.2). The normalised Beta function is scaled according to the length reached by leaf *n* at E_{n-1} and is slightly regulated by the concentrations of sucrose and AA in the *hz* (Table S1.1.1 Eqn. 4a). Finally, the increase in leaf structural mass is described as in the first phase as the leaf is still fully enclosed in the pseudostem (Table S1.1.1 Eqn. 3).

Leaf *n* emergence

At leaf *n* emergence (E_n), the model defines several variables that will be used to calculate the dimensions and mass of the emerged laminae and sheaths. First, we define a provisional estimate of the final length of the leaf assuming that the trophic factor regulating the sigmoidal elongation will keep equal to one (Table S1.1.1 Eqn. 5). This allows the calculation of a provisional estimate of the final lamina and sheath length based on an ontogenic lamina:sheath ratio (Table S1.1.1 Eqn. 6a,b). Secondly, the estimate of final lamina length is used to calculate its maximal width from an allometric width:length ratio modulated by C availability (see below). Finally, the model defines the Structural Specific Mass (SSM) of both lamina and sheath *n* according to C availability. The ratio between maximal width and final length of the lamina (Table S1.1.1 Eqn. 7), the Structural Specific Lamina Mass (SSLM, Table S1.1.1 Eqn. 8) and the Structural Lineic Sheath Mass (SLSM, Table S1.1.1 Eqn. 9) were assumed to vary linearly (within bounds) with the mean sucrose concentration in the *hz* during the two phyllochrons preceding leaf emergence. A single relation was used for all leaves for maximum width and SSLM, while an

ontogenic parameter was introduced for SLSM. The maximum width, SSLM and SLSM are set at leaf emergence and kept unchanged during leaf lifetime.

After leaf emergence, the provisional estimate of lamina length is updated at each time step (Table S1.1.1 Eqns. 6a) in order to calculate the end of lamina elongation which will trigger the emergence of sheath tissues (see below).

From leaf emergence to the end of its elongation (Phases IIb and IIc)

Throughout these phases, the leaf elongation rate is still calculated according to the Beta function described earlier (Table S1.1.1 Eqns. 4). However, the leaf is now represented by several compartments: a *hz*, an emerged lamina (Figure 5IIb) and later on, an emerged sheath (Figure 5IIc). The emerged tissues are attributed to the exposed lamina compartment until its length equals the current provisional estimate of final lamina length (Figure 5III; Table S1.1.1 Eqn. 10a). From that stage on, the exposed lamina is considered to have reached its final length (the leaf is considered to be ligulated) and the new emerging tissues belong to the exposed sheath (Table S1.1.1 Eqn. 10b). At the end of leaf elongation, the *hz* compartment is deleted of the model and an enclosed mature sheath compartment is created with same dimensions, structural mass and metabolites as the former *hz.*

From leaf emergence, the structural dry mass of the *hz* increases nearly linearly, until it reaches the final structural mass of the sheath at the end of leaf elongation (Table S1.1.1 Eqn. 11a and 11b). For this, a provisional estimate of the final structural mass of the sheath is calculated at each time step from the current pseudostem length and the SLSM of the sheath which was calculated at previous leaf emergence (Table S1.1.1 Eqn. 12). The increase in *hz* structural mass becomes exactly linear when the pseudostem has reached its final length, which happens shortly after leaf emergence. The structural mass increase of the emerged lamina (Table S1.1.1 Eqn. 13) is calculated according to its area and the SSLM calculated at leaf emergence (Table S1.1.1 Eqn. 8). The area of the emerged lamina is calculated by the Adel-Wheat model according to its length, maximal width and rank (Fournier *et al.*, 2003; Dornbusch and Andrieu, 2010). Finally, the structural mass of the whole leaf is given by the sum of the structural masses of the *hz*, emerged lamina and sheath (Table S1.1.1 Eqn. 14). The structural N mass is computed as a constant ratio of the structural mass for each compartment.

Carbon and Nitrogen metabolism of the growing leaf

The former version of the CN-Wheat model describes the metabolic activities for mature photosynthetic tissues and roots. In the present version, the metabolic activity of *hz* was implemented, while that of emerged tissues was assumed to be same as that of mature organs (except for a few aspects detailed in S1.4).

Costs of mass growth and related metabolite fluxes

Leaf growth implies metabolic costs to fuel the synthesis of cell walls, metabolic compounds and respiration. In our model, the increase in leaf structural mass results in the consumption of sucrose and AA in the *hz*, assuming a constant amount of C and N per g of structural mass (Table S1.1.1 Eqn. 15 and 16). Growth respiration (Table S1.1.1 Eqn. 17) is calculated by assuming a constant growth yield, estimated from Cannell & Thornley (2000).

Fluxes of metabolites between the *phloem*, the hidden part of the growing leaf and the emerged tissues

We assume a passive transport of C and N between the *phloem* and the *hz*. Fluxes of sucrose and AA between the two compartments therefore follow diffusion laws, with conductances depending on the structural mass of the *hz* and on temperature (Table S1.1.1 Eqn. 18 and 19). After leaf emergence, the model accounts for a passive transport of sucrose and AA from the emerged (photosynthetic) growing tissues to the *hz*. Since the main source of C of the growing zone after leaf emergence is coming from its own exposed tissues (Anderson and Dale, 1983), we did not consider any direct transport between exposed tissues and the *phloem* compartment.

The emergence of tissues leads to a mass transfer from the *hz* to the exposed lamina or sheath compartment. In the model, newly emerged tissues are fulfilled with mobile and storage metabolites so that their initial concentration equals that in the *hz*.

At maturity, sheath and lamina directly load sucrose and AA into the *phloem* according to the transport formalism described in Barillot *et al.* (2016*a*).

Fluxes of C and N between mobile and storage metabolites within the hidden part of the growing leaf

Storage forms of C (fructans) and N (proteins) are considered in the composition of the *hz* since these metabolites are important storage pools of the growing leaf (Schnyder *et al.*, 2000).

For fructans, the treatment is the same in the *hz* as in photosynthetic tissues and follows Barillot *et al.* (2016*a*). The synthesis and degradation of fructans depend on their own local concentration as well as sucrose concentration. Fructan synthesis is downregulated by the rate of sucrose loading from the *hz* to the *phloem* (see equations T4.13, T4.14 and T4.15 in Barillot *et al.* (2016*a*)).

For proteins, the rate of synthesis is calculated from a Michaelis-Menten function of AA concentration, like for photosynthetic tissues (equation T4.20 in Barillot *et al.* (2016*a*)). Since Gastal and Nelson (1994) noted that protein deposition occurred mainly in the division zone of growing tall fescue leaves, we introduced a dependency of the maximal rate of protein synthesis to a length ratio representing the size of the division zone in the *hz* (Table S1.1.1 Eqn. 20). Before previous leaf emergence, the leaf is considered to be fully meristematic, the ratio therefore equals 1. After previous leaf emergence, the ratio follows a Beta function of the normalised leaf length (Table S1.1.1 Eqn. 21) as estimated from the literature on wheat (Beemster and Masle, 1996; Schuppler *et al.*, 1998; Fournier *et al.*, 2005). The rate of protein degradation in the *hz* follows a first order kinetics (Table S1.1.1 Eqn. 22)

Metabolism of the emerged tissues of the growing leaf

The emerged tissues of a growing leaf have the same metabolism as the mature photosynthetic organs described in the former version of CN-Wheat, the only differences are (i) the loading of sucrose and AA takes place towards the *hz* instead of the *phloem* and (ii) there is an import of new tissues from the *hz,* according to leaf emergence rate. Because SSM was fixed at E_n, we assumed the emerged tissues to be a homogeneous compartment, pooling the metabolites coming from the newly emerged tissues. As in Barillot *et al.* (2016*a*), emerged photosynthetic tissues have a cytokinin compartment which regulates the rate of protein degradation. This regulation has been

largely reported in the literature (Pons *et al.*, 2001; Sakakibara *et al.*, 2006; Criado *et al.*, 2009) and allowed simulation of realistic dynamics of protein concentration and green area (Barillot *et al.*, 2016*b*). For the sake of model simplification, cytokinins are not simulated in the *hz* but we assumed tissues of lamina and sheath to emerge with a constant initial amount of cytokinins in order to account for the fact that cytokinins are synthesised in growing leaves, especially at the leaf base (Ulvskov *et al.*, 1992; Nordstrom *et al.*, 2004; El-Showk *et al.*, 2013).

Leaf death

The former version of CN-Wheat only accounted for the last stages of leaf senescence *i.e.* the loss of green area through tissue death. At each time step, a constant fraction of the green area of a mature organ dies if one of the two following conditions is met. The first one is related to protein concentration, which triggers death when it goes below a fraction of the maximum protein concentration reached since leaf ligulation. The second mechanism was implemented for the new version of CN-Wheat and only applies to laminae: lamina tissues die if their physiological age (Protocol S1.1.2) is higher than a threshold (calibrated from experimental observations). Following tissue death, structural mass and structural N mass of green tissues are reduced proportionally to the loss in green area. A fraction of mobile and storage metabolites of the dead tissue are remobilised towards the remaining green tissue of the organ as sucrose, AA or nitrates. Following the experimental data on wheat from Bertheloot (2009) and Bertheloot *et al.* (2011*a*), we considered that N residual fraction in dead tissues depended on leaf rank (lower laminae have highest N residuals). The emerging behaviour is that N remobilisation from a senescing lamina stops when the lamina N content has dropped below a threshold which depends on lamina rank.

Table S1.1.1 - Equations describing leaf growth (1/4)

Equation	Description	Unit	Equation number
Phase I			
$\frac{dL_{leaf,n}}{dt} = L_{leaf,n}(t) \times RER_{leaf,n}(t)$	Rate of leaf elongation	m s^{-1}	Eqn 1
$RER_{leaf,n}(t) = \frac{RER_{leaf,n}^{max}}{\left(1 + K_C^I / [C_{hz,n}^{suc}](t)\right) \times \left(1 + K_N^I / [N_{hz,n}^{AA}](t)\right)} \times \frac{Arr(T_{leaf,n}(t))^{(*)}}{Arr(T_{ref}^{growth})}$	Relative Elongation Rate	s^{-1}	Eqn 2
$\frac{dM_{leaf,n}^{struct}}{dt} = \frac{dM_{hz,n}^{struct}}{dt} = \left[\alpha \times \beta \times L_{leaf,n}(t)^{(\beta-1)} \times \frac{dL_{leaf,n}}{dt}\right]\left(\frac{M_{leaf,n}^{mstruct}}{M_{leaf,n}^{total}}(t)\right)$	Rate of leaf structural mass growth	g s^{-1}	Eqn 3
Phase IIa (to III)			
If $[C_{hz,n}^{suc}](t)$ and $[N_{hz,n}^{AA}](t) > 0$:			
$\frac{dL_{leaf,n}}{dt} = \frac{dBeta(t)}{dt} \times \frac{Regul_{CN}^{max}}{\left(1 + K_C^{II} / [C_{hz,n}^{suc}](t)\right) \times \left(1 + K_N^{II} / [N_{hz,n}^{AA}](t)\right)} \times A \times L_{leaf,n}(t_{E_{n-1}})$	Rate of leaf elongation	m s^{-1}	Eqn 4a
Else:			
$\frac{dL_{leaf,n}}{dt} = 0$			
For $Age_{base} < Age_{leaf,n}^{\rightarrow t_{E_{leaf,n-1}}} < Age_{end}$:			
$Beta(t) = \left(1 + \frac{Age_{end} - Age_{leaf,n}^{\rightarrow t_{E_{n-1}}}(t)}{Age_{end} - Age_{max}}\right)\left(\frac{Age_{leaf,n}^{\rightarrow t_{E_{n-1}}}(t) - Age_{base}}{Age_{end} - Age_{base}}\right)^{\left(\frac{Age_{end} - Age_{base}}{Age_{end} - Age_{max}}\right)}$	Relative Beta function of leaf length according to leaf physiological age	dimensionless	Eqn 4b

(*) For the early vegetative stages simulated here, the temperature of the growing leaf ($T_{leaf,n}$) was approximated from soil temperature. (continued)

Table S1.1.1 - Equations describing leaf growth (2/4)

Equation	Description	Unit	Equation number
$\frac{dAge_{leaf,n}^{\rightarrow t_{E_{n-1}}}}{dt} = \frac{Arr(T_{leaf,n}(t))^{(*)}}{Arr(T_{ref}^{growth})}$	Rate of increase in leaf physiological age according to temperature	dimensionless	Eqn 4c
${}^{*}\mathrm{L}_{\mathrm{leaf,n}}^{\max}(\mathrm{t}) = \mathrm{L}_{\mathrm{leaf,n}}(\mathrm{t}) + \frac{\mathrm{L}_{\mathrm{leaf,n}}(\mathrm{t}_{\mathrm{E_{n-1}}})}{\mathrm{Beta}(0)} \times (1 - \mathrm{Beta}(\mathrm{Age}_{\mathrm{leaf,n}}^{\rightarrow \mathrm{t_{E_{n-1}}}}(\mathrm{t})))$	Provisional estimation of final leaf length	m	Eqn 5
${}^{*}\mathrm{L}_{\mathrm{lamina,n}}^{\max}(\mathrm{t}) = {}^{*}\mathrm{L}_{\mathrm{leaf,n}}^{\max}(\mathrm{t}) \Big/ (1 + \mathrm{sheath{:}\,lamina}_{\ \mathrm{n}})$	Provisional estimation of final lamina length	m	Eqn 6a
$\mathrm{sheath{:}\,lamina}_{\ \mathrm{n}} = \mathrm{a} \times \mathrm{rank}_{\mathrm{n}}^{3} + \mathrm{b} \times \mathrm{rank}_{\mathrm{n}}^{2} + \mathrm{c} \times \mathrm{rank}_{\mathrm{n}} + \mathrm{d}$	Ontogenic ratio of sheath : lamina length	dimensionless	Eqn 6b
E_n			
$W_{lamina,n}^{max} = {}^{*}L_{lamina,n}^{max}(t_{E_n}) \times \left(\mathrm{a_w} + \mathrm{b_w} \times \frac{\int_{t_{E_{n-2}}}^{t_{E_n}} [C_{hz,n}^{suc}](t)}{t_{E_n} - t_{E_{n-2}}} \right); \in [\mathrm{WL_{min}}, \mathrm{WL_{max}}]$	Maximal lamina width	m	Eqn 7
$SSLM_{lamina,n} = \mathrm{a_{SSLM}} + \mathrm{b_{SSLM}} \times \frac{\int_{t_{E_{n-2}}}^{t_{E_n}} [C_{hz,n}^{suc}](t)}{t_{E_n} - t_{E_{n-2}}}; \in [\mathrm{SSLM_{min}}, \mathrm{SSLM_{max}}]$	Structural Specific Lamina Mass	g m^{-2}	Eqn 8
$SLSM_{sheath,n} = \mathrm{a_{SLSM}} + \mathrm{a'_{SLSM}} \times \mathrm{n} + \mathrm{b_{SLSM}} \times \frac{\sum_{t_{E_{n-2}}}^{t_{E_n}} [C_{hz,n}^{suc}](t)}{t_{E_n} - t_{E_{n-2}}}; \in [\mathrm{SLSM_{min}}, \mathrm{SLSM_{max}}]$	Structural Lineic Sheath Mass	g m^{-1}	Eqn 9
Phases IIb and IIc			
$\frac{dL_{lamina\ exp,n}}{dt} = \frac{dL_{leaf,n}}{dt} - \frac{dL_{pseudostem,n}}{dt}, for\ L_{lamina\ exp,n}(t) \leq {}^{*}L_{lamina,n}^{max}(t)$	Rate of lamina elongation	m s^{-1}	Eqn 10a
$\frac{dL_{sheath\ exp,n}}{dt} = \frac{dL_{leaf,n}}{dt} - \frac{dL_{pseudostem,n}}{dt} - \frac{dL_{lamina\ exp,n}}{dt}, for\ L_{leaf,n}(t) \leq {}^{*}L_{leaf,n}^{max}(t)$	Rate of sheath elongation	m s^{-1}	Eqn 10b
$\frac{dM_{hz,n}^{struct}}{dt} = \frac{{}^{*}M_{hz,n}^{struct,max}(t) - M_{hz,n}^{struct}(t)}{Age_{end} - age_{leaf,n}^{\rightarrow t_{E_{n-1}}}(t)} \times \frac{dAge_{leaf,n}^{\rightarrow t_{E_{n-1}}}}{dt}$	Rate of *hz* structural mass growth	g s^{-1}	Eqn 11a

(continued)

Table S1.1.1 - Equations describing leaf growth (3/4)

Equation	Description	Unit	Equation number
${}^{*}M_{hz,n}^{struct,max}(t) = M_{sheath\ enc,n}^{struct,max}(t) = L_{pseudostem,n}(t) \times SLSM_{sheath,n}$	Provisional estimate of the final structural mass of *hz*	g	Eqn 11b
$\frac{dM_{sheath\ exp,n}^{struct}}{dt} = \frac{dL_{sheath\ exp,n}}{dt} \times SLSM_{sheath,n}$	Rate of exposed sheath structural mass growth	g s^{-1}	Eqn 12
$\frac{dM_{lamina\ exp,n}^{struct}}{dt} = \frac{dA_{lamina\ exp,n}}{dt} \times SSLM_{lamina,n}$	Rate of exposed lamina structural mass growth	g s^{-1}	Eqn 13
$\frac{dM_{leaf,n}^{struct}}{dt} = \frac{dM_{hzn,n\ or\ sheath\ enc,n}^{struct}}{dt} + \frac{dM_{lamina\ exp,n}^{struct}}{dt} + \frac{dM_{sheath\ exp,n}^{struct}}{dt}$	Rate of whole leaf structural mass growth	g s^{-1}	Eqn 14
Carbon and Nitrogen metabolism of the growing leaf			
$C_{hz,n}^{suc \rightarrow mstruct}(t) = \frac{dM_{hz,n}^{struct}}{dt} \times \frac{ratio_{C:mstruct}}{MM_C}$	Rate of sucrose consumption for leaf growth	µmol s^{-1}	Eqn 15
$N_{hz,n}^{AA \rightarrow mstruct}(t) = \frac{dM_{hz,n}^{struct}}{dt} \times \frac{ratio_{N:mstruct}}{MM_N}$	Rate of amino acids consumption for leaf growth	µmol s^{-1}	Eqn 16
$R_{hz,n}^{growth}(t) = \frac{1 - Y_g}{Y_g} \times C_{hz,n}^{suc \rightarrow mstruct}(t)$	Rate of growth respiration	µmol s^{-1}	Eqn 17
$L_{phlo \rightarrow hz,n}^{C,suc}(t) = \left([C_{phlo}^{suc}](t) - [C_{hz,n}^{suc}](t) \right) \times G_{phlo \rightarrow hz,n}(t)$ $L_{phlo \rightarrow hz,n}^{N,AA}(t) = \left([N_{phlo}^{AA}](t) - [N_{hz,n}^{AA}](t) \right) \times G_{phlo \rightarrow hz,n}(t)$	Rate of sucrose loading Rate of amino acids loading	µmol s^{-1}	Eqn 18
$G_{phlo \rightarrow hz,n}(t) = \sigma \times \beta \times \left(M_{hz,n}^{struct}(t) \right)^{2/3} \times \left(Q_{10}^{phloem} \right)^{\frac{T_{air(t)} - T_{ref}^{phloem}}{10}}$	Conductance between *hz* and *phloem*	g s^{-1}	Eqn 19

(continued)

Table S1.1.1 - Equations describing leaf growth (4/4)

Equation	Description	Unit	Equation number
$Smax_{hz,n}^{N,prot}(t) = Smax_{DZ}^{N,prot} \times ratio_{DZ:hz,n}(t) + Smax_{hz-DZ,n}^{N,prot} \times \left(1 - ratio_{DZ:hz,n}(t)\right)$	Maximal rate of protein synthesis in *hz*	µmol g^{-1} s^{-1}	Eqn 20
$ratio_{DZ:hz,n}(t) = 1 - \frac{L_{leaf,n}^{norm}(t)}{min\left(l_{leaf,n}^{norm}(t), l_{pseudostem,n}(t)\right)} \times \left(1 + \frac{L_{end}^{DZ} - L_{leaf,n}^{norm}(t)}{L_{end}^{DZ} - L_{mid}^{DZ}}\right)\left(\frac{L_{leaf,n}^{norm}(t) - L_{beg}^{DZ}}{L_{end}^{DZ} - L_{beg}^{DZ}}\right)^{\frac{L_{end}^{DZ} - L_{beg}^{DZ}}{L_{end}^{DZ} - L_{mid}^{DZ}}}$	Length ratio of the division-only zone to the whole *hz*	dimensionless	Eqn 21
$D_{hz,n}^{N,prot}(t) = \delta_{hz,n}^{N,prot} \times \left[N_{hz,n}^{AA}\right](t)$	Rate of protein degradation in *hz*	µmol g^{-1} s^{-1}	Eqn 22

Table S1.1.2 - Description of parameters, values and units of the leaf growth model (1/4)

Parameter	Description	Value	Unit	Related equation	Reference
Phase I					
plastochron	Time interval between initiation of successive primordia with a length of 50 µm	547920	s at 12°C	-	[(b)] (Ljutovac, 2002)
$RER_{leaf,n}^{max}$	Maximum Relative Elongation Rate of leaves 5 to 11	[3.35, 2.25, 2.12, 1.99, 1.92, 1.65, 1.56] x 10^{-6}	s^{-1} at 12°C	Eqn 2	[(c)]
K_C^I	Michaelis-Menten constant for regulation of the RER by sucrose concentration in *hz*	100	µmol C g^{-1}	Eqn 2	[(c)]
K_N^I	Michaelis-Menten constant for regulation of the RER by amino acids concentration in *hz*	15	µmol N g^{-1}	Eqn 2	[(c)]
α	Parameter relating leaf length and mass before emergence	0.106	g $m^{-\beta}$	Eqn 3	[(b)] (Williams, 1960)
β	Parameter relating leaf length and mass before emergence	1.28	Dimensionless	Eqn 3	[(b)] (Williams, 1960)
Phase IIa (to III)					
$Regul_{CN}^{max}$	Maximal regulation of leaf elongation by C-N status	1.35	Dimensionless	Eqn 4a	[(c)]
K_C^{II}	Michaelis constant for the regulation of elongation rate by sucrose concentration in *hz*	150	µmol C g^{-1}	Eqn 4a	[(c)]
K_N^{II}	Michaelis constant for the regulation of elongation rate by amino acids concentration in *hz*	10	µmol N g^{-1}	Eqn 4a	[(c)]

(continued)

Table S1.1.2 - Description of parameters, values and units of the leaf growth model (2/4)

Parameter	Description	Value	Unit	Related equation	Reference
Age_{base}, Age_{max}, Age_{end}	Leaf physiological age at the beginning, maximum rate and endpoint of the Beta function describing leaf elongation in the second phase, respectively	-822960, 1473120, 2160000	s at 12°C	Eqn 4b	[(b)] (Fournier *et al.*, 2005)
a, b, c, d	Ontogenic parameters of the sheath to lamina length ratio	-0.002, 0.037, 0.153, 0.496	Dimensionless	Eqn 6b	[(b)] (Dornbusch *et al.*, 2011)
E_n					
WL_{min}, WL_{max}	Minimal and maximal width:length ratio for laminae	0.025, 0.1	Dimensionless	Eqn 7	[(c)]
a_w, b_w	Offset and slope of the relation between maximal lamina width and the mean concentration of sucrose in the *hz*	0.022, 1.56×10^{-5}	Dimensionless, g µmol C^{-1}	Eqn 7	[(c)]
$SSLM_{min}$, $SSLM_{max}$	Minimal and maximal Structural Specific Lamina Mass	5, 45	g m^{-2}	Eqn 8	[(c)]
a_{SSLM}, b_{SSLM}	Offset and slope of the relation between SSLM and the mean concentration of sucrose in the *hz*	1.67, 0.0083	g m^{-2}, g^2 m^{-2} µmol C^{-1}	Eqn 8	[(c)]
$SLSM_{min}$, $SLSM_{max}$	Minimal and maximal Structural Lineic Sheath Mass	0.05, 0.8	g m^{-1}	Eqn 9	[(c)]
a_{SLSM}, a'_{SLSM}, b_{SLSM}	Offsets and slope of the relation between SLSM and the mean concentration of sucrose in the *hz*	-0.0949, 0.0403, 0.00005	g m^{-1}, g m^{-1}, g^2 m^{-1} µmol C^{-1}	Eqn 9	[(c)]

(continued)

Table S1.1.2 - Description of parameters, values and units of the leaf growth model (3/4)

Parameter	Description	Value	Unit	Related equation	Reference
Carbon and Nitrogen metabolism of the growing leaf					
$ratio_{C:mstruct}$	Relative content in C of the structural mass	0.44	Dimensionless	Eqn 15	[b] (Penning de Vries *et al.*, 1979)
$ratio_{N:mstruct}$	Relative content in N of the structural mass	0.005	Dimensionless	Eqn 16	[b] (Penning de Vries *et al.*, 1979)
Y_g	Growth yield used to compute the respiratory cost of growth	0.75	Dimensionless	Eqn 17	[a] (Cannell & Thornley, 2000)
σ	Conductivity between the *phloem* and the *hz*	0.025 at 12°C	$(g\ m^{-3})^{-2/3}$	Eqn 19	[c]
β	Scale factor to estimate the section of the *hz* with the *phloem*	1	$g\ m^{-2}\ s^{-1}$	Eqn 19	[c]
$[cytokinins^{init}_{organ}]$	Initial cytokinins concentration in newly emerged tissues of a growing leaf	200	AU	-	[c]
$Smax\_pot^{C,fruc}_{tp,i}$	Potential maximum rate of fructan synthesis in *hz*	10	$\mu mol\ C\ g^{-1}\ s^{-1}$ at 12°C	-	[c] Barillot *et al.*, (2016*a*) ; Eqn T4.14[*]
$Smax^{N,prot}_{DZ}$	Maximum rate of protein synthesis in the division zone	0.345	$\mu mol\ N\ g^{-1}\ s^{-1}$ at 12°C	-	[c] Barillot *et al.*, (2016*a*) ; Eqn T4.20[*]
$Smax^{N,prot}_{hz-DZ,n}$	Maximum rate of protein synthesis in the part of the *hz* which is not the division zone	0.1125	$\mu mol\ N\ g^{-1}\ s^{-1}$ at 12°C	-	[c] Barillot *et al.*, (2016*a*) ; Eqn T4.20[*]

(continued)

Table S1.1.2 - Description of parameters, values and units of the leaf growth model (4/4)

Parameter	Description	Value	Unit	Related equation	Reference
$L_{beg}^{DZ}, L_{mid}^{DZ}, L_{end}^{DZ}$	Parameters describing the dynamics of length ratio between the division zone and the normalised leaf length.	-1.19, -1.15, -0.16	Dimensionless	Eqn 21	[(b)] (Beemster & Masle, 1996; Schuppler *et al.*, 1998; Fournier *et al.*, 2005)
$\delta_{hz,n}^{N,prot}$	Relative rate of protein degradation in the *hz*	2.5 x 10^{-7}	s^{-1} at 12°C	-	[(c)] Barillot *et al.*, (2016*a*) ; Eqn T4.21[(*)]
Leaf senescence and C-N remobilization					
age_{senesc}	Lamina age above which senescence is triggered	2851200	s at 12°C	-	[(b,c)] (Abichou, 2016)
$rate\_death_{tp,i}^{area}$	Rate of photosynthetic tissue *(tp, i)* death	9 x 10^{-10}	$m^2\ s^{-1}$ at 12°C	-	[(c)] Barillot *et al.*, (2016a)[(*)]
$residual_{lamina,n}^{N}$	Residual N of senesced lamina 1 to 11 (N content reported to the structural mass of the lamina before senescence)	0.02, 0.02, 0.02, 0.02, 0.0175, 0.015, 0.01, 0.005, 0.005, 0.005, 0.005	$g\ g^{-1}$	-	[(b)] (Bertheloot, 2009; Bertheloot *et al.*, 2011b)

Method for parameter estimation: [(a)] taken from literature, [(b)] recalculated, adapted or calibrated from literature, [(c)] calibrated on experimental data.
[(*)] Parameters which were adapted from the initial post-flowering version of the CN-Wheat model (Barillot *et al.*, 2016*a*)

Internode growth

During the vegetative stages simulated in the present paper, internodes remain very short (length of whole stem < ~1cm). For ensuring whole model consistency and preparing further developments, we fully implemented internode growth with a level of description similar to that of leaf growth. However, we have not yet implemented the regulation of the elongation rates by metabolite concentrations. This implies that the growth of internodes and the associated metabolite costs calculated by the model are those for optimal conditions of growth.

Structure of the growing internode

As for the growing leaf, the growing internode is represented by: (i) a hidden growing zone (denoted hz_{IN}), where growth occurs and which is enclosed inside the previous mature sheaths, and (ii) exposed mature tissues if the internode becomes longer than the previous sheath.

Phases of internode elongation and coordination rules

In wheat, as in most grass species, internodes of basal phytomers remain short while those of upper phytomers elongate. All internodes show a phase of meristematic growth, but only in upper phytomers the meristematic phase is followed by a phase of cell elongation. Studies on various species have identified leaf ligulation and floral transition as major regulators for this behaviour: (i) fast elongation occurs only after floral transition of the shoot apical meristem (SAM) (Kirby and Faris, 1970; Malvoisin, 1984*a*,*b*; Kirby *et al.*, 1994), (ii) the onset of fast elongation of successive internodes is closely coordinated with leaf ligulation (Kirby *et al.*, 1994; Fournier and Andrieu, 2000; Nakamura *et al.*, 2011) and (iii) for internodes which do not elongate, the meristematic growth stops shortly after leaf ligulation. In sorghum (Nakamura *et al.*, 2011) and wheat (Malvoisin, 1984*b*; Kirby *et al.*, 1994; Ljutovac, 2002), the length of all elongating internodes of a culm follows approximately the same sigmoidal curve when expressed as a function of time relative to leaf ligulation, defined here when the lamina fully emerges outside of the pseudostem (Figure S1.1.2).

Based on this, internode elongation was modelled as a two-phase kinetics with a transition triggered by previous leaf ligulation. From initiation to previous leaf ligulation, all internodes follow an exponential-like phase whose RER is a rank-dependent parameter. At previous leaf ligulation, the internode acquires, for a constant period of time, the ability to follow a sigmoidal elongation. The internode will effectively start sigmoidal elongation only if floral transition has already taken place or occurs before the end of that period. The mechanisms behind floral transition have not yet been taken into account in the model. Thus, floral transition is considered to happen after a delay following the emission of the last foliar primordium which is a model parameter.

Below, we detail model equations and assumptions following the chronology of internode growth, from its initiation by the shoot apical meristem to the end of its elongation (equations and parameters are given in Table S1.1.3 and Table S1.1.4, respectively). As supported by several sources (Malvoisin, 1984*b*; Kirby *et al.*, 1994), the internode is initiated after a delay since the initiation of the leaf on the same phytomer. Initial length and structural mass are identical for all phytomers.

From internode initiation to previous leaf ligulation

Before ligulation of leaf *n-1*, the elongation rate of internode *n* follows an exponential kinetics whose RER is a fitted parameter depending on phytomer rank (Table S1.1.3 Eqn. 1). As for leaves, internode structural mass (Table S1.1.3 Eqn. 2) is estimated from an empirical relationship with internode length and the structural N mass is computed as a constant ratio ($ratio_{N:mstruct}$) of the structural mass.

From previous leaf ligulation to the end of internode elongation

During this phase, the internode is only represented by a hz_{IN}. At previous leaf ligulation, the internode enters a time-window of potential elongation depending on floral transition. The SAM status is tested at each time step throughout this window. Sigmoidal elongation and structural mass increment are realized if SAM is reproductive, while no growth occurs if SAM is vegetative. The sigmoidal phase is modelled by a Beta function, which is scaled according to the length of the internode at ligulation of leaf *n-1* (Table S1.1.3 Eqn. 4). This implies that the length of internodes at the start of their sigmoidal elongation determines their final length. Parameters were estimated from literature (Malvoisin, 1984*a*; Figure S1.1.2). The Beta function depends on internode's physiological age *i.e.* the temperature-compensated time elapsed since ligulation of leaf *n-1* (Table S1.1.3 Eqn. 5). Structural mass of the internode is calculated according to its length and to its Structural Lineic Mass, which is rank-dependent (Table S1.1.3 Eqn. 6). The structural N mass is computed as a constant ratio of the structural mass for each compartment ($ratio_{N:mstruct}$).

Carbon and Nitrogen metabolism of the growing internode

As for leaves, the increase in internode mass results in consumption of sucrose and AA of the hz_{IN} (Table S1.1.3 Eqn. 15, 16, 17). C and N metabolism of the hz_{IN} is identical to that of the leaf *hz* (see main text) and we assume that *hz* and hz_{IN} have the same metabolite concentration at any time. At the end of internode growth, the hz_{IN} is replaced by the mature internode. C and N metabolism (transport, synthesis, degradation of metabolites and senescence) of mature internodes is the same as in other mature photosynthetic organs (Barillot *et al.*, 2016*a*).

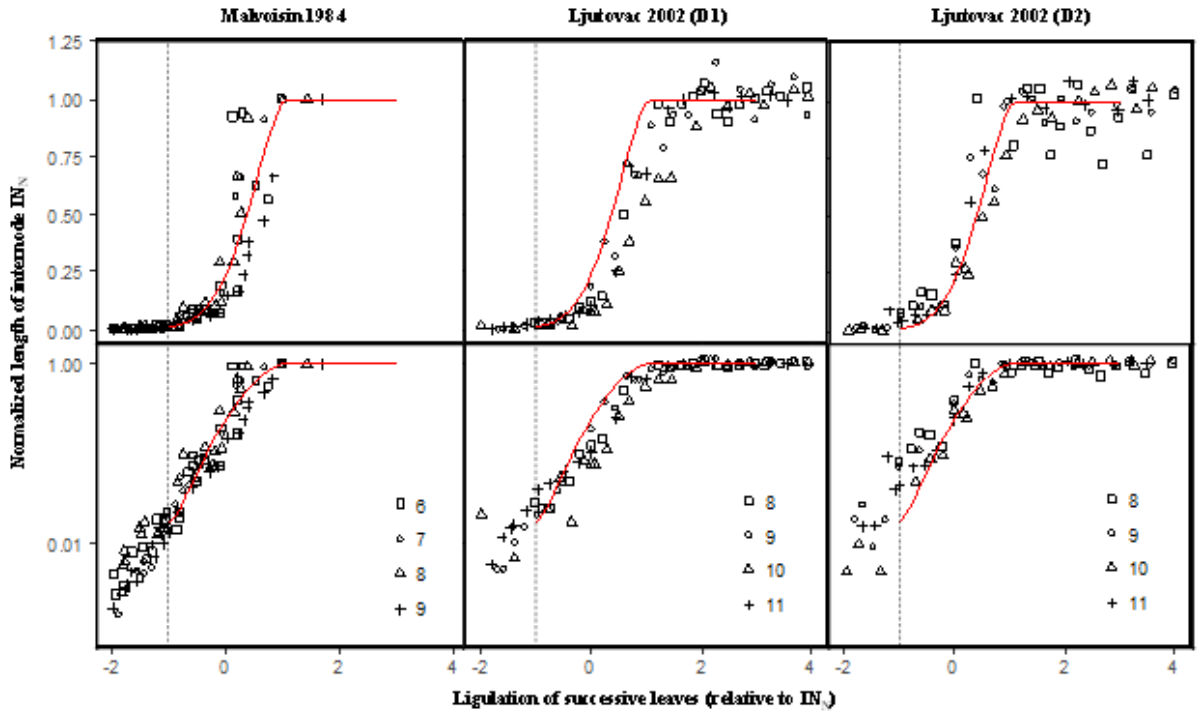

Figure S1.1.2 - Kinetics of internode elongation according to a time relative to leaf ligulation. Normalised length (log scale on the lower panels) of main stem internodes in function of phyllochronic time relative to leaf ligulation is presented for three datasets from Malvoisin 1984a and Ljutovac 2002. For the latter dataset, D1 and D2 are for two plant densities, 250 and 70 plants.m^{-2}, respectively. Symbols are phytomer ranks. Each point is the median of 3 to 10 observations. Red lines are the model simulations obtained from the $Beta_{IN}$ function. Dotted vertical lines mark previous leaf ligulation.

Table S1.1.3 - Equations describing internode growth

Equation	Description	Unit	Equation number
Before previous leaf ligulation			
$\frac{dL_{IN,n}}{dt} = L_{IN,n}(t) \times RER_{IN,n} \times \frac{Arr(T_{hz,n}(t))}{Arr(T_{ref})}$	Rate of internode elongation	m s^{-1}	Eqn. 1
$\frac{dM_{IN,n}^{struct}}{dt} = \left[\alpha \times \beta \times L_{IN,n}(t)^{(\beta-1)} \times \frac{dL_{IN,n}}{dt}\right]\left(\frac{M_{IN,n}^{struct}}{M_{IN,n}^{total}}(t)\right)$	Rate of internode structural mass growth	g s^{-1}	Eqn. 2
After previous leaf ligulation			
$\frac{dAge_{IN,n}^{\rightarrow t_{L_{leaf,n-1}}}}{dt} = \frac{Arr(T_{IN,n}(t))}{Arr(T_{ref}^{growth})}$	Rate of increase in internode physiological age according to temperature	Dimensionless	Eqn. 3
$L_{IN,n}^{max} = \frac{L_{IN,n}\left(t_{L_{leaf,n-1}}\right)}{Beta_{IN}(0)}$	Final internode length	m	Eqn. 4
Case SAM reproductive			
If $L_{IN,n}(t) \leq L_{IN,n}^{max}$: $\frac{dL_{IN,n}}{dt} = \frac{dBeta_{IN}(t)}{dt} \times L_{IN,n}^{max}$ Else: $\frac{dL_{IN,n}}{dt} = 0$	Rate of leaf elongation after previous leaf emergence	m s^{-1}	Eqn. 5a
$Beta_{IN}(t) = \left(1 + \frac{Age_{IN,end} - Age_{IN,n}^{\rightarrow t_{L_{leaf,n-1}}}(t)}{Age_{IN,end} - Age_{IN,max}}\right)\left(\frac{Age_{IN,n}^{\rightarrow t_{L_{leaf,n-1}}}(t) - Age_{IN,base}}{Age_{IN,end} - Age_{IN,base}}\right)^{\left(\frac{Age_{IN,end} - Age_{IN,base}}{Age_{IN,end} - Age_{IN,max}}\right)}$	Beta function defining internode length	Dimensionless	Eqn. 5c
$\frac{dM_{IN,n}^{struct}}{dt} = \frac{dL_{IN,n}}{dt} \times SLM_{IN,n}$	Rate of internode structural mass growth	g s^{-1}	Eqn. 6
Case SAM vegetative			
$\frac{dL_{IN,n}}{dt} = 0$	Update of internode maximal length	m	Eqn. 7

Table S1.1.4 -Description of parameters, values and units of the internode growth model.

Parameter	Description	Value	Unit	Related equation	Reference
Before previous leaf ligulation					
delay_init_IN	Delay between leaf and internode initiation on a phytomer	2739600	s^{-1} at 12°C	-	[(b)] (Malvoisin, 1984a)
$RER_{IN,n}$	Maximum Relative Elongation Rate at 12°C of internodes 3 to 11	[2.4, 2.4, 2.4, 2.4, 2.16, 1.8, 1.91, 1.9, 1.76] x 10^{-6}	s^{-1} at 12°C	Eqn. 1	[(b)] (Ljutovac, 2002)
α	Parameter relating internode length and mass before previous leaf ligulation	0.106	g m-β	Eqn. 2	[(c)]
β	Parameter relating internode length and mass before previous leaf ligulation	1.28	Dimensionless	Eqn. 2	[(c)]
After previous leaf ligulation					
delay_SAM_transition	Delay between emission of the last foliar primordium and the transition of the shoot apical meristem to a reproductive status	2739600	s^{-1} at 12°C	-	[(c)]
$Age_{IN,end}$	Duration of the potential elongation period of the internode	2388627	s^{-1} at 12°C	Eqn. 5c	[(b)] (Malvoisin, 1984a)
$Age_{IN,base}$, $Age_{IN,max}$	Beta function parameters describing the beginning of internode elongation in the second phase and the time of maximum rate	-2694901, 1820015	s at 12°C	Eqn. 5c	[(b)] (Malvoisin, 1984a)
$SLM_{IN,n}$	Structural Lineic Mass of internodes 3 to 11	[2.8, 2.8, 2.8, 2.8, 2.8, 2.8, 2.3, 1.7, 1.6, 1.4, 0.7]	g m-1	Eqn. 6	[(b)] Exp3

Method for parameter estimation: [(a)] taken from literature, [(b)] recalculated, adapted or calibrated from literature, [(c)] calibrated on experimental data.

Tillering

We developed a simplified model of tillering, which covers tiller induction, tiller elongation, coordination of elongation rate with the main stem (MS) and fluxes between the MS and tillers due to tiller growth. This simple approach is based on the high degree of similarity between main stem and tiller development.

Tiller induction

The number and topological position of emerging tillers are given as inputs of the model. Since non-emerging tillers remain short inside the pseudostem, their growth is neglected.

Leaf production and extension

It has been widely reported that the emergence, dynamics of elongation and final length of tiller leaves are coordinated with the MS (Kirby *et al.*, 1985; Evers *et al.*, 2005; Dornbusch *et al.*, 2011; Abichou *et al.*, 2018). These observations led to the concept of cohorts (Table S1.1.5), according to which leaves of the same cohort share common properties. Following this concept, the model assumes all leaves of the same cohort have (Table S1.1.5), at any time, the same length (see illustration in Figure S1.1.3).

The similarity existing between tiller leaves and the corresponding MS leaves for length and timing of elongation does not fully hold for leaf width: the width of the lowermost laminae (on short-internode phytomers) is about 50% of the width of the relative lamina of the MS (Dornbusch *et al.*, 2011). Since our simulations correspond only to the early stages of plant development, the area of the tiller leaves was set to 50% of the area of the corresponding MS leaves.

Metabolite fluxes between the main stem and tillers

As a provisional choice, the metabolite pools of tillers are not simulated in the present version of the model. The effects of tillers on MS metabolism were accounted for by defining common roots and *phloem* compartments whose structural masses represent the whole plant. Using the principle of analogy between the MS and tillers (Figure S1.1.3), we assumed that tiller leaves have the same behaviour as the corresponding MS leaves in terms of fluxes of sucrose, nitrates, cytokinins and AA with the *phloem* and root compartments. Since the area of a tiller leaf is 50% of the area of the corresponding MS leaf, we calculated the fluxes from/to a tiller leaf as 50% of the fluxes from/to the corresponding MS leaf. For example, in Figure S1.1.3, MS.L5, T1.L2 and T2.L1 belong to the same cohort. Consequently, the fluxes of sucrose and AA between the whole cohort and the *phloem* are calculated as the fluxes between MS.L5 and the *phloem*, multiplied by 2 (1 + 0.5 + 0.5). With the same rational, the fluxes of sucrose and AA for the cohort associated to MS.L4 are those for MS.L4, multiplied by 1.5. The same method is applied to the transpiration flow which transports AA, nitrates and cytokinins from the root compartment to the leaves.

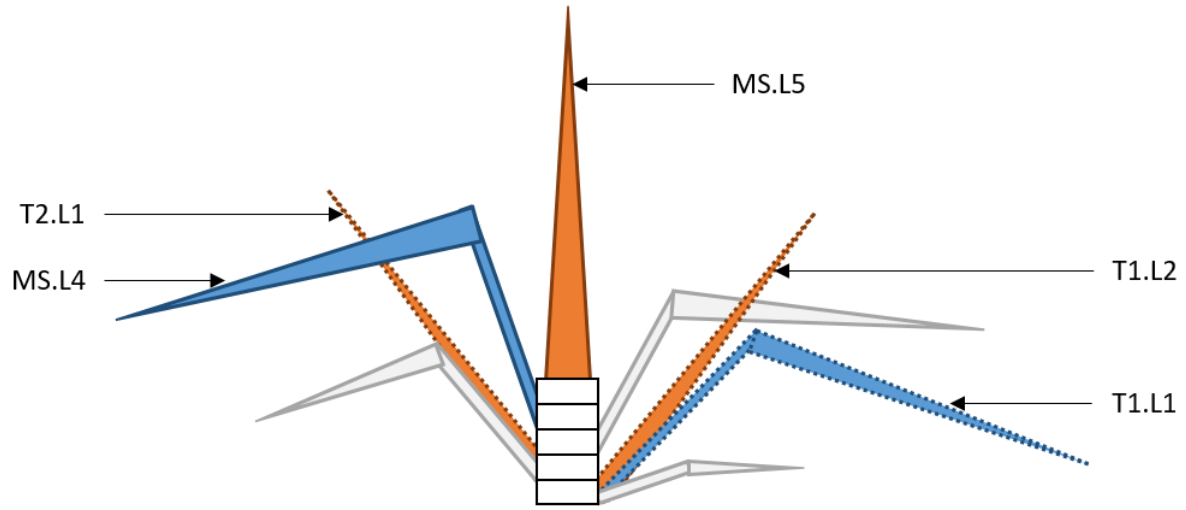

Figure S1.1.3 - Analogy between main-stem leaves and tiller leaves as implemented in the model. The plant has a main stem (MS, solid lines) with five emerged leaves and each of the two bottom phytomers bears an emerged first-order tiller (T1 and T2, dotted lines). Tiller T1 has two emerged leaves, one mature (T1.L1) and one growing (T1.L2). Tiller T2 has one growing emerged leaf (T2.L1). The model assumes that T1.L2 and T2.L1 have same behaviour as MS.L5 (orange); and T1.L1 has the same behaviour as MS.L4 (blue). The calculation is also made for non-emerged leaves and higher order tillers.

Table S1.1.5 - Cohorts of phytomers used in the model to account for similarities between the main stem (MS) phytomers and the tiller phytomers. Only primary tillers T1 to T4 are considered.

Axes	**MS**	**T1**	**T2**	**T3**	**T4**
Phytomers	1				
	2				
	3				
	4	1			
	5	2	1		
	6	3	2	1	
	7	4	3	2	1
	8	5	4	3	2
	9	6	5	4	3
	10	7	6	5	4

Protocol S1.1.2: Modelling responses to temperature

Temperature effects on photosynthesis and respiration were already described in Barillot *et al.* (2016*a*). Here, we present the novel implementations, related to the effects of temperature on the processes of elongation, aging, synthesis and degradation of metabolites, and inter-organ fluxes. The general principle consisted in modulating the rates of the above-mentioned processes by non-linear responses to temperature. Depending on the process concerned, the temperature of plant organs was estimated by different approaches. For photosynthesis and respiration, we used the actual organ temperature as estimated from an energy balance model. The rates of enzymatic activities and fluxes between organs and *phloem* are modulated by air temperature. Because the growth zones of leaves remained close to the soil for the simulated period, the rate of organ growth are modulated by soil temperature. The different curve-responses are illustrated in Figure S1.1.4.

Growth processes

For leaf initiation and leaf elongation, the literature extensively demonstrates that the response to temperature can be described by an Arrhenius-like function which is common to most of the developmental processes of a species (Parent and Tardieu, 2012). In our model, the rates of primordium emission, leaf and internode elongation and root growth in dimension are modulated by a nonlinear function of temperature normalised by the value of the function at a reference temperature (Table S1.1.1, Table S1.1.3).

The growing zone temperature ($T_{hz,n}$;°C) was approximated by soil temperature during the vegetative stage (Jamieson *et al.*, 1995). The reference temperature can be arbitrarily chosen; for the present study we used 12°C because it was the mean temperature throughout the vegetative period of wheat growth for our location. We used modified Eyring's equation (Johnson and Lewin, 1946) fitted on data from Kemp & Blacklow (1982):

$$If\ T_{hz,n}(t) \leq 0: \qquad Arr\big(T_{hz,n}(t)\big) = 0$$

$$If\ 0 < T_{hz,n}(t) < T^*: \qquad Arr\big(T_{hz,n}(t)\big) = a \times T_{hz,n}(t)$$

$$If\ T_{hz,n}(t) \geq T^*: \qquad Arr\big(T_{hz,n}(t)\big) = {}^{K}T_{hz,n}(t) \times \frac{e^{-\frac{E_a/R}{K_{T_{hz,n}(t)}}}}{1+e^{\Delta S/R - \frac{\Delta H/R}{K_{T_{hz,n}(t)}}}} \times k$$

Eqn. S1.1.2. 1

with ${}^{K}T_{hz,n}(t)$, the temperature expressed in K. Parameters are given in Table S1.1.6.

Aging

In the model, some processes - namely the sigmoidal phase of leaf elongation and in some cases the onset of leaf senescence - are driven by the physiological age of the organ. We assumed that the rate of physiological aging depends on temperature according to the same function which modulates the rate of leaf initiation and elongation (Table S1.1.1, Table S1.1.3).

Inter-organ fluxes modelled by transport-resistance formalism

In the model, all organs of a tiller exchange sucrose and AA through a common pool called *phloem*. Fluxes between an organ and the *phloem* are approximated by Poiseuille's law with a conductivity depending on fluid viscosity (Johnson and Thornley, 1985). Farrar (1988) proposed that the dependence of the inverse of *phloem* viscosity to temperature can be approximated by a Q_{10} equation. We implemented this formalism to modulate the conductivity of loading and unloading fluxes between an organ and the *phloem*, thus modifying equations T4.17 and T4.25 in Barillot *et al.*, (2016*a*). The conductivities for sucrose and AA ($\sigma^{C,suc}$and $\sigma^{N,AA}$, respectively) were fitted for a temperature of 20°C in the former version of CN-Wheat (Barillot *et al.*, 2016*b*), they are now modulated by temperature according to a scaling function $Regul_{Phoem}$:

$$Regul_{phloem} = Q_{10_{phloem}}^{\frac{T_{organ,n} - T_{ref}^{viscosity}}{10}} \qquad \text{Eqn. S1.1.2. 2}$$

with $T_{organ,n}$ the organ temperature (°C) which was here approximated by air temperature. Parameters are given in Table S1.1.6.

Enzymatic activity

Temperature affects all the enzymatic activities described in CN-Wheat. *In vitro*, for constant enzyme concentrations, enzymatic activity increases with temperature. The temperature response of the maximum rate of enzymatic activities is described in Parent *et al.* (2010) for several enzymes on maize and rice and can be described by the following equation :

$$Regul_{enzyms}(t) = exp\left(\frac{\Delta Hap\left({}^{K}T_{organ,n}(t) - {}^{K}T_{ref}^{enzyms}\right)}{R\ 10^{-3}\ T_{ref}\ T_K(t)}\right) \times \frac{1 + exp\left[\left({}^{K}T_{ref}^{enzyms}\ \Delta S_2 - \Delta Hd\right) / {}^{K}T_{ref}^{enzyms}\ R\ 10^{-3}\right]}{1 + exp\left[\left({}^{K}T_{organ,n}(t)\ \Delta S_2 - \Delta Hd\right) / {}^{K}T_{organ,n}(t)\ R\ 10^{-3}\right]} \qquad \text{Eqn. S1.1.2.3}$$

with ${}^{K}T_{ref}^{enzyms}$ the reference temperature (set to 293.15 K, *i.e.* 20°C) and ${}^{K}T_{organ,n}$ the organ temperature (K) which was here approximated by air temperature. Parameters are given in Table S1.1.6. This formalism was implemented to modulate the maximum rate of all the reactions of synthesis and degradation as well as

exudation by the roots (Eqn. T4.5 in Barillot *et al.*, 2016*a*). We also used it for the rate of mineralisation (Dessureault-Rompré *et al.*, 2010). Table S1.1.7 lists the parameters fitted at 20°C in Barillot *et al.* (2016*b*) which are now modulated by the temperature, as well as the related equations in Barillot *et al.* (2016*a*).

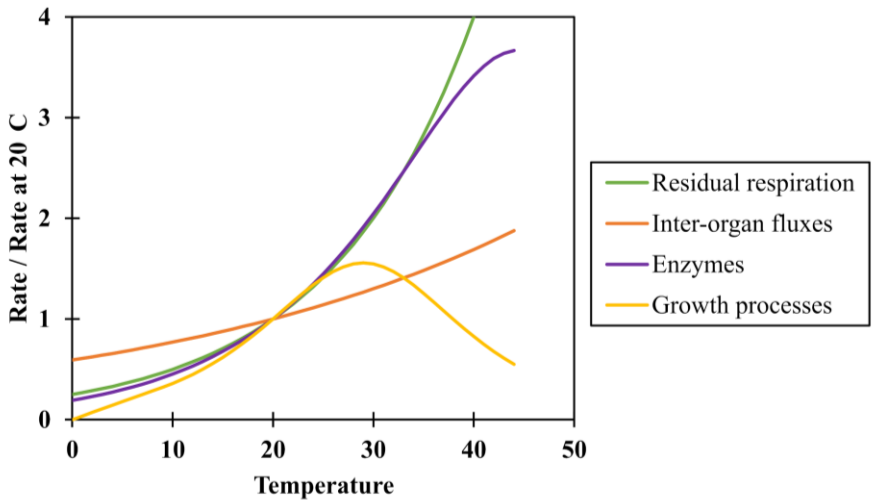

Figure S1.1.4 - Effects of temperature on several processes as implemented in the model. The rate of each process is normalised by its rate at 20°C. The rates of residual respiration and enzymatic activity are represented in function of organ temperature, inter-organ fluxes (transport-resistance formalism) are function of air temperature and growth processes are function of the temperature of soil temperature. The effect of temperature on gross photosynthesis is not presented as it largely depends on surfacic nitrogen.

Table S1.1.6 - Parameters related to the modelling of responses to temperature

Parameter	Description	Value	Unit	Related equation	Reference
T^*	Temperature below which a growth process linearly depends on the temperature	9	°C	Eqn. S1.1.2. 1	[b] (Kemp & Blacklow, 1982)
a	Slope of the effect of temperature on a growth process between 0°C and T^*	6.23 x 10^{-13}	$°C^{-1}$ s^{-1}	Eqn. S1.1.2. 1	[b] (Kemp & Blacklow, 1982)
k	Constant	3.8 x 10^{10}	K^{-1} s^{-1}		
R	Gas constant	8.3144	J mol^{-1} K^{-1}		
E_a	Enthalpy of activation of inter-organ fluxes	73995	J mol^{-1}	Eqn. S1.1.2. 1	[b] (Kemp & Blacklow, 1982)
ΔS	Entropy of inter-organ fluxes	569	J mol^{-1} K^{-1}	Eqn. S1.1.2. 1	[b] (Kemp & Blacklow, 1982)
ΔH	Enthalpy of inter-organ fluxes	172403	J mol^{-1}	Eqn. S1.1.2. 1	[b] (Kemp & Blacklow, 1982)
$Q10_{phloem}$	Dependence of *phloem* translocation conductivity on temperature	1.3	Dimensionless	Eqn. S1.1.2. 2	[a] (Farrar, 1988)
ΔH_{ap}	Enthalpy of activation of enzymatic activity	55	kJ mol^{-1}	Eqn. S1.1.2. 3	[b] (Parent *et al.*, 2010)
ΔH_d	Enthalpy of deactivation of enzymatic activity	154	kJ mol^{-1}	Eqn. S1.1.2. 3	[b] (Parent *et al.*, 2010)
ΔS_2	Entropy of enzymatic activity	0.48	kJ mol^{-1} K^{-1}	Eqn. S1.1.2. 3	[b] (Parent *et al.*, 2010)

Method for parameter estimation: [a] taken from literature, [b] recalculated, adapted or calibrated from literature, [c] calibrated on experimental data.

Table S1.1.7 - Parameters of enzymatic activity which are modulated by temperature. Parameters values were fitted at 20°C in Barillot *et al.* (2016*b*).

Parameter	**Description**	**Equation number in Barillot *et al.* (2016*a*)**
$Vmax_{roots}^{N,nit\ HATS}$	Maximum rate of nitrate uptake for HATS	3
$K_{roots}^{N,nit\ LATS}$	Rate of nitrate uptake for LATS	4
$Miner_{soil}^{N,nit}$	Rate of N mineralisation in soil	8
$Smax_{roots}^{N,org}$	Maximum rate of organic N synthesis in roots	T4.4
$Smax_{tp,i}^{C,star}$	Maximum rate of starch synthesis in *(tp,i)*	T4.10
$Smaxpot_{tp,i}^{C,fruc}$	Potential maximum rate of fructan synthesis in *(tp,i)*	T4.14
$Smax_{tp,i}^{C,suc}$	Maximum rate of sucrose synthesis in *(tp,i)*	T4.10
$Smax_{tp,i}^{N,AA}$	Maximum rate of amino acid synthesis in *(tp,i)*	T4.11
$Smax_{tp,i}^{N,prot}$	Maximum rate of protein synthesis in *(tp,i)*	T4.20
$\delta_{tp,i}^{C,star}$	Relative rate of starch degradation in *(tp,i)*	T4.12
$Dmax_{tp,i}^{C,fruc}$	Maximum rate of fructan degradation in *(tp,i)*	T4.15
$\delta max_{tp,i}^{N,prot}$	Maximum rate of protein degradation in *(tp,i)*	T4.21
$\delta_{tp,i}^{cyto}$	Rate of cytokinin degradation in *(tp,i)*	T3.3

Protocol S1.1.3: Dynamic 3D-architecture and light interception modelling

Plant geometry is an important aspect which determines which tissues are enclosed or exposed, and the light distribution on exposed tissues. The dynamics of 3D architecture is simulated with a modified version of ADEL-Wheat (Fournier *et al.*, 2003; Abichou *et al.*, 2018). First, ADEL-Wheat was adapted to provide an external and dynamic control of its parameters during the simulation. This allowed us to dynamically add and remove organs and control the rate of organ elongation from model calculations instead of the original predefined parameterisation of ADEL-Wheat. Second, we included a new model for leaf insertion angle and midrib curvature as a function of leaf age, based on experimental data (Fournier *et al.*, 2016) and the mathematical model of Fournier and Pradal (2012). The dynamics was simulated by interpolating among a discrete time series of leaf shapes, obtained after grouping leaves by age and type (presence or absence of an elongated internode). For each leaf type, a median shape is calculated from emergence to full senescence, by averaging the curvature as a function of the normalised distance to leaf base.

Absorption of PAR at organ scale was computed by the radiation model Caribu using the projective method (Chelle and Andrieu, 1998). Light distribution was simulated for an overcast sky (SOC, Moon and Spencer, 1942) approximated by a set of 20 light sources represented by 20 solid angle sectors including five zenith angles. Calculations were done using the built-in algorithm of the infinite periodic canopy, allowing simulation of light absorption in small canopies without border effects. In principle, CN-Wheat model could be run for each plant of a stand. However, the computational time for simulating the whole pre-flowering period with a personal computer was typically two hours per plant. In order to deal with available computer resources, CN-Wheat was run for one 'average plant' but calculations of PAR absorption were performed on virtual canopies consisting of 1000 plants having the same dimensions but variable sowing positions and organ orientations in terms of leaf inclination and azimuth as well as tiller azimuth. PAR absorption of each organ was therefore averaged across the 1000 plants.

Protocol S1.1.4: Changes to CN-Wheat as compared to Barillot et al. (2016ab)

CN-Wheat was initially developed for the post-flowering period (Barillot *et al.*, 2016*ab*). For the present paper, changes have been made to the initial version of CN-Wheat: (i) we introduced regulations for the effects of temperature on metabolism, (ii) we modified some formalisms related to the transport of metabolites, (iii) as a consequence of (i) and (ii) we recalibrated some parameters to simulate correctly both vegetative and post-flowering stages and (iv) four parameters regarding root growth and functioning have been specifically adapted for the vegetative stages. The effects of temperature on the metabolism were presented in Protocol S1.1.2. Below, we first describe the changes relative to (ii) to (iv). Then, we present simulations illustrating that the modifications (i) to (iii) did not alter the behaviour of the model for the post-flowering period.

Changes to the description of metabolite fluxes among organs (ii)

Three sets of formalisms were adapted to improve model behaviour throughout pre-flowering stages: unloading of sucrose from the *phloem* to the root compartment, export of metabolites from the roots toward the photosynthetic organs through the transpiration flow and the rate of protein degradation.

Sucrose unloading from phloem to roots

The rate of sucrose unloading was previously calculated from sucrose concentration in the *phloem* by using a Michaelis-Menten equation (Eqn. T4.3 in Barillot *et al.*, 2016*a*) which implied that this process is mainly active. Following Münch's theory, we now use a transport-resistance formalism (Table S1.1.8).

Exports from the roots through the transpiration flow

In CN-Wheat, three metabolites are exported from the roots to the shoot: nitrates, AA and cytokinins. In the former version, the rate of export of these metabolites (Eqn. T3.2, T4.6, T4.9 in Barillot *et al.*, 2016*a*) was a non-linear function of the surfacic rate of culm transpiration ($f_{Tr}(t)$). Because the tillers' surface strongly increases during pre-flowering stages, the rate of export is now proportional to the total culm transpiration (Tr_{culm}^{tot}, mmol water s^{-1}). Equations are given in Table S1.1.8 and parameters in Table S1.1.9.

Rate of protein degradation

Previously, the rate of protein degradation in the photosynthetic organs was directly proportional to the protein concentration, and downregulated by cytokinin concentration (Eqn. T4.21 in Barillot *et al.*, 2016*a*). We now calculate the rate of protein degradation with a Michaelis-Menten equation in order to saturate this process in case of high protein concentration as in young growing lamina. Equation is given in Table S1.1.8 and parameters in Table S1.1.9.

Recalibration of some parameters presented in Barillot et al. (2016b) (iii)

Some parameters were re-calibrated compared to Barillot *et al*. (2016*b*) to allow for a correct behaviour throughout both vegetative stages and post flowering period. There are presented Table S1.1.10.

Adaptation of some root parameters to the vegetative stages (iv)

In CN-Wheat, the root compartment is represented by a single compartment defined by its structural mass, without description of its architecture. The metabolic activities described for roots are nitrates uptake from the soil, unloading of sucrose and AA from the *phloem*, synthesis of AA and cytokinins, C respiration and the export of nitrates, AA and cytokinins to the shoot. The rate of root growth in structural dry mass depends on sucrose concentration and is modulated by soil temperature, while the rate of senescence is a model parameter. Since the architecture and functioning of the root compartment vary widely from the seedling stage (seminal roots) to the post-flowering stages (adventitious roots of several culms), several parameters had to be adapted for the vegetative stages. Adapted parameters are related to the rate of root mass growth, root senescence and exports of nitrates and AA from the roots (Table S1.1.11).

Table S1.1.8 - New set of equations replacing those of Barillot *et al.* (2016*a*).

New equation	**Description**	**Unit**	**Equation number in Barillot *et al.* (2016*a*)**
$U^{C,suc}_{phloem\rightarrow roots}(t) = \left(\left[C^{suc}_{phloem}\right], [C^{suc}_{roots}]\right)(t) * \left(\left[C^{suc}_{phloem}\right](t) - [C^{suc}_{roots}](t)\right) * G^{C,suc}_{roots}(t)$	Rate of sucrose unloading from *phloem* to roots	g s^{-1}	T4.3
$G^{C,suc}_{roots}(t) = \beta_{roots} * \left(M^{struct}_{roots}(t)\right)^{\frac{2}{3}} * \sigma^{C,suc}_{roots} * Regul_{phloem}(t)$	Conductance between the root compartment and the *phloem*	g^2 µmol^{-1} s^{-1}	-
$f_{Tr}(t) = Tr^{tot}_{culm} * K^{Tr}_{roots}$	Regulation the rate of exports from the roots through the transpiration flow	Dimensionless	12
$D^{N,prot}_{tp,i} = \frac{Dmax^{N,prot}_{tp,i} * \left[N^{prot}_{tp,i}\right](t)}{Kd^{N,prot}_{tp,i} + \left[N^{prot}_{tp,i}\right](t)} * \delta^{N,prot}_{tp,i}(t)$	Rate of protein degradation	µmol N g^{-1} s^{-1}	T4.21

Table S1.1.9 - Values for new parameters.

Parameter	Description	Value	Unit	Reference
β_{roots}	Scalar factor to estimate the section between the roots and the *phloem*	1	$(g\ m^{-3})^{2/3}$	(c)
$\sigma_{roots}^{C,suc}$	Conductivity for sucrose in the roots	10^{-7}	$g^2\ \mu mol^{-1}\ s^{-1}$	(c)
K_{roots}^{Tr}	Proportionality coefficient between total culm transpiration and the rate of root exportations	25	$mmol\ water^{-1}$	(c)
$Kd_{tp,i}^{N,prot}$	Affinity coefficient for protein degradation in *(tp,i)*	8000	$\mu mol\ N\ g^{-1}$	(c)
$Dmax_{tp,i}^{N,prot}$	Maximum rate of protein degradation in *(tp,i)* at 20°c	6000	$\mu mol\ N\ g^{-1}\ s^{-1}$	(c)

Method for parameter estimation: (a) taken from literature, (b) recalculated, adapted or calibrated from literature, (c) calibrated on experimental data.

Table S1.1.10 - Values for parameters re-calibrated as compared to Barillot *et al.* (2016*b*) and used to simulate both vegetative and post-flowering stages (1/2)

Parameter	Description	New value	Value in Barillot *et al.* (2016*b*)	Unit	Equation number in Barillot *et al.* (2016*a*)
$K_{roots}^{C,CHO}$	Regulation of nitrate uptake by carbohydrate concentration in roots	7000	4000	µmol C g^{-1}	7
$K_{roots}^{CHO,cytok}$	Affinity coefficient for cytokinin synthesis according to root carbohydrates	1200	1250	µmol C g^{-1}	T3.1
n_{CHO}	Parameter for the regulation of cytokinin synthesis according to root carbohydrates	3	10	Dimensionless	T3.1
$K_{roots}^{nit,cytok}$	Affinity coefficient for cytokinin synthesis according to root nitrates	50	200	µmol N g^{-1}	T3.1
n_{nit}	Parameter for the regulation of cytokinin synthesis by nitrates in roots	1	0.7	Dimensionless	T3.1
$Smax_{roots}^{cytok}$	Maximum rate of cytokinin synthesis in roots at 20°C	9 x 10^{-4}	4.5 x 10^{-4}	AU g^{-1} s^{-1}	T3.1
$Smax_{tp,i}^{C,star}$	Maximum rate of starch synthesis in *(tp,i)* at 20°C	8	2	µmol C g^{-1} s^{-1}	T4.10
$Smax_{tp,i}^{C,suc}$	Maximum rate of sucrose synthesis in *(tp,i)* at 20°C	4	1	µmol C g^{-1} s^{-1}	T4.10
$Smax_{tp,i}^{N,AA}$	Maximum rate of amino acids synthesis in *(tp,i)* at 20°C	4	1	µmol N g^{-1} s^{-1}	T4.11
$K_{tp,i}^{N,AA}$	Affinity coefficient for protein synthesis in *(tp,i)*	250	100	µmol N g^{-1}	T4.20

(Continued)

Table S1.1.10 - Values for parameters re-calibrated as compared to Barillot *et al.* (2016*b*) and used to simulate both vegetative and post-flowering stages (2/2)

Parameter	Description	New value	Value in Barillot *et al.* (2016*b*)	Unit	Equation number in Barillot *et al.* (2016*a*)
$Smax_{tp,i}^{N,prot}$	Maximum rate of protein synthesis in *(tp,i)* at 20°C	0.0045	0.0015	µmol N g^{-1} s^{-1}	T4.20
$Dmax_{tp,i}^{C,fruc}$	Maximum rate of fructan degradation in *(tp,i)* at 20°C	0.07	0.035	µmol C g^{-1} s^{-1}	T4.15
$\delta_{tp,i}^{cytok}$	Rate of cytokinin degradation in *(tp,i)* at 20°C	1.5 x 10^{-5}	3x10^{-6}	s^{-1}	T3.4
$K_{roots}^{cytok\ export}$	Relative rate of cytokinins export from roots	1.7 x 10^{-4} / 25	2 10^{-4}	s^{-1}	T3.2

(tp,i) : Photosynthetic organ *tp*, bared by the phytomer *i*

Table S1.1.11 - Values for root parameters that differ between vegetative and reproductive stages

Parameter	Description	Value for the vegetative stages	Value for post-flowering stages from Barillot *et al.* (2016*b*)	Unit	Equation number in Barillot *et al.* (2016*a*)
$Gmax_{roots}^{C\ mstruct}$	Maximal rate of root structural growth at 20°C	0.0854	0.015	µmol C s^{-1} g^{-1}	T4.1
$\delta_{roots}^{mstruct}$	Death rate of root structural mass at 20°C	0	3.5	s^{-1}	9
$K_{roots}^{N,nit\ export}$	Relative rate of nitrates export from roots	5 x 10^{-3} / 25	1 10^{-6}	s^{-1}	T4.6
$K_{roots}^{N,AA\ export}$	Relative rate of amino acids export from roots	4.5 x 10^{-2} / 25	3 10^{-5}	s^{-1}	T4.9

Validation of model modifications for post-flowering stages.

In order to assess the effects of the modifications (i) to (iii) described above for the post-flowering stages, we performed the same evaluation as in Barillot *et al.* (2016*b*). Briefly, we simulated C and N distribution within a wheat culm during the post-flowering period, for three N fertilization treatments (H0, H3, and H15). The results show that the revised model simulate dynamics and spatial patterns of green area and C-N content which are in accordance with the experimental observations (Figure S1.1.5). Based on this test, we concluded the revised model is still capable of simulating the post-flowering stages.

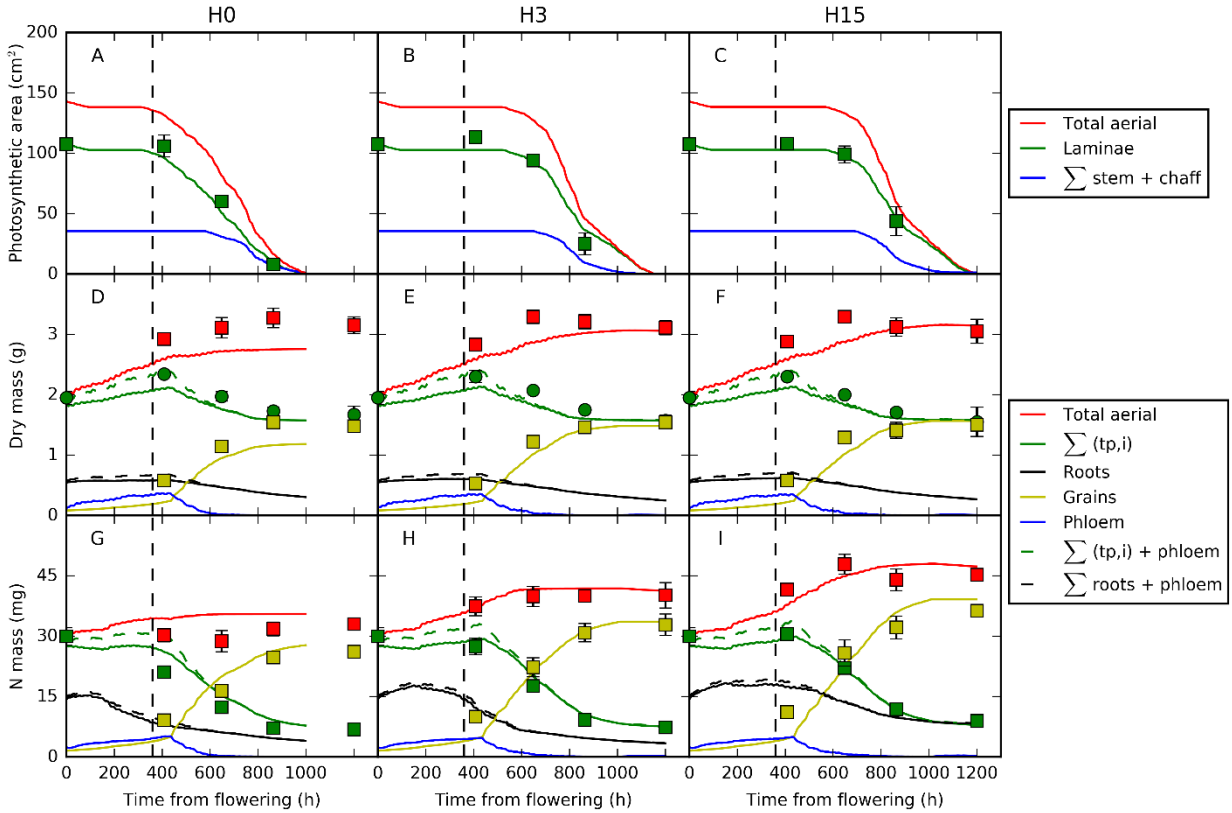

Figure S1.1.5 - Comparison of simulations from the modified CN-Wheat model with observations for post-flowering wheat cultivated under three nitrogen treatments. Culm photosynthetic projected area (A,B,C), dry mass (D,E,F) and N mass (G,H,I) during the post-anthesis period for treatments H0 (A,D,G), H3 (B,E,H) and H15 (C,F,I). Model simulations are in solid lines while experimental data is represented by squares (vertical bars represent ± s.d.). For H0, simulate stopped after 1000h as the shoot was fully senescent. The colour code is detailed in the key: Σ(tp,i) accounts for the sum of all photosynthetic organs and 'stem' accounts for the sum of sheaths, internodes and the peduncle. The *phloem* contribution to the shoot (green dotted line) and roots (black dotted line) is calculated using the fraction of shoot and root structural mass among the whole plant. The vertical dashed line represents the beginning of the rapid filling stage of grains.

Protocol S1.1.5: Model calibration and evaluation

Experimental datasets

Model initialisation and calibration required extensive experimental data describing leaf dimensions, mass and composition. We used three complementary datasets originating from field experiments (Exp1, Exp2 and Exp3) which were conducted over different years, with similar agronomic conditions (including optimal fertilization), at the same location (Grignon, France) and with the same genotype of winter wheat (*cv.* Soissons). Variables of interest of each experiment are summarised in Table S1.1.12 and details of the experimental methods are presented below.

Table S1.1.12 - Experimental datasets used for model initialisation and calibration

Experiment	Sowing date	Sowing density (plants/m^2)	Variables	Reference
Exp1	15/10/98	250	Weather data, Length dynamic of the laminae, sheaths and internodes, lamina maximum width, phyllochron	(Ljutovac, 2002)
Exp2	27/10/05	250	Specific structural mass of the laminae, Lineic structural mass of the sheaths and of the internodes, N content of the structural mass	(Bertheloot, 2009; Bertheloot *et al.*, 2011)
Exp3	23/10/14	170	N content of several compartments of the plant at early seedling stage	Unpublished

The first experiment (Exp1) gathered detailed kinetics of leaf elongation of plants cultivated in a field sown on 15/10/98 with a usual sowing density (250 plants/m^2) and optimal N conditions (Ljutovac, 2002; Fournier *et al.*, 2005). At flowering, median plants had 11 phytomers and internode 7 was the lowest elongated internode (longer than 1 cm). Twice a week, 5 to 10 median plants were dissected and all main stem leaves longer than 90 µm were measured. Maximum width of mature laminae was measured with a ruler. A meteorological station recorded on an hourly basis air temperature at 2m high, incident PAR and humidity, and on a daily basis, the average wind speed at 2m (Figure S2.1). In addition, near-surface soil temperature was recorded hourly using small copper-constantan thermocouples.

The second experiment (Exp2) gathered dry mass and N content of mature leaves 1 to 11 at several dates from ligulation to full senescence (Bertheloot, 2009; Bertheloot *et al.*, 2011*b*). Wheat was sown on 27/10/05 with a density of 250 plant/m^2 and cultivated under optimal N conditions. On seven occasions from 02/03/06 to 11/07/06 (*i.e.* from

4 ligulated leaves to full senescence), five median plants were sampled, then the dry mass, length, green and non-green surface and N content of all mature laminae and sheaths were assessed.

The third experiment (Exp3) provided data (unpublished) of dry mass and N allocation within wheat plants at an early stage (two ligulated leaves). Wheat was sown on 23/10/14 with a density of 170 plants/m^2. Thirty plants randomly chosen were tagged at seedling emergence and their leaf stage (Abichou *et al.*, 2018) was measured once or twice weekly. On 09/12/14, 30 independent plants were collected (shoot and roots until 15cm depth), among which 12 representative plants were selected for having the length of the last ligulated lamina and the leaf stage similar to the median calculated for the tagged plants (two ligulated leaves and two emerged growing leaves). The selected plants were randomly grouped in three lots. Their main stem was dissected into the following groups: root system, mature lamina and mature sheath per phytomer rank, hidden part of the growing leaf, emerged part of the growing leaf. Plants within each lot were pooled together in order to obtain enough material for analysis. The samples were dried for 48 hours at 80°C to measure dry mass and grinded to a fine powder. Total N content was quantified using the DUMAS method (Dumas, 1831).

Procedure of model initialisation

The model was initialised to describe a wheat plant at leaf 4 emergence in the conditions of experiments Exp1-Exp3. The model requires information of plant density and soil N concentration, and information about the plant: leaf dimensions, mass of the compartments, their contents in metabolites as well as integrated variables (Table S1.1.13). The procedure is described below for the *phloem*, the root compartment and the main stem leaves. Tillers T1 to T4 are represented in the 3D-architecture (Table S1.1.5).

Plant density and soil nitrate concentration

Plant density was set to 250 plants.m^{-2} with an inter-row spacing of 15 cm as in Exp1 and Exp2. In all experiments (Exp1-3), soil was a deep clay-loam and emergence of leaf 4 occurred around mid-December. N soil concentration under nitrate form was initialised at 6 g m^{-2}, which is a concentration commonly measured for this location at this time of the year.

Dimensions of leaves

The model was initialised at an early seedling stage using leaf dimensions from Exp1 with the median leaf lengths of 3 to 10 plants measured on 17/12/98. On that date, leaf 3 has emerged but not yet ligulated, leaf 4 was about to emerge and leaves 5 to 10 were hidden. Leaves 3 to 4 were therefore already in the second growth phase of the model. Leaves 5 to 10 were fully meristematic and still in the exponential-like growth phase of the model.

Structural mass and structural nitrogen mass

Structural mass of the mature laminae and sheaths were approximated by the mass of recently fully senescent organs measured in Exp2. Structural mass of *hz* was defined from the relationship with leaf length (Eqn. 3) and structural mass of hz_{IN} from the relationships with internode length Table S1.1.3 Eqn. 2). Structural mass of the root compartment was defined to meet a shoot : root biomass ratio of 0.8, as estimated from literature for this stage (Lawlor *et al.*, 1988; Siddiqi *et al.*, 1990). The N fraction of the structural mass was set to 0.5% for all organs (Martre *et al.*, 2006).

Metabolite contents in physical compartments

Carbohydrate content was estimated from literature on wheat seedlings (Lawlor *et al.*, 1988; Bancal and Gaudillère, 1989; Engels, 1994). Sucrose of any compartment (except *phloem*) was set to 10% of compartments' biomass. Fructans mainly accumulate in hidden photosynthetic tissues and in the elongation zone of growing leaves (Schnyder and Nelson, 1987 on tall fescue; Roth *et al.*, 1997 on barley). Consequently, fructan content was set to 3% of the biomass in the enclosed part of sheath 2, 10% in the hidden part of the growing leaf 3 (*hz* 3) and 5% in *hz* 4 as its elongation zone was shorter. Fructan content was set to zero in other compartments.

N-metabolite contents were estimated in two steps: (i) we estimated the total N fraction of the compartment, (ii) we decomposed the N non-structural mass in nitrates, AA and proteins. Total N fractions of the root compartment and of the leaves 1 to 4 were derived from Exp3. Total N fraction in *hz* 5 to 10 was set to 9.5%, as measured by Gastal and Nelson (1994) in the division zone of elongating leaves of tall fescue. Then, we assumed that proteins, AA and nitrates in the photosynthetic elements represented respectively 80%, 20% and 0% of the non-structural N, as in Barillot *et al.* (2016*b*). In the root compartment, the model accounts for nitrates and a pool of organic N. We assume they represented respectively 10% and 90% of the non-structural N.

Cytokinins do not contribute to the mass balance in the model. Cytokinins content in photosynthetic elements was set proportionally to their protein content (0.014 AU μmol^{-1} N of protein) as vertical protein gradients are likely related to the distribution of cytokinins (Pons *et al.*, 2001). Cytokinins content in the root compartment was initialized at the steady state reached by the model after testing several initial values in the simulation.

Integrated variables

The model requires two integrated variables related to metabolites concentrations: (i) the maximum protein concentration reached during organ's lifespan (used to trigger tissue death) and (ii) the mean sucrose concentration in the hz_n integrated since leaf *n-2* emergence which defines the maximal width of lamina *n* and structural specific mass of both lamina and sheath *n*.

Data (Exp2 and Exp3) indicate that N content decreases in laminae over time. Therefore, we supposed that laminae 1 and 2 had reached their maximum protein content prior to model initialisation and that it corresponds to a total N content of 4.5%.

The mean sucrose concentration integrated from leaf n-2 emergence was set 150 µmol to in all *hz*.

Metabolite contents in the *phloem*

In our model, the *phloem* compartment is the common pool of mobile metabolites *i.e.* sucrose and AA. *Phloem*ic sucrose and AA were initialised at zero as simulations showed these compartments quickly filled from source organs following the diffusion equation.

Table S1.1.13 - Initialisation of state variables at early seedling stage for the soil, the *phloem* compartment, the root compartment and the main stem (MS) leaves: definitions, symbols and values (1/3)

Definition	**Symbol**	**Unit**	**Value**	**Definition**	**Symbol**	**Unit**	**Value**
(a) Soil				(c) Root compartment			
Nitrate concentration	$[N_{soil}^{nit}]$	g m^{-3}	6	Structural mass	M_{roots}^{struct}	mg	34.4
				Structural N mass	N_{roots}^{struct}	µg	172
(b) *Phloem*				Carbohydrates	C_{roots}^{CHO}	µmol C	203
Sucrose	C_{phloem}^{suc}	µmol C	0	Nitrates	N_{roots}^{nit}	µmol N	21.9
Amino acids	N_{phloem}^{AA}	µmol N	0	Organic N	N_{roots}^{org}	µmol N	2.2
				Cytokinins	$cytok_{roots}$	AU	8.6

(d) Stage of plant development

				Lamina			**Sheath**				
Definition	**Symbol**	**Unit**	**MS**	**1**	**2**	**3**	**1 exposed**	**2 enclosed**	**2 exposed**		
Growing organ				no	No	yes	no	no	no		
Physiological age since emergence of leaf *n-1*	$Age_{leaf,n}^{\rightarrow t_{E_{leaf,n-1}}}$	days at 12°C		20	13	7	20	-	13		
(e) Stage of *hz* development											
Definition	**Symbol**	**Unit**	**MS**	**3**	**4**	**5**	**6**	**7**	**8**	**9**	**10**
Age since previous leaf emergence	$Age_{hz,n}^{\rightarrow t_{E_{leaf,n-1}}}$	days at 12°C		13.0	6.3	0	0	0	0	0	0
Internode age since previous leaf ligulation	$Age_{int,n}^{\rightarrow t_{E_{leaf,n-1}}}$	days at 12°C		7.1	0	0	0	0	0	0	0

(Continued)

Table S1.1.13 - Initialisation of state variables at early seedling stage for the soil, the *phloem* compartment, the root compartment and the main stem (MS) leaves: definitions, symbols and values (2/3)

(f) Mature tissues

				Lamina			Sheath		
Definition	**Symbol**	**Unit**	**MS**	**1**	**2**	**3**	**1 exposed**	**2 enclosed**	**2 exposed**
Length	L_n	cm		8.2	9.2	6.04	2.85	2.85	0.05
Green area	A_n^{green}	cm^2		1.96	2.3	1.99	2.69	2.48	0.05
Senesced area	A_n^{senesc}	cm^2		0	0	0	0	0	0
Structural mass	M_n^{struct}	mg		4.1	4.8	4.2	1.7	2.3	0.04
Structural N mass	N_n^{struct}	µg		20.5	24.2	20.9	8.6	11.4	0.2
Triose phosphates	$C_n^{trioseP}$	µmol C		0	0	0	0	0	0
Sucrose	C_n^{suc}	µmol C		24.2	28.5	24.5	10.1	13.4	0.2
Starch	C_n^{star}	µmol C		0	0	0	0	0	0
Fructans	C_n^{fruct}	µmol C		0	0	0	0	6.7	0
Nitrates	N_n^{nit}	µmol N		0	0	0	0	0	0
Amino acids	N_n^{AA}	µmol N		1.7	2.4	2.2	0.2	0.4	0
Proteins	N_n^{prot}	µmol N		16.9	23.6	22.4	2.0	3.8	0.1
Cytokinins	$cytok_n$	AU		0.35	0.49	0.46	0.04	0.08	0.0014

(Continued)

Table S1.1.13 - Initialisation of state variables at early seedling stage for the soil, the *phloem* compartment, the root compartment and the main stem (MS) leaves: definitions, symbols and values (3/3)

(g) Hidden growing zone *hz*

Definition	**Symbol**	**Unit**	**MS**	**3**	**4**	**5**	**6**	**7**	**8**	**9**	**10**
Provisional estimate of final leaf length	${}^{*}L_{leaf,n}^{max}$	cm		12.28	13.31	-	-	-	-	-	-
Lamina width max	$W_{lamina,n}^{max}$	cm		0.4	-	-	-	-	-	-	-
Structural specific lamina mass	$SSM_{lamina,n}$	g m^{-2}		21	-	-	-	-	-	-	-
Structural lineic sheath mass	$SLM_{sheath,n}$	g m^{-1}		0.09	-	-	-	-	-	-	-
Structural mass of the enclosed leaf	$M_{encl\ leaf,n}^{struct}$	µg		2048	496	11	3	1.05	0.47	0.18	0.13
Provisional estimate of final internode length	${}^{*}L_{IN,n}^{max}$	cm		-	-	-	-	-	-	-	-
Structural mass of the enclosed internode	$M_{encl\ IN,n}^{struct}$	µg		1.33	0.17	0	0	0	0	0	0
Structural N mass of *hz*	$N_{hz,n}^{struct}$	µg		10.3	2.3	5.6 e-2	1.5 e-2	5.3 e-3	2.3 e-3	9 e-4	6.3 e-4
Sucrose	$C_{hz,n}^{suc}$	µmol C		12.1	2.9	6.6 e-2	1.8 e-2	6.2 e-3	2.7 e-3	1.1 e-3	7.4 e-4
Fructans	$C_{hz,n}^{fruct}$	µmol C		6.0	3.5	0	0	0	0	0	0
Amino acids	$N_{hz,n}^{AA}$	µmol N		1.0	0.5	2.1 e-2	5.8 e-3	2.0 e-3	8.8 e-4	3.4 e-4	2.4 e-4
Proteins	$N_{hz,n}^{prot}$	µmol N		10.1	4.8	2.1 e-1	5.8 e-2	2.0 e-2	8.8 e-3	3.4 e-3	2.4 e-3

Parameter estimation

The initial version of CN-Wheat for the post-flowering period gathered about 60 parameters covering the processes of C and N acquisition, synthesis and degradation of metabolites, their fluxes among organs and tissue death. The development of the growth model required about 100 parameters (Tables S1.2 and S1.4) which are related to (1) leaf and internode elongation and mass growth, (2) the regulation by C-N metabolism, (3) the synthesis, degradation and metabolite fluxes with(in) the *hz*, (4) tissue death and metabolite remobilisation, and (5) temperature dependencies. Among these parameters, about 70 were either taken from literature (method 'a' in Tables S1.2 and S1.4) or estimated from experimental data of the literature (method 'b'). The other ~30 parameters were calibrated pragmatically (method 'c'). We calibrated the parameters in order to (i) fit the available experimental measurements *i.e.* leaf final dimensions and phyllochron from Exp1 and (ii) simulate realistic behaviour at molecular (metabolite allocation and dynamics), organ (dynamics of growth, organ mass, lifetime, *etc.*) and plant level (shoot:root ratio, N content, LAI, *etc.*). Because we did not use any numerical optimisation method and our calibration dataset is limited, calibrated parameter values are only intermediate propositions which would require further investigation on more detailed datasets for contrasted growth conditions.

Supplementary Data S1.2 – Model evaluation

Protocol S1.2.1 Indices for comparison of simulations with observations

We present below the calculation of the different indices used to compare simulations with observations.

Temperature-compensated time and thermal time

As detailed in Protocol S1.1.2, we implemented non-linear effects of temperature on biological processes. The model runs with a calendar time but we considered temperature-dependent rates for processes. Besides, in order to compare experimental data with model simulations, it was necessary to express process durations and rates in unit compensated for temperature (*e.g.* phyllochron, relative elongation rate, leaf area index kinetic). As proposed in Parent *et al.* (2010), it is interesting to express the time required for a given progress in terms of temperature-compensated time, that is the calendar time this process would require at a reference temperature (*Tref*). Similarly, the rate of development can be expressed as temperature-compensated, that is the value of the rate if temperature was *Tref*.

However, it was generally not possible to calculate temperature-compensated duration or temperature-compensated rate from bibliographic data, as authors usually use thermal time. For this reason, some results are expressed in degree days, to allow comparison with bibliography, even when we recognize that degree-days are an imperfect scale to account for temperature dependency.

Averaged Relative Elongation Rate (RER)

Leaf elongation follows an exponential-like kinetics from initiation to previous leaf emergence (Figure 4 of the main text). In both experimental data and simulations, an average temperature-compensated RER was estimated as the slope of the linear regression between log of leaf length and temperature compensated-time. The confidence interval is calculated as +/- twice the standard error of the slope.

Phyllochron

The phyllochron is the time duration between the emergence of two successive leaves (°Cd). CN-Wheat simulates plant growth in an hourly basis, while observations were less frequent in experimental data (Exp1). Consequently, we estimated an average phyllochron defined as 1/A, with A being the slope of the linear regression between the number of emerged leaves and temperature-compensated time for both experimental data and simulations.

Green Leaf Number (GLN)

The GLN was defined following Abichou (2016) as the decimal number of non-senescing laminae of the main stem. It is calculated as:

$$GLN = \sum_{n=nb\ leaves}^{n=1} \frac{A_{lamina,n}^{green}}{\left(A_{lamina,n}^{green} + A_{lamina,n}^{senesc}\right)} \qquad \text{Eqn. S1.2.1}$$

Green Area Index (GAI)

The GAI was calculated following Lang *et al.* (1991) as the cumulated surface of all green lamina tissues, plus half of the developed surface of the pseudo-stems (main stem + tillers) per unit soil area. Since the plant density was 250 plants m^{-2}, the GAI was calculated as:

$$GAI = 250 \times \sum_{n=nb\ leaves}^{n=1} \left(A_{lamina,n}^{green} + \frac{A_{sheath,n}^{green,exp}}{2}\right) \qquad \text{Eqn. S1.2.2}$$

Leaf Area Index (LAI)

The LAI is the cumulated surface of green lamina tissues of the main stem and tillers per unit soil area. The LAI was calculated as:

$$LAI = 250 \times \sum_{n=nb\ leaves}^{n=1} A_{lamina,n}^{green} \qquad \text{Eqn. S1.2.3}$$

Dry mass (DM)

The DM of an organ *n* ($M_{organ,n}^{total}$) was calculated as the sum of its structural mass ($M_{organ,n}^{struct}$) and the mass of metabolites. In order to provide more accurate estimates of organ DM, the model accounts for the mass of metabolites located in the *phloem* compartment according to the ratio of the organ's structural mass to the whole plant structural mass.

$$\begin{aligned} M_{organ,n}^{total} = {} & M_{organ,n}^{struct} + C_{organ,n}^{trioseP}\, G_{trioseP} + \left(C_{organ,n}^{suc} + C_{phloem}^{suc} \frac{M_{organ,n}^{struct}}{M_{plant}^{struct}} \right) \times G_{suc} \\ & + C_{organ,n}^{star}\, G_{star} + C_{organ,n}^{fruct}\, G_{fruct} + N_{organ,n}^{nit}\, G_{nit} \\ & + \left(N_{organ,n}^{AA} + N_{phloem}^{AA} \frac{M_{organ,n}^{struct}}{M_{plant}^{struct}} \right) \times G_{AA} + N_{organ,n}^{prot}\, G_{prot} \end{aligned} \qquad \text{Eqn. S1.2.4}$$

Nitrogen (N) fraction

The N fraction of an organ is the ratio between N mass and total dry mass (Eqn. S1.2.4) of this organ. The N mass of an organ accounts for part of the N mass of the amino acids (AA) located in the *phloem* according to the ratio of the organ's structural mass to the whole plant structural mass. The N fraction was expressed in percentage and is calculated according to:

$$\begin{aligned} N(\%) = {} & \left[ratio_{N:mstruct}\, M_{organ,n}^{struct} + N_{organ,n}^{nit}\, G_{nit} \right. \\ & \left. + \left(N_{organ,n}^{AA} + N_{phloem}^{AA} \frac{M_{organ,n}^{struct}}{M_{plant}^{struct}} \right) G_{AA} + N_{organ,n}^{prot}\, G_{prot} \right] \\ & \times \frac{100}{M_{organ,n}^{total}} \end{aligned} \qquad \text{Eqn. S1.2.5}$$

Photothermal Quotient (PTQ)

The PTQ is a biometeorological variable governing photosynthetic assimilate availability (Nix, 1976) which is usually computed as the ratio of daily cumulated radiation over daily cumulated thermal time. Since our model considers a non-linear response of growth to temperature, we computed the PTQ (mol m^{-2} d^{-1} at 12°C) as the cumulated PAR_i (µmol.m^{-2}) over a time interval compensated for the effect of temperature (dt_{eq}, s at 12°C). Integration was done one a weekly basis:

$$PTQ = \frac{PAR_i}{dt_{eq}} \times 3600 \times 10^{-6} \qquad \text{Eqn. S1.2.6}$$

PTQ was only computed when the averaged air temperature was above 2.5°C to prevent outliers.

Additional results

See next pages

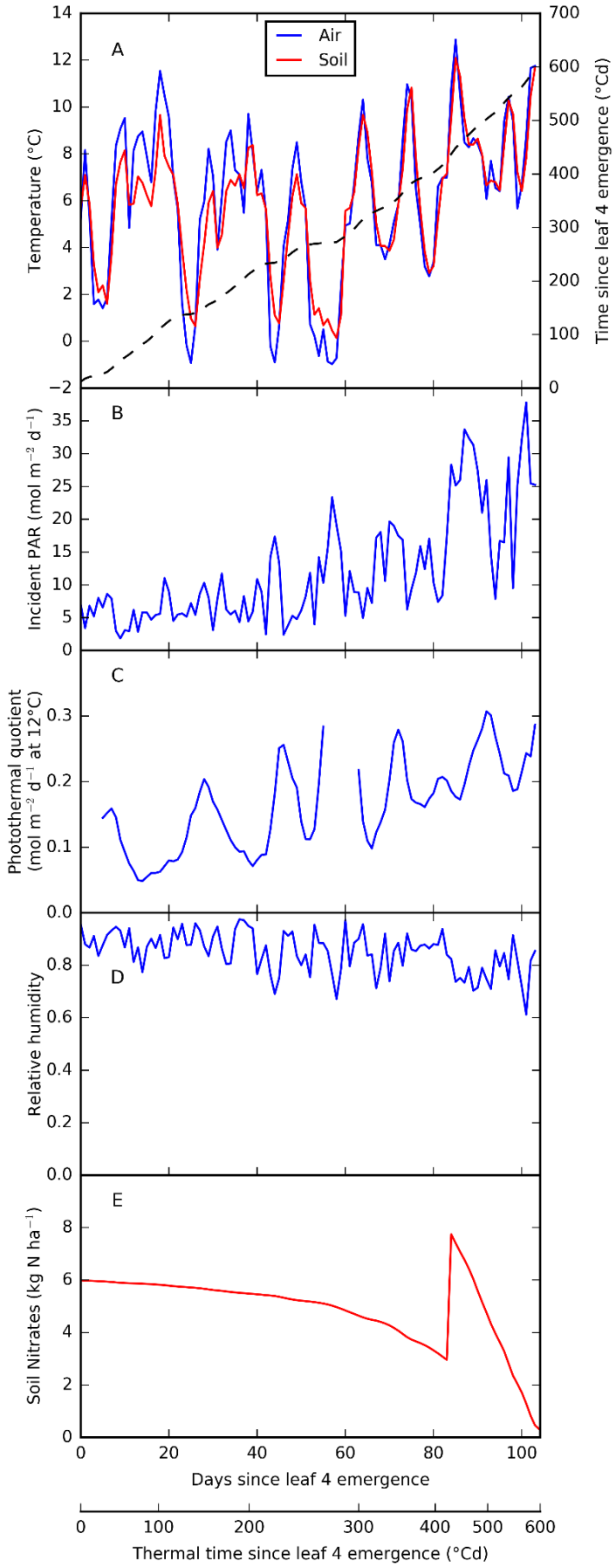

Figure S1.2.1 - Environmental conditions for the simulated period. The model uses hourly data but daily averages are presented for the sake of clarity. A: air temperature at 2m height (blue), near-surface soil temperature (red) and thermal time since model initialization (dashed curve); B: incident PAR above the canopy; C: photothermal quotient of the previous seven days; D: relative humidity; E: soil content in nitrates as simulated by the model. On day 84, soil was fertilised with 5 g m-2 of N (Exp1).

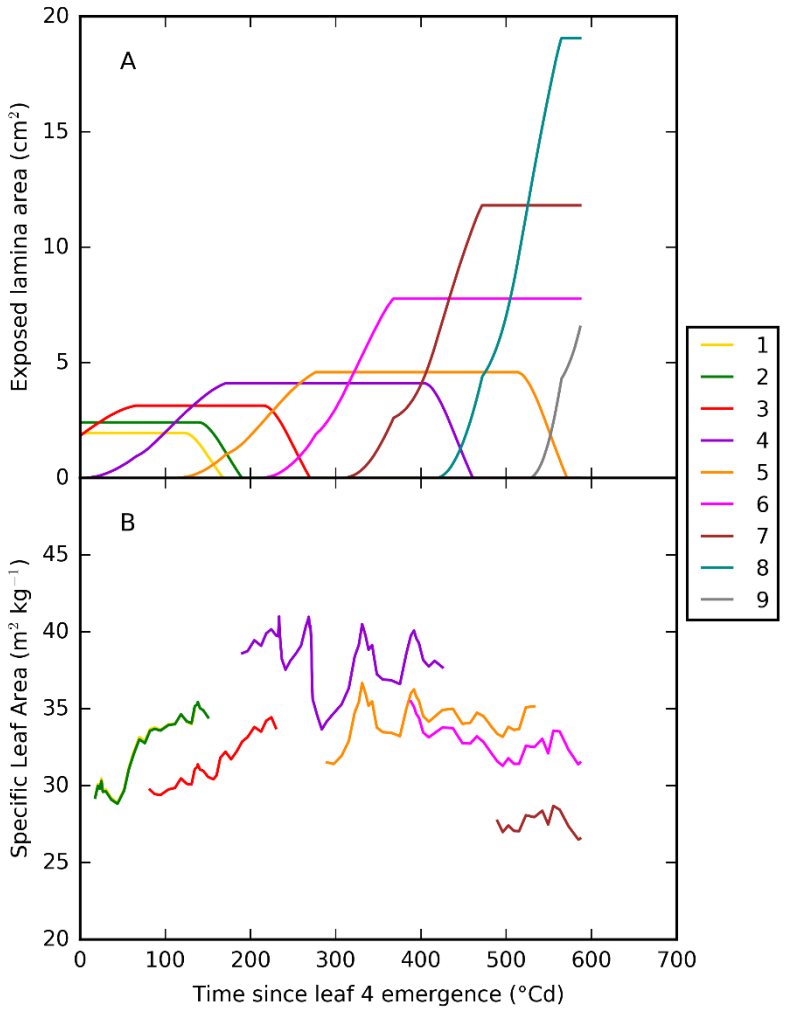

Figure S1.2.2 - Dynamics of lamina traits. A: exposed lamina area. B: Specific Leaf Area of laminae from leaf ligulation to senescence onset. Different colours represent the phytomers (see lateral panel).

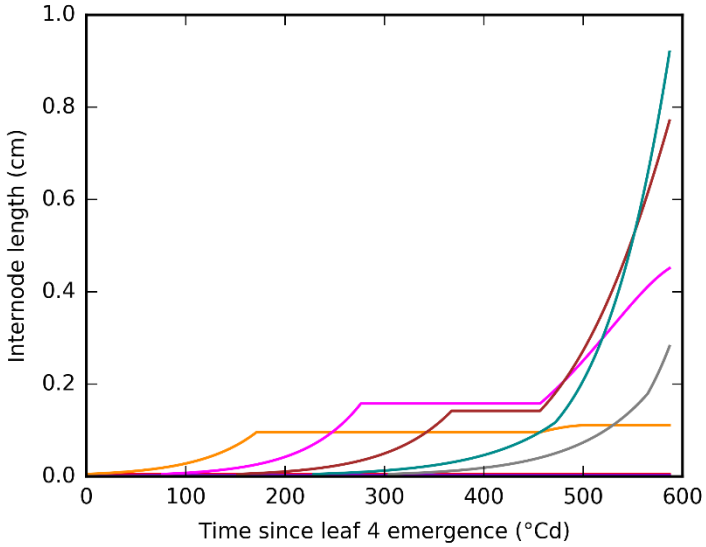

Figure S1.2.3 - Dynamic of internode length. Colours are used to represent the phytomers and are the same as in Figure S1.2.2

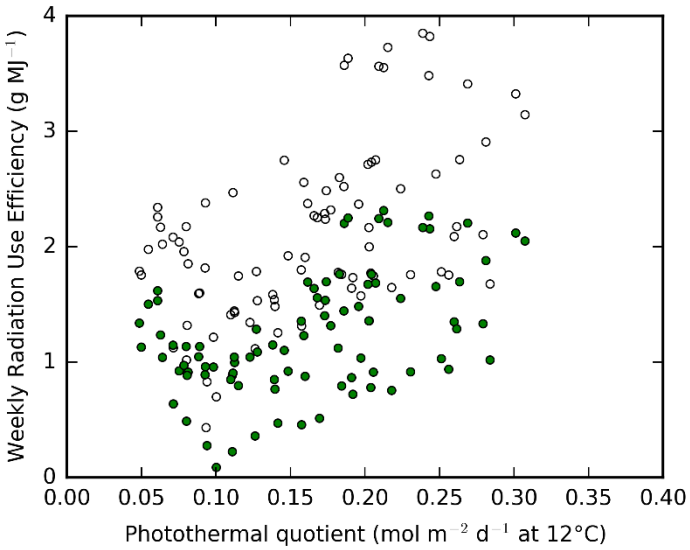

Figure S1.2.4 - Radiation Use Efficiency (RUE) versus photothermal quotient (PTQ). RUE was calculated based on shoot (green circles) or shoot + root (black circles) biomass; calculations are integrated over weekly intervals.

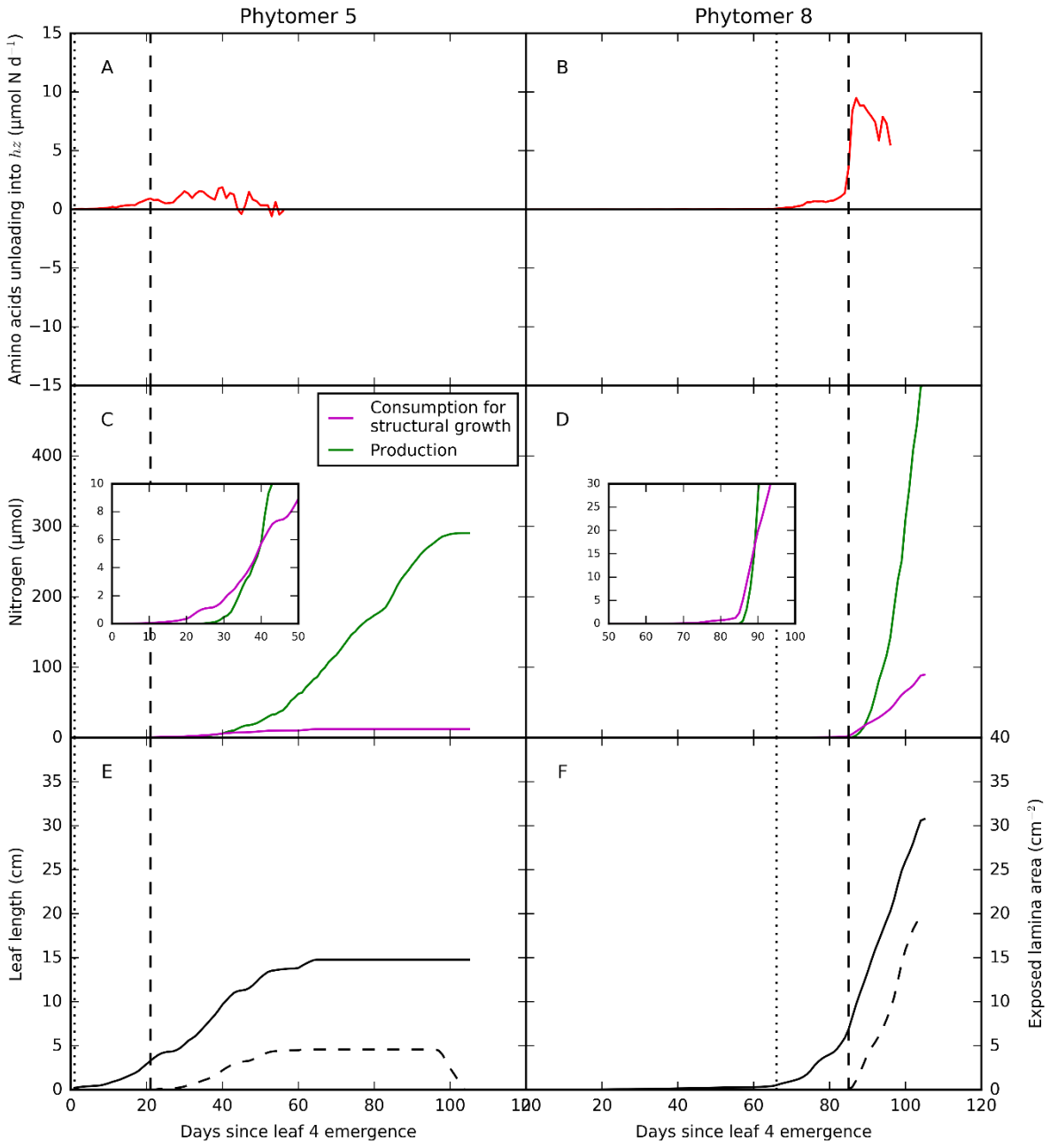

Figure S1.2.5 - Dynamics of nitrogen in phytomers 5 (left) and 8 (right) of the main stem. A,B: Daily fluxes of amino acids from the *phloem* to the hidden part of the growing phytomers (*hz*). Simulations are shown for the period during which the impact of internode growth on *hz* fluxes is insignificant. C,D: Cumulated nitrogen imported as nitrates and assimilated into amino acids in exposed leaf tissues (green) and consumed for structural growth (purple). E,F: Dynamics of leaf length and exposed green area of the laminae (dashed line). The dashed and dotted vertical lines show the time of leaf emergence and previous leaf emergence, respectively.

Supplementary Data S1.3 – Glossary

Grass morphology

Culm	The above-ground part of a grass axis, which may be the main stem or a tiller.
Ligule	Membrane at the junction between lamina and sheath.
Pseudostem	Tube formed by the mature sheaths that enclose the growing zone of younger leaves. In the model, the length of the pseudostem is calculated for each growing leaf along time, as it depends on the length of the internode bearing the growing leaf (Figure S1.1.1).
Tiller	Axis produced by an axillary bud, with same botanical organization that the main stem (Figure S1.1.3). Primary tillers are produced by main stem's buds; secondary tillers are produced by primary tillers' buds, *etc.*

Model's components

Compartment	Botanical element of the plant, which is described in the model by a set of states variables: metabolite concentrations, and (except for the *phloem*), dimensions and structural mass (Figure 1.3).
Phloem	Common pool of mobile metabolites, which is connected to all compartments (except the emerged part of growing lamina and sheath). The *phloem* is a model abstraction, which does not have explicit spatial representation. The concentration of a mobile metabolite in the *phloem* is defined as the ratio between the quantity of the metabolite and the structural mass of the whole plant.
Structural mass	The dry mass of the plant materials that are not available for metabolic activities as they are immobilized in stable compounds (mainly cell walls).

Morphogenesis

Emergence	The moment when the tip of a growing leaf is higher than the highest ligule *i.e.* it emerges out of the pseudostem.
Ligulation	The moment when the ligule of a leaf emerges out of the pseudostem *i.e.* when the full lamina is emerged.
Plastochron	Time interval between the initiations of two successive leaf primordia by the shoot apical meristem.
Phyllochron	Time interval between the emergences of two successive leaves (calculation in Protocol S1.2.1).
Phyllochronic time	A time scale defined in Fournier *et al.* (2005). Phyllochronic time is calculated as the thermal time since the emergence of a leaf, divided by the thermal time between the emergences of two successive leaves.
Elongation	Increase in length.
Extension	Increase in dimensions/area.
Growth	Increase in dimensions and mass.

Résumé du chapitre 1

L'architecture est un élément clé des interactions entre les plantes et leur environnement. Nous présentons un nouveau modèle de croissance de Poacées, qui intègre la morphogenèse aérienne et le métabolisme du carbone (C) et de l'azote (N) à l'échelle des organes, dans une représentation 3D de l'architecture aérienne des plantes. La morphogénèse des plantes est considérée comme un système autorégulé par deux mécanismes principaux. Premièrement, la vitesse d'allongement des organes et l'acquisition des traits foliaires sont régulés par les concentrations de métabolites C et N dans les zones de croissance et la température. Deuxièmement, le moment auquel s'effectue la croissance est régulé par des règles de coordinations entre les phytomères successives, au lieu d'un calendrier fixe en temps thermique qui est utilisé dans la plupart des modèles. Les concentrations locales sont calculées à partir d'un modèle du métabolisme du C et du N à l'échelle des organes. La représentation 3D permet de calculer avec précision la répartition de la lumière et de la température au sein de l'architecture.

Le modèle a été calibré pour le blé (*Triticum aestivum*) et évalué pour les stades végétatifs. Cette approche a permis de simuler des caractéristiques réalistes des dimensions foliaires, de la dynamique d'extension, de la masse et de la composition des organes. Le modèle a simulé, en tant que propriétés émergentes, des traits foliaires et agronomiques majeurs qui sont forcées en entrée ou simulées de façon empiriques dans la plupart des modèles. Les activités métaboliques des feuilles en croissance ont été étudiées en relation avec le fonctionnement de la plante entière et les conditions environnementales. Le chapitre 1 a donc démontré la capacité du modèle à simuler les caractéristiques observées à différentes échelles (organe, plante, peuplement), dans des conditions de croissance usuelles au champ.

Dans le chapitre 2, nous évaluons la capacité du modèle à simuler la plasticité des plantes pour des conditions de croissance contrastées en lumière et en azote.

Chapter 2 - Simulations of phenotypic plasticity for contrasting light and nitrogen conditions

2.1 - Introduction

Variability in climate and diversity in farming practices expose crop plants to a wide range of growth conditions, which is currently still extending in the context of climate change. Plants adapt their architecture to growth conditions, which is called phenotypic plasticity, by variations of growth rate, number of organs, final dimensions, structural masses and biochemical composition. In turn, plant architecture defines the ability of the plants to interact with their abiotic (light, CO2, etc.) and biotic (*e.g.* foliar fungus, other plants) environment. Thus, many feedback loops exist between the plant and its environment. In such context, models integrating these interactions are useful tools to explore and anticipate plant responses to novel environments. To simulate the phenotypic plasticity of plant, function-structural plant models (FSPM) that provide a framework to simulate plant growth regarding its trophic status are of special interest, as they account for an explicit description of the shoot architecture (Godin and Sinoquet, 2005; Vos *et al.*, 2010; Louarn and Song, 2020).

To date, most models are based on a demand-driven approach (Poorter *et al.*, 2013): the potential growth rate of an organ (sink strength) is met only in case of sufficient resource availability (mainly C). In addition, key architectural traits are usually not simulated by process-based formalism but be empirical relations, *e.g.* the phyllochron, specific leaf area. Simulating phenotypic plasticity using such classical approaches implies that the underlying sink strengths and empirical relations that set key architectural traits must be correct in the range of explored growth conditions. However, such property is limited considering the wide range of new and upcoming growth conditions that cannot be fully explored experimentally.

In order to move towards a better simulation of phenotypic plasticity, we proposed, in Chapter 1, a FSPM of a growing wheat plant, which simulates organ growth as driven by (i) the concentration in carbon (C) and nitrogen (N) metabolites in growing organs, (ii) coordination rules between successive phytomers. We demonstrated the ability of the model to simulate realistic behaviour of a wheat plant during the early vegetative stages by comparing the simulation results to one set of experimental data and to expected behaviour from the literature.

In this chapter, we test to what extent our model allows to simulate phenotypic plasticity. In particular, the aims were to:

- Evaluate the ability of the model to simulate realistic values and dynamics of leaf and plant traits, and realistic trends and magnitude of response to contrasting growth conditions, by comparing the simulated results with the literature on grass species
- Test the sensibility of the model to the initial plant state

To do so, the growth of grass monoculms, with traits similar to a wheat stem, was simulated for a wide range of growth conditions differing by the planting density, the irradiance and the soil N concentration. The monoculms were kept vegetative, meaning that they produced an indeterminate number of phytomers and that internodes

remained short. In order to focus our analysis on the plasticity of leaf growth, we simulated the growth of monoculms, thus disregarding the tillering process. To disentangle the effects of ontogenic and environmental changes on plant growth dynamics, we simulated growth chamber conditions, where environmental conditions are stable. In addition, we simulated hydroponic conditions, where the NO_3^- concentration of the nutrient solution remains constant, in order to impose soil N concentration for plants, independently of the planting density treatments and irradiance.

Consequently, comparison of our simulation results with field experiments is limited because (i) we simulated the plant response to constant N concentration with unlimited N availability while field experiments study the response to changing soil N concentration with limited N availability, (ii) the simulated plant is a monoculm and is kept vegetative. However, these experiments intended to define a set of conditions that facilitate the interpretation of model behaviour in the theoretical frame of a monoculm in controlled growth conditions. We specifically chose a wide range of growth conditions that were expected to simulate a wide range of leaf and plant traits. It implied making some adaptation to the model compared to previous chapters.

2.2 - Material and Methods

Two virtual experiments were performed to simulate the growth of vegetative grass monoculms in growth chambers in hydroponic conditions:

- Experiment 1 aimed at exploring the phenotypic plasticity. We simulated plant growth under 72 contrasting conditions in terms of planting density (from isolated plants to dense stands), N concentration of the nutrient solution, and incident PAR.
- Experiment 2 aimed at studying the sensitivity of the model to the initial state of the plant, using eight different initial states under eight environmental conditions (64 simulations).

Making these simulations required to bring some changes to the model compared to the description in chapter 1. We present below: (i) the changes made, (ii) the simulation conditions, and (iii) the calculation of indices to compare simulations with observations.

Model description

In Chapter 1, we presented the dynamic version of CN-Wheat. The model was developed and calibrated to simulate the growth of a wheat plant under usual field conditions during the early vegetative stages. Simulation conditions of the present chapter contrast with those of Chapter 1 on the following points:

a- Simulated plant does not have tillers (monoculm)
b- The culm remains vegetative and produces an indeterminate number of phytomers
c- Growth conditions are extreme and contrasted in terms of planting density, irradiance and N concentration in the soil.
d- A constant soil N concentration is maintained through time, independently of plant uptake, meaning that there is no upper bound to the amount of N available for plants.

Because of these differences, some changes in the model were required. An overview of these changes is presented below while a detailed description and underlying motivations are presented in Supplementary Data S2.1.

Changes related to leaf and root growth

First, we changed the empirical functions that define the lamina maximum width and structural specific lamina mass (SSLM) according to sucrose concentration (Table S2.2); these changes were necessary to simulate more realistically the plasticity of these traits under a wide range of growth conditions. Second, we introduced an upper bound to leaf length prior to previous leaf emergence, which reflects a maximum length of the growth zone of the leaf; this change was necessary to simulate realistic leaf length in case of high number of leaves. Also, we adapted the ontogenic equations and parameters so that they could account for an indeterminate number of phytomers. Finally, we recalibrated a parameter related to the rate of root growth to simulate the monoculm case.

Changes to the initial photosynthesis sub-model (Barillot* et al.*, 2016a)

Preliminary simulations using the initial calibration of the model (Chapter 1) revealed that the photosynthesis rate was unlikely high for the situations of high irradiance and for conditions resulting in high specific leaf N (SLN, g $N.m^{-2}$)

Consequently, the initial photosynthesis sub-model was adapted by (i) implementing a feedback regulation by non-structural carbohydrate (NSC) concentration, (ii) changing the N dependences of the initial photosynthesis sub-model. Such implementations were possible because CN-Wheat simulates the concentration of metabolites in each organ, which allows implementing detailed regulations that are not considered in most models.

The initial photosynthesis sub-model (see Barillot *et al.*, 2016*a* for details) is based on a biochemical model of photosynthesis (Farquhar *et al.*, 1980). The initial photosynthesis sub-model did not limit photosynthesis in the case of accumulation of NSC due to high irradiance at normal atmospheric CO_2 concentration. However, the model simulated unrealistically high NSC concentrations in case of high irradiance. So, we introduced a putative

direct retro-inhibition of the photosynthesis by NSC, based on experimental data (Azcón-Bieto, 1983). The initial photosynthesis sub-model used the SLN in the N-dependence functions of the photosynthesis parameters, because they are the only functions for which the literature proposed a calibration for wheat. However, we identified that the fraction of the total N involved in photosynthesis is not constant, especially in some special cases (very thick leaves and very high foliar N contents). Thus, the calculation of photosynthesis was modified by relating photosynthesis parameters to the N specific mass of the non-structural proteins instead of the SLN. Specifications of the changes to the initial photosynthesis sub-model are given in Supplementary Data S2.1.

Definition of plant death in the model

Regarding the extreme stresses that we imposed in our simulations, we had to define a new status defining plant death in order to avoid anomalous results (*e.g.* negative sucrose concentration in the *phloem*). In the modified version of the model, plant death is triggered (and the simulation stopped) if one of the two following conditions is met:

- All photosynthetic organs of the shoot are fully senescent
- Sucrose concentration in the phloem drop below a negative threshold (– 50 µmol C g^{-1}).

Virtual experiments

We first present the model calibration, the model time steps and simulations runs. Then, we present the environmental conditions and the initialization of the simulated plants of the two experiments.

Model calibration, time steps and simulation runs

The model parameters (~160) were set as in Chapter 1[1], with the exception of the changes that have been described in the previous section.

As in Chapter 1, the model was run with an hourly time step in both virtual experiments, except for the distribution of light between phytoelements, which was updated every 4 h. This means that the absorbed PAR was calculated from hourly values of incident PAR, applied to a 3D-structure of the canopy updated every 4 h, to limit the computational cost of the calculation of the distribution of light between phytoelements.

Each simulation run in ~2.5 h on a personal computer. In total, the virtual experiments consisted in 136 simulations and ~500 preliminary simulations were performed. Thus, the model has been deployed on a computing center (MESO@LR-Platform, Université de Montpellier, France), which allowed to perform all the simulations in parallel.

[1] Table S1.1.2 for leaf growth parameters, Table S1.1.4 for internode growth parameter, Table S1.1.6 and Table S1.1.7 for parameters related to the response to temperature, other parameters were set as in the post-flowering version of CN-Wheat (Barillot *et al.*, 2016*b*) expect for the parameters in Table S1.1.9 and Table S1.1.10

Environmental conditions

The whole-plant model was run to simulate the plant for 3500 h at day/night air temperatures of 13/7°C and a 12h-photoperiod. Soil temperature was constant at 10°C. Atmospheric CO_2 concentration, relative humidity and wind speed at the top of the canopy were set at 360 ppm, 75 % and 3 m s^{-1}, respectively.

Experiment 1 consisted in 72 simulations with 3 planting densities, 6 soil N concentrations and 7 irradiances (Table 2.1). Three planting densities were simulated (1, 500 and 750 culm m^{-2}). For comparison, a commercial wheat field would typically count between 500 and 600 culms m^{-2} at flowering in France. The NO_3^- concentration of the soil was set at constant values (thus mimicking hydroponic conditions), ranging from 0.5 to 10 g m^{-3}. Since the model considers a soil of 1m-depth, such concentrations are equivalent to constant soil N concentrations ranging from 5 to 100 kg ha^{-1}. For comparison, 80 kg ha^{-1} is a concentration that can be found immediately following fertilizations in a commercial wheat field. However, in such field, the concentration would decrease rapidly with plant uptake (Devienne-Barret *et al.*, 2000). A common value for total N uptake of a wheat crop is 250 kg ha^{-1} of N in France (Gate, 1995). Finally, four incident PAR levels were simulated, from 80 to 250 µmol m^{-2} s^{-1} for isolated plants and from 250 to 1500 µmol m^{-2} s^{-1} for plants in stands. Different ranges of incident PAR were applied to isolated plants and plants in stands because of the differences in light interception per plant (Figure 2.1). For comparison, PAR of 500 µmol m^{-2} s^{-1} with 12h-photoperiod and 10°C daily mean air temperature corresponds to the usual weather conditions in Grignon (France) in March.

Experiment 2 consisted in 64 simulations under a subset of environmental conditions as compared to experiment 1 (2 planting densities, 2 soil N concentrations and 3 irradiances, Table 2.1).

The simulated plant

The plant is a grass monoculm with traits similar to a wheat stem. During the simulation, no floral transition was simulated meaning that the culm continuously produced new vegetative phytomers and that the internodes stayed short.

In experiment 1, the initial state of the plant ($Init_{VE1}$) was defined as the main-stem and the root as in Chapter 1 (Table S1.1.13). Briefly, it corresponded to a wheat plant grown in the field in Grignon, France, at leaf 4 emergence (mid-December).

In experiment 2, eight initial states of the plant were defined from modifications of $Init_{VE1}$ by changing the length of leaves 1 to 4 ($Init_{Length}$), and the total N fraction of the plant ($Init_N$). Six $Init_{Length}$ were defined by modulating the length of leaves 1 to 4 (+/- 10 %, 25 %, 50 %), which were the only leaves that were no longer at the meristematic stage at the time of model initialization. At model initialization, leaves 3 and 4 were still growing but their potential final length was already set; therefore, the same length deformation was also applied to the potential final length of leaves 3 and 4. $Init_N$ was defined by decreasing the initial shoot N fraction to 2.4 and 3.4 % (compared to 4.4 % in $Init_{VE1}$) while keeping the same repartition of N within the plant as in $Init_{VE1}$.

Table 2.1 - Summary of the virtual experiments (VE). All combinations of conditions of one row were simulated.

VE	Initial state of the plant	Planting density (plants m^{-2})	NO_3^- concentration in the nutrient solution (g m^{-3})	Incident PAR (µmol m^{-2} s^{-1})
1	$Init_{VE1}$	1	0.5, 1, 1.5, 2.5, 5, 10	80, 100, 175, 250
		500, 750	0.5, 1, 1.5, 2.5, 5, 10	250, 500, 1000, 1500
2	$6 \times Init_{Length}$, $2 \times Init_N$	1	0.5, 5	80, 250
		500	0.5, 5	250, 1000

Indices calculated on simulation results

The following indices related to plant growth and trophic status were calculated from simulation results with same method as in Chapter 1: the dry mass, the specific leaf area (SLA), the specific leaf N (SLN), the phyllochron and the N fraction.

The fraction of non-structural carbohydrates (NSC), the radiation use efficiency (RUE), the photosynthetic efficiency, the C use efficiency (CUE) were calculated as presented below.

Fraction of non-structural carbohydrates (NSC)

The NSC fraction of an organ *n* is the ratio between NSC mass and total dry mass ($M_{organ,n}^{total}$) of this organ. The NSC mass of an organ accounts for part of the mass of the sucrose located in the *phloem* according to the ratio of the organ's structural mass to the whole plant structural mass. The NSC fraction was expressed in percentage and is calculated according to:

$$NSC(\%) = \left[C_{organ,n}^{trioseP} G_{trioseP} + \left(N_{organ,n}^{suc} + N_{phloem}^{suc} \frac{M_{organ,n}^{struct}}{M_{plant}^{struct}} \right) G_{suc} + C_{organ,n}^{star} G_{star} + C_{organ,n}^{fruct} G_{fruct} \right] \times \frac{100}{M_{organ,n}^{total}} \quad \text{Eqn. 2.1}$$

with G_x the molar mass of the metabolite *x*.

Radiation use efficiency (RUE)

The RUE was calculated as the slope of the linear regression between the dry mass of the plant across time (dry mass and structural mass of the senesced tissues) and the cumulative absorbed PAR.

Carbon use efficiency (CUE)

The CUE is the fraction of assimilated C ($C_{plant}^{assimilated}$) that is integrated in the plant biomass *i.e.* not lost by respiration ($C_{plant}^{respired}$) or exudation ($C_{plant}^{exudated}$). The CUE is calculated over the whole simulation period as:

$$CUE \quad = 1 - \frac{C_{plant}^{respired} + C_{plant}^{exudated}}{C_{plant}^{assimilated}} \qquad \text{Eqn. 2.2}$$

Photosynthetic efficiency

The photosynthetic efficiency is the ratio of assimilated C ($C_{plant}^{assimilated}$) to absorbed PAR (PAR_a) over the simulated period. The photosynthetic efficiency is expressed in µmol C MJ^{-1} and is calculated as:

$$\text{photosynthetic efficiency} \quad = \frac{C_{plant}^{assimilated}}{PAR_a} \qquad \text{Eqn. 2.3}$$

2.3 - Results

Virtual experiment 1: Phenotypic plasticity of plants architecture

The growth of vegetative monoculms was simulated under 72 conditions contrasted by planting density, soil N concentration and incident PAR. For clarity's sake, we refer to growth condition treatments by short name as following: *e.g.* Density 1 x N 5 x PAR 100 refers to a density of 1 plant per m^2, a soil N concentration of 5 g m^{-3} and an incident PAR of 100 µmol m^{-2} s^{-1}.

First, we present the simulated resource capture. Then, we give an outlook on C and N concentrations in the *phloem* because the *phloem* is and common pool between sources and sink and represents CN availability at plant scale. We also present the simulations that led to plant death. Finally, we present the phenotypic plasticity at leaf scale and then at plant scale.

Resource capture

Comparison of the PAR x density treatments

The PAR absorbed per plant during the whole simulation period (3500 h) varied in the range of 0.3 – 15 mol depending on growth conditions. The effects of PAR and planting density on the absorbed PAR was similar for all soil N concentrations; Figure 2.1 illustrates the simulations for N 5. As expected, higher planting density reduced the amount of absorbed PAR per plant during the simulation due to higher shading in stands. In addition, the effect of planting density on PAR absorption increased progressively during the simulations depending on the rate of LAI development. Whatever the density, plants grown at PAR 250 absorbed similar amounts of PAR until t=500 h, when LAI was 0.68 and 1, and the fraction of incident PAR absorbed by the canopy was 0.36 and 0.46, for density 500 and density 750, respectively (Figure 2.1 D,E,F). For all N x PAR treatments, a LAI of 3 was reached around t=1100 h (min 984 h – max 1512 h) for density 500 (Figure 2.1 E), and around t=910 h (min 840 h – max 1032 h) for density 750 (Figure 2.1 F). At the time of LAI=3, the fraction of incident PAR absorbed by the canopy was slightly higher for density 500 with an average over PAR treatments of 0.77 (0.76 – 0.78), than for density 750 with an average of 0.75 (0.73 – 0.77).

Thus, simulations at densities 500 and 750 evolved rapidly from a situation where plants were isolated as in density 1, to totally closed canopies. The total absorbed PAR over the simulation, and the dynamic of fraction of PAR interception were highly modulated by planting density.

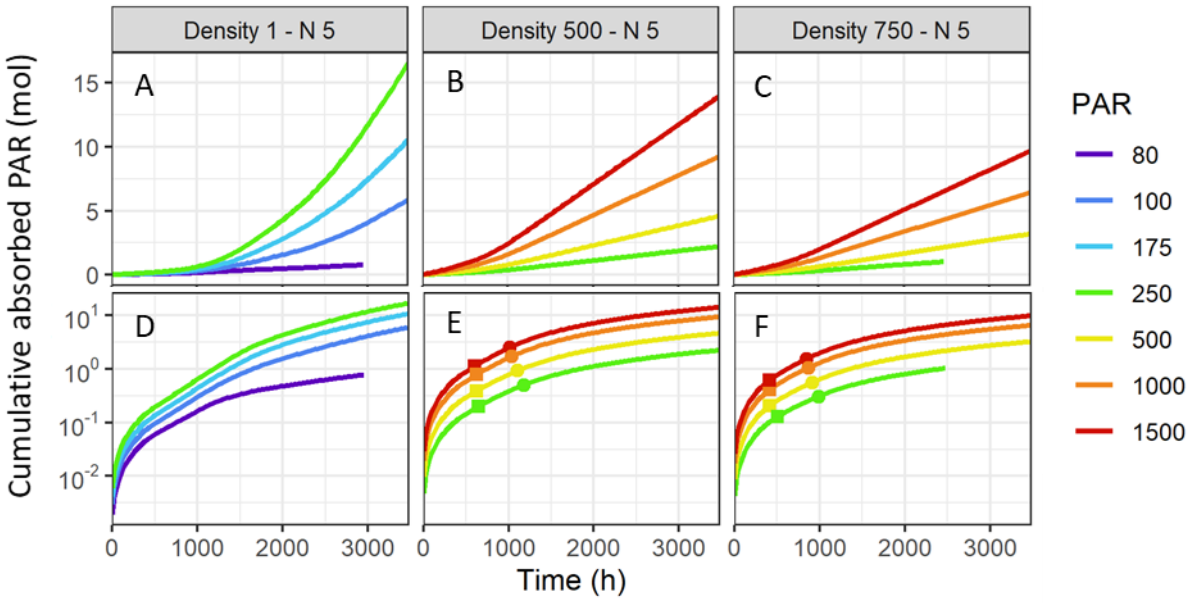

Figure 2.1 – Cumulative PAR absorbed by the green phytoelements of one plant across time (higher row: regular scale; lower row: log scale). Each line shows the outcome of one simulation. Colours refer to the treatment of incident PAR (µmol m^{-2} s^{-1}, see right key). Each column is one planting density (plant m^{-2}, see column title). The squares and dots show the time at which the leaf area index equals 1 and 3, respectively (canopy closure).

Dry mass production and leaf area

At the end of the simulation, plants reached highly contrasting sizes and masses depending on growth conditions (Figure 2.2). Total area of laminae per plant ranged from 50 to 320 cm^2, while the living dry mass ranged from 0.5 to 6.5 g and the senesced dry mass from 0.05 to 2.3 g.

For similar levels of incident PAR, both total lamina area and plant dry mass were higher with lower planting density, which highly affects absorbed PAR (Figure 2.1). Incident PAR also positively affected lamina area and plant dry mass. A 50 % reduction in incident PAR reduced total lamina area by 50 % for plants in stands, but only by ~20 % for isolated plants. Thus, total lamina area of isolated plant was less sensitive to incident PAR than that of plants in stands. In contrast, dry mass varied proportionally with incident PAR in both isolated plants and stands: a 50 % reduction in incident PAR let to a 50 % reduction in plant dry mass. Thus, for isolated plants, a reduction in lamina area was associated to a reduction in plant dry mass, which was not the case for plant in stand, probably because of canopy closure.

Both total lamina area and plant dry mass were higher with higher soil N concentration up to 4.5 g m^{-3}, and were then almost stable. For isolated plants, increasing soil N concentration from 0.5 to 2.5 g m^{-3} led to ~50 % increase in total lamina area but ~70 % increase in plant dry mass. This result is consistent with the simulated effect of incident PAR for isolated plants. In contrast, total lamina area and dry mass of plants in stands had a similar sensibility to soil N concentration. In contrast, Dreccer *et al.* (2000) observed, for two densities of wheat stands, that leaf area index was more affected by N fertilization than plant biomass.

In the following sections, the simulation results for density 750 are not further presented since the changes in plant architecture from density 750 to 500 were similar to those following a decrease in incident PAR, as pointed out by the literature (Poorter *et al.*, 2019). In addition, variations with soil N concentration were monotonous. So, for clarity' sake, when presenting variables across time or per phytomer rank, the effect of soil N concentration are exemplified for N 0.5 and N 5, that are very low and very high soil N concentrations, respectively.

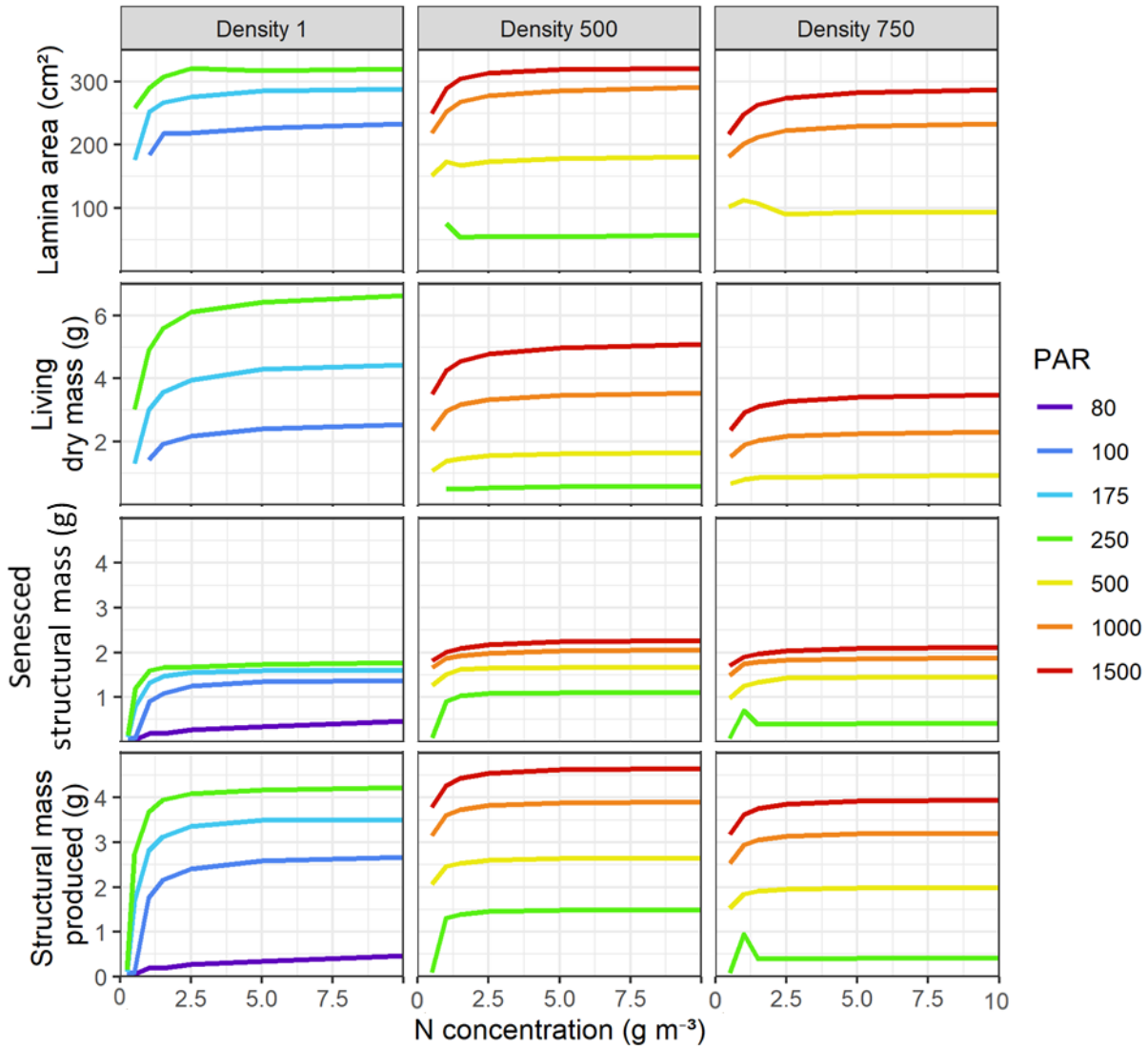

Figure 2.2 – Development of one plant at the end of the simulation (t=3500 h) for various conditions of incident PAR and soil N concentration and for three plant densities. Top row: Total green area of the laminae of one plant. Second row: Dry mass of the living tissues of one plant. Third row: Structural mass of the senesced tissues of one plant. Bottom row: Total structural mass produced by one plant (g). Colours refer to the treatment of incident PAR (µmol m^{-2} s^{-1}, see right key). Each column is one planting density (plant m^{-2}, see column title).

Concentrations in the hidden part of the growing leaves and in the phloem

In the context of simulating phenotypic plasticity, the concentrations in the *hz* are of special interest since, in our model, sucrose and AA concentrations drive the leaf elongation rate, and sucrose concentration drives lamina maximum width and specific mass of lamina and sheath. The concentrations of sucrose and AA in the *phloem* are an indicator of the trophic status of the plant as they represent the amounts of mobile C and N that can flow from sources to sinks, in relation to the plant structural mass. In our simulations, the concentrations of sucrose and AA in the hidden part of the growing leaf (*hz*) were always in equilibrium with those of the *phloem* because of low flux resistance between these compartments. Below, we present, first, the dynamic of concentrations during the simulation and, then, the effects of growth conditions on the concentrations.

Sucrose

Ontogenic pattern. Sucrose concentration showed a marked peak at ~500 h ranging from 400 to 2800 µmol g^{-1} depending on the treatment (Figure 2.3). The initial increase in sucrose concentration until 500 h (leaf 6 mergence) was found to be related to the initial state of the plant (see results of virtual experiment 2 and discussion). Then, rapid growth of leaves 6 and 7 consumed sucrose in the *hz*, which caused a decrease of the sucrose concentration until 1500 h. At low PAR and low soil N concentrations, growth of leaves 6 and 7 completely emptied the *phloem* and the *hz*, which resulted in plant death. From 1500 h onward, sucrose concentration of the plants in stands was relatively stable or slightly decreased (Figure 2.3 C,D) while sucrose concentration of the isolated plants increased and ended at 3500 h with similar values as at 500 h (Figure 2.3 A,B).

Effect of PAR. The sucrose concentration was higher for higher incident PAR following the same trend as the cumulative absorbed PAR (Figure 2.1). Concentration differences between PAR treatments started as soon as t=0 h and were maintained until the end of the simulation. Sucrose concentration were lower for higher planting density as soon as LAI was ~0.5 meaning that even low shading level impacted the trophic status of the plants.

Effect of N. Overall, the effect of soil N concentration on sucrose concentration was less strong than that of incident PAR. Figure 2.3 shows that sucrose concentration started to be higher with increasing soil N concentration from t~1000 h. Sucrose concentration was more sensitive to soil N concentration for the isolated plants (Figure 2.3 A,B) than for plants in stands (Figure 2.3 C,D).

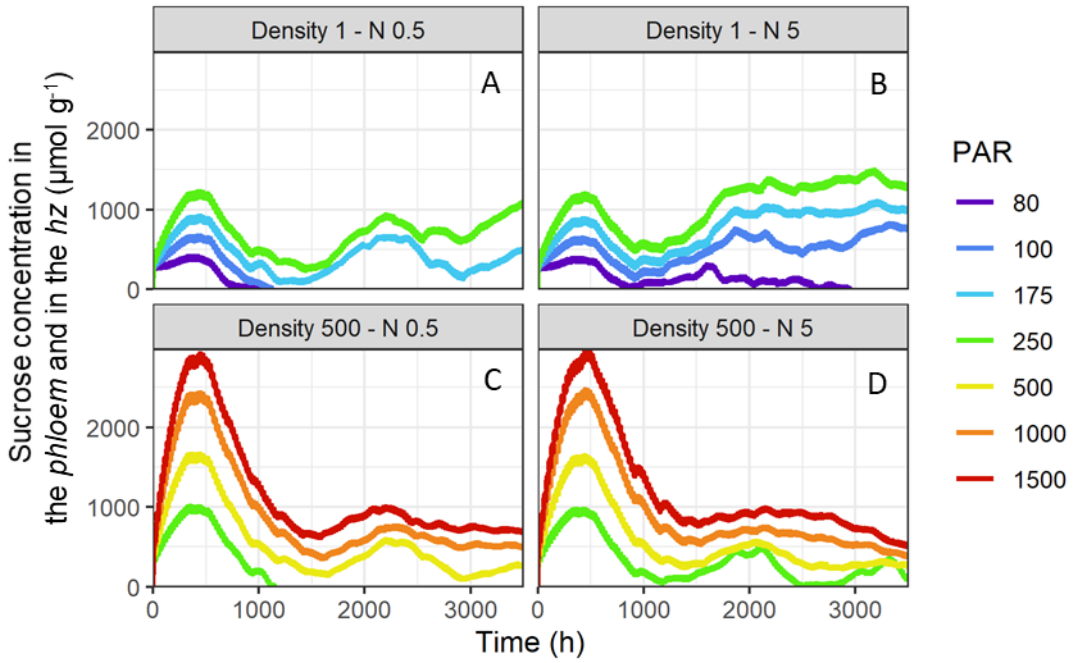

Figure 2.3 – Concentration of sucrose in the *phloem* and in the hidden part of the growing leaves (*hz*). Each line is one simulation. Colours refer to the treatment of incident PAR (µmol m^{-2} s^{-1}, see right key). Each panel groups the light treatments for one planting density (plant m^{-2}) and one soil nitrogen concentration (g m^{-3}, see panel title).

Amino acids

Ontogenic pattern. AA concentration was relatively stable until 1500 h, ranging from 20 to 250 µmol N g^{-1} depending on the growth conditions (Figure 2.4). After 1500 h, AA concentration increased across time in situations of high incident PAR and high soil N concentration conditions, reaching 1100 µmol N g^{-1} at 3500 h in the simulation D500 x N 5 x PAR 1500 (Figure 2.4 D). In these cases, the start of AA accumulation at t=1500 h was found to be related to a rapid growth of the roots, due to high sucrose concentration in the *phloem* and thus in the roots, associated to a decrease of the shoot:root ratio from t=1500 h (see Figure S2.27 in Supplementary Data S2.2). In the other cases, AA concentration was relatively stable from 1500 h onward. The transient drops (and also in the total amount of AA per plant) appeared to be synchronized with the ligulation of successive leaves (Figure 2.11). It seems that a transient increase is due to the young ligulated leaf (leaf *n*) loading the *phloem* with AA. Then, the following decrease in AA concentration is probably due to the rapid growth leaf *n+1* (soon after leaf *n* ligulation), which consumes AA for the synthesis of structural mass and of proteins.

Effects of PAR and N. AA concentration were higher in low planting density simulations (see Figure 2.4 PAR250) and with higher incident PAR and soil N concentrations (Figure 2.4) from t=150 h.

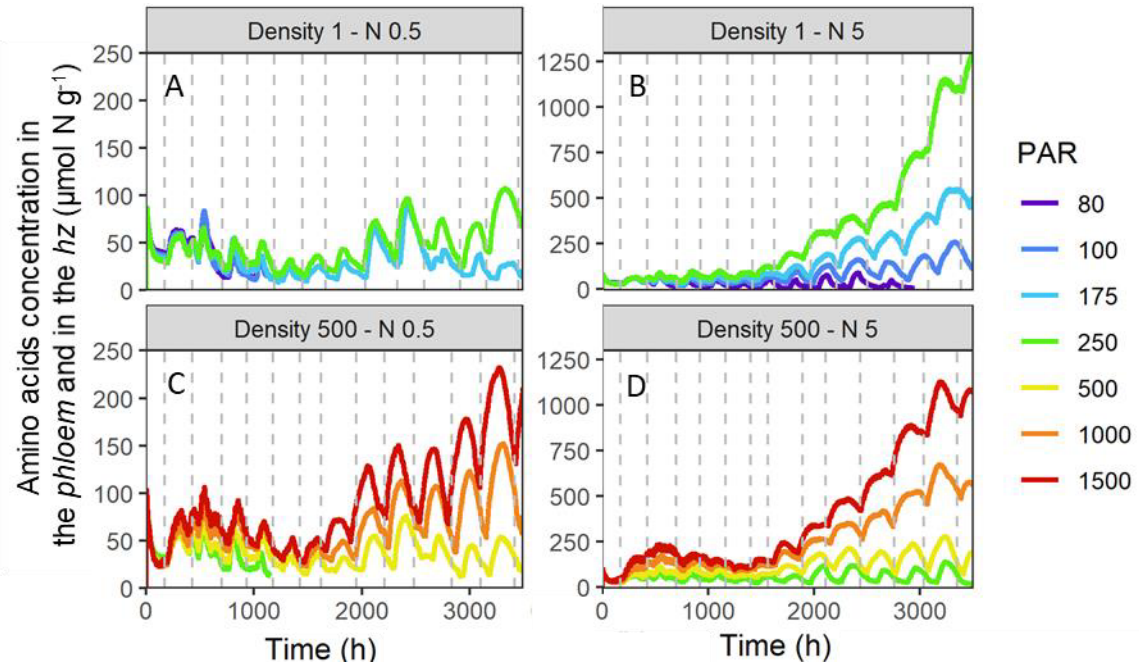

Figure 2.4 - Concentration of amino acids in the *phloem* and in the hidden part of the growing leaves (*hz*). Each line is one simulation. Colours represent the treatment of incident PAR (µmol m^{-2} s^{-1}, see right key). Each panel groups the light treatments for one planting density (plant m^{-2}) and one soil nitrogen concentration (g m^{-3}, see panel title). Dashed lines represent the averaged time of ligulation of the successive leaves for the combination of planting density and soil nitrogen concentration.

Plant death

Plants died before 3500 h in the following growth conditions:

- At density 1: at PAR 80 for all soil N concentrations, and at PAR 100 for N 0.5
- At density 500: at PAR 250 and N 0.5
- At density 750: at PAR 250 for all soil N concentrations

The time of plant death varied from ~ 900 h to 3150 h depending on growth conditions. Higher soil N concentration or higher incident PAR delayed the time of death.

In the case of plants that die before 3500 h, sucrose and AA concentrations in the *phloem* and in the *hz* were low relatively to surviving plants (Figure 2.3 and Figure 2.4). Consequently, rates of leaf and root growth were highly reduced but did not reach zero, meaning that the synthesis of structural mass still consumed sucrose and AA. In addition, respiration consumed sucrose. This resulted in higher C consumption than available in the plant, leading to death.

To sum up, incident PAR and soil N concentration had positive effects on sucrose and AA concentrations. Isolated plants had higher sucrose and AA concentrations than plants in stands. In most growth conditions, sucrose and AA concentrations showed marked temporal dynamics and, in most conditions, did not reach a steady state. AA concentrations presented large fluctuations synchronous with the ligulation of successive leaves, which were not observed in sucrose concentrations.

Phenotypic plasticity of leaf traits

Leaf length

Ontogenic pattern. Overall, the pattern of leaf length along the stem was the same for all growth conditions as final leaf length generally increased with phytomer rank up to leaf 12 and was then almost stable (Figure 2.5). Exceptions were observed for some phytomer ranks, *e.g.* leaf 10 was always shorter than leaf 9. In the contrary, monotonous leaf profiles are observed in the absence of transient stress for the leaves beard on internodes that remain short (Williams, 1960; Gallagher, 1979; Dornbusch *et al.*, 2011; Abichou, 2016). The relative stability of leaf length from phytomer 12 that was simulated in most growth conditions revealed that these leaves reached the maximum leaf length set in the model ($L_{leaf,max}^{En-1}$) for the hidden growth phase *i.e.* before previous leaf emergence. Length of leaves 1 to 6 was almost insensitive to growth conditions as their potential final lengths were already set at model initialization.

Effect of PAR. Leaf length increased with increasing incident PAR. For high incident PAR values (above a PAR threshold that depended on density and soil N concentration), leaf length was almost stable with the incident PAR. The simulated increase of leaf length with increasing incident PAR was a consequence of higher elongation rate due to the higher simulated AA concentrations. The reason for the small effect of PAR above a PAR threshold is that sucrose and AA concentrations in the *hz* reached levels saturating the response of the leaf elongation rate. Literature reports a small positive effect of PAR on leaf length (Friend *et al.*, 1962; Ljutovac, 2002; Dornbusch *et al.*, 2011), except for very low light levels which increase leaf length *e.g.* (Friend *et al.*, 1962) on wheat, by (Allard *et al.*, 1991) on tall fescue, by (Paciullo *et al.*, 2017) on Guinea grass, and by (Bos *et al.*, 2000) on maize. In fact, our model does not consider the photomorphogenetic response of leaf growth.

*Effect of N. S*oil N concentration strongly increase leaf length as extensively reported in the literature (Robson and Parsons, 1978; Wilman and Mohamed, 1980; Volenec and Nelson, 1983; Fricke *et al.*, 1997). Since we simulated constant soil N concentrations, it is difficult to compare quantitatively the magnitude of the simulated effects with the literature. However, on vegetative tall fescue and ryegrass, Wilman and Mohamed (1980) reported a reported 25 % increase of leaf length with N fertilization, which is of same order of magnitude than the simulated length increase of intermediate leaves (leaves 6-12) at Density 500 x PAR 1500.

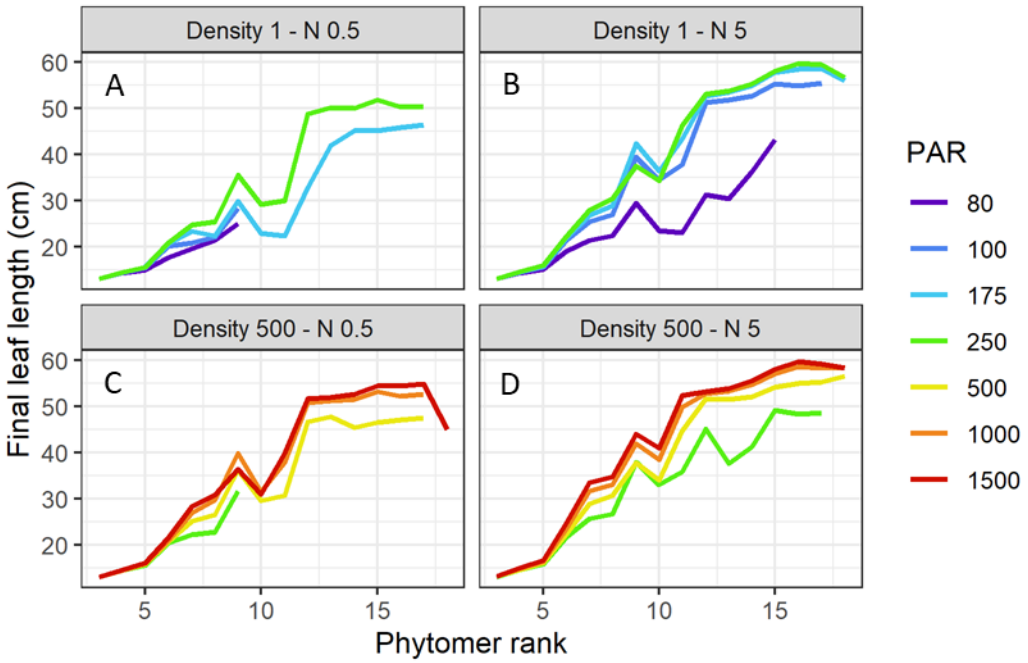

Figure 2.5 – Final length of the leaves (lamina + sheath) per phytomer rank. Each line is one simulation. Colours refer to the treatment of incident PAR (µmol m^{-2} s^{-1}, see right key). Each panel groups the light treatments for one planting density (plant m^{-2}) and one nitrgen concentration (g m^{-3}, see panel title).

Lamina maximum width and specific leaf area

In our model, maximal lamina width is modulated by the mean sucrose concentration in the *hz* integrated over two phyllochrons prior leaf emergence. Consequently, lamina maximum width of leaves 3 to 6 was almost insensitive to growth conditions because they were (at least partially) defined at model's initialization. On the contrary, SLA of leaves 3 to 6 was affected by growth conditions since the beginning of the simulation.

Simulated lamina maximum width varied in the range of 0.4 to 3.1 cm, and specific leaf area (SLA) varied in the range of 15 to 67 m^{-2} kg^{-1}. Both lamina maximum width (Figure 2.6) and SLA (Figure 2.7) presented large variations from one phytomer to the following one, specifically around lamina 10 and lamina 15. These variations were due to lower sucrose concentration in the *hz* around t=1500 h and t=2800 h (Figure 2.3).

Effect of PAR. As shown before, the incident PAR highly affected sucrose concentrations in leaf growth zones, which therefore led to a positive effect on lamina maximal width and SLA. These trends are consistent with literature (Friend *et al.*, 1962; Rawson *et al.*, 1987; Bos *et al.*, 2000; Dornbusch *et al.*, 2011; Poorter *et al.*, 2019).

Friend *et al.*[2] (1962) cultivated stands of spring wheat at same mean daily temperature than our simulations, under a range of incident PAR. Figure 2.8 shows together their observations and our simulations. They observed that incident PAR had almost a linear effect on the ratio of lamina maximum width to lamina length (Figure 2.8 A,B), and a linear negative effect on SLA (Figure 2.8 C,D), which diminished for PAR above 500 µmol m^{-2} s^{-1}. Overall, the simulations were close to observations. Surprisingly, leaf 9 was also almost insensitive to incident PAR. Leaf 9 was ligulated around 2000 h for all treatments; Sucrose concentration in its *hz* prior to the ligulation of leaf 9 (~2000 h for all treatments) was at saturating levels of the response laws of ratio of lamina maximum width to potential final length (Figure S2.21 A) and of SSLM (Figure S2.21 B). Thus, according to the model, organs that grow during a high source:sink are almost insensitive to growth conditions.

Effect of N. Lamina maximum width slightly increased with increasing soil N concentrations (Figure 2.6). This trend is consistent with the literature (Wilman and Mohamed, 1980). In contrast, SLA decreased with increasing soil N concentrations in our simulations (Figure 2.7) while literature reports contrasting effects of soil N concentrations on SLA depending on grass species: a decrease of SLA with soil N concentrations has been reported for barley (Fricke *et al.*, 1997) and wheat (Dreccer *et al.*, 2000) but the opposite has been observed for rye grass (Robson and Parsons, 1978) and tall fescue (Wilman and Mohamed, 1980).

Overall, simulated maximum values of lamina width and SLA are higher than those reported in experimental studies (Rawson *et al.*, 1987; Dornbusch *et al.*, 2011; Abichou, 2016). In particular, we did not find experimental lamina maximum width values above 2 cm for wheat, nor experimental SLA values above 40 m^{-2} kg^{-1} for wheat and ryegrass. However, the simulations performed in the present work covered a larger range of growth conditions than those reported in the literature.

[2] Care must be taken when comparing our simulations with the with the observations by Friend *et al.* (1962) because: (i) observations were made on the third leaf, which is already developed in the seed, (ii) authors used continuous illumination, which is why we doubled their experimental PAR values to compare with our incident PAR applied on a 12h-photoperiod

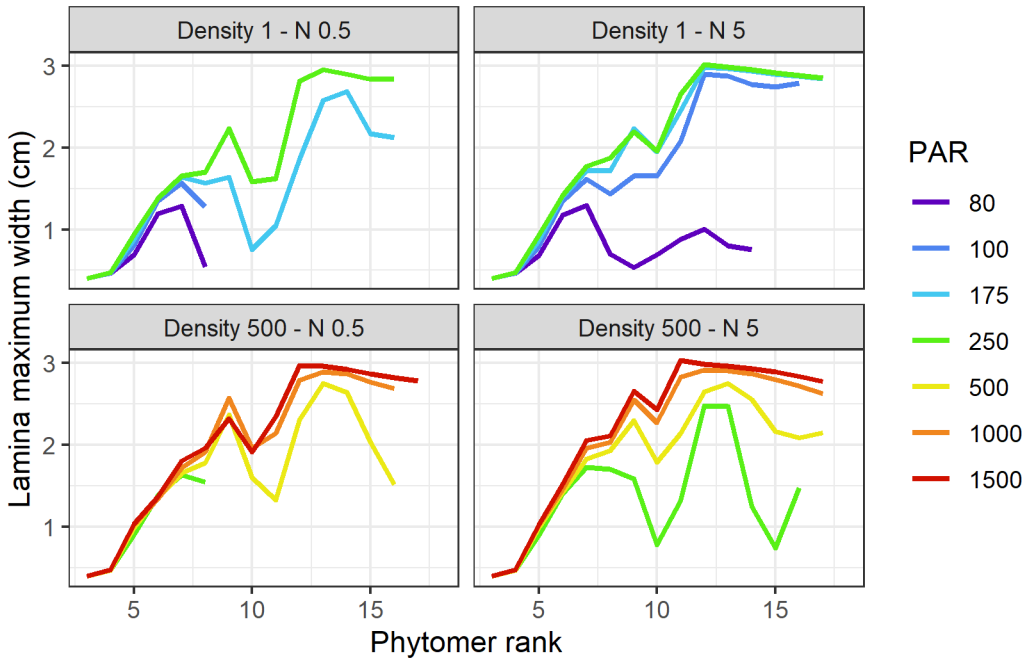

Figure 2.6 – Maximal lamina width per phytomer rank Each line is one simulation. Colours refer to the treatment of incident PAR (µmol m^{-2} s^{-1}, see right key). Each panel groups the light treatments for one planting density (plant m^{-2}) and one nitrgen concentration (g m^{-3}, see panel title).

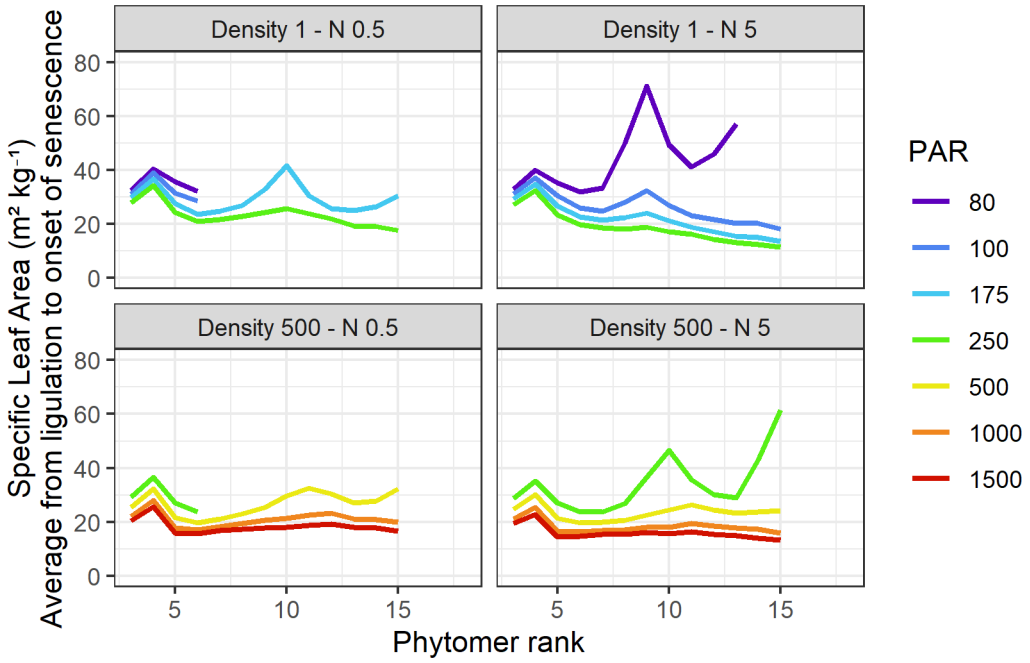

Figure 2.7 – Specific leaf area, averaged from ligulation to the onset of leaf senesence, per phytomer rank Each line is one simulation. Colours refer to the treatment of incident PAR (µmol m^{-2} s^{-1}, see right key). Each panel groups the light treatments for one planting density (plant m^{-2}) and one nitrgen concentration (g m^{-3}, see panel title).

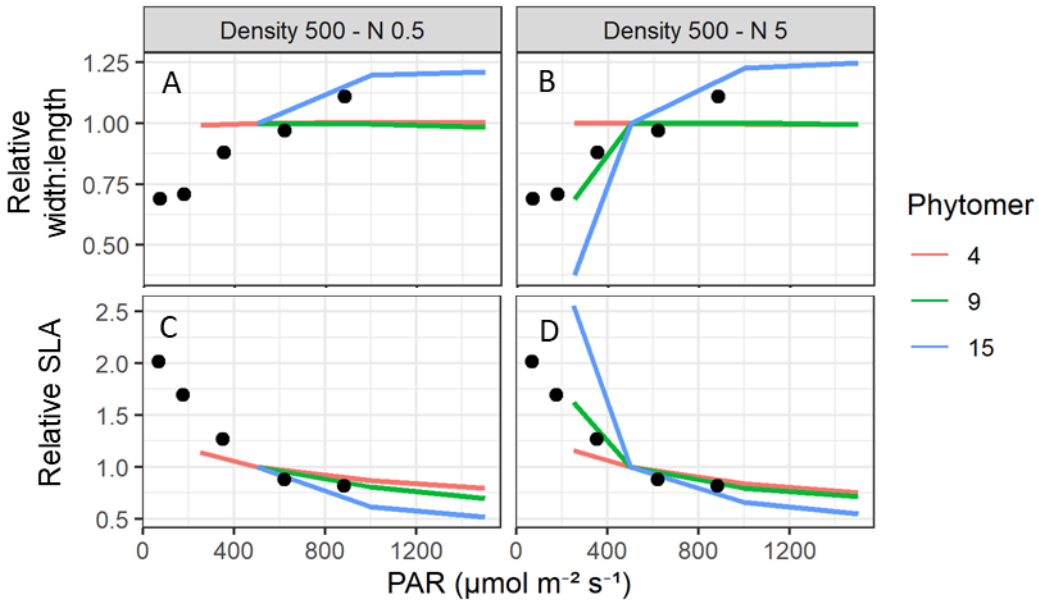

Figure 2.8 – Comparison of the observed and simulated effect of incident PAR on lamina width and SLA. Top row: Ratio between maximal lamina width and the final lamina length (relative to the value at PAR 500 µmol m^{-2} s^{-1}). Bottom row: Average SLA from ligulation to the onset of leaf senescence (relative to the value at PAR 500 µmol m^{-2} s^{-1}). Each panel groups the simulated treatments for one planting density (plant m^{-2}) and one soil nitrogen concentration (g m^{-3}, see panel title). Colours refer to the phytomer rank (see right key). Points show observations on the third leaf of spring wheat seedlings cultivated on stands in growth chambers at 10°C under several continuous PAR (Friend *et al.*, 1962); experimental PAR values have been doubled for comparison with simulations which were performed with a 12h-photoperiod.

Specific leaf nitrogen

Specific leaf nitrogen (SLN) at ligulation of leaves 3 to 9 slightly decreased with phytomer rank and was in the range of 0.6 to 1.4 g m^{-2} (Figure 2.9). Then, SLN increased with phytomer rank and SLN of leaf 15 reached up to 4 g m-2 which is higher the maximum SLN of 3 g m^{-2} that was reported for wheat in the literature (Braune *et al.*, 2009). In our simulations, SLN variations with leaf rank closely followed the dynamic of AA concentration in the *hz* (Figure 2.4).

Effect of planting density. The SLN at ligulation of leaves 6 to 14 was systematically lower for isolated plants (Figure 2.9 A,B, PAR 250) than for plants in stands (Figure 2.9 C,D, PAR 250). At ligulation, the leaf was little affected by self-shading and therefore received the incident PAR.

Effects of PAR and N. The effects of incident PAR and soil N concentration is presented in Figure 2.10 for phytomer 7, which was unaffected by later AA accumulation in the *hz*. The SLN increased with increasing incident PAR. The SLN also increase with increasing soil N concentrations, mainly up to 2.5 g m^{-3}. The direction of the effects of incident PAR and soil N concentration are consistent with the literature (Evans, 1983, 1989; Dreccer *et al.*, 2000).

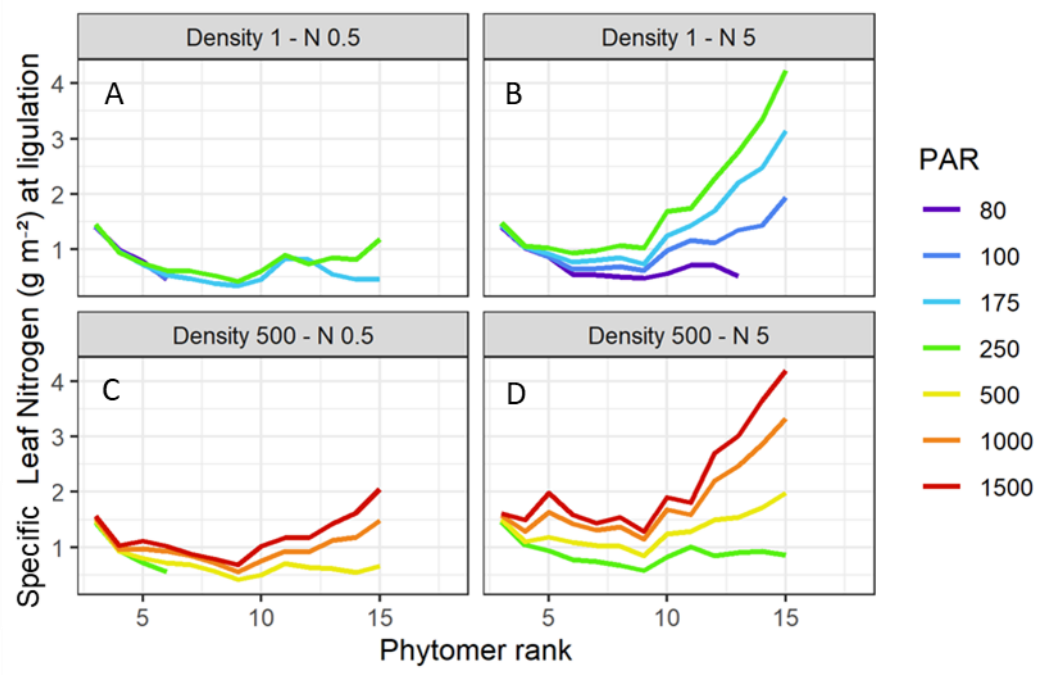

Figure 2.9 - Specific leaf nitrogen at leaf ligulation per phytomer rank Each line is one simulation. Colours refer to the treatment of incident PAR (µmol m^{-2} s^{-1}, see right key). Each panel groups the light treatments for one planting density (plant m^{-2}) and one nitrgen concentration (g m^{-3}, see panel title).

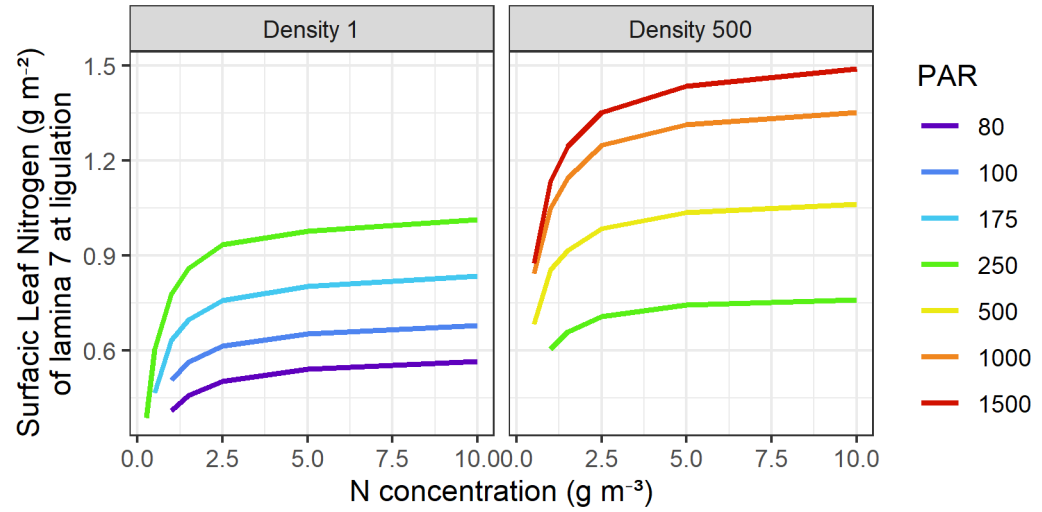

Figure 2.10 – Specific leaf nitrogen of lamina 7 at leaf ligulation. Colours refer to the treatment of incident PAR (µmol m^{-2} s^{-1}, see right key). Each panel is one planting density (plant m^{-2}, see panel title).

Phyllochron

For all treatments, leaves emerged at a constant rate up to leaf 9-10, and at a slightly higher constant rate for upper leaves, as exemplified in Figure 2.11. The rate of leaf ligulation followed the rate of leaf emergence. The stability of the time interval between the emergence (or ligulation) of successive leaves is an emergent property of the model, which appeared with all growth conditions. A trend for a longer phyllochron for higher leaves is

frequently reported for wheat although not specifically corresponding to a break at leaf 9-10. Authors rather report a break at leaf 3-5 or a progressive increase of phyllochron (Abichou *et al.*, 2018). The reported break has been related by several authors to the floral transition of the shoot apical meristem (Boone *et al.*, 1990; Abichou *et al.*, 2018). In our virtual experiment, no floral transition of the shoot apical meristem was simulated. Because the break in time of leaf emergence was simulated for all treatments, the dynamics of concentrations in the *phloem* and in the *hz* could not explain the simulated break. Leaf dimensions at model initialization and/or the ontogenic change in $(RER_{leaf,\,n}^{max})$ (Table S1.1.1 Eqn. 2) might be an explanation of the simulated break.

Effects of density and PAR. When averaged over the whole simulation period, the phyllochron ranged from 106 to 114 °Cd depending on growth conditions (Figure 2.12). The phyllochron was longer for plants in stands (Figure 2.12 B) than for isolated plants (Figure 2.12 A). The phyllochron decreased with increasing incident PAR with a weak effect for PAR above 1000 (plants in stands). The simulated negative effect of PAR on phyllochron is consistent with the literature, but its magnitude is smaller than what has been reported. Indeed, Triboï and Ntonga (1993) observed a 25 % increase of the phyllochron of wheat cultivated at low density in a glasshouse with a 60 % shading. Likewise, Baumont *et al.* (2019) observed a 20 % increase of the phyllochron with a 50 % reduction of the incident PAR for wheat cultivated at 250 µmol m^{-2} s^{-1} with 16h-photoperiod and 28/24°C. In comparison, the maximum simulated phyllochron increased by 5 % in the case of isolated plants when PAR was reduced by 60 % (250 *vs.* 100 µmol m^{-2} s^{-1}), and by 10 % for Density 500 after a reduction by 80 % reduction of incident PAR (1500 *vs.* 250 µmol m^{-2} s^{-1}).

Effect of N. Soil N concentrations decreased the phyllochron and the effect was stronger for low soil N concentrations. The literature reports an effect of soil N concentration on the phyllochron for high N deprivation only (Longnecker and Robson, 1994). For instance, Longnecker *et al.* (1993) applied weekly doses of nutritive solution of several soil N concentrations on two wheat genotypes. They reported that phyllochron increased by 5 % when reducing the soil N concentration from 22.4 to 4.2 g m^{-3}, and by ~15 % when reducing the soil N concentration from 11.2 to 0.7 g m^{-3}. The maximum simulated phyllochron increase was 6 % and 4 % for Density 1 and Density 500, respectively, with a reduction of the soil N concentration from 10 to. 0.5 g m^{-3}. The latter concentration of 0.5 g m^{-3} led to strong N deprivation (low SLN, low shoot N fraction). We conclude that even if a direct comparison with the literature is not possible, the simulated effect of light and N on the phyllochron might be too small.

The small effect of PAR (and maybe of N) on the phyllochron suggests that our model of leaf elongation may not be maintained under light or N stress whereas, in our model, the following rules are unaffected by growth conditions: (i) the emergence of one leaf (leaf *n*) triggers the transition of elongation phase of the next leaf (leaf *n+1*), and (ii) the duration of the sigmoidal elongation phase is constant in temperature-compensated time.

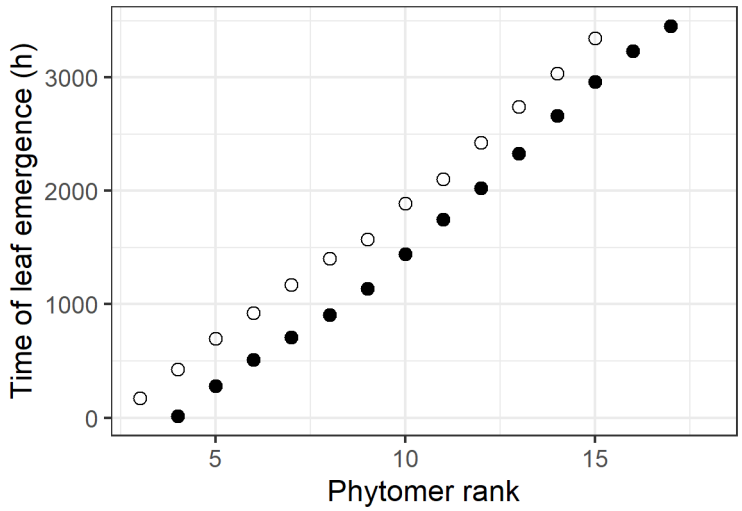

Figure 2.11 –Time of emergence (filled circles) and ligulation (open circles) of the successive leaves of one simulation (Density 500, PAR 500, N 5).

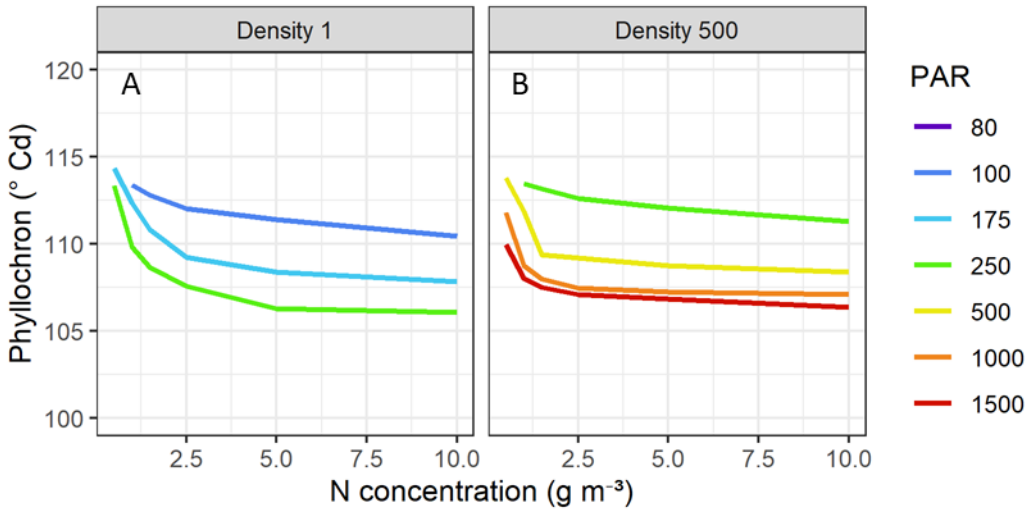

Figure 2.12 – Average phyllochron during the simulation period (3500 h). Colours refer to the treatment of incident PAR (µmol m^{-2} s^{-1}, see right key). Each panel is one planting density (plant m^{-2}, see panel title).

Summary of the simulations of leaf traits

To sum up, the model simulated an overall realistic response of leaf traits to the range of growth conditions that has been applied. With increasing incident PAR, the model simulated leaves that were thicker, wider, with a higher SLN and that emerged faster. With increasing soil N concentration, the model simulated leaves that were longer, thicker, wider, with a higher SLN and that emerged faster. The model failed at simulating the observed lengthening of leaves under low light conditions PAR but this result was expected because the model did not account for the processes underlying etiolation. In addition, for some growth conditions, the model simulated values of lamina width and SLA presented sharped changes with phytomer rank. It suggests that, in our model, the time integration of the effect of sucrose concentration on lamina width and SSLM is too short.

Phenotypic plasticity of whole-plant traits

In our model, traits at plant scale emerge from the integration of processes at local scale. In this section, we present the consequences of growth conditions on selected plant traits: the shoot:root ratio, the N and non-structural carbohydrate fractions, and the radiation use efficiency (RUE).

These plant traits did not vary monotonously across time, as exemplified in Figure S2.27 (Supplementary Data S2.2) for the shoot:root ratio. Thus, we chose to study the consequences of growth conditions on the values of the shoot:root ratio and the N and non-structural carbohydrate fractions, at the end of the simulation period (t=3500 h). RUE was calculated over the whole simulation period.

Shoot:root dry mass ratio

At the end of the simulation, the shoot:root ratio ranged from 1.9 to 5.5 (Figure 2.13). Experimental shoot:root ratio from literature on vegetative ryegrass during the first year of growth ranged from 1.5 to 8 for several treatments of N and PAR (Hunt, 1975; Robson and Parsons, 1978). Experiments on rice and wheat showed that manual detillering or a tillering inhibition gene resulted in lower shoot:root (Nada and Abogadallah, 2016; Hendriks *et al.*, 2016). Such results must be considered when comparing simulated shoot:root values with the literature. All in all, simulated values of shoot:root ratio seem consistent with observations.

Effects of PAR and N. Overall, the shoot:root ratio decreased with incident PAR and increased with soil N concentrations. These trends are in line with the literature (Hunt, 1975; Robson and Parsons, 1978; Poorter *et al.*, 2012) and with the optimal partitioning theory, which states that the plant allocates preferentially resources to the most limiting component, which is the shoot in case of a C limitation, and the root in case of N limitation (Bloom *et al.*, 1985). However, there were a few deviations from this behaviour. First, for isolated plants and low values of N (N 0.5 at PAR 175 or 250, and N 1 at PAR 100; Figure 2.13 A), the shoot:root ratio was higher than expected when compared to other growth conditions. In these cases, the development of the aerial apparatus had not reached its maximum dimensions and mass, whereas leaf length, width and SSM reached maximum values in all other cases. Second, for all N treatments at density 500 x PAR 250 (Figure 2.13 B), and at density 750 x PAR 500, the shoot:root ratio was lower than expected when compared to other growth conditions. In these cases, SSM of the uppermost leaves were much lower than in all other cases. Hence, the ranking of the simulated shoot:root ratios seemed to be largely modulated regardless of whether the leaves had reached the maximum dimensions and/or mass allowed in the model.

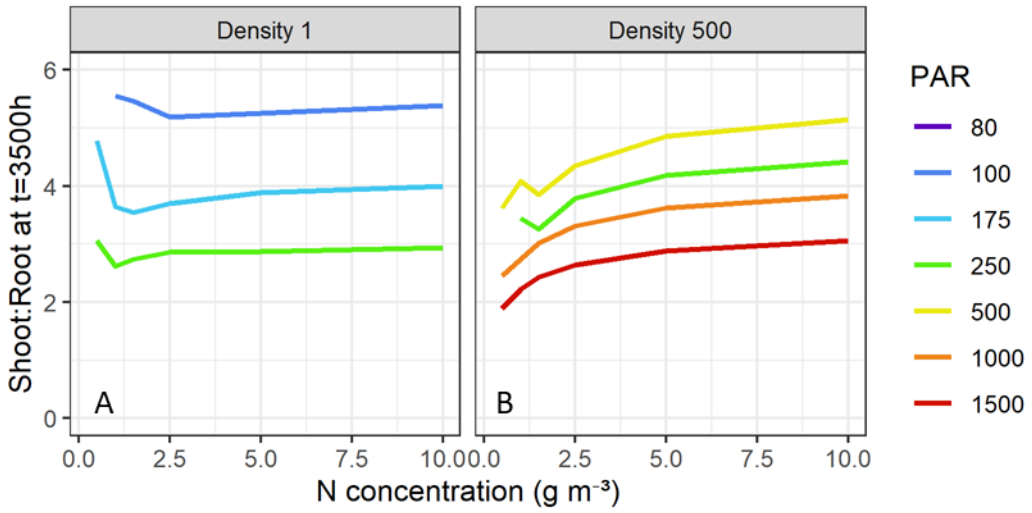

Figure 2.13 – Shoot :root dry mass ratio at the end of the simulation period (t=3500 h). Colours refer to the treatment of incident PAR (µmol m^{-2} s^{-1}, see right key). Each panel is one planting density (plant m^{-2}, see panel title).

Nitrogen fraction

The N fraction of the shoot dry mass varied with growth conditions similarly to the N fraction of the roots. Therefore, only the shoot N fraction is presented.

At t=3500 h, the N fraction of the shoot ranged from 1.6 % to 6 % (Figure 2.14). Comparison of simulation values with the literature is difficult because (i) hydroponic experiments were performed on short periods of time (Siddiqi *et al.*, 1990; Devienne *et al.*, 1994), and (ii) in field experiments, soil N concentration changed across time and plants produced fewer leaves than in our simulations. However, the range of simulated values matches the observed range [1.5 % - 6.5 %] for shoot N fraction of closed canopy of wheat and ryegrass cultivated under field conditions with contrasting available N quantities (Lemaire and Salette, 1984; Devienne-Barret *et al.*, 2000).

Effect of PAR. The shoot N fraction increased with increasing incident PAR, indicating that additional PAR favoured N absorption to a higher degree than it favoured photosynthesis. Such result departs from experimental observations reported in the literature on vegetative barley (Ellen and Van Oene, 1989), tall fescue (Gastal and Saugier, 1986), ryegrass (Luxmoore and Millington, 1971) and Guinea grass (Paciullo *et al.*, 2017). On tall fescue cultivated under high N fertilization, Gastal (1984) observed that N absorption was proportional to C assimilation for low PAR levels, and that, for high PAR levels, the ratio of N absorption to C assimilation decreased with increasing PAR levels. Figure 2.15 shows that the plant N fraction was correlated with the plant transpiration rate. In our simulations, higher PAR led to higher transpiration and so to higher exports of nitrates from the root to the photosynthetic organs, as in the model they occur through the transpiration flow. Consequently, nitrate concentration in the root remained at levels that could only weakly inhibit N uptake. The simulated increase in N fraction with increasing PAR might, which is not consistent with literature, might be due to a misrepresentation, in our model, of the consequences of transpiration on nitrate export from the roots.

Effect of N. The shoot N fraction increased with increasing soil N concentrations; the effect of soil N concentration was more marked for low soil N concentrations. The positive effect of soil N concentration on shoot N fraction and the shape of the curve are widely reported by the literature (Lemaire and Salette, 1984; Gastal and Saugier, 1986; Devienne *et al.*, 1994; Devienne-Barret *et al.*, 2000).

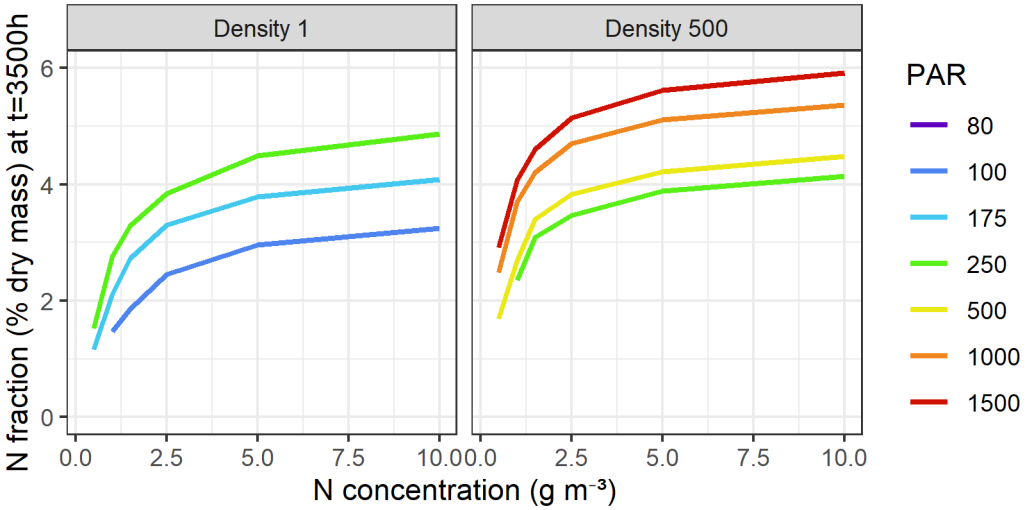

Figure 2.14 – Nitrogen fraction of the shoot at the end of the simulation period (t=3500 h). Colours refer to the treatment of incident PAR (µmol m^{-2} s^{-1}, see right key). Each panel is one planting density (plant m^{-2}, see panel title).

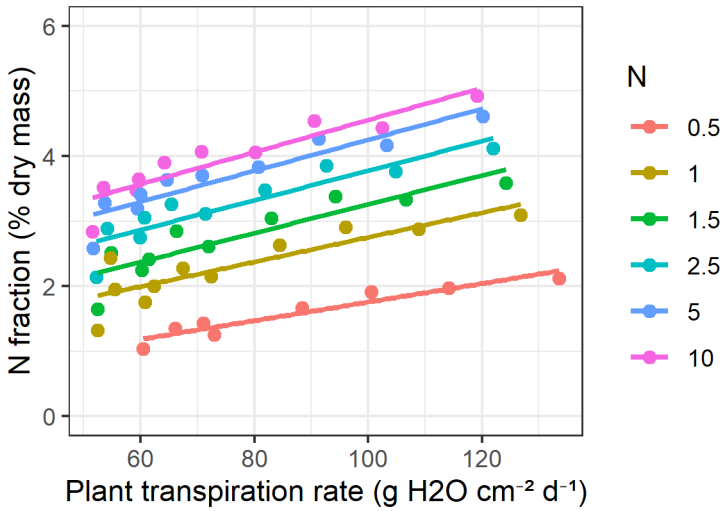

Figure 2.15 - Nitrogen fraction of the plant at the end of the simulation period (t=3500 h) as a function of the average plant transpiration per unit of green phytoelement area over the simulation period (3500 h). Each point is a simulation. All densities are plotted together. Colours represent the soil nitrogen concentration (g m^{-3}, see right key).

Fraction of non-structural carbohydrates

Simulated values and effect of density. At t=3500 h, the fraction of the non-structural carbohydrates (NSC) was much higher in isolated plants (Figure 2.16 A,C) than in plants in stands (Figure 2.16 B,D). NSC was in the range of 25-42 % *vs.* 5-28 % in the laminae (Figure 2.16 A,B), 30-44 % *vs.* 12-32 % in the sheaths (Figure 2.16 C,D), and 25-45 % *vs.* 5-31 % in the roots (Figure S2.29 in Supplementary Data S2.2) for isolated plants and plants in stands, respectively. We found in the literature only NSC fractions of plants cultivated in stands. The simulated maximum NSC fraction of sheaths in plants in stands is comparable to the maximum value found in literature: ~50 % in sheath of winter wheat (Savitch *et al.*, 2000) and ryegrass (Robson and Deacon, 1978). In contrast, the simulated maximum NSC of roots of plants in stands was higher than the maximum values found in the literature, which is 10 % in roots of perennial grass (J.-L. Durand, unpublished experiment). Simulations of plants in stands suggest that the model allocated too much NSC to the roots and not enough to the sheaths, in the case of large NSC accumulation. However, simulated NSC values may not be accurately comparable with the literature because monoculms have reduced sinks and the sink-source balance is expected to interact with photosynthesis (Dingkuhn *et al.*, 2020).

Effect of PAR. NSC factions increased with increasing incident PAR (Figure 2.16), as a higher proportion of the C assimilated was allocated to non-structural compounds (Figure S2.30 in Supplementary Data S2.2). The effect of incident PAR on NSC fraction was more marked for exposed organs (laminae *vs.* sheaths, isolated plants *vs.* plants in stands).

Effect of N. Overall, NSC factions decreased with increasing soil N concentrations (Figure 2.16) and the NSC fractions of both laminae and sheaths had same sensibility to soil N concentration. This trend is consistent with the literature (Robson and Deacon, 1978; Wilman, 1980; Volenec and Nelson, 1984) but Robson and Deacon (1978) found on ryegrass that NSC fraction of sheath was more sensitive to N fertilization than laminae, which indicates that NSC are preferentially stored in sheaths than in laminae. Our model did not simulate the effect of soil N concentrations on the NSC partitioning within the plant.

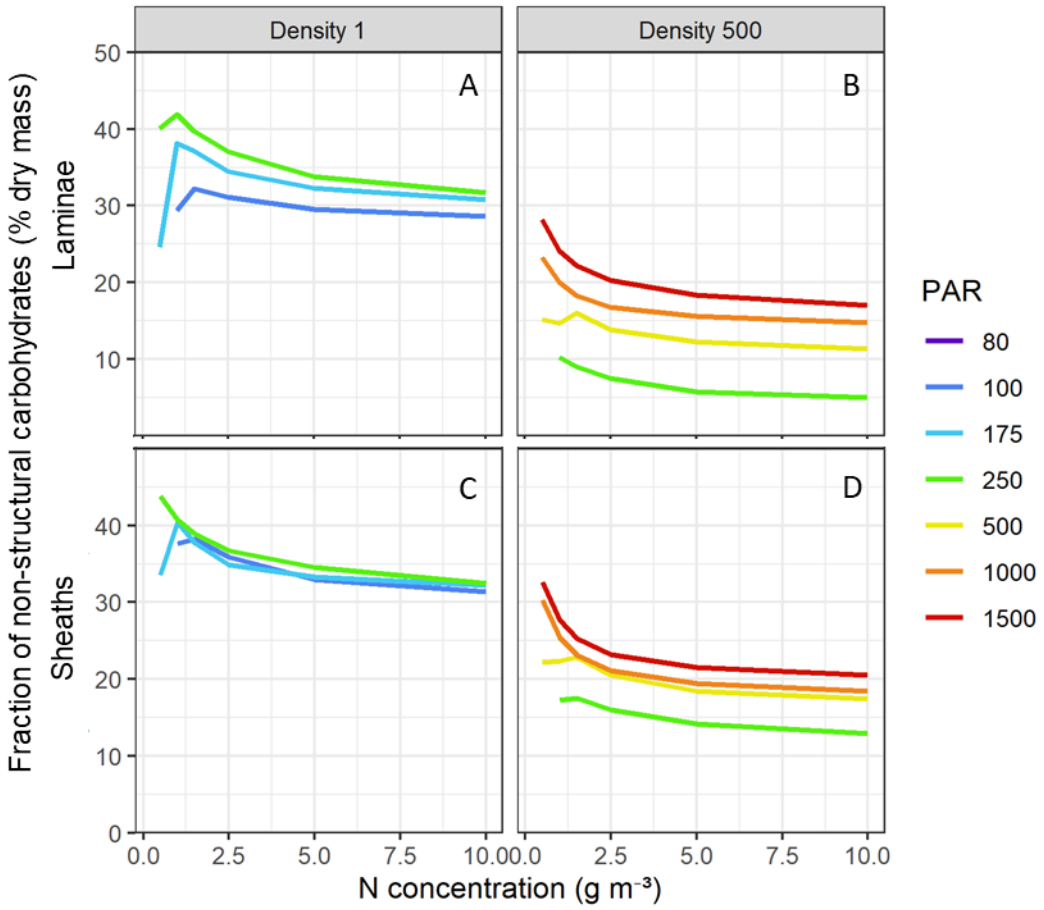

Figure 2.16 - Fraction of non-structural carbohydrates in the shoot at the end of the simulation period (t=3500 h). Top row: aggregated green laminae. Bottom row: aggregated sheaths and *hz*. Colours refer to the treatment of incident PAR (µmol m^{-2} s^{-1}, see right key). Each column is planting density (plant m^{-2}, see panel title).

Radiation use efficiency

Simulated values. Simulated RUE, calculated from absorbed PAR and plant dry mass (including structural mass of the senesced tissues), varied between 1.6 and 3.4 g MJ^{-1}. These simulated values are in the range of observed RUE and of RUE that drives some crop models (Sinclair and Amir, 1992). In particular, our higher simulated RUE is consistent with maximum RUE reported in the literature: 3 g MJ^{-1} for wheat and barley before heading (Gallagher and Biscoe, 1978; Reynolds *et al.*, 2012) and 4.2 g MJ^{-1} for vegetative ryegrass (Akmal and Janssens, 2004). Because the maximum simulated RUE are plausible values, the high NSC fractions simulated in laminae and roots might result from a restriction in plant growth (monoculm, maximum leaf dimensions and mass) rather than an overestimation of C assimilation.

Effects of PAR and N. Simulated RUE increased with decreasing incident PAR as reported in the literature (Sinclair and Horie, 1989), and increasing N fertilization, mainly up to soil N concentration of 2.5 g m^{-3}. The positive effect of N fertilization on RUE was also reported by literature (Bélanger *et al.*, 1992). The simulated negative effect of incident PAR on RUE was due to both decreasing photosynthetic efficiency (Figure S2.31 in Supplementary Data S2.2) and decreasing carbon use efficiency (Figure S2.32 in Supplementary Data S2.2) with increasing incident

PAR. The simulated positive effect of soil N concentration on RUE was due to an increasing photosynthetic efficiency with increasing soil N concentrations (Figure S2.31 in Supplementary Data S2.2). Photosynthesis efficiency increased with increasing soil N concentrations because of higher SLN (Figure 2.10). Nevertheless, despite higher SLN with higher incident PAR, photosynthesis efficiency decreased with increasing incident PAR because of the non-linear response of photosynthesis.

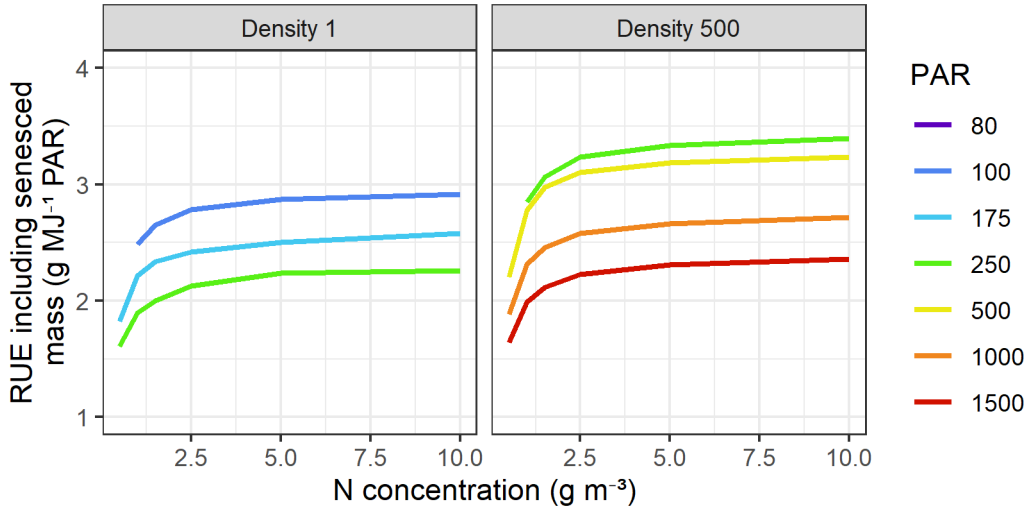

Figure 2.17 – Average radiation use efficiency over the simulation period (3500 h). Colours refer to the treatment of incident PAR (µmol m^{-2} s^{-1}, see right key). Each panel is one planting density (plant m^{-2}, see panel title).

Summary of the simulations of whole-plant traits

To sum up, the model simulated an overall realistic response of whole-plant traits to the range of growth conditions that has been applied. With increasing incident PAR, the model simulated lower shoot:root and RUE, and higher NSC fraction of the dry mass. With increasing soil N concentration, the model simulated higher shoot:root, N fraction and RUE, and lower NSC fraction. The model failed at simulating the observed decrease of N fraction width increasing incident PAR. In addition, the model might overestimate NSC fraction of isolated plants for all the range of applied PAR.

Virtual experiment 2: Sensitivity of the model to the initial state of the plant

The growth of vegetative monoculms of eight plants contrasted in terms of their initial states was simulated, under eight growth conditions contrasted by planting density, soil N concentration and incident PAR. The initial plant states were defined as modifications of $Init_{VE1}$. The simulation results are compared to those in virtual experiment 1 with same growth conditions. The present section gives an overview of some key results on leaf length and sucrose concentration in the *phloem* and in the *hz*. After specifying general outcomes of the simulations, we sequentially present the simulation results of the initial plant states for which the length of leaves 1 to 4 were modulated ($Init_{Length}$), and then of the initial plant states for which the shoot N fraction was modulated ($Init_N$).

General outcomes. The effect of the modulation of the initial plant state on the final leaf length varied with growth conditions as exemplified in Figure 2.18 for three growth conditions. The response of final leaf length to the initial plant state was usually weaker for plant in stands (Figure 2.18 B,E) than for isolated plants (Figure 2.18 A,D). We did not identify another trend in the effect of growing conditions on the response to the initial plant state.

Effect of $Init_{Length}$ vs. $Init_{VE1}$. Changing the length of leaves 1 to 4 at model initialization impacted the final length of leaves 6 and above (Figure 2.18 A,B,C). In general, the impact on higher leaves was of same magnitude as the change made on leaves 1 to 4. However, for some growth conditions, the higher length of leaves 1 to 4 had almost no effect on upper leaves, or even resulted in shorter leaves (*e.g.* Figure 2.18 B). Leaf 5 was only slightly because its final length was mainly set at the emergence of leaf 4, which occurred few hours after model initialization. Besides, the final length of leaves above leaf 12 was usually unaffected because these leaves were limited in their elongation in virtual experiment 1. The propagation of length modification to the upper leaves is consistent with the literature that reported that a reduction of the pseudostem length reduced the final length of growing leaves, and conversely in the case of an artificial increase in the pseudostem length (Begg and Wright, 1962; Wilson and Laidlaw, 1985; Casey *et al.*, 1999). In our model, the propagation resulted from (i) the coordination rules, and (ii) the consequent changes in the trophic status of the plant.

Effect of $Init_N$ vs. $Init_{VE1}$. Lowering the shoot N fraction of the initial plant state from 4.4 % to 3.4 % and to 2.4 % resulted in shorter leaves by ~10 % and 30 %, respectively (Figure 2.18 D,E,F). The reduction in leaf length was caused by a lower elongation rate due to lower sucrose (mainly up to 1500 h for plants in stands, see Figure 2.19 B,C) and AA concentration (during the entire simulation period) in the *hz*. The reduction in AA concentration was first directly imposed by model initialization. Because the shoot N fraction at model initialization was reduced, photosynthesis was reduced, which also resulted in a lower N uptake and ultimately, in a reduction of sucrose and AA concentration. Figure 2.19 illustrates the changes in sucrose concentration in the *phloem* and in the *hz* for some growth conditions. The peak of sucrose concentration simulated at ~500 h in virtual experiment 1 decreased with decreasing shoot N fraction at model initialization, and even disappeared in some growth conditions with $Init_N$ of 2.4 % (Figure 2.19 A,B). The simulated peak of sucrose concentration in virtual experiment 1 was then associated to the high N fraction of the plant at model initialization in $Init_{VE1}$. $Init_{VE1}$ corresponded to the main stem of a wheat plant in the field in Grignon during December (high N fraction), while the air temperature of our simulations was similar to the mean air temperature in Grignon during March. Thus, these results suggest that plants have a lower N fraction if they had grown in the simulated growth conditions since germination. The simulated peak of sucrose concentration could then be interpreted as a result of the transfer of the plants between environmental conditions.

To sum up, the effect of the initial plant state was often long-lasting, sometimes during 3500 h, which is more than a wheat growth season. We can wonder if stem elongation would have changed the effect of initial plant state since stem elongation has a impact on the trophic status of the plant. The effect of initial plant state was highly dependent on growth conditions; we did not identify clear patterns in the effect of growth conditions on the response to the initial plant state.

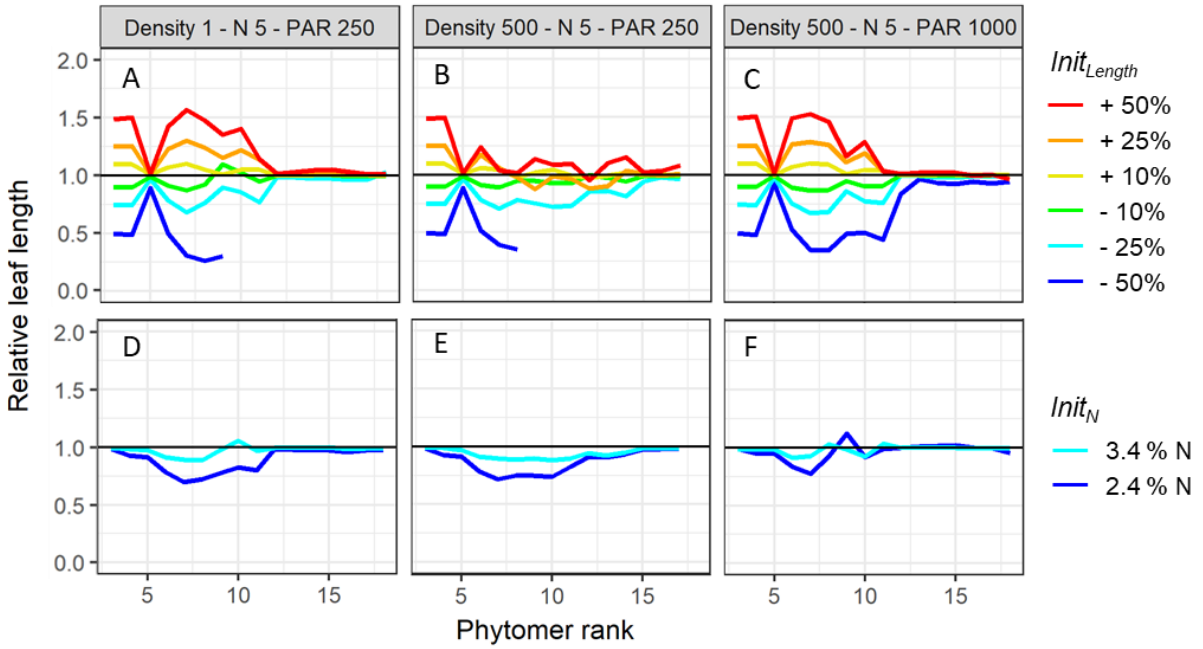

Figure 2.18 – Effect of the initial state of the plant on the final length of leaves. Initial plant states were defined as modulations of the initial state of the plant used in virtual experiment 1($Init_{VE1}$): A,B,C) Modulation of the length of leaves 1 to 4 (+/- 10 %, 25 %, 50 %); C,D,E) Modulation of the shoot N fraction (2.4 %, 3.4 % *vs.* 4.4 % in $Init_{VE1}$). Leaf lengths are expressed relatively to the simulated length in virtual experiment 1. Each line is one simulation. Colours represent the initial plant state (see right key). Each panel groups the initial plant states for one planting density (plant m^{-2}), one soil nitrogen concentration (g m^{-3}) and one incident PAR (µmol m^{-2} s^{-1}, see panel title).

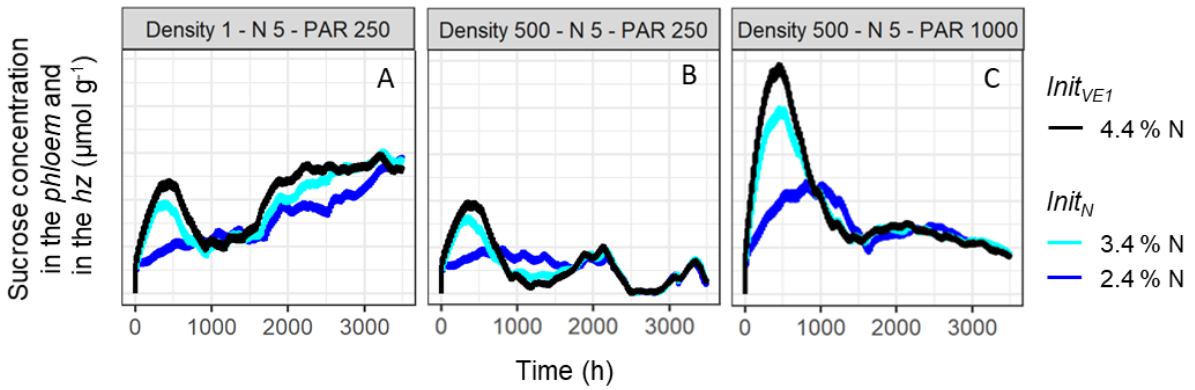

Figure 2.19 - Effect of the initial state of the plant on the concentration of sucrose in the *phloem* and in the hidden part of the growing leaves (*hz*). Initial plant states were defined by decreasing the shoot N fraction (2.4 %, 3.4 % *vs.* 4.4 % in $Init_{VE1}$). Each line is one simulation. Colours represent the initial plant state (see right key). Each panel groups the initial plant states for one planting density (plant m^{-2}), one soil nitrogen concentration (g m^{-3}) and one incident PAR (µmol m^{-2} s^{-1}, see panel title).

2.4 - Discussion

CN-Wheat relies on a bottom-up approach in which the growth processes are driven at a local scale by (i) the C-N metabolite concentrations of each organ, and by (ii) coordination rules that set the timing of elongation of successive leaves as well as the timing of definition of key leaf traits (width and specific structural masses of lamina and sheath). The integration of these local processes builds whole-plant traits (*e.g.* shoot:root ratio), temporal patterns (*e.g.* phyllochron stability) and spatio-temporal pattern (*e.g.* patterns of leaf dimensions along the axis). In the first virtual experiment, the growth a vegetative monoculm was simulated in a wide range of growth conditions in terms of planting density, soil N concentration, and incident PAR. This enabled us to (i) explore the model's behaviour when simulating growth dynamics, and (ii) test the ability of the model's underlying assumption to simulate the phenotypic plasticity of traits at whole-plant scale and at the leaf scale. In the second virtual experiment, we briefly tested the sensitivity of the model to the initial state of the plant.

Our model simulates realistic phenotypic plasticity of plant architecture for contrasting light availability and N fertilization.

Overall, CN-Wheat simulated realistic phenotypic plasticity of leaf and plant traits in contrasting growth conditions of planting density, incident PAR and soil N concentration. As a response to increasing incident PAR, our model simulated, at the whole-plant level, a decreasing fraction of dry mass allocated to roots and faster leaf emergence, and, at leaf level, thicker and wider leaves with increasing SLN. The response to increasing planting density was similar to decreasing incident PAR. As a response to increasing N fertilization, our model simulated, at the whole-plant level, a decreasing shoot:root dry mass and faster leaf emergence, and, at leaf level, increasing thickness, width, length and SLN.

Our approach is highly innovative compared to models in which the responses of some key variables (*e.g.* RUE, shoot N content, SLA) to growth conditions must be set as empirical functions of growth conditions, or to models that rely on teleonomic approaches, or on growth potentials and sink priorities. As highlighted by Muller and Martre (2019), such models are limited in their ability to simulate growth under extreme conditions, and/or in the case of multiple stresses because environmental stresses do not have independent effects on the plant but are interacting through complex feedback control loops. To overcome these limitations, we have moved towards a better simulation of phenotypic plasticity by proposing an explicit formalism of the underlying processes of growth. The phenotypic plasticity of leaf and plant traits, and of their dynamics, are an emergent property of our model. In particular, the acquisition of dry mass and its partitioning among plant's organs are built by local rules. The present set of simulations under 72 contrasting growth conditions demonstrated the validity of our approach to simulate phenotypic plasticity in the theoretical frame of a vegetative monoculm cultivated under hydroponic-like conditions. Our approach still needs further evaluation, against experimental results, in the case of field grass *i.e.* with tillers.

It is worth mentioning that our model did not simulate the expected responses to growth conditions for some architectural traits; we will particularly focus this discussion on final leaf length and the phyllochron because

these two variables are major determinants of the dynamic of photosynthetic area. First, the model simulated a decrease in final leaf length with decreasing PAR (Figure 2.5). Conversely, literature reports the lengthening of leaves in case of very low PAR due to higher leaf elongation rate in response to low blue light (Gautier and Varlet-Grancher, 1996; Christophe *et al.*, 2006) but the mechanisms involved have not yet been elucidated. The response to low blue light could be associated to a signal transmitted by specific photoreceptors (Smith, 2013; Ballaré and Pierik, 2017). Another mechanism would be stomatal induced variations of plant transpiration that ultimately affect leaf elongation (Barillot *et al.*, 2020*a*). Thus, our simulations highlighted the need to consider light as a signal *per se* and water to simulate leaf growth in low light environment (*e.g.* crop mixture). More widely, implementing hydraulic regulation of leaf growth would allow addressing the responses to water availability. Second, our model simulated weak responses of the phyllochron to the environment (Figure 2.12). This result suggests that our model of leaf elongation might not be maintained in case of stresses. Our coordination rules state that, at the emergence of the previous leaf, the leaf starts a sigmoidal elongation phase, in which the elongation rate is modulated by the environment but elongation duration remains constant. However, it has been observed on barley and spring wheat that, in the case of C or N limitation, the elongation rate is slower but the duration of the linear elongation phase is longer (Dale, 1982; Fricke *et al.*, 1997). Similarly, the duration of the linear elongation phase of maize leaves was modulated after a transient early chilling stress (Louarn *et al.*, 2010). Consequently, this virtual experiment pointed out that more experiments are needed to investigate the elongation kinetic of successive leaves, from their meristematic stages, in contrasting growth conditions. However, such experiments are highly time-consuming because they require frequent manual dissections over a long period.

Extreme growth conditions revealed a need for better simulation of C and N economy of the growing plant.

Models often simulate an increase in plant dry mass solely based on intercepted PAR and RUE. Similarly, N uptake is often derived from the shoot dry mass and the critical N dilution curve. Such approaches are limited when the growth conditions depart from the one used to set the underlying empirical functions of RUE and N dilution curve. One originality of our model is that it simulates plant's C and N economy, which required formalising the processes of C and N acquisition, as well as C and N losses (respiration, exudation, tissue death), and C and N partitioning among the different metabolic compartments (different forms of metabolites and organ structure) and organs. In the context of a growing plant, the simulated system has a constantly changing structure. It implies that (i) the quantities of C and N inside the plant constantly change because the surfaces of exchanges with the environment are growing, and that (ii) in our model, C and N investments in the plant structure (and in the different forms of metabolites) might not be a constant share of the net C and N entries in the plant, leading to dynamic concentrations of sucrose and AA (ratio of sucrose and AA quantities in an organ to the organ's structural mass). Because fluxes between the model compartments are regulated by the concentrations of sucrose and AA, the growing plant is settled by complex feedback loops. Thus, the simulation of C and N economy of the growing plant is particularly challenging.

We tested our model for a wide range of growth conditions, including some extreme conditions that led to very thick leaves with a very high SLN, and to plants with very high NSC fraction. Preliminary simulations with the model used in Chapter 1 allowed us to identify limitations of the initial photosynthesis sub-model, so that we switched from dependency on SLN to dependency on the specific non-structural proteins, and we implemented an empirical feedback regulation by the NSC concentration. These changes remain to be tested on the available datasets that cover the early vegetative stages (Chapter 1) and the post-flowering stages (Barillot *et al.*, 2016*b*) of wheat, which were used to evaluate the model. The present set of simulations showed that, overall, our approach simulated realistic values of N fraction (Figure 2.14) and NSC fraction (Figure 2.16). In addition, the trend of the responses of N fraction to N fertilization, and the trends of NSC responses to incident PAR and N fertilization were consistent with the literature. Nevertheless, the model failed at simulating the decreasing N fraction that is observed for increasing incident PAR. In addition, simulations under some growth conditions revealed that our model overestimated the quantities of C and N metabolites, as detailed below.

The implemented feedback regulation of photosynthesis relied on an empirical function that decreases the rate of photosynthesis in function of NSC concentration, which has been calibrated from experimental results on wheat (Azcón-Bieto, 1983). Despite this implementation, the large simulated NSC fraction in the laminae and in the roots (Figure 2.16 A,B; Figure S2.29) suggested that the model might overestimate the sugar production. One reason for such likely overestimation might be that the simulated response of photosynthesis to the source-sink balance is incorrect, as a consequence of the lack of mechanistic implementation; however, the underlying mechanism is not yet elucidated (Sharkey, 2019; Dingkuhn *et al.*, 2020) so a mechanistic implementation is not yet considered. The high simulated N fractions, and the fact that the current formalism of leaf senescence is not able to simulate the anticipation of senescence that is observed at high irradiance level (Ellen and Van Oene, 1989), might be other (complementary) reasons for this probable simulated overestimation of NSC. Therefore, it seems that a better understanding of the response of photosynthesis to the source-sink balance is needed to simulate plant growth in the cases of large available sources. Dingkuhn et al. (2020) also pointed out that this understanding is needed to tackle burning challenging like forecasting crop production in the case of further CO_2 enrichment of the atmosphere.

In the present work, we simulated the growth of plants under unlimited N availability for a long growth period, while in field-conditions the plant has access to limited N quantities. Experiments on wheat under high N fertilization and over the whole crop cycle showed that plant N fraction was highly related to the plant dry mass (N dilution curve, Justes *et al.*, 1994). The maximum plant N fraction recorded in these experiments was ~75 % above the N dilution curve (Devienne-Barret *et al.*, 2000), which corresponds to a N fraction of ~6.5 % for vegetative plants with shoot dry mass below 1 g, and ~4.5 % for plants with shoot dry mass of ~6 g, that were plants after stem elongation. In contrast, plants simulated under high PAR and high N fertilization accumulated N up to 7 % in the shoot and produced 6 g of shoot dry mass after 4600 h (Figure 2.20). Thus, experimental results suggest that the simulated N fraction is too high; but care must be taken when comparing our simulations with experimental data due to the differences in plant stages and in fertilization methods, as already mentioned in the Results section. Although, in the model, the nitrate concentration in the roots inhibits N uptake, the current

parameterisation of the model does not limit enough N accumulation in the plant. Three aspects of N metabolism have been identified as weaknesses of the model, and are detailed below.

- The model might underestimate N losses through exudation and tissue death. First, in the model, exudation was estimated from experimental results of the literature but quantifications of exudation are imprecise because of methodological difficulties. Second, the model accounts for N losses at tissue death by assuming that part of the N is not remobilised because used in tissue structure. N losses at tissue death are considered a fixed fraction of the structural mass that solely depends on leaf rank (in the range of 0.5 – 2 %, with lower laminae having highest N losses at tissue death). However, there are experimental evidence that, for leaves, this fraction is modulated by environmental conditions. N fraction of senescent leaves was indeed higher by ~0.5 % (N fraction unit) at high *vs.* low N fertilization on wheat (data from Bertheloot, 2009; see Chapter 3), and at low *vs.* high irradiance on barley (Ellen and Van Oene, 1989) and on tall fescue (Gastal and Saugier, 1986). Nevertheless, these potential additional N losses at tissue death account for a small fraction of the N budget of the plant. Indeed, a rough estimate indicates that increasing the N losses at leaf death by 0.5% would only reduce the shoot N fraction from 7 % to 6.7 % for the simulation in Figure 2.20 (simulation of 4600 h without root senescence). Thus, it appears that, first, progress need to be done on the simulation of N uptake, as detailed on the next two points.

- In our model, root dry mass increases exponentially, without limit, if the sucrose concentration in the roots is sufficient. As nitrate uptake is proportional to root dry mass, N uptake also increases exponentially (if sufficient sucrose and no accumulation of nitrates in the roots). Thus, N uptake highly depends on the root dry mass. We illustrate this dependency by performing simulations with two versions of the model: without root senescence (as in Results section) and with a complete senescence of the root tissues 1900 h (800°Cd) after their synthesis. A delay of 800°Cd has been chosen to reflect the common view in models (*e.g.* Johnson and Thornley, 1985; Asseng *et al.*, 1997) that root senescence of a wheat plant cultivated in usual field condition starts at the beginning of stem elongation. Figure 2.20 presents the consequences of the changes on root dry mass and on AA concentration in the *phloem,* which are both visible from ~2500 h. In turn, shoot dry mass was later affected from ~3700 h. The implementation of root senescence reduced the shoot N fraction at t=4600h from 7 % to 6.3 %, which is still higher than what would be expected when considering above-cited experimental results (Devienne-Barret *et al.*, 2000).

- In our model, the rate of nitrate uptake is favoured by the sucrose concentration in the roots, and is inhibited by the nitrate concentration in the roots so that excessive N accumulation in the plant is avoided. However, with the current parameter calibration, the model did never simulate nitrate accumulation in the roots. In all cases, nitrates were quickly exported towards the shoot through the transpiration flow. The parameters of nitrate export were not defined from literature but calibrated to simulate values and dynamic of N uptake that were consistent with observations. Thus, the high rate of nitrate export was defined so that the model could simulate realistic N uptake in Chapter 1. More generally, most parameters related to N metabolism (N uptake, N assimilation and N fluxes) were not taken from literature but were calibrated to simulate realistic behaviour at plant scale. We should try finding another set of parameters that allows

simulating both expected results in Chapter 1 and in these virtual experiments. Interestingly, the calibrated rate of nitrate export was higher for early vegetative stages than for post-flowering stages (see Chapter 1), suggesting that the rate of nitrate export may vary with the plant ontogeny, perhaps due to changes in root architecture. While the parameters related to N metabolism might be revised, the formalism of nitrate export might additionally need further revision. Indeed, in our model, the export rate of nitrates is proportional to the transpiration rate, which led to increasing N fraction with increasing incident PAR, while the opposite was observed in the literature. Nevertheless, at high transpiration rate, the export rate of nitrates could be limited by the rate of nitrates loading into the xylem, which is not implemented in our model; one reason being the fact that the xylem is not formalised as a compartment of our model.

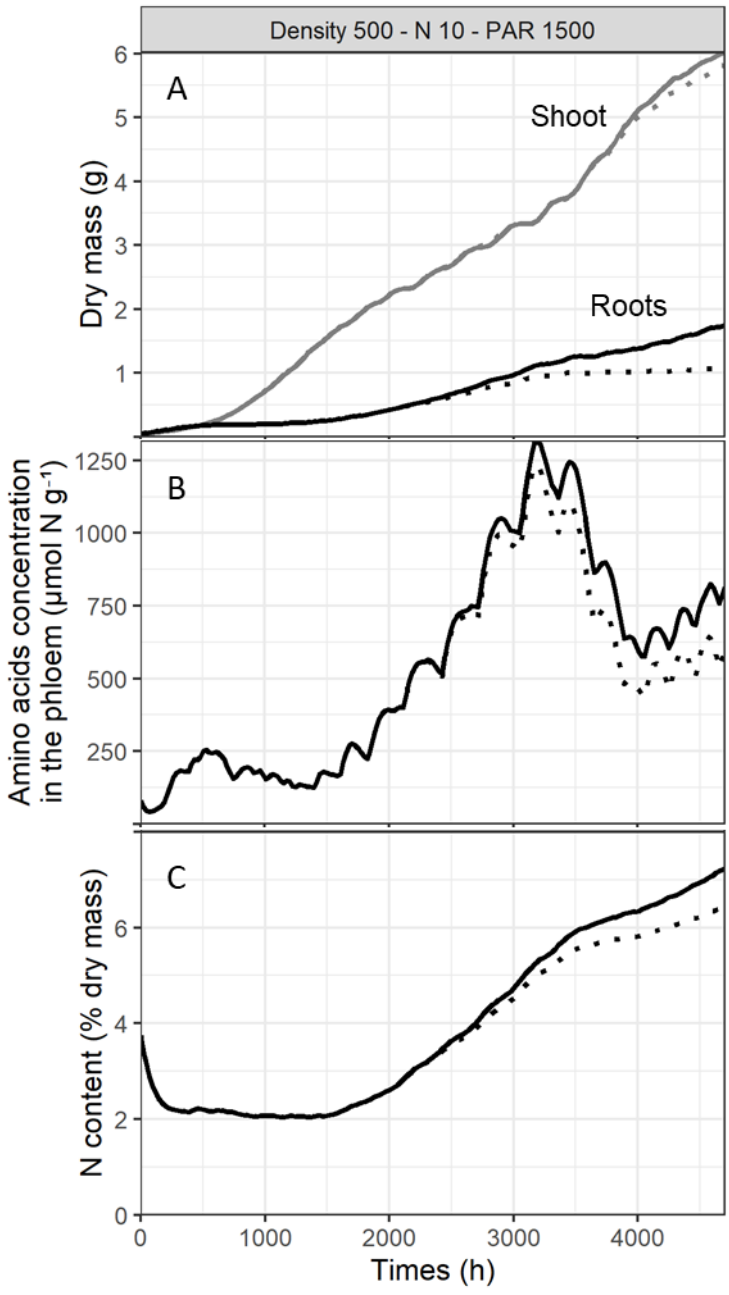

Figure 2.20 –Influences of root dry mass on the plant structure and functioning. A: Shoot (grey) and root (black) dry masses across time. B: Amino acids concentration in the phloem and in the *hz* across time C: Nitrogen fraction of the shoot dry mass across time. Plain curves are simulation results of a model without root senescence as presented in previous sections (but further extend to 4600h). Dotted curves are simulation results of the same model with a complete senescence of the root tissues 400°Cd after their synthesis. The growth conditions of both simulations were Density 500 x N 10 x PAR 1500.

Towards the implementation of additional growth mechanisms to leverage our simulations of phenotypic plasticity and to further evaluated our model.

The present simulations were performed in the theoretical case of a monoculm grass that would have similar behaviour as a wheat main culm. In the real world, cultivating wheat plants under such contrasting conditions would have led to highly contrasting tillering levels (Friend, 1965; Casal *et al.*, 1986; Longnecker *et al.*, 1993; Nelson, 2000; Evers *et al.*, 2006). We can then wonder to what extent simulation results would have differed if tillering processes had been implemented. At least two main changes may be expected. First, tillers result in a higher density of culms, but they result in a different LAI dynamic compared to that produced by a higher density of monoculms. Second, tillering plants are expected to have higher shoot:root ratio than plants with few or no tillers (Nada and Abogadallah, 2016; Hendriks *et al.*, 2016), which would likely result in a lower N:C ratio of the plant. To date, the mechanisms that underlie tiller induction are not yet implemented in the model. As a result, the next modelling step should be to develop a tillering sub-module in order to simulate tillering grass. This requires modelling the underlying processes of early axillary bud development up to tiller emergence, the processes that define the termination of the meristematic activity of tillers, and the metabolic fluxes between axes. The underlying mechanisms of growth of tiller leaves are then same as the main stem, and thus are already implemented in our model. We expect our model to simulate the observed coordination between the main stem and tillers (Kirby *et al.*, 1985; Abichou *et al.*, 2018) as an emergent property.

The conditions leading to germination and the growth of the first three leaves are not taking into account in the model. The main reason is that the first three leaves are already developed in the seed (Williams, 1974), so that (i) their growth is fulfilled by seed reserves, (ii) we miss data to evaluate the reliability of our coordination rules for these leaves. The consequence is that our model is initialized at the emergence of leaf 4, when leaves 1 and 2 are already mature and leaf 3 is close to ligulation. Although the emergence of leaf 4 is an early vegetative stage, in favourable conditions, the faith of three primary tillers is already defined (the coleoptile tiller [Tc] and the tillers that emerged at the axils of leaf 1 [T1] and leaf 2 [T2]; Kirby *et al.*, 1985; Abichou *et al.*, 2013). Because the outgrowth of these tillers varies with growth conditions, simulating the growth of tillering wheat, from leaf 4 emergence, under contrasting conditions would imply to initialize our model with the state of these three primary tillers. Therefore, simulating the emergence of Tc, T1 and T2 as a result of contrasting growth conditions requires to implement the mechanisms of germination and the growth of the first three leaves in our model.

Even though our aim was to simulate mechanistically the construction of leaf and plant traits, we have not proposed process-based formalism for all leaf traits yet:

- First, lamina maximum width and specific structural masses have been defined empirically as a function of sucrose concentration in the *hz* averaged over an arbitrarily chosen period of time. We used empirical functions because of: (i) the lack of knowledge about the mechanisms that lead to the construction of these variables, (ii) the lack of empirical data that link these variables with internal plant parameters instead of environmental conditions, which prevent from a calibration of response laws. It was therefore preferred to keep simple relationships, which only intend to be preliminary proposals. Because they are empirical

function of the sucrose concentration in the *hz*, the time interval during which the sucrose concentration is considered had to be arbitrarily defined. We chose to consider the average sucrose concentration in the *hz* during two phyllochrons prior to leaf emergence. A short time interval was chosen so that lamina width and SSD of the leaves that were already initiated at model initialization (up to leaf 10), were not directly dependent on initial values. However, sucrose concentration in the *phloem* presented large variations in a two-phyllochron time (Figure 2.3) leading to an oscillating behaviour of our model (Figure 2.6; Figure 2.7). We expect that a mechanistic implementation of the processes that build leaf width and thickness would not lead to such oscillating behaviour as it would integrate the trophic status of the plant for a longer period of time.

- Second, the model set lamina width and SSM at leaf emergence. This choice was constrained by (i) the fact that we consider a homogeneous lamina, (ii) the 3D-architectural model ADEL-Wheat which draws the growing leaf from a predefined mature shape defined by length and width, meaning that provisional estimates of final leaf dimensions are needed as soon as the leaf tip emerges out of the pseudostem. However, Fricke (2002) demonstrated that cutting laminae 1 and 2 of barley when leaf 3 was half-emerged led to a leaf 3 that was thinner with 15% higher SLA at ligulation. The determination of lamina width and SSM as soon as leaf emergence therefore appears to be too early.

So far, in our model, the plant has been considered as a shoot system with a highly detailed 3D-architecture connected to a non-architectured and homogeneous root system that is solely described by its structural mass and metabolite contents. An explicit root architecture would open-up new possibilities to account for the interaction between the root structure and the whole-plant functioning. In particular, it would enable to have specific root processes, such as N uptake and root exudation, to be spatially distributed. N uptake is higher in fine, ephemeral roots compared to thick, older roots in various plant species (Lazof *et al.*, 1992; Pregitzer *et al.*, 2002; McCormack *et al.*, 2015). For this reason, the modulation of root architecture has been considered a key factor in plants' ability to adapt to contrasting soil N availability (Pregitzer et al. 2002). Similarly, root exudation has been shown to be maximal near root apices and to decrease in more mature parts of the roots (Jones *et al.*, 2009). In addition, a better quantification of C investments in the root structure is needed in order to refine the simulated C budget of the plant. Finally, because of C and N fluxes between the shoot and the root, accounting for an explicit root architecture would ultimately lead to a better understanding of the whole-plant functioning. To reach such comprehensive view, several root processes remain to be understood and formalised. An explicit root architecture implies to describe root elongation, root branching, initiation of tillers' roots and root senescence. In particular, it is still unclear when the onset of root senescence occurs during ontogeny (Deacon and Mitchell, 1985; Pagès *et al.*, 2004), how root senescence varies with growth conditions, and what are the consequences on the root functions. Furthermore, spatialising function-related processes along the roots (*e.g.* N uptake, exudation and C partitioning) requires a large amount of experimental evidence about how each metabolite's concentration and flux may actually evolve depending on the root type, root topological order, or root age. Eventually, we can hypothesise that reaching a similar level of complexity for the root system as for the aboveground parts will help to better simulate plant's adaptability to contrasting environments.

Acknowledgements

We gratefully acknowledge Alexandre Dehne-Garcia (UAR 1413 Ingenum) for his help in deloying CN-Wheat on the computing center. This work has been realized with the support of MESO@LR-Platform at the University of Montpellier.

List of Supplementary Data

Supplementary Data S2.1 – Details of the changes to CN-Wheat compared to Chapters 1 and 2

Changes related to leaf and root growth

Lamina maximum width, structural specific lamina mass

Preliminary simulations revealed that the model, as presented in Chapter 1, did not simulate a response of lamina maximum width and structural specific lamina mass (SSLM) to incident PAR for medium to high PAR values. The ratio between maximal width and final length of the lamina and the SSLM are defined at leaf *n* emergence (E_n) according to the mean sucrose concentration in the *hz* during the two phyllochrons preceding E_n (Table S1.1.1 Eqn. 7-8). For the present Chapter, we substituted the former linear (within bounds) formalism, by functions that vary on a wider range of concentrations (Figure S2.21) but that would let ~unchanged the results of the simulations in Chapter 3. The equations are given in Table S2.2 and parameter values are in Table S2.3.

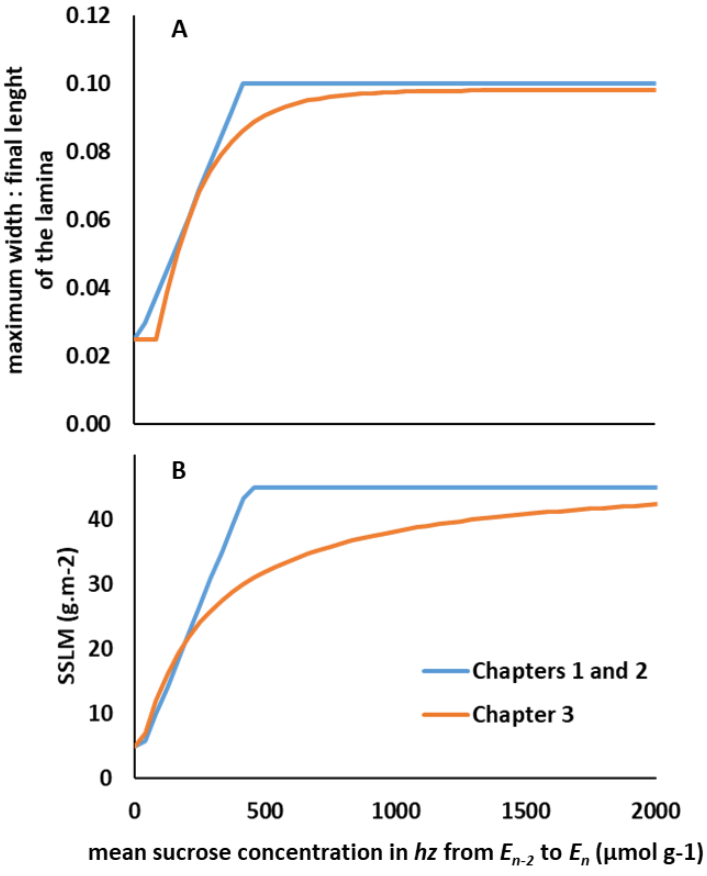

Figure S2.21 – Versions of the empirical functions defining leaf traits as a function of the mean sucrose concentration in the hidden part of the growing leaf (*hz*) during the two phyllochrons preceding leaf emergence. A: ratio of maximum lamina width to final lamina length. B: structural specific lamina mass (SSLM)

Maximum leaf length

Preliminary simulations revealed that the model, as presented in Chapter 1, resulted in values of final leaf length that increased continuously with phytomer rank, reaching length above 1m for upper leaves. By contrast, there is experimental evidence that leaf lengths reach a plateau for high phytomer ranks in perennial grass (Lestienne *et al.*, 2002) and the maximum leaf length usually observed for wheat is ~55 cm (Ljutovac, 2002; Abichou, 2016). We hypothesised that a limitation of leaf length might originate from an upper bound to the length of the elongation zone, which would reflect constraints that were not introduced in the model (*e.g.* hydraulic limitations). To reflect this idea of an upper bound to the length of the elongation zone, we introduced in our model a new parameter $L_{leaf,max}^{En-1}$ of maximum leaf length prior E_{n-1} *i.e.* during the meristematic growth phase of the leaf (Table S2.3).

Changes to simulate an indeterminate number of vegetative phytomers

A grass plant with floral transition presents strong gradients of leaf elongation dynamics and leaf dimensions with phytomer rank, which closely depend on final leaf number (Ljutovac, 2002; Abichou, 2016). Consequently, it is reasonable to assume that the time of floral transition of the shoot apical meristem shapes these gradients. In our model, some parameters are set per phytomer rank (ontogenic parameters) and were estimated in Chapter 1 based on field experiments in which wheat plants reached reproductive stage. As a result, when simulating no floral transition of the shoot apical meristem, we had to adapt the ontogenic parameters as detailed below. In addition, preventing floral transition was implemented in the model by setting to infinity the parameter $delay\_SAM\_transition$ (Table S1.1.3 Eqn. 1) , which triggers the onset of the rapid internode growth.

In the model, three types of parameters are ontogenic:

- the upper bound of leaf relative elongation rate ($RER_{leaf,n}^{max}$, Table S1.1.1 Eqn. 2) which regulates leaf elongation before leaf tip has emerged out of the pseudostem (before E_{n-1})
- the internode RER ($RER_{IN,n}$,Table S1.1.3 Eqn. 1) which defines the internode elongation before ligulation of leaf *n-1*
- the sheath:lamina ratio ($\mathrm{sheath:lamina}_{\mathrm{n}}$, Table S1.1.1 Eqn. 6a,b) which defines lamina and sheath lengths from leaf length

Both observed RER and $RER_{leaf,n}^{max}$ showed a strong decrease for the first leaves and reached a plateau for the uppermost leaves (Figure 1.7B). Although the pattern of these key ontogenic parameters might be affected by floral transition, we could not find information to define the pattern of $RER_{leaf,n}^{max}$ of a grass plant remaining vegetative. Thus, the leaves from phytomers 11 and above were set with same $RER_{leaf,n}^{max}$ *i.e.* that previously defined for leaf 11.

As for $RER_{leaf,n}^{max}$, the internodes from phytomers 11 and above were set with same $RER_{IN,n}$ as internode 11.

The sheath:lamina ratio is a function that depends on leaf rank. The parameters proposed in Chapter 1 leads to a pattern of sheath:lamina ratio that is typical of a wheat plant with 11 leaves at flowering, whereas

sheath:lamina ratio increases approximately linearly with leaf rank for vegetative ray-grass (Lestienne *et al.*, 2002). Thus, the sheath:lamina ratio was adapted as shown in Figure S2.22. The adapted parameters are given in Table S2.4.

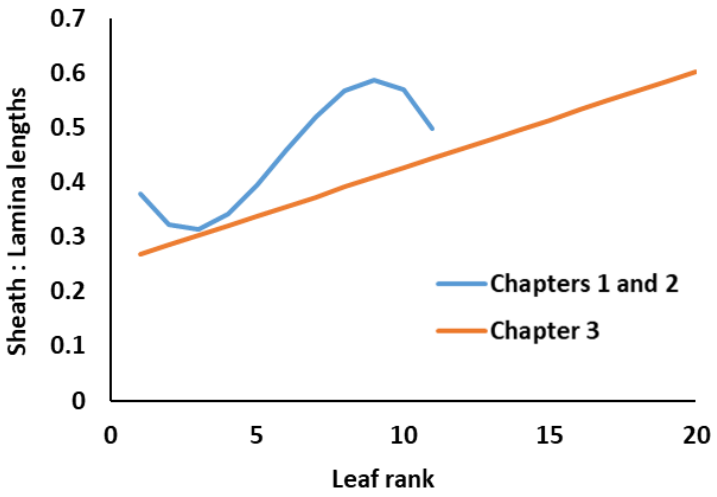

Figure S2.22 - Versions of the ratio of sheath length to lamina length as a function of the leaf rank

Root growth

The version of CN-Wheat presented in Chapter 1 considered a single root compartment, common to the main-stem and four tillers. The rate of root growth in structural dry mass depends on a fraction ($Gmax_{roots}^{C\ mstruct}$) of the root structural dry mass and is regulated by the sucrose concentration, mimicking that only a fraction of the root system can lengthen and ramify if sufficient sucrose. Since we simulate the growth of a monoculm plant in the present chapter, we used a lower value of $Gmax_{roots}^{C\ mstruct}$. The adapted parameter is given in Table S2.4.

Table S2.2 - New set of equations replacing those of Chapter 1.

New equation	Description	Unit	Equation number Chapter 1
$W_{lamina,n}^{max} = {}^{*}L_{lamina,n}^{max}(t_{E_n}) \times \max\left(\alpha_w - \frac{\beta_w}{\gamma_w} \times \left(1 - \exp(-\gamma_w \times \int_{t_{E_{n-2}}}^{t_{E_n}} [C_{hz,n}^{suc}](t))\right), WL_{min}\right)$	Maximum lamina width	m	TS1.1.1 Eqn 7
$SSLM_{lamina,n} = \frac{\alpha_{SSLM} \times \int_{t_{E_{n-2}}}^{t_{E_n}} [C_{hz,n}^{suc}](t)}{\beta_{SSLM} + \int_{t_{E_{n-2}}}^{t_{E_n}} [C_{hz,n}^{suc}](t)}$; $\in [SSLM_{min}, SSLM_{max}]$	Structural Specific Lamina Mass	g m^{-2}	TS1.1.1 Eqn 8

Table S2.3 - Values for new parameters.

Parameter	Description	Value	Unit
α_w	Parameter of maximum lamina width	-0.0203	dimensionless
β_w	Parameter of the maximum lamina width	-5.4458 × 10^{-5}	µmol C g^{-1}
γ_w	Parameter of the maximum lamina width	4.595 × 10^{-4}	g µmol C^{-1}
α_{SSLM}	Parameter of Structural Specific Lamina Mass	47.5	g m^{-2}
β_{SSLM}	Affinity of the Structural Specific Lamina Mass to sucrose concentration	2928	µmol C g^{-1}
$L_{leaf,max}^{En-1}$	Maximum leaf length before previous leaf emergence (E_{n-1})	0.006949	m

Table S2.4 - Values for parameters re-calibrated compared to Chapter 1.

Parameter	Description	New value	Value in Chapter 1	Unit	Equation number
$RER_{leaf,n}^{max}$	Maximum Relative Elongation Rate of leaves from leaf 5	Idem up to leaf 11, 1.56 x 10^{-6} if *n* > 11	[3.35, 2.25, 2.12, 1.99, 1.92, 1.65, 1.56] x 10^{-6}	s^{-1} at 12°C	TS1.1.1 Eqn 2 in Chapter 1
$RER_{IN,n}$	Maximum Relative Elongation Rate at 12°C of internodes from internode 3	Idem up to internode 11, 1.76 x 10^{-6} if *n* > 11	[2.4, 2.4, 2.4, 2.4, 2.16, 1.8, 1.91, 1.9, 1.76] x 10^{-6}	s^{-1} at 12°C	TS1.1.3 Eqn 1 in Chapter 1
a, b, c, d	Ontogenic parameters of the sheath to lamina length ratio	0, 0, 0.01763, 0.25	-0.002, 0.037, 0.153, 0.496	Dimensionless	TS1.1.1 Eqn 6b in Chapter 1
$Gmax_{roots}^{C\ mstruct}$.	Maximal rate of root structural growth at 20°C	0.03416	0.0854	µmol C s^{-1} g^{-1}	T4.1 in Barillot *et al.* (2016*a*)

Changes to the initial photosynthesis sub-model (Barillot et al.*, 2016a)*

Based on the results of preliminary simulations with the model as calibrated in Chapter 1, we adapted the initial photosynthesis sub-model by (i) implementing a feedback regulation by NSC concentration, (ii) changing the nitrogen dependences of the initial photosynthesis sub-model.

First, we remind general knowledge about photosynthesis, and we present key aspect aspects of the initial photosynthesis sub-model in order to contextualize the changes to the sub-model that are outlined afterwards. Then, we present the specifications of the new photosynthesis model equations. Finally, we present some results that illustrate the consequences of the changes made to the initial photosynthesis sub-model.

General knowledge about the photosynthesis process and its dependency on nitrogen

Photosynthesis is a two-phase process. During a light-dependent phase, photons are collected by the chlorophyll molecules that act as light antenna located in the membrane of the thylakoids, inside the chloroplasts. Chlorophyll molecules then lose electrons that are transported along a reaction chain that creates energy and redox potential. The second phase is light independent. The produced energy and redox potential are then used in the stroma of the chloroplast by the Calvin cycle. During the Calvin cycle, CO_2 is fixed by the RubisCo enzyme and incorporated to the ribulose bisphosphate (RuBP). Triose phosphate is produced and enters the carbohydrate metabolism, and RuBP is then regenerated for the next cycle of C fixation.

Many proteins are involved in the different steps of photosynthesis. Two main groups of photosynthetic proteins are generally considered: thylakoid proteins and soluble proteins in the chloroplast stroma. There are strong correlations between the specific content (per area) of photosynthetic proteins and the specific content of total foliar N (Evans, 1989). These correlations exist because photosynthetic proteins account for a large proportion of total foliar N: in wheat, thylakoid proteins and RubisCo together account for about 50 % of total foliar N (Evans, 1989). When parametrising the relationship between photosynthesis and foliar N, total foliar N per area (SLN, g N m^{-2}) is generally considered rather than proteins alone, because SLN is easier to measure, and different forms of foliar N are generally not distinguished in plant models.

Overview of the initial photosynthesis sub-model (Barillot* et al.*, 2016a)

The CN-Wheat model (Barillot *et al.*, 2016*a*) uses a biochemical model of photosynthesis (Farquhar *et al.*, 1980) and an empirical model of stomatal conductance (Ball *et al.*, 1987). The gross photosynthetic rate (A_g, µmol m^{-2} s^{-1}) is modelled as the minimum of three rates, each one representing a step of the photosynthesis: (i) the carboxylation rate of RubisCO (A_c) which depends on the amount and properties of RubisCo, (ii) the regeneration rate of RuBP (A_j) which depends on the electron transport rate, and (iii) the triose phosphate utilization rate (A_p) which reflects a limitation of the photosynthetic rate by the release of inorganic phosphate. Note that A_p does not depend explicitly on the triose phosphate utilization nor on the non-structural carbohydrate concentration, but on parameters related to the RubisCo and on temperature. Actually, A_p only limits the photosynthesis in cases of high atmospheric CO_2 concentration or low temperature (Caemmerer, 2000).

The N dependence of the photosynthesis and of the stomatal conductance is formalised by empirical relationships (mainly linear) between some parameters and the SLN. These relationships are derived from (Braune *et al.*, 2009; Evers *et al.*, 2010) and were established for wheat and barley following two steps: (1) models were calibrated for a wide range of SLN (0.5 - 2.8 g m^{-2}) and environmental conditions, and then (2) simple formalism was adjusted to the relationships between some parameters calibrated in step 1 and the SLN. In CN-Wheat, the SLN is calculated dynamically as a function of the four N pools of the organ, namely the structural N and the N metabolites, which in the model are nitrates, amino acids and proteins.

Overall strategy to implement a sugar-feedback regulation in the photosynthesis sub-model

A decrease in the photosynthetic efficiency has been widely reported in the literature (Dingkuhn *et al.*, 2020) in case of accumulation of NSC. The underlying mechanisms are not well understood, and two possible mechanisms of feedback regulation of the photosynthetic rate have been suggested (Paul and Pellny, 2003; Kasai, 2008; Burnett *et al.*, 2016; Yang *et al.*, 2016). Accumulation of NSC could limit the recycling of inorganic phosphate, which is used in many photosynthesis' reactions. In addition, sucrose or glucose have been shown to decrease photosynthetic gene expression. By limitation of the sink strength of spring wheat, Azcón-Bieto (1983) estimated that net CO_2 decreased by up to 10 µmol m^{-2} s^{-1}, which would represent 30 % of the assimilation rate in conditions free of sink limitation. It appears that feedback regulation of the photosynthesis is a key factor of C economy in case of accumulation of NSC (Azcón-Bieto, 1983; Huber and Huber, 1992; Iglesias *et al.*, 2002; Fabre *et al.*, 2019). Hence, we implemented a sugar-feedback regulation in the photosynthesis sub-model. This implementation relied on the empirical relation observed by Azcón-Bieto (1983) between NSC concentration and the decrease of the photosynthetic rate. This implementation is a first attempt to formalise the sugar-regulation of photosynthesis, which obviously requires further evaluation.

Overall strategy to change the nitrogen dependence of the initial photosynthesis sub-model

Although CN-Wheat distinguishes different forms of foliar N, the initial photosynthesis sub-model used the SLN in the N dependence function of the photosynthesis parameters. This implicitly assumed that there is a stable correlation between total N and photosynthetic proteins, and that the limitations occurs when usual correlations are not maintained. We identify that the classical correlations were not respected in at least the following two cases: for very thick leaves and for very high foliar N contents. In the case of thick leaves, structural N might account for a high SLN although this N is not involved in photosynthesis. A lower proportion of photosynthetic N is one hypothesis to explain the lower photosynthesis per unit area in thick leaves for a given value of SLN as revealed by several meta-analyses (Niinemets, 1999; Wright *et al.*, 2004). A lower proportion of photosynthetic N may also occur in cases of very high foliar N levels when photosynthetic organs may accumulate nitrates (Zhen and Leigh, 1990) and amino acids, which do not participate in the photosynthetic activity.

Since CN-Wheat distinguishes between the different forms of N, the initial photosynthesis sub-model was then modified by controlling its parameters by the N specific mass of the non-structural proteins ($Prot_S$, g $N.m^{-2}$) instead of by SLN.

Based on the forms of the SLN-dependent equations in the initial photosynthesis sub-model (Braune *et al.*, 2009; Evers *et al.*, 2010), we assumed that the photosynthetic variables actually depend on $Prot_S$. The relations between the photosynthetic variables and $Prot_S$ were defined so that the model would provide similar results as in (Braune *et al.*, 2009; Evers *et al.*, 2010). The general forms of the N dependence equations of the photosynthesis model were kept but the parameters of these equations were modified.

Specification for the sugar feedback regulation in the photosynthesis sub-model

Preliminary simulations with the initial photosynthesis sub-model under normal atmospheric CO_2 concentration and contrasting N fertilization rate, irradiance and density showed that A_c and A_p had, in all cases, similar values, and that the gross photosynthetic rate (A_g) was limited by A_j. In particular, in the cases of large NSC concentrations at high irradiance and low density, A_g was not limited by A_p.

We introduced a direct regulation of A_g by NSC concentration. This feedback regulation was formalised as an empirical factor $inhib_{Ag}$ derived from (Azcón-Bieto, 1983) that downgrades A_g as a function of the specific NSC concentration (NSC_S, µmol C.m^{-2}). The empirical factor $inhib_{Ag}$ was formalised as a Michaelis-Menten equation (Eqn. S2.4) calibrated on data from literature (Figure S2.23). The empirical factor $inhib_{Ag}$ regulates A_g as given in Eqn. S2.5.

$$inhib_{Ag} = \begin{cases} 0 & if\ NSC_S \leq NSC_{S,min} \\ \min\left(1, \dfrac{NSC_S - NSC_{S,min}}{K_{inhib} + NSC_S - NSC_{S,min}}\right) & if\ NSC_S > NSC_{S,min} \end{cases} \quad \text{Eqn. S2.4}$$

$$A_g = (1 - inhib_{Ag}) \times \min(A_c, A_j) \quad \text{Eqn. S2.5}$$

With this novel empirical sugar-regulation, A_g was downregulated under high CO_2 or low temperature due to high NSC_S. However, A_g was also limited by A_p under such conditions. Consequently, we removed A_p to prevent from an underestimation of photosynthesis at high CO_2 or low temperature.

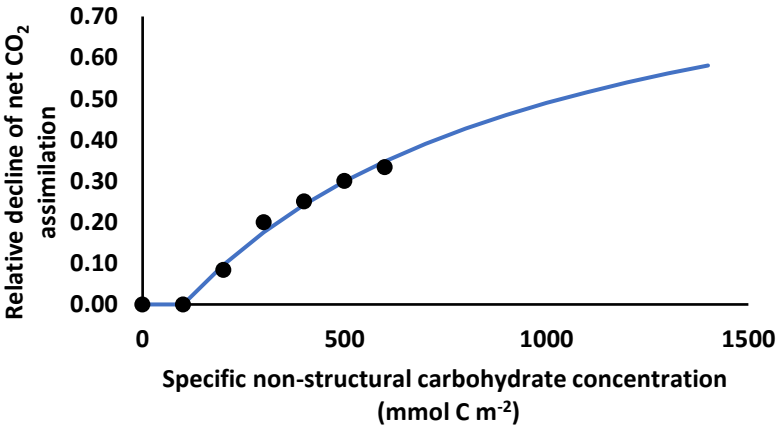

Figure S2.23 – Relative decline of the net CO_2 assimilation in relation to the specific non-structural carbohydrate concentration. Dots are experimental observations derived from (Azcón-Bieto, 1983). The curve is the factor $inhib_{Ag}$.

Specifications for the change of nitrogen dependence in the photosynthesis model

The initial photosynthesis sub-model (Barillot *et al.*, 2016*a*) included three SLN dependent equations (Table S2.6) whose parameters are given in Table S2.7:

- An affine function which is zero for a minimum theoretical SLN value (SLN_{min}). This function is implemented for the following potential rates (collectively referred to as P_{25} for parameter acclimatized at 25°C): the maximum carboxylation rate of RubisCO (V_{cmax}), the maximum electron transport rate (J_{max}), the maximum rate of triose phosphate utilization (TPU), the mitochondrial respiration rate that continues in the dark (R_{dark}) (Table S2.6, S1.15)
- A strictly positive affine function for the parameter *α* which is a parameter of the electron transport rate (Table S2.6, S1.16)
- A polynomial function for the parameter *m* which is a parameter of the stomatal conductance (Table S2.6, S1.17)

For each type of formalism, our modification are listed below (Table S2.8 and Table S2.9).

Dependence of P_{25} (*V_{cmax}*, *J_{max}*, *TPU* and *R_{dark}*) to $Prot_S$

Affine functions of P_{25} with SLN including a constant coefficient SLN_{min} (Table S2.6, S1.15) were replaced by affine functions of $Prot_S$ with no constant (Table S2.8, T3.1). Thus, the constant coefficient SLN_{min} was removed and the slope S'^{P25}_{ProtS} was estimated from the literature and from simulation results. The underlying arguments are presented below.

SLN_{min} is around 0.2 g m^{-2}, in the range of 0.118 to 0.229 g m^{-2} for all P_{25} parameters.

We estimated that SLN_{min} is of the order of the mass of structural specific nitrogen of a wheat leaf blade grown under conventional conditions considering a structural specific mass of 40 g m^{-2} (Rawson *et al.*, 1987; Barillot *et al.*, 2016*b*) with 0.5 % of structural nitrogen (Martre *et al.*, 2006; Bertheloot, 2009; Barillot *et al.*, 2016*b*).

The specific mass of non-structural nitrogen ($SLN_{non\ struct}$) is the ratio of nitrogen mass of the metabolites (nitrates, amino acids and proteins) to lamina area, and can be estimated as:

$$SLN_{non\ struct} = SLN - SLN_{min} \qquad \text{Eqn. S2.6}$$

For laminae of wheat cultivated under contrasting nitrogen fertilization and temperature regimes, the ratio $SLN_{non\ struct} : Prot_S$ varies only within a narrow range (1.05 to 1.15) and is not correlated to $SLN_{non\ struct}$ (Figure S2.24). As a first approximation, it is therefore assumed that $Prot_S$ is proportional to $SLN_{non\ struct}$. The proportionality coefficient (Eqn. S2.7) was estimated from our simulations under conventional growing conditions for the Paris basin at the vegetative and post-flowering stages (Barillot *et al.*, 2016*b*) and is within the range observed in the literature (Figure S2.24).

$$SLN_{non\ struct} = 1.06 \times Prot_S \qquad \text{Eqn. S2.7}$$

From equations 1 and 2, equation S1.15 (Table S2.6) of the initial photosynthesis sub-model is replaced by equation T3.1 (Table S2.8).

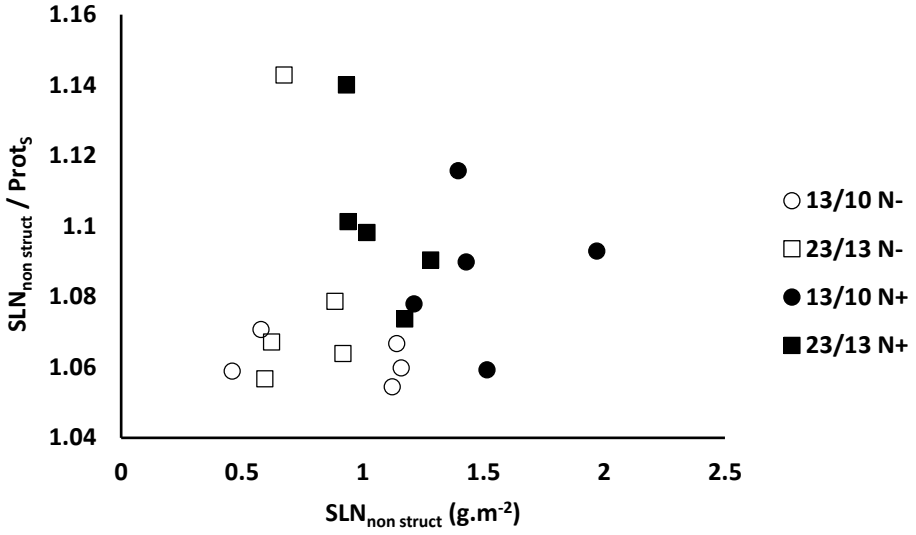

Figure S2.24 - Nitrogen specific mass of the non-structural proteins ($Prot_S$, g N.m-2) as a function of the specific mass of non-structural nitrogen ($SLN_{non\ struct}$) for lamina 3 of wheat cultivated under two nitrogen fertilizations and two temperature regimes (fives sampling dates per treatment). Data from (Lawlor et al., 1987). $Prot_S$ in the figure does not account for the insoluble proteins contrary to $Prot_S$ in the model.

Dependence of α to $Prot_S$

The above reasoning is applied to α. Equation S1.16 (Table S2.6) of the initial photosynthesis sub-model is replaced by equation T3.2 (Table S2.8).

Dependence of *m* to $Prot_S$

The experimental observations of the parameter *m* in function of SLN show a wide dispersion (+/- 50 %) around the adjusted polynomial relation (Braune *et al.*, 2009) which implies that (i) *m* is not well explained by SLN in the initial photosynthesis sub-model, (ii) we can substitute SLN by $SLN_{non\ struct}$ without modifying the precision of the polynomial adjustment. Thus, SLN was substituted with $SLN_{non\ struct}$ and the equation 2 was applied. Equation S1.16 (Table S2.6) of the initial photosynthesis sub-model is replaced by equation T3.3 (Table S2.8).

Simulation results before/after the changes to the initial photosynthesis sub-model

To illustrate the changes made to the photosynthesis sub-model, simulations were performed with three versions of the photosynthesis sub-model: (i) the initial sub-model (v.0), (ii) the version with dependencies to specific proteins instead of specific leaf nitrogen (v.1), (iii) the version used in the present chapter, which relies on dependencies to specific proteins and includes the sugar-feedback inhibition (v.2). The rest of the model was as described in the present chapter. Simulation conditions were chosen to create leaves with high NSC concentrations and high SLN.

In this set of simulation conditions, A_g was reduced by 10-20 % due to the switch to a $\mathrm{Prot_S}$ -dependency (v.1 *vs.* v.0), and by 20-50 % due to the implementation of a sugar-feedback regulation (v.2 *vs.* v.1, Figure S2.25 A). The NSC fraction of the shoot was also reduced (Figure S2.25 B). The radiation use efficiency, calculated from the total dry mass produced and the cumulative absorbed PAR of the simulation was 4.5 g M^{J-1} with v.0, it decreased to 3.8 g M^{J-1} with v.1 and to 2.4 g M^{J-1} with v.2.

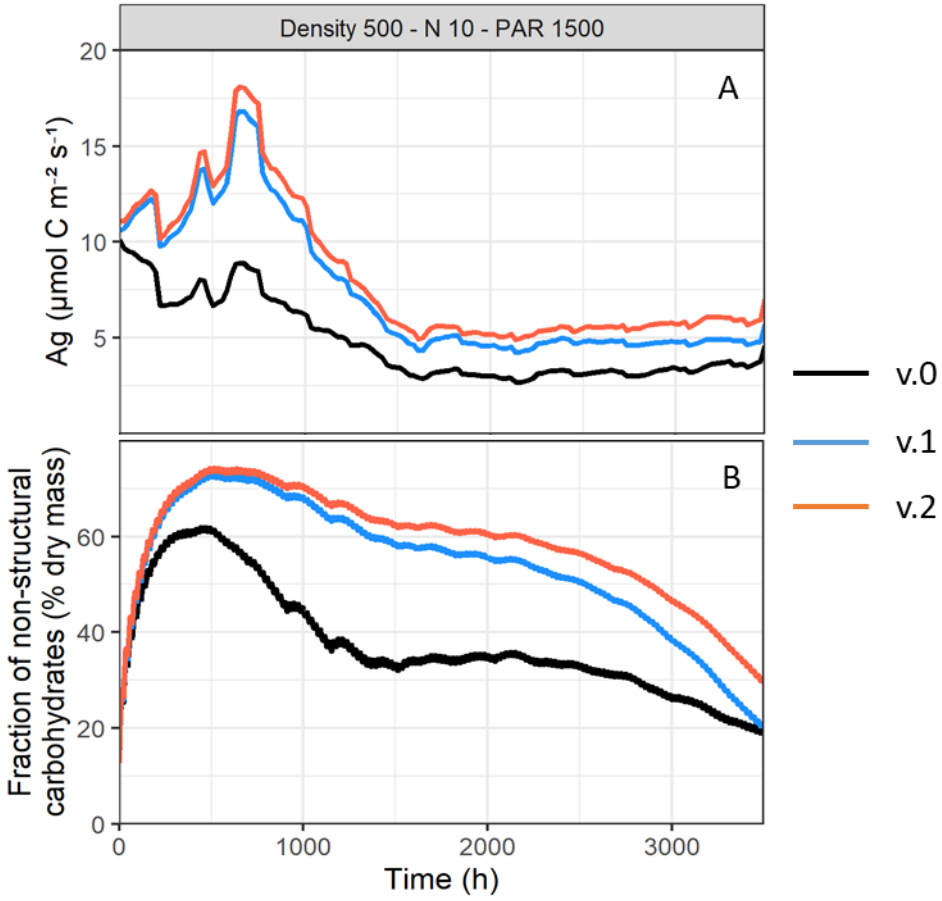

Figure S2.25 – Influences across time of the changes of the photosynthesis sub-model on: A) the gross photosynthetic rate (A_g), B) the fraction of non-structural carbohydrates (NSC) of the shoot dry mass. Each colour is one version of the photosynthesis sub-model: v.0) the initial version (orange), v.1) the version with dependencies to specific proteins instead of specific leaf nitrogen (blue), v.2) the version used in Chapter 3, which relies on dependencies to specific proteins and included the sugar-feedback inhibition (black). The growth conditions of the simulations were Density 500 x N 10 x PAR 1500 (see section 'Virtual experiments' for description).

Table S2.5 - Values for new parameters related to feedback regulation in the photosynthesis sub-model.

Parameter	Description	Value	Unit	Equation number
$NSC_{S,min}$	Value of *NSC* above which A_g is inhibited	100000	µmol C g^{-1}	Eqn. S2.4
K_{inhib}	Affinity coefficient of A_g inhibition to *NSC*	938000	µmol C g^{-1}	Eqn. S2.4

Table S2.6 - Equations related to nitrogen dependence in the initial photosynthesis sub-model (Barillot *et al.*, 2016*a*).

Equation	Description	Unit	Equation number in (Barillot *et al.*, 2016*a*)
$P_{25} = S_{SLN}^{P25} * (SLN - SLN_{min}^{P25})$	SLN dependence function of P_{25}; P_{25} stands for V_{cmax}, J_{max}, *TPU* or R_{dark} at 25°C	µmol m^{-2} s^{-1}	S1.15
$\alpha = S_{SLN}^{\alpha} * SLN + \beta$	SLN dependence function for α; α is a parameter of the electron transport rate	mol e^- mol^{-1} photon	S1.16
$m = \delta_1 * SLN^{\delta_2}$	SLN dependence function for *m*; *m* is a parameter of the stomatal conductance	Dimensionless	S1.17

Table S2.7 - Parameter values related to nitrogen dependence in the initial photosynthesis sub-model (Barillot *et al.*, 2016*a*).

Parameter	Description	Value	Unit	Equation number in (Barillot *et al.*, 2016*a*)
S_{SLN}^{Vcmax}	Slope of the regression between V_{cmax} and SLN at 25°C	84.965	µmol CO_2 g^{-1} N s^{-1}	S1.15
SLN_{min}^{Vcmax}	Minimum SLN value under which V_{cmax} equals 0	0.17	g m^{-2}	S1.15
S_{SLN}^{Jmax}	Slope of the regression between J_{max} and SLN at 25°C	117.6	µmol e^- g^{-1} N s^{-1}	S1.15
SLN_{min}^{Jmax}	Minimum SLN value under which J_{max} equals 0	0.17	g m^{-2}	S1.15
S_{SLN}^{TPU}	Slope of the regression between TPU and SLN at 25°C	9.25	µmol CO_2 g^{-1} N s^{-1}	S1.15
SLN_{min}^{Jmax}	Minimum SLN value under which TPU equals 0	0.229	g m^{-2}	S1.15
S_{SLN}^{Rdark}	Slope of the regression between R_{dark} and SLN at 25°C	0.493	µmol CO_2 g^{-1} N s^{-1}	S1.15
SLN_{min}^{Rdark}	Minimum SLN value under which R_{dark} equals 0	0.118	g m^{-2}	S1.15
S_{SLN}^{α}	Slope of the regression between α and SLN at 25°C	0.0413	mol e^- m^2 mol^{-1} photon g^{-1} N	S1.16
β	Theoretical value of α when SLN equals 0	0.2101	mol e^- mol^{-1} photon	S1.16
δ_1	Parameter of the SLN dependence of *m*	14.7	m^2 g^{-1}	S1.17
δ_2	Parameter of the SLN dependence of *m*	-0.548	Dimensionless	S1.17

Table S2.8 - New equations related to nitrogen dependence in the photosynthesis sub-model replacing those of (Barillot *et al.*, 2016*a*).

Equation	Description	Unit	Equation number
$P_{25} = S'^{P25}_{ProtS} * Prot_S$	SLN dependence function of P_{25}, with P_{25} being V_{cmax}, J_{max}, *TPU* and R_{dark} at 25°C	µmol m^{-2} s^{-1}	T3.1
$\alpha = S'^{\alpha}_{ProtS} * Prot_S + \beta'$	SLN dependence function for α which is a parameter of the electron transport rate	mol e^- mol^{-1} photon	T3.2
$m = \delta_1 * (\delta_3 \times Prot_S)^{\delta_2}$	SLN dependence function for m which is a parameter of the stomatal conductance	Dimensionless	T3.3

Table S2.9 - Values for new parameters related to nitrogen dependence in the photosynthesis sub-model.

Parameter	Description	Value	Unit	Equation number
S'^{Vcmax}_{ProtS}	Slope of the regression between V_{cmax} and $Prot_S$ at 25°C.	90.063	µmol CO_2 g^{-1} N s^{-1}	T3.1
S'^{Jmax}_{ProtS}	Slope of the regression between J_{max} and $Prot_S$ at 25°C.	124.656	µmol e^- g^{-1} N s^{-1}	T3.1
S'^{TPU}_{ProtS}	Slope of the regression between TPU and $Prot_S$ at 25°C.	9.805	µmol CO_2 g^{-1} N s^{-1}	T3.1
S'^{Rdark}_{ProtS}	Slope of the regression between R_{dark} and $Prot_S$ at 25°C.	0.523	µmol CO_2 g^{-1} N s^{-1}	T3.1
S'^{α}_{ProtS}	Slope of the regression between α and $Prot_S$ at 25°C.	0.044	mol e^- m^2 mol^{-1} photon g^{-1} N	T3.2
β'	Theoretical value of α when $Prot_S$ equals 0.	0.2184	mol e^- mol^{-1} photon	T3.2
δ_3	Proportionality factor between $Prot_S$ and $SLN_{non\ struct}$	1.06	Dimensionless	T3.3

Supplementary Data S2.2 – Additional results

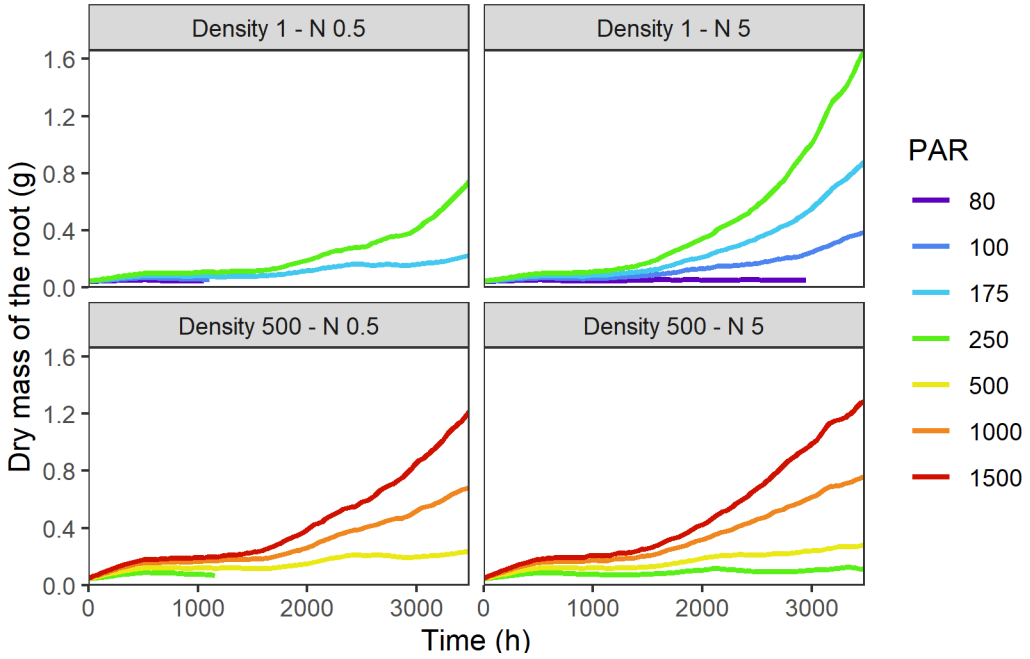

Figure S2.26 – Simulated dry mass of the roots across time. Each line is one simulation. Colours refer to the treatment of incident PAR (µmol m^{-2} s^{-1}, see right key). Each panel groups the light treatments for one planting density (plant m^{-2}) and one soil nitrogen concentration (g m-3, see panel title).

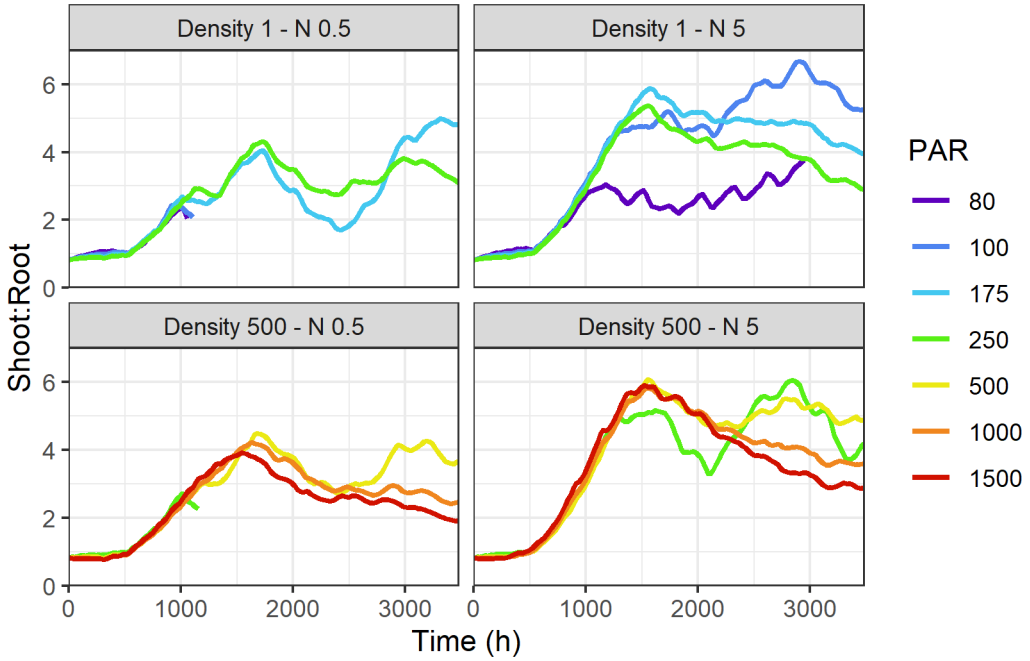

Figure S2.27 - Simulated shoot :root dry mass ratio across time. Each line is one simulation. Colours refer to the treatment of incident PAR (µmol m^{-2} s^{-1}, see right key). Each panel groups the light treatments for one planting density (plant m^{-2}) and one soil nitrogen concentration (g m-3, see panel title).

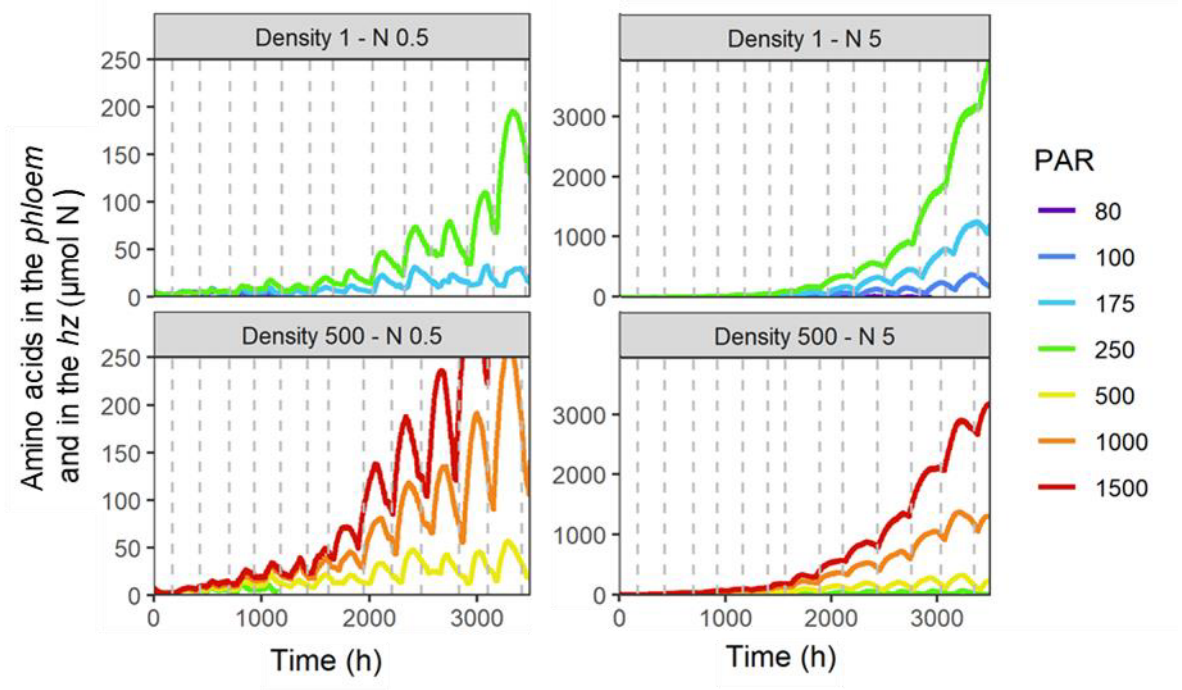

Figure S2.28 - Quantity of amino acids in the *phloem* and in the hidden part of the growing leaves (*hz*) across time. Each line is one simulation. Colours refer to the treatment of incident PAR (µmol m^{-2} s^{-1}, see right key). Each panel groups the light treatments for one planting density (plant m^{-2}) and one soil nitrogen concentration (g m^{-3}, see panel title). Dashed lines represent the averaged time of ligulation of the successive leaves for the combination of planting density and soil nitrogen concentration.

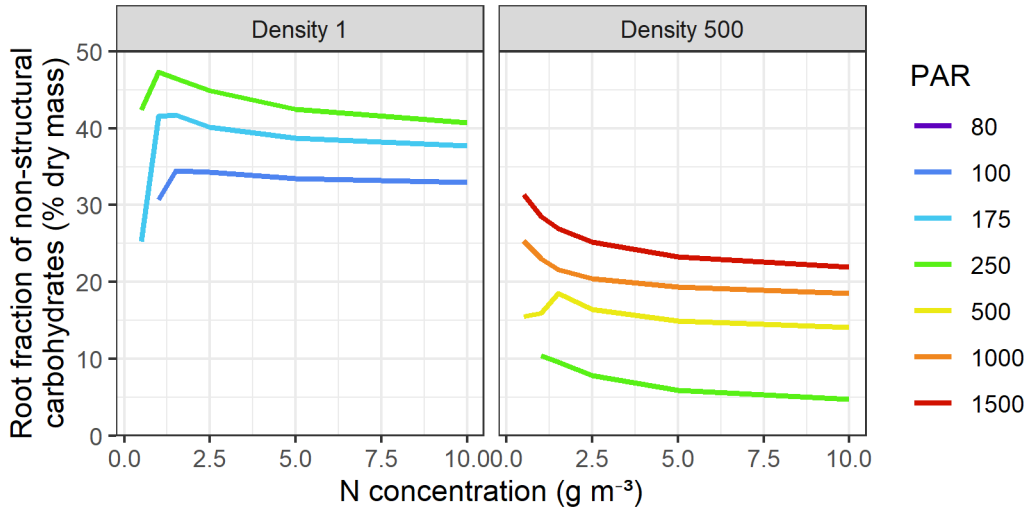

Figure S2.29 - Non-structural carbohydrates fraction of the root dry mass at the end of the simulation period (t=3500h). Colours refer to the treatment of incident PAR (µmol m^{-2} s^{-1}, see right key). Each panel is one planting density (plant m^{-2}, see panel title).

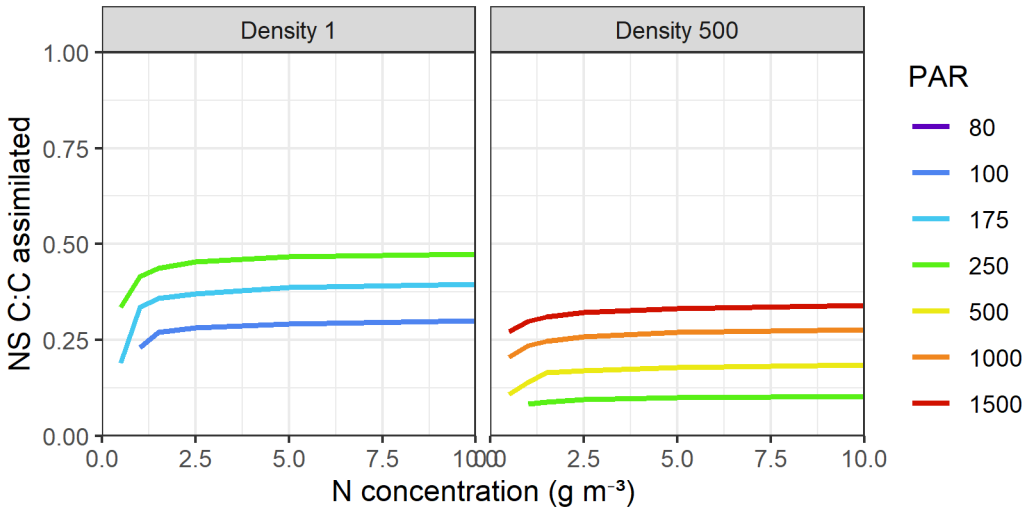

Figure S2.30 – Fraction of the carbon assimilated which is in non-structural compounds at the end of the simulation period (t=3500h). Colours refer to the treatment of incident PAR (µmol m^{-2} s^{-1}, see right key). Each panel is one planting density (plant m^{-2}, see panel title).

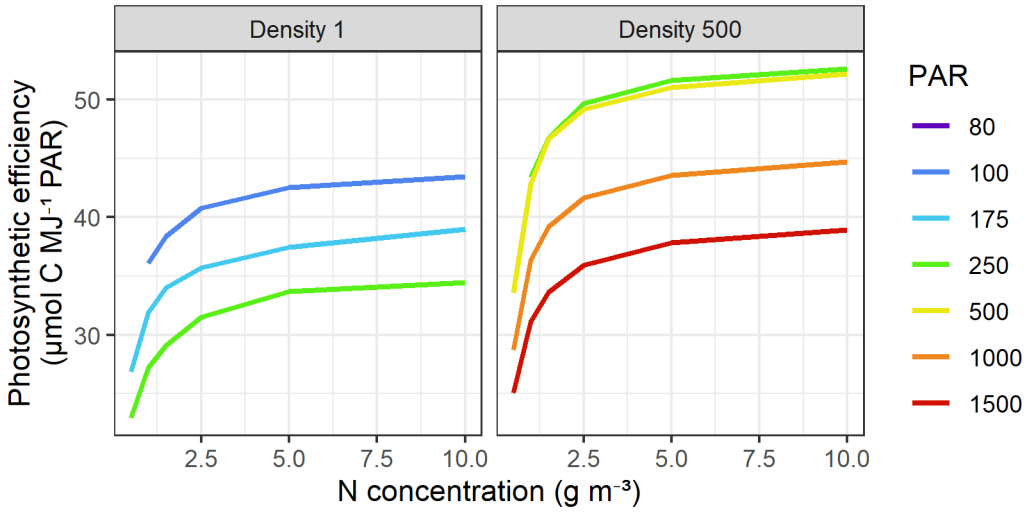

Figure S2.31 - Average photosynthetic efficiency over the simulation period (3500h). Colours refer to the treatment of incident PAR (µmol m^{-2} s^{-1}, see right key). Each panel is one planting density (plant m^{-2}, see panel title).

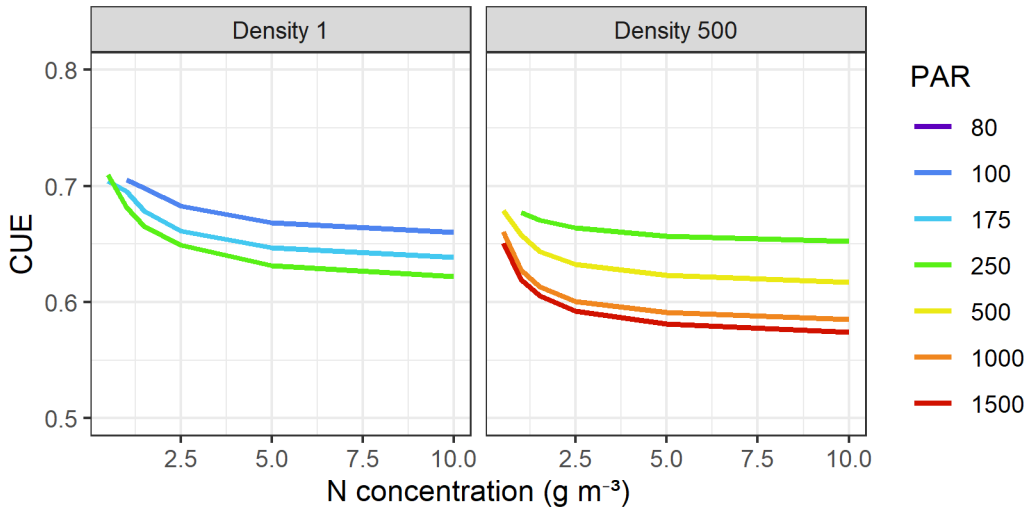

Figure S2.32 - Average carbon use efficiency (CUE) over the simulation period (3500h). CUE = 1 – fraction of assimilated C which is lost by respiration and exudation. Colours refer to the treatment of incident PAR (µmol m^{-2} s^{-1}, see right key). Each panel is one planting density (plant m^{-2}, see panel title).

Résumé du chapitre 2

La variabilité du climat et la diversité des pratiques agricoles exposent les plantes cultivées à une large gamme de conditions de croissance, qui s'étend encore dans le contexte du changement climatique. Au chapitre 1, nous avons présenté un nouveau FSPM de de morphogenèse de Poacées qui considère le fonctionnement de la plante entière et qui simule l'acquisition de traits comme propriétés résultant des interactions entre la morphogenèse, les facteurs environnementaux et les activités source-puits au sein de la plante. Nous avons montré qu'un tel modèle permettait de simuler, comme propriétés émergentes, les caractéristiques observées à différentes échelles (organe, plante, peuplement), dans des conditions de croissance usuelles au champ. L'objectif du chapitre 2 était d'évaluer la capacité du modèle à simuler la réponse des plantes à des conditions de croissance contrastées en lumière et en azote.

Deux expérimentations virtuelles ont été réalisées. La première est un ensemble de simulations dans des conditions contrastées de densité de plante, de rayonnement et de fertilisation azotée. La seconde correspond à des simulations avec différents états initiaux de plante, dans plusieurs conditions de croissance. Ces deux expérimentations virtuelles ont conduit à certaines adaptations du modèle par rapport à la version présentée chapitre 1. Les simulations ont été comparées au comportement du blé tel que rapporté par la littérature.

Nous avons montré qu'une même calibration du modèle permettait de simuler de façon réaliste la plasticité phénotypique des dimensions, du phyllochrone, du SLA, des compositions d'organes, de la répartition de la biomasse au sein de la plante et de la RUE. Ce chapitre démontre que des règles définies à une échelle locale permettent de simuler, comme propriété émergente, les schémas d'organisation et de composition de la plante, leur cinétique et leurs réponses des conditions de croissance contrastées en lumière et en azote. De plus, nous avons monté que le modèle simule la propagation d'une déformation précoce, ouvrant la voie à la simulation des conséquences d'un stress précoce sur le développement ultérieur de la plante.

Chapter 3 - Experimental work

3.1 - Introduction

In the context of climate change and new farming practices, models are useful tools for anticipating the response of plants to novel growth conditions. Because current models are limited in their ability to simulate phenotypic plasticity due to empirical formalism, we developed CN-Wheat, a new Functional Structural Plant Model (FSPM) that simulates wheat growth according to local carbon (C) and nitrogen (N) availability (Barillot *et al.*, 2016*a*,*b*; Gauthier *et al.*, 2020). CN-Wheat considers an explicit shoot architecture and a root system. The plant is represented as a collection of compartments, which have a structural mass (cellular structures that cannot be recycled at tissue death), mobile (nitrates, amino acids, sucrose) and storage metabolites (fructans, starch, proteins). In particular, the growing leaf is represented by two compartments: a hidden part, which is located inside the pseudostem, and actually encompasses a wide diversity of tissues, and a compartment made of the exposed mature tissues. The model also considers a common pool of mobile metabolites that mimics the role of the phloem. The main biological processes are represented for each compartment and are regulated at a local scale by the exogenous (temperature, light) and endogenous (concentrations of C and N metabolite) environments of the compartment. In addition, coordination rules between successive leaves set the timing of leaf growth and create dependencies between leaves.

In the previous chapter of this thesis, CN-Wheat was used to simulate the plasticity of wheat in response to various growth conditions (planting density, light, N) and to contrasting initial plant state. The aim of the latter was to investigate how early stresses on seedlings can further alter plant growth after the stress was removed. Studying the propagation of stresses over time is useful for a better understanding of how plants integrate the effects of their environment. This is particularly the case for grasses as leaf elongation strongly depends on the length of the pseudostem that is made of mature sheaths (Volenec and Nelson, 1983; Wilson and Laidlaw, 1985; Casey *et al.*, 1999). Thus, any increase or decrease of leaf length due to a stress will affect the pseudostem length and therefore affect the following leaves as a delayed consequence of the same stress (Durand *et al.*, 1999; Louarn *et al.*, 2010). Moreover, C and N that are necessary for growth are supplied to the growth zone by exposed and photosynthetic leaves (Patrick, 1972; Felippe and Dale, 1973; Dale, 1985). It therefore appears that shoot morphogenesis does not respond only to current growth conditions but also to former conditions. As such, transient stresses can have a lasting effect on the trophic status of the plant and its architecture.

Information about plant composition lacks in the literature to calibrate some processes of the model, and to evaluate its ability to simulate the C and N economy of a wheat plant in contrasting conditions. Indeed, we still lack an evaluation of the ability of the model to simulate the distribution of C and N within the plant compartments, and between the C and N forms (structural mass, mobile metabolites, storage metabolites). Indeed, only few data are available on the dynamic of the biochemical composition within the plant compartments as defined in CN-Wheat, during the vegetative stages. Moreover, simulating an accurate

composition in the hidden part of the growing leaf is crucial to CN-Wheat because it drives leaf elongation rate and key leaf traits such as leaf maximal width and specific structural mass. Literature reported gradients of composition along the growing leaf (Schnyder and Nelson, 1987; Gastal and Nelson, 1994), but we did not find compositional data about the hidden part of the growing leaf as a whole. Finally, CN-Wheat must account accurately for the gains and losses of C and N during plant growth, which includes C and N losses at tissue death. Models usually consider that N mass represents a constant fraction (~0.5 %) of the dry mass of the senesced tissues (Martre *et al.*, 2006; Drouet and Pagès, 2007; Martre and Dambreville, 2018). However, only scarce data are available in the literature regarding the N fraction of the senesced tissues (Aerts, 1996; Franklin and Ågren, 2002), and experiments on various species reported higher N fraction of the senesced laminae with higher N fertilization (Hunt, 1983; Killingbeck, 1996; Wright and Westoby, 2003; Li *et al.*, 2020). Thus, more data are needed to better account for the N losses at tissue death.

The aims of this chapter are to (i) characterise the propagation of an early stress on the growth of wheat plants, (ii) gather information about plant composition, in particular, the dynamic of composition of several compartments of CN-Wheat across the vegetative stages, the dynamic of composition of the hidden part of the growing leaf during leaf growth, and the N fraction of the senesced laminae. For these purposes, an experiment was conducted outdoors on wheat plants submitted to early shading. After the shade was removed at the emergence of leaf 4 outside the pseudostem, we measured the dynamics of plant growth and biochemical composition of the main compartments considered in CN-Wheat, including mature leaves, roots and hidden parts of the growing leaves. Finally, we discussed the ability of CN-Wheat to simulate the delayed impact of early stress and the dynamics of composition within the plant, and we showed how we used some of these results for the developing our leaf growth sub-model.

3.2 - Material and methods

The design and growth conditions of the experiment have been adapted to the specificity of CN-Wheat in order to facilitate the comparison of the results with the simulations. First, because the current version of CN-Wheat does not account for the underlying processes of tillering, plants were grown with low N fertilization and at high-density to limit tiller emergence. We chose not to use monoculm varieties as they may show an unstable behaviour (J. Le Gouis, personal communication).

Second, we anticipated that the root mass has a strong impact on our model of leaf growth because roots modulate N uptake and represent a sink that strongly affects metabolites allocation within the plant. Therefore, our experiment was conducted in hydroponic conditions, which facilitated the measure of root biomass and composition. Although hydroponic conditions lead to different root characteristics than field conditions, this cultivation technique allows acquiring information about the whole plant.

Finally, a shade net was applied in half of the plants from transplanting to the emergence of leaf 4, which corresponds to the stage of initialization of CN-Wheat simulations. Once the shade net was released, control and shaded treatments grew under the same conditions, thus mimicking the simulations presented in chapter 2.

Plant material and growth conditions

Seeds of *Triticum aestivum* (*cv.* Soissons) were selected according to their weight (range 44-51 mg). Seeds were soaked in water and left on humid tissue for germination at ambient temperature for two days. Then, 50 % of the seedlings were selected for similar coleoptile length and number of radicles. Selections on seed weight and then on seedlings were performed to improve the stand homogeneity regarding leaf dimensions, biomass and phenology. Seedlings were then transplanted at 2 cm depth in 1.5 L plastic tubes (PVC, 7.5 cm diameter, 40 cm height) filled up with expanded silica (Perlite). Seedlings were fully covered by 2 cm expanded silica. The bottom 10 cm of the tubes remained in water throughout the experiment and nutrients were supplied regularly to the water. Tubes were bound together in trays (40 x 60 cm, 18 cm height, Figure 3.1 A) to form stands and kept outdoors in Grignon, France.

The experiment comprised four treatments: two growth conditions (G1 and G2) crossed with presence/absence of early shading. G1 was a classical plant density (280 plants m^{-2}, 2 plants per tube) transplanted at mid-October 2017. G2 was a high density (560 plant m^{-2}, 4 plants per tube) transplanted at the end of October 2017. G1 and G2 were supplied in nutrients at the same dates with the same quantities so that the supply/plant was contrasted. Both G1 and G2 received low N fertilization compared to usual field conditions to limit tillering. Over the whole growth period, individual plants in G1 and G2 received respectively 87.5 and 52 mg N $plant^{-1}$ under the form of $Ca(NO_3)_2$, $4H_2O$ (*vs.* ~ 120 mg N $plant^{-1}$ in usual field conditions). However, because of heavy rains, trays have overflowed leading to uncontrolled loss of the nutritive solution until the end of January *i.e.* emergence of leaf 4 and leaf 5 for G1 and G2, respectively. Trays were then entirely flushed several times over winter, and water and nutritive solution renewed, so the quantity of N available per plant is unknown.

Early shading was obtained using a black shade net transmitting 80 % of the incident light, which was fixed at 1 m above the top of the canopy, and covered half of the area of G1 and G2 (Figure 3.1 B,C), thus, resulting in the four treatments G1s, G2s (shaded) and G1c, G2c (control). The treatments were spatially orientated to avoid a drop shadow of the net over the controls (Figure 3.1 C). The net was put at transplanting and was let in place until leaf 4 emerged from the pseudostem (in the following, E_n will refer to the emergence of leaf *n*). Before setting up the experiment, preliminary measurements revealed that the shade net did not modify the red:far red ratio but decreased the mean daily temperature by ~ 0.2 °C. Therefore, we anticipated a slower plant development for plants under the net. Thus, G1s and G2s, were transplanted slightly before G1c and G2c, so that E_4 would occur simultaneously in shaded and control; plants were transplanted on 17 and 19 October for G1s and G1c and 27 and 30 October for G2s and G2c.

Temperature and photosynthetically active radiation (PAR) were continuously monitored from transplanting to the complete ripening of all plants and averaged over 15 min intervals. Air temperature and soil temperature were recorded with small copper-constantan thermocouples: in each treatment, three thermocouples were fixed inside the canopy (between the soil surface and the top of the canopy) and three thermocouples were fixed at 2 cm depth below soil level. PAR was monitored at the top and at the bottom of the canopy with one and five hemispherical sensors of 32 mm^2 (Solems, Palaiseau, France, DPAR/OBE 80) per treatment, respectively.

The development of the plants was expressed in temperature-compensated time to consider the non-linear effect of temperature. Calculations were done as in Chapter 1 (Supplementary Protocol S1.2.1) using a reference temperature of 12°C and the temperature of the shoot apical meristem for each treatment. The latter was estimated as the temperature at 2 cm-depth when the shoot apical meristem was below the perlite surface and later as the air temperature.

The photothermal quotient (PTQ) is a biometeorological variable governing photosynthetic assimilate availability (Nix, 1976), which is usually computed as the ratio of daily cumulated radiation to daily cumulated thermal time. The PTQ (mol m^{-2} d^{-1} at 12°C) was calculated for the ten days prior to each sampling as the ratio of the cumulated PAR (mol m^{-2}) to the temperature-compensated time (s at 12°C, see above).

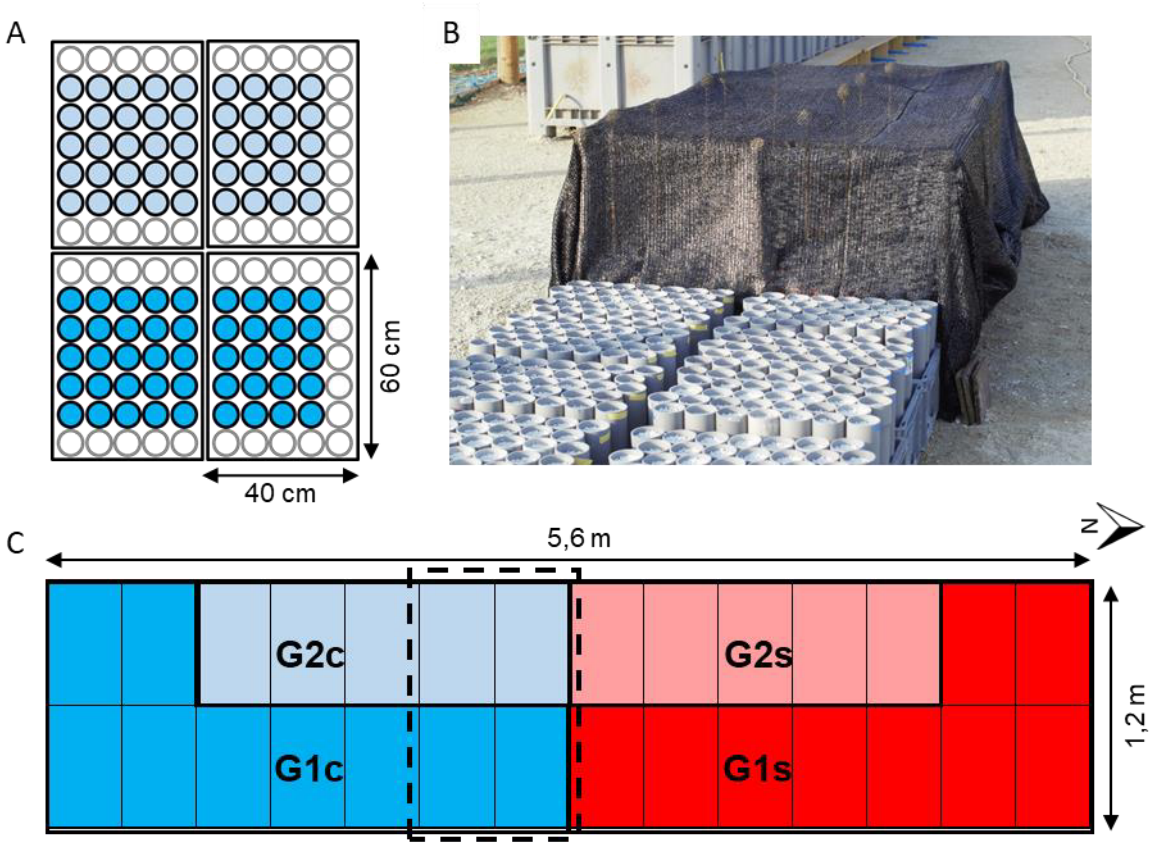

Figure 3.1 – Experimental setting. A: Scheme of the arrangement of the tubes inside four trays. Each circle is one tube containing two (G1, deep blue) or four plants (G2, light blue). Grey circles are border tubes of the treatment; plants inside the border tubes were not used for any measurements. B: Picture of the experimental setting before transplantation. Half of the trays were covered with a shade net fixed at 1 m above the top of the canopy. After plant transplanting, the bottom of the sides of the net were maintained away from the trays to allow air circulation below the net (not shown on the picture). C: Scheme of the arrangement of the trays. For growth conditions G1, control (c) and early shading (s) treatments were made each of nine trays. G2c and G2s were made each of five trays as the plant density was higher than G1. The dashed square indicates the trays that are detailed in panel B.

Phenology and development of reference plants

Continuous and non-destructive measurements of phenology and development were first conducted in a set of reference plants during the whole experiment duration. When plants had two visible leaves, the length of the laminae 1 and 2 were measured in 60 plants per treatment and their Haun's Stages (HS, Haun, 1973) were calculated. Ten reference plants per treatment were selected and tagged such that their leaf length and HS were close to the median calculated over the 60 plants. We checked along the experiment that the HS of the reference plants remained similar to the median of each treatment. Once to twice a week, from E_2 to flowering, the number (n) of ligulated leaves (leaves with exposed ligule), the length of the last ligulated lamina (L) and the exposed length (l) of the oldest growing lamina of the main stem (MS) and of all primary tillers of the reference plants was measured and the HS of each axis was calculated as in Eqn. S2.5.

$$HS = n + \frac{l}{L}$$ Eqn. 3.1

Internode elongation of reference plants was estimated using the collar displacement method described in Fournier and Andrieu (Fournier and Andrieu, 2000). The elevation of the leaf collar was measured twice a week. Knowing final sheath length, this method allowed monitoring internode elongation during their linear and declining rates.

Organ dimensions, biomass and biochemical composition

For each treatment, plants were sampled randomly at seven occasions and then median plants were selected to assess the dimensions of all shoot organs, and the mass and compositions of the shoot organs and of the root system.

Plant sampling procedure

Once the shade net was released at the E_4, tubes were collected at five occasions during the vegetative stages, at targeted plant stages E_4, E_5, E_6, E_7 and E_9 for G1, and at E_4, E_5, E_6, E_7 and E_8 for G2, and then at flowering and complete ripening. Samplings were performed close to solar noon. For each treatment, sampling dates were defined when these stages occurred for 80 % of the reference plants. On each sampling occasion of one treatment, tubes were randomly collected (except border tubes, Figure 3.1 A) to provide between 40 and 64 plants used for destructive measurements. The number of collected plants decreased with plant stage as plant dry mass increased, so sufficient plant tissue for compositional analyses was obtained on fewer plants. The reminding tubes of the treatment were grouped together in the trays to avoid creating gaps in the canopy. For each collected plant, HS of all axes were noted. Lamina length was measured using a ruler.

Based on the collected plants, median values were calculated for each treatment for (i) the length of the last ligulated lamina of the MS, (ii) the HS of the MS. According to these two criteria, plants were sorted into three groups for different usages described in detail in the next sections. Briefly:

- the ten plants closest to the median were used to assess the dimensions of all organs;
- between 33 and 9 plants close to the median were used to estimate organ mass and biochemical composition. This number of plants decreased during the growth period because the number of organs necessary to reach the minimum dry mass for biochemical analysis decreased as plants grew;
- the remaining plants, *i.e.* those departing the most from the median values of either HS or size, were rejected.

Organ dimensions

The length of all laminae, sheaths and internodes were measured using a ruler for organs longer than 1.5 cm, and using a video-microscope (x300) for shorter organs. Growing leaves were successively removed and all primordia longer than 50 µm were measured. The stage of development, length and diameter of the shoot apical meristem of the MS were also assessed. Mature organs were scanned and their surface was evaluated using an

image processing software (ImageJ). Maximal width of each mature lamina was also measured on the numerical images.

Dimensions of mature organs of each treatment were determined by pooling the measurements made at several sampling occasions on green mature organs. As a result, dimensions of the first organs of the MS were assessed on 15 to 45 plants, whereas dimensions of organs held on phytomers above 6 for G1 and 5 for G2 were assessed on 10 plants because they were measured on only one sampling occasion.

Organ mass and composition

The selected plants were randomly grouped into three groups used as three replicates of the measurements of organ mass and composition. Within each group, corresponding organs from all plants were collected and pooled together to get enough material for all analyses. So, each measurement of mass and composition refers to the mean of a pool of plants (between 3 and 11 plants).

On each sampling occasion E_n during the vegetative stages, leaf *n-2* was recently ligulated and leaf *n-1* had emerged and was growing; the exposed length of lamina *n* was at least 80 % of that lamina *n-2* (Figure 3.2). We considered the following samples:

- the lamina and sheath of the last ligulated leaf (each being one sample)
- the visible part and the hidden part of the next growing leaf (each being one sample)
- the hidden part of the emerging leaf, which was sometimes fully enclosed in the pseudostem
- any fully senesced lamina and sheath (each being one sample)
- the emerging tiller
- all older tillers
- the rest of the shoot (other leaves and crown) was grouped into one sample.

At flowering and complete ripening, all mature organs were sampled.

On each sampling occasion, three tubes were randomly chosen and all roots of the two (in G1) or four plants (in G2) inside each tube were gathered in one group (one replicate) for analysis.

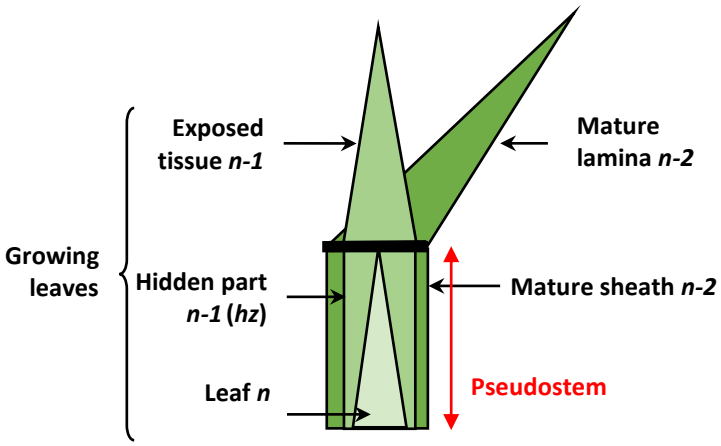

Figure 3.2 - Organs sampled during the vegetative stages, each time a leaf (here leaf *n*) emerges out of the pseudostem

No later than 2 h after harvest, samples were stored at -80°C to stop the metabolic alteration. Storage lasted between one week and two months, then samples were freeze-dried for one week (Christ, Osterode am Harz, Germany, Beta 1-8 LDplus), dry weighted and ground. Powder was used to (i) quantify total C and N content using the DUMAS method (Dumas, 1831) and (ii) dose contents of water-soluble carbohydrates (denoted "WSC" that are glucose, fructose, sucrose and fructans) using an enzymatic colorimetric method based on (Bergmeyer *et al.*, 1974) and detailed below.

Water-soluble carbohydrates quantification

WSC were extracted from 10 mg of tissue powder mixed with 750 µL of extraction solution made of 90 % (v/v) water / 10 % DiMethylSulfOxyde (Sigma Aldrich D4540) in 96-well storage plates (Thermo Scientific 421111 1 mL). Plates were smoothly rotated for 60 min at 5°C, and then centrifuged (Sigma 3K15) for 10 min at 4000 rpm. 400 µL were put at -20°C before WSC quantification.

Extracts were acid-hydrolysed to release glucose and fructose from sucrose and fructans, and then neutralized to perform the enzymatic colorimetric quantification that consisted in the quantification of NADH produced by the reaction of Glucose-6-Phosphate and the enzyme glucose-6-phosphatedehydrogenase in the presence of NAD. Details of the method are given below.

10 µL of extract were transferred into a PCR 96-well plate (4TITUDE, Wotton, UK, 4TI-0750) with 50 µL of hydrochloric acid (2 mol L^{-1}) for 15 min at 90°C. Then, 50 µL of sodium hydroxide were added, and 30 µL of the neutralized solution were transferred into standard 96-well microtiter plates (Geiner Bio-One, Les Ulis, France, 655101). For WSC quantification, the assay mixture consisted of 100 mM Tris(hydroxymethyl)aminomethane (AnalaR Normapur), 20 mM $MgSO_4$ (pH 7.4), 1 mM NAD+, 1 mM ATP, 0.2 units of yeast glucose-6-phosphate dehydrogenase (G6PDH), 0.4 units of hexokinase (HK) and 0.2 units of yeast phosphoglucose isomerase (PGI). Enzymes were purchased from Roche Diagnostics, Manheim, Germany (10127825001 for G6PDH and HK, 10127396001 for PGI). The reaction was allowed to proceed for 90 min at 20°C. NADH production was quantified by measuring absorbance at 340 nm in the microtiter plate, using a plate reader (Labsystem iEMS Reader MF,

Helsinki, Finland) and Thermo Scientific Ascent Software (Fisher Scientific, Göteborg, Sweden). Each plate was calibrated against a series of known concentrations of sucrose.

Calculation of variables related to plant mass and composition

The plant dry mass and shoot:root dry mass ratio

On each sampling occasion of a treatment, shoot dry mass and root dry mass were assessed on different plants, so we could not calculate the plant dry mass and the shoot:root dry mass ratio for individual plants nor for groups of plants. Because shoot and root dry masses were independently measured, we assumed that they followed independent Normal distributions. Consequently, the mean and variance of the plant dry mass were estimated as the sum of the means and variances of the shoot dry mass and the root dry mass, respectively. In addition, the mean shoot:root dry mass ratio was estimated as the ratio of the mean shoot dry mass to the mean root dry mass. However, the distributions of the shoot:root dry mass ratios could not be approximated by Normal distributions (Díaz-Francés and Rubio, 2013), so we could not estimate the standard deviation of the shoot:root dry mass ratio. As a result, no confidence interval around the means of shoot:root dry mass ratio could be calculated.

Structural mass and structural nitrogen mass

Structural mass and structural N mass of laminae, sheaths and internodes were estimated as the dry mass and N mass, respectively, of fully senesced organs *i.e.* after the end of the remobilisation of the mobile metabolites. Fully senesced leaves 1 were collected at the emergence of leaf 7, leaves 2 and 3 were collected at the emergence of leaf 9, leaves 4 to 7 were collected at flowering, leaves 8 were collected at flowering in G1 and at complete ripening in G2, and leaves 9 and above were collected at complete ripening. Fully senesced elongated internodes were collected at complete ripening.

Specific mass and composition of the ligulated laminae

As already explained, the composition of the laminae was assessed on a pool of laminae of the same phytomer from several plants. The length of each lamina in the pool was noted.

Leaf Mass per Area (LMA, g m^{-2}) and Specific Leaf Nitrogen (SLN, g m^{-2}) were computed for the ligulated laminae as follow. First, the total surface S of the sample was estimated from lamina length and a polynomial relation (degree 2) of lamina length and lamina surface per phytomer rank and per treatment. Then, LMA and SLN were calculated from the sample dry mass (DMg) and N mass (Ng): LMA = DMg/Sg; SLN = Ng/Sg.

Specific structural lamina mass (SSLM, g m^{-2}) was estimated from the dry mass of the sampled of senesced laminae (DMs): SSLM = DMs/Sg.

Nitrogen nutrition index

The Nitrogen Nutrition Index (NNI) of the treatments was computed from shoot dry mass and N content as proposed by Justes (1994). Note that experimental data underlying the N critical curve of Justes (1994) were

gathered from plants since mid-tillering stage. Therefore, the NNI calculation has not been demonstrated for such early stages.

Data analysis

To investigate the distribution of compositional variables within the plant, we compared the composition of the plant organs two-by-two. To do so, we adjusted linear relationships between the values of one compositional variable in one plant organ (x_1) *vs.* its values in another plant organ (x_2). Because both x_1 and x_2 are measurements (so random variables), we conducted model II regressions (also called 'least rectangle regression') in which x_1 and x_2 have equivalent roles (Legendre and Legendre, 2012). In contrast to the usual regression (based on the ordinary least squares estimation method), the slope of the model II regression $x_1 = f(x_2)$ is the reciprocal of the slope of the regression $x_2 = g(x_1)$.

All data analyses were conducted in R (R Core Team, 2020). The library "smatr" (Warton *et al.*, 2012) was used to perform model II regression with the standardised major axis estimation method.

3.3 - Results

First, we present the growth conditions and the plant development at the removal of the shade net. Second, we analyse the effect of the transient early shading on plant dynamics and final organ dimensions. Finally, we focus on three results about plant composition, which were common to all experimental treatments: the dynamics and gradients of WSC and N fraction within the plant during the vegetative stages, the N fraction of the senesced laminae, and the dynamic of N fraction of the growing leaf.

Growth conditions and plant state

On average, the daily incident PAR at the top of the canopy below the net was 18 % of that of the controls (Figure 3.3 A). Under the net, the incident PAR was between 0.2 and 3.5 mol m^{-2} compared to 1.3 – 19.4 mol m^{-2} for the controlsFigure 3.3. The absolute difference in incident PAR between treatments was higher at the beginning of the experiment and then slightly decreased during winter.

The time of emergence of the shoot apical meristem outside the soil was estimated as the date of the end of the elongation of the lower long internode, which was internode 9 for G1 treatments, and internode 8 for G2 treatments (Figure 3.9 G,H) and was 23 April for all treatments. Thus, the temperature of the shoot apical meristem of the MS was calculated in each treatment as the temperature at 2 cm-depth in the perlite before April 23, and the air temperature inside the canopy afterward (Figure 3.3 B). Figure 3.3 C shows the temperature-compensated time cumulated since transplanting, which is used to express plant development.

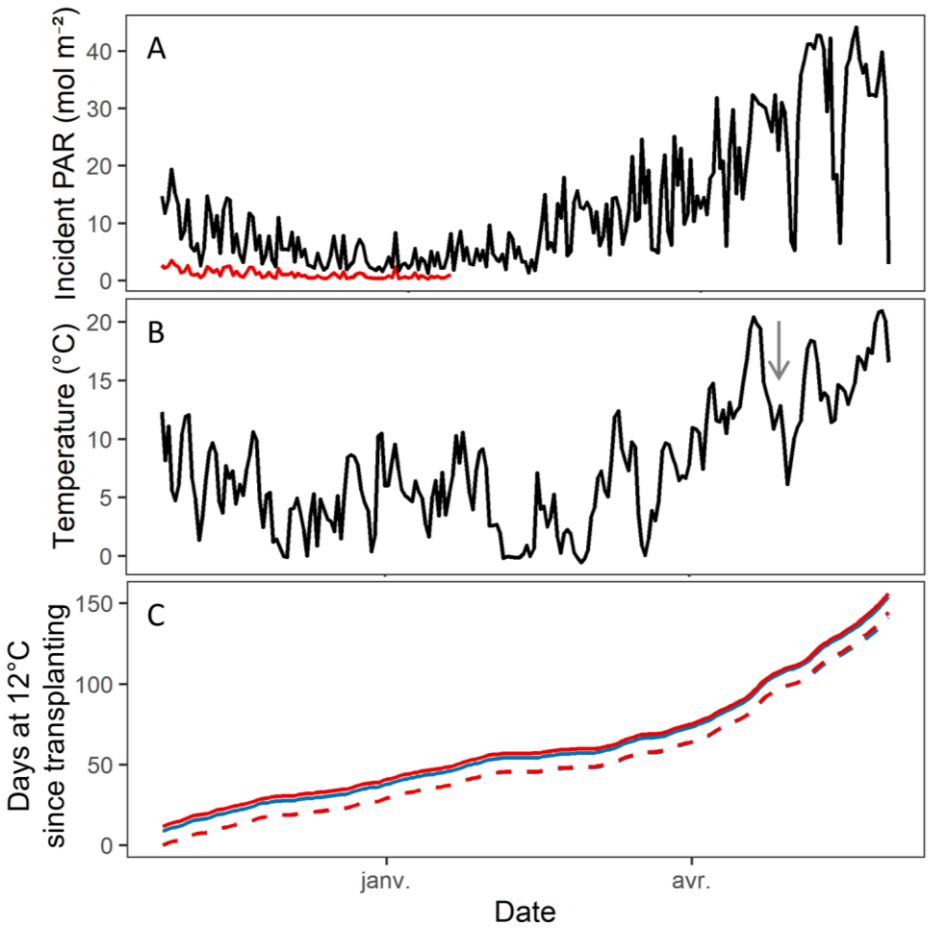

Figure 3.3 – Daily weather conditions of the experiment. A: Daily incident PAR at the top of the canopy (black) at the top of the canopy under the shade net (red). B: Daily averaged temperature close to the shoot apical meristem (SAM), which is the near-surface soil temperature before the date of emergence of the SAM from the soil (grey arrow) and daily averaged air temperature inside the canopy afterward. The time of emergence of the SAM outside the soil was nearly the same for all experimental treatments. C: Days equivalent at 12°C since transplanting for two growth conditions (solid curves: G1, dashed curves: G2), with (red) and without (blue) transient early shading of the stands

Uncontrolled nitrogen stress

All treatments had similar Nitrogen Nutrition Index (NNI) during the experiment, suggesting that G1 and G2 were exposed to similar soil N concentration. However, due to heavy rain in December and January, we were not able to measure the actual N concentration of the nutrient solution. NNI values were ~0.9 until beginning of March (E_7 for G1 and E_6 for G2) and then rapidly decreased, reaching ~0.5 in June at flowering (Figure 3.4). This result potentially indicates that N nutrition was near the optimum during the first half of the experiment, despite the low N fertilization Figure 3.4. However, the N dilution curve that we used to compute the NNI was taken from the literature (Justes *et al.*, 1994), based on experiments where plants were more developed than in our work, usually starting from mid-tillering stages. Thus, the present NNI values calculated for the period from December to ~March are uncertain and may have been over-estimated. As expected from the low N fertilization, tillering levels were very low as exemplified at E_7, when controls of G1 and G2 had on average 0.5 and 0.3 tillers (Table

3.1), respectively, compared to ~4 and ~2 to 3 primary tillers that would be expected without N stress for corresponding plant density. Thus, the weak tillering suggests that all treatments actually suffered from N stress early in the experiment as N deficiency limit tillering (Longnecker *et al.*, 1993). In addition, the final length of all organs (whole leaf, sheath, and internode) and the maximum lamina width of all phytomers were markedly lower than those reported by Ljutovac (2002) for field experiments conducted at the same location and with the same wheat genotype (Figure 3.9). Reduction in organ length (Robson and Parsons, 1978; Wilman and Mohamed, 1980; Volenec and Nelson, 1983; Fricke *et al.*, 1997) and lamina width (Wilman and Mohamed, 1980) are expected consequences of N deficiency. Therefore, our results strongly suggest that all treatments suffered from N stress during the entire experimental period, which was more intense than initially intended, but we cannot assess the magnitude of this stress during the first stages of growth.

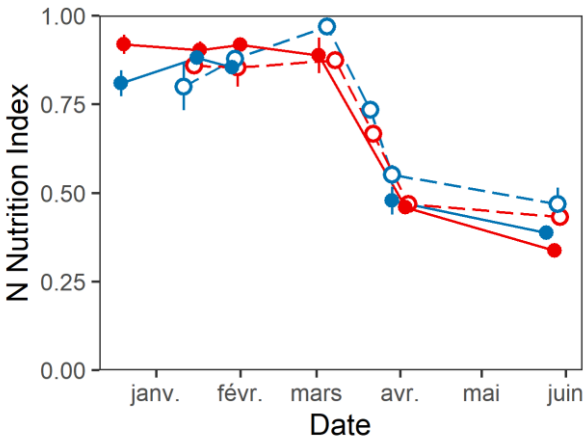

Figure 3.4 – Nitrogen nutrition index across time, for two growth conditions (closed symbols: G1, open symbols: G2), with (red) and without (blue) transient early shading of the stands. Vertical bars represent the 95 % confidence intervals. No vertical bar indicates that they are smaller than symbols.

Comparability of the experimental treatments

G1 treatments were transplanted ~15 calendar days before G2 treatments. G1 treatments reached the stage E_4 ~20 calendar days (~10 days at 12°C) before G2 treatments, and a marked delay in development was maintained between G1 and G2 treatments (15-30 calendar days, 5-10 days at 12°C), except for flowering that was reached at the end of May for all treatments (Table 3.1). The final number of leaves of the MS was 12 in G1 and 11 in G2 as expected from the later sowing date in G2 (Dornbusch *et al.*, 2011). Because of the delay between G1 and G2 development, comparisons between G1 and G2 must take into account that plants did not sense the same environment (weather and N fertilization) for the same phenological stage.

Plant development at the removal of the shade net

At the removal of the shade net (E_4), leaves 1 and 2 were mature, leaf 3 was exposed and was growing, leaf 4 was about to emerge, and ~ five younger leaves were growing (Figure 3.5). Indeed, 9.8 and 9.6 leaves were initiated (> 50 µm) for control and early shading treatment in G1, respectively, and 9.7 and 9.5 for control and early shading treatment in G2, respectively (Table 3.1). Figure 3.6 illustrates the state of the shoot apical meristem of a median plant of the control in G1 at E_4. In conclusion, the transient early shading affected leaves at a wide range of developmental stages.

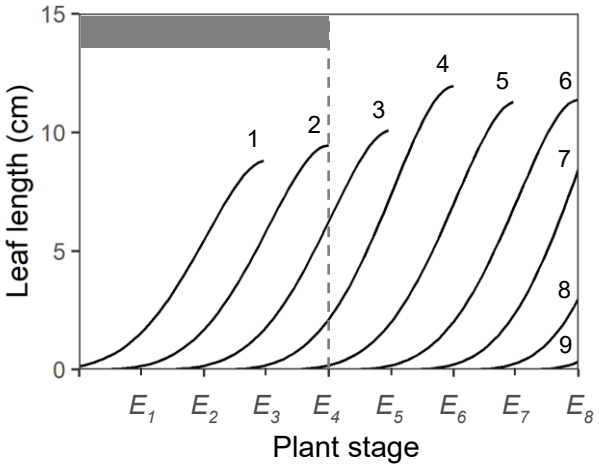

Figure 3.5 – Schematic representation of the elongation of successive leaves as a function of the plant stage. Final lengths are the observed leaf length of G2s, and leaf elongation kinetics are plotted according to the leaf elongation model in Chapter 1. The grey rectangle represents the time of application of the shade net, and the dashed line the time of shade net removal (E_4). All represented leaves (1 to 9) were initiated at E_4.

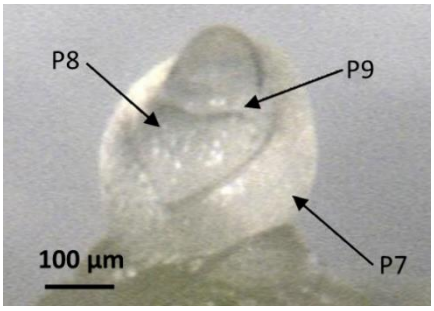

Figure 3.6 –Shoot apical meristem of the main stem of a median plant of the control treatment (no early shading) for the growth conditions G1, on 2017-12-19, which is close to the emergence of leaf 4 out of the pseudostem. The dome of the shoot apical meristem is surrounded by three primodia (P) that correspond to leaves 7 to 9.

Table 3.1 – State of the main stem of the median plant on each sampling occasion of the growth conditions G1 and G2. Targeted plant stage at sampling E_n refers to the emergence of leaf n outside the pseudostem as illustrated in Figure 3.2. $L_n : L_{pseudostem}$ is the ratio of the length of leaf n to the length of the pseudostem that is made of sheath n-2. Shoot apical meristem (SAM) state refers, first, to the mean number of primodia longer than 50 µm, and then to the morphological aspect of the SAM, which was noted only once after floral transition. DR: double ridge stage. The number of tillers is, before flowering, the mean number of tillers that were emerged and not fully senesced, and, at flowering, the number of tillers bearing an ear. No secondary tiller emerged.

G1

Targeted plant stage	Date		$L_n : L_{pseudostem}$		Haun's stage		SAM state		Number of tillers	
	Control	Early shading	Control	Early shading	Control	Early shading	Control	Early shading	Control	Early shading
E_4	2017-12-19	2017-12-20	1.6	0.8	2.8	2.7	9.8	9.6	0.0	0.0
E_5	2018-01-16	2018-01-17	2.2	1.5	4.3	3.8	12.1	12.4	0.9	0.3
E_6	2018-01-29	2018-02-01	1.5	1.8	5.0	4.8	14.6	15.3	0.5	0.9
E_7	2018-03-01	2018-03-02	1.5	1.0	5.8	5.6	18.0	16.7	0.5	0.5
E_8	-	-	-	-	-	-	-	-	-	-
E_9	2018-03-29	2018-04-03	1.4	1.1	7.7	7.5	-	-	0.4	0.7
Flowering	2018-05-25	2018-05-28	-	-	-	-	-	-	0.4	0.4

G2

Targeted plant stage	Date		$L_n : L_{pseudostem}$		Haun's stage		SAM state		Number of tillers	
	Control	Early shading	Control	Early shading	Control	Early shading	Control	Early shading	Control	Early shading
E_4	2018-01-11	2018-01-15	0.9	0.9	2.7	2.8	9.7	9.5	0.1	0.0
E_5	2018-01-30	2018-01-31	1.1	0.4	4.0	3.6	11.2	11.3	0.2	0.0
E_6	2018-03-05	2018-03-08	2.4	1.6	5.0	4.7	14.7	16.8	0.2	0.1
E_7	2018-03-21	2018-03-22	0.7	0.5	5.6	5.5	DR	DR	0.3	0.3
E_8	2018-03-29	2018-04-04	1.1	0.7	6.6	6.5	-	-	0.6	0.3
E_9	-	-	-	-	-	-	-	-	-	-
Flowering	2018-05-29	2018-05-30	-	-	-	-	-	-	0.3	0.0

Effects of the transient early shading on plant dynamics and on final organ dimensions

Phyllochron

The rate of emergence of leaves above 2 was approximatively constant during the experiment in all treatments; the first two leaves emerged more slowly, except for the control of G2 (Figure 3.7). Calculated over the entire growth period, the phyllochron was 8.7 and 8.8 days at 12°C for G1c and G1s, respectively, and 8.5 and 8.6 days at 12°C for G2c and G2s, respectively. Early shading did not have a significant effect on the phyllochron.

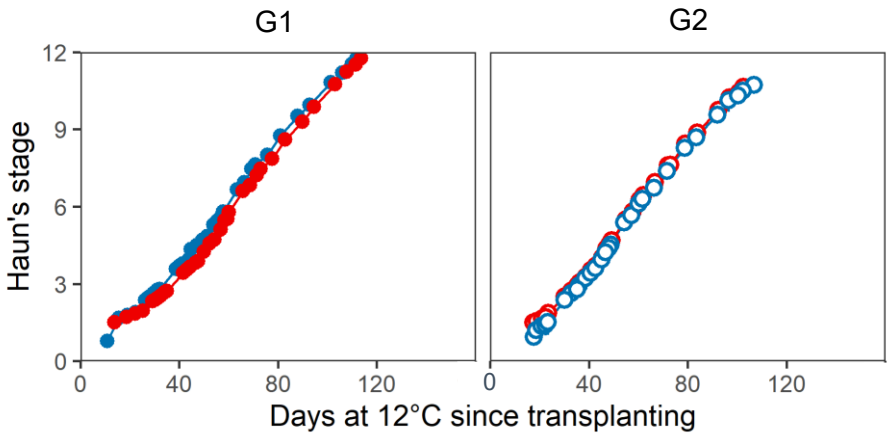

Figure 3.7 – Haun's stage of the main stem across time, for two sets of growth conditions (G1, G2), with (red) and without (blue, control) transient early shading of the stands.

Dynamic of dry mass and shoot:root ratio

The plant dry mass increased ~exponentially in all treatments (Figure 3.8 A). The plant dry mass was markedly higher in G1 than in G2 (i) at the beginning of the experiment (E_4, E_5), which is consistent with the higher incident PAR in G1 before E_4 due to earlier sowing date; and (ii) at flowering, which is consistent with the lower plant density in G1. However, there was not a clear ranking between G1 at G2 at intermediate sampling occasions. In G1, the plant dry mass was significantly lowered by the early shading at the first sampling date only (E_4). A lower dry mass in the early shading treatment was expected because of the strong decrease of incident PAR beneath the shade net. In contrast, contradictory results were observed in G2, as the early shading did not affect plant dry mass in the early stages and even resulted in an increased dry mass at E_6 and E_7. The mechanisms that led to higher plant dry mass in G2 after the removal of the shade net are unknown.

At the removal of the shade net (E_4), early shading had resulted in a higher shoot:root dry mass ratio than control (Figure 3.8 B) in both G1 and G2. A relative increase of the root compartment under low light conditions is also commonly reported in the literature (Hunt, 1975; Poorter *et al.*, 2012). Differences in shoot:root ratio between early shading treatment and control were larger for G1 than G2. Differences were maintained after removal of

the shade net until E_7 for G1, and at least until E_8 for G2, and differences were even amplified after removal of the shade net. We have not a clear explanation for the latter observation but our conclusion of a marked and durable impact of early shading on shoot:root ratio is supported by the consistency of the results over the two growth conditions and over independent samplings, even though no confidence interval could be calculated on values of shoot:root ratio.

Thus, while early shading had a short effect on the dry mass in G1 only, it had a lasting impact on the dry mass repartition.

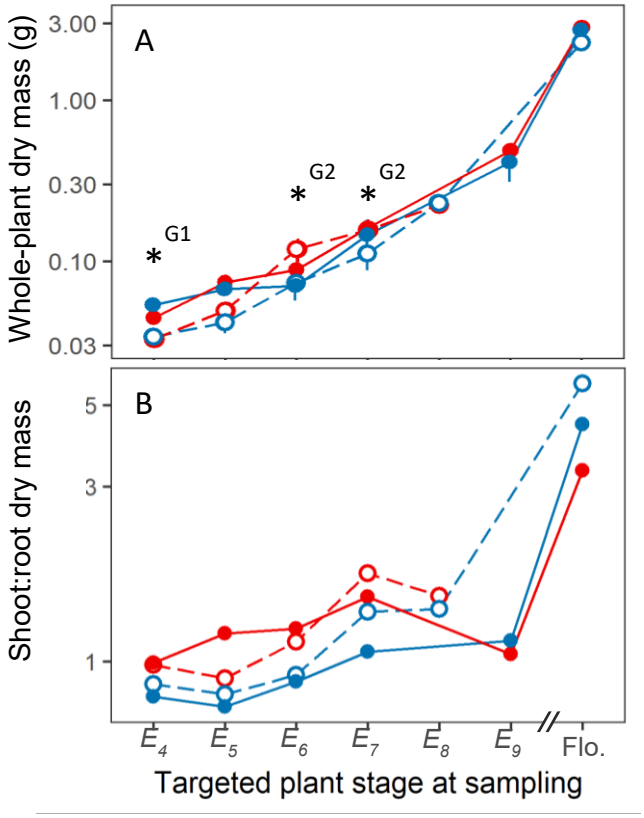

Figure 3.8 – Dynamic of the plant dry mass (A, log scale) and shoot:root dry mass ratio (B, log scale) across time, for two growth conditions (closed symbols: G1, open symbols: G2), with (red) and without (blue) transient early shading of the stands. No confidence intervals could be calculated for shoot:root ratio. Star above symbols indicates that the mean value of early shading treatment was significantly different from the mean value of the control for the growth condition indicated in exponent (Student's t-test, $p < 0.05$).

Final organ dimensions

Early shading had mainly an impact on leaf length of the lower phytomers, and had a small impact on lamina width and internode length (Figure 3.9), as detailed below.

Early shading resulted in longer leaves compared to control plants in both G1 and G2. The effect lasted until leaf 4 in G1 and leaf 6 in G2. Decomposing the effect of early shading between laminae and sheaths showed that sheaths 1 to 3 and laminae 2 to 4 were affected in G1, while sheaths 1 to 7 and laminae 2 to 7 were affected in G2 (Figure 3.9 A,B,C,D). An enhanced elongation of leaves is a widely reported characteristic of leaves that grow under low irradiance (Friend *et al.*, 1962; Allard *et al.*, 1991). Length difference between early shading treatment and control was maximum (both in absolute and relative terms) for leaves 2 and 3 for G1 and G2, respectively, and these leaves were ~50 % longer in the early shading treatments than in the controls. Early shading mostly affected the length of leaves 2 and 3, which grew almost fully below the shade net (Figure 3.5), and did not affect leaves 8 and 9 although they were initiated during the period of shading. Early shading slightly decreased the lamina width of all phytomers above 1 for G1 (only significant for laminae 2 and 11, Figure 3.9 E) but not for G2 ($p>0.1$, Figure 3.9 F).

In G2, internodes were slightly longer in the early shading treatment than in the control (Figure 3.9 H). However, the impact on total stem length was not statistically significant (53 and 54 cm for G1c and G1s, and 50.5 and 53 for G2c and G2s; $p>0.1$).

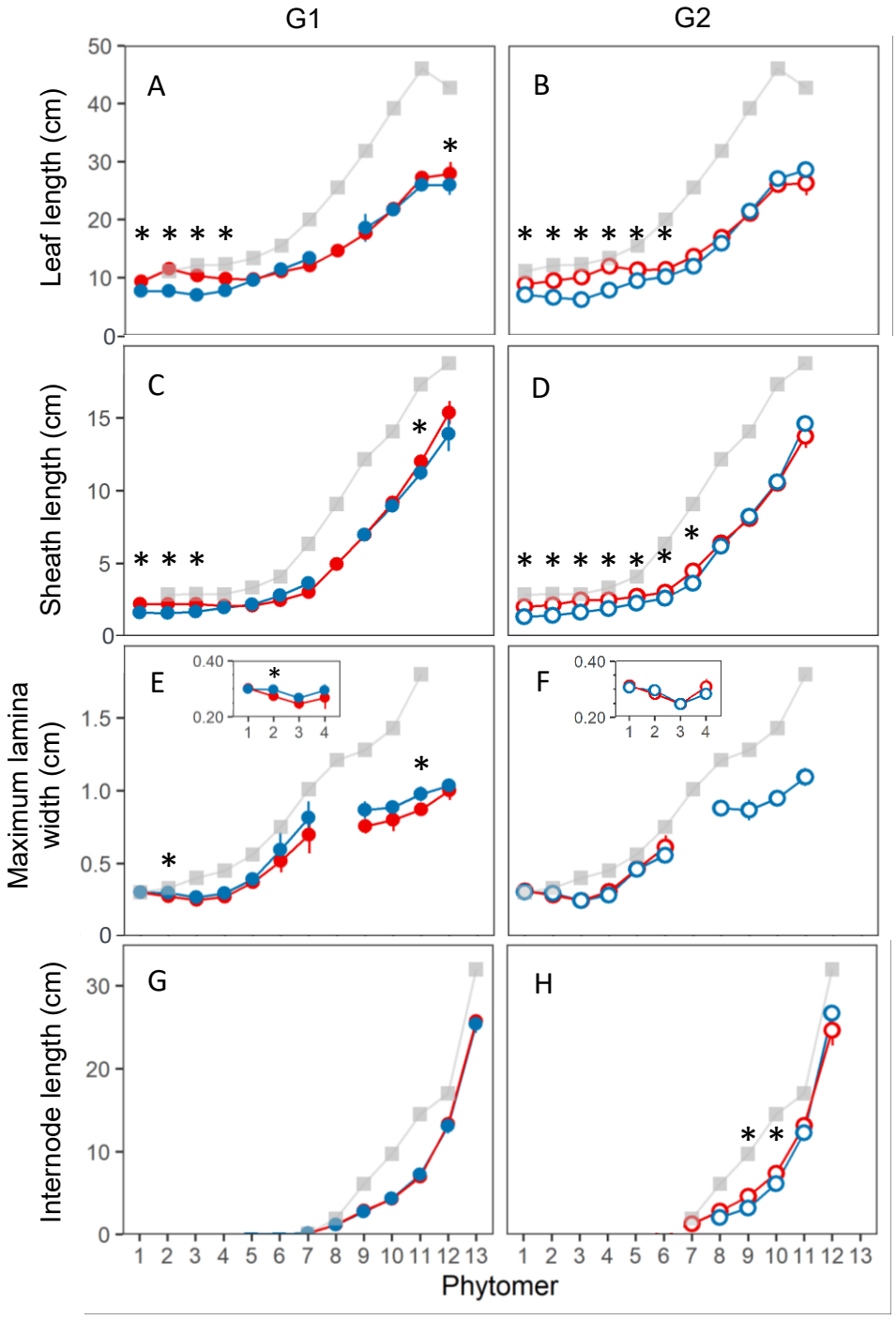

Figure 3.9 - Final dimensions of the phytomers of the main stem for two sets of growth conditions (G1, G2), with (red triangles) and without (blue circles) transient early shading of the stands. A, B: Final leaf length. C, D: Final sheath length. E, F: Maximum lamina width. Insets show the maximum width of the first four laminae. G, H: Final internode length and peduncle length. For comparison, grey squares are experimental data for the same wheat cultivar under usual field conditions on the same location (Ljutovac, 2002), where median plants had 11 leaves. Median plants in G1 had 12 leaves so data from (Ljutovac, 2002) were shifted to align flag leaves. Vertical bars represent the 95 % confidence intervals. No vertical bar indicates that they were smaller than symbols, except for width observations of (Ljutovac, 2002) for which no confidence interval was available. Star above symbols indicates that the mean dimension of early shading treatment was significantly different from the mean dimension of the control (Student's t-test, p-value < 0.05).

Mass per area and composition of the last ligulated leaf

Because LMA and SLN of one lamina decline after leaf ligulation (Rawson *et al.*, 1987; Bertheloot, 2009), we only present the mass and composition of successive laminae measured shortly after their ligulation (Figure 3.10).

At the removal of the shade net, the last ligulated lamina (lamina 2) had a lower LMA (Figure 3.10 A,B) and a higher N fraction (Figure 3.10 G,H), which resulted in a lower SLN (Figure 3.10 G,H) than the control in both growth conditions. Lower LMA and higher N fraction are expected impacts of shading (Friend *et al.*, 1962; Ellen and Van Oene, 1989; Poorter *et al.*, 2019). Early shading also resulted in lower LMA of lamina 3 (measured at E_5) but had no effect on LMA of upper laminae (4-7). The lower LMA of laminae 2 and 3 were not associated with a lower Specific Structural Mass (SSLM) (Figure 3.10 C,D; data available only for G1), so they likely resulted from the lower WSC fraction, but data are missing to confirm this hypothesis (Figure 3.10 E,F). Surprisingly, early shading had a marked positive impact (+50 %, $p<0.05$) on the SSLM of laminae 4 and above in G1 but the effect was not found in G2. So far, we have no clear interpretation for this observation.

From E_6 to E_9, the N fraction of the last ligulated lamina showed a marked negative while the WSC fraction increased in both growth conditions (Figure 3.10 E,F,G,H). Early shading resulted in lower N fraction of laminae 3-7, which was more marked in G2 ($p<0.05$ for lamina 6 only, Figure 3.10 H) than in G1 (not significant, Figure 3.10 G). In G2, early shading also resulted in higher WSC fraction of laminae 4-6 ($p<0.05$ for lamina 5 only, Figure 3.10 F). Even though differences of N fraction were significant only for one lamina, the trend was found for all laminae 3-7 in both growth conditions indicating that a lower N fraction is a long-term effect of early shading. This could be explained by the higher shoot:root ratio, which is expected to lower root N uptake (Figure 3.8 B). In contrast, we cannot conclude that the lower WSC fraction was a later impact of early shading as such effect existed only in G2.

SLN is the result of LMA and N fraction. Early shading resulted in systematically lower SLN of laminae 3-7 in G2 (Figure 3.10 J) but had a marked influence only on laminae 3-4 in G1 (Figure 3.10 I).

At flowering, no effect of early shading was observed for the LMA, SSLM and WSC fractions of the green laminae (10 to 12 in G1, 9 to 11 in G2; not shown). The only effect of early shading at flowering was slightly lower N fractions (~0.3 % of N fraction unit) of the green laminae, which was significant in G2 only ($p=0.03$, 0.06, 0.08). Lower N fractions in early shading treatment were associated with lower SLN but this effect of early shading was not significant in either growth conditions. Thus, at flowering, laminae had similar mass and composition, except that the lower N fraction of the laminae propagated from E_5 to flowering with a fading across time of the N fractions differences between early shading treatment and control.

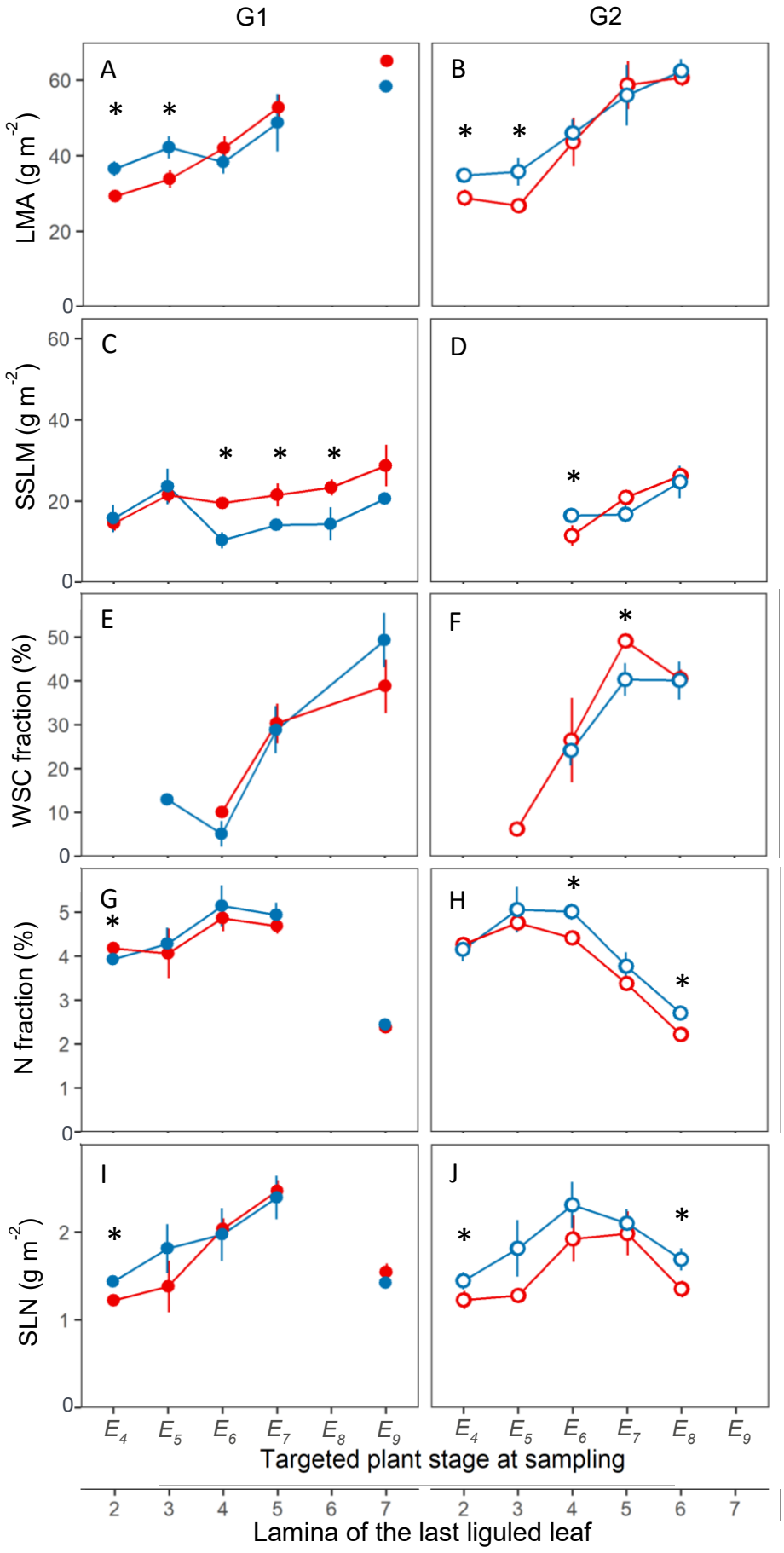

Figure 3.10 – Structure and composition of the last ligulated lamina on each sampling occasion for two sets of growth conditions (G1, G2), with (red) and without (blue) transient early shading of the stands. A, B: Leaf mass per area (LMA), C, D: specific structural lamina mass (SSLM, CD), E, F: Fraction of water-soluble carbohydrates (WSC) of the dry mass, G, H: N fraction of the dry mass, I, J: specific leaf nitrogen (SLN). Samplings were performed at the time of emergence of a leaf *n* out of the pseudostem, which is denoted E_n. Vertical bars represent the 95 % confidence intervals. No vertical bar indicates that they are smaller than symbols. Star above symbols indicates that the mean value of early shading treatment was significantly different from the mean value of the control (Student's t-test, $p < 0.05$).

To sum up, early shading treatments resulted, at E_4, in a higher shoot:root dry mass ratio, longer, slightly wider (in G1 only) and thinner leaves that had higher N fraction of the dry mass but lower SLN. After removal of the shade net, differences between early shading treatment and control lasted for several phyllochrons. The higher shoot:root ratio lasted up to ~E_8/E_9. Differences of leaf length propagated longer in G2 (up to sheath 7) than in G1 (up to lamina 4). Laminae had lower N fraction from E_5 to flowering. At flowering, early shading plants and controls only slightly differed by the N fractions of the laminae.

Plant composition

We now focus on three results regarding plant composition, which were common to all experimental treatments.

Dynamics and gradients of WSC and N fractions within the plant

On each sampling occasion, the N fraction and the fraction of WSC of the dry mass were measured in several plant organs, thus allowing studying their distribution within the plant at regular intervals during development. In this section, we used the mean values calculated for each treatment at each sampling occasion during the vegetative stages.

Relations between WSC fraction, N fraction and weather conditions

Figure 3.11 A presents the relation between the WSC fraction and the N fraction for different elements of the plants. For any sampled element of the shoot, the N fraction of the dry mass was negatively correlated to the WSC fraction (Pearson's correlation, r in [-0.85, -0.65], p in [2.8 10^{-4}, 2.5 10^{-2}]; Figure 3.11 A). The correlation was weaker for the roots (r=-0.51, p=0.01), and for the whole shoot (r=-0.5, p=0.2). The distributions of the data in Figure 3.11 A suggests that the WSC fraction in the range [20%-40%] decreased linearly with N fraction. Below 20%, variations in WSC were poorly related to the N fraction. Very few differences were observed between treatments.

We investigated if the weather could explain the dynamics of WSC fractions. We found that the WSC fraction was strongly correlated to the PTQ of the 10 days prior sampling (r in [0.80, 0.89], p in [1.6 10^{-7}, 1.6 10^{-4}]; Figure 3.11 B). Thus, the marked positive trend observed for the lamina of the last ligulated leaf from E_6 to E_9 (Figure 3.10 E,F) seems to originate from increasing assimilate availability across time, rather than to reflect differences due to phytomer position, and such trend was observed in all sampled elements of the plant.

The dynamics of compositional fractions were parallel within the plant.

We calculated correlations of the WSC fractions between each pair of plant elements and we found that they were always positive and significant (not shown). Similar results were obtained for paired correlations of the N fractions. To illustrate these correlations, we selected a subset representing the plant elements having the fewest missing values. Table 3.2 presents the relation of WSC fraction of each plant element with that of the roots (Table 3.2 A) and the relation between the N fraction of each plant element with that of the last ligulated lamina (lamina *n-2*, Table 3.2 B). The correlation coefficients were high (r in [0.83, 0.94] for the root WSC fraction *vs.* WSC fraction of other plant elements, r in [0.74, 0.97] for the N fraction of the lamina *n-2 vs.* N fraction of other elements; see Table 3.2). In addition, we looked at the relation between the composition of the hidden part of two successive

growing leaves, which are key compartments driving leaf growth in CN-Wheat. Figure 3.12 shows that the composition of these plant elements was highly correlated (r=0.96 and p = 5.3 10^{-10} for the WSC fractions, Figure 3.12 A; r=0.79 and p = 6.1 10^{-3} for the N fractions, Figure 3.12 B). There was no significant effect of the treatments in these relations (*e.g.* Figure 3.12). Thus, during the vegetative stages, the WSC fraction of all plant elements varied similarly across time, and the N fraction as well. This occurred in all treatments.

To illustrate the parallel dynamics of the WSC fractions within the plant, with focussed on plant elements for which the composition is rarely determined in the literature (Figure 3.13)÷ (i) the roots, (ii) the sheath of the last ligulated leaf (*n-2*) and (iii) the hidden part of the leaf that was emerging outside the pseudostem at the time of sampling (leaf *n*). As illustrated in Figure 3.13, the dynamic of WSC fraction was similar in these three plant elements in both G1 and G2. Immediately after the shade net was removed (at E_4), WSC fraction was lower in the early shading treatment than in the control for each plant element; these differences at E_4 were significant in both growth conditions and were an expected direct effect of shading. The difference was more marked in G1 than in G2, but we cannot conclude that it resulted from a higher impact of early shading in G1 because samplings were performed on different dates, so it could have resulted from different weather conditions. Surprisingly, early shading resulted in WSC fraction higher than in the control after the removal of the shade net (from E_5 to E_7 in G1, and from E_5 to E_8 in G2). This result was found for both growth conditions and was consistent over independent samplings made at several developmental stages of the plants.

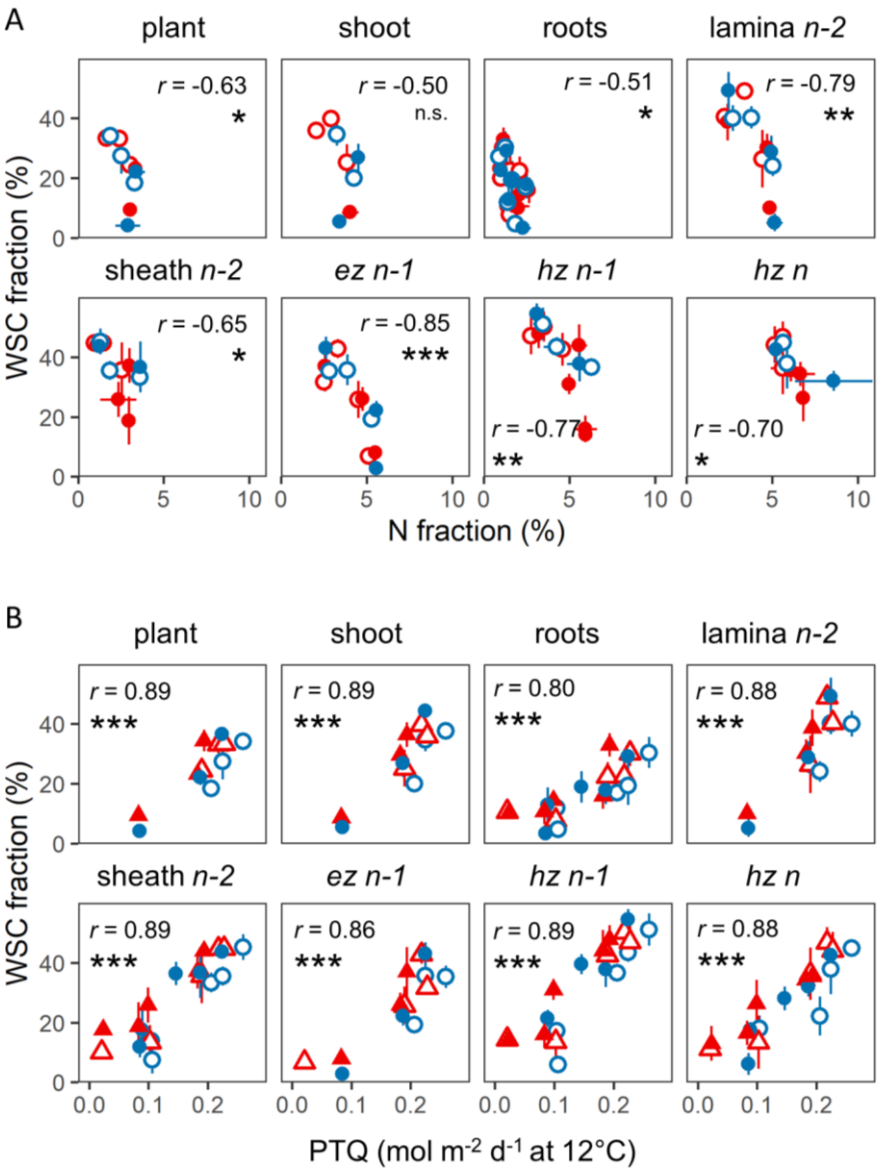

Figure 3.11 - Relation between the water-soluble carbohydrate (WSC) fraction and the N fraction of each plant part of the plant (A), and the photothermal quotient (PTQ) calculated for the 10 days prior the sampling (B). Each point is the mean of one treatment on one sampling occasion that was the emergence of leaf *n* outside the pseudostem (two or three replicates). Leaf *n-1* was emerged and growing, and leaf *n-2* was recently ligulated. *ez* and *hz* refer to the exposed and hidden parts of a growing leaf, respectively. Closed and open symbols represent the growth conditions G1 and G2, respectively; red and blue symbols represent the transient early shading treatments and the controls, respectively. *r* is the Pearson correlation coefficient, and the following row indicates the related p-value: ***: $p<0.001$, **: $0.001<p<0.01$, *: $0.01<p<0.1$, n.s.: $p>0.1$.

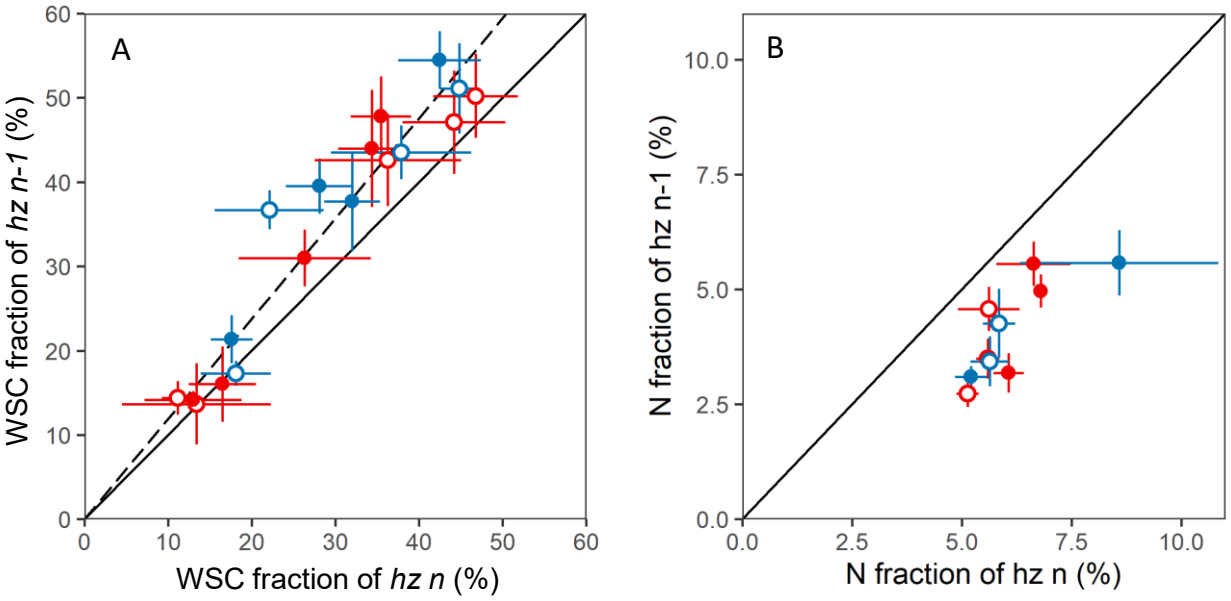

Figure 3.12 – Relation between the composition of the hidden part (*hz*) of two successive growing leaves. A: water-soluble carbohydrate (WSC) fractions, B: N fractions; leaf *n* has just emerged a few mm outside the pseudostem and leaf *n-1* is the growing leaf that emerged one phyllochron before. Each point is the mean of one treatment at one sampling occasion that was the emergence of leaf *n* outside the pseudostem (two or three replicates). Closed and open symbols represent the growth conditions G1 and G2, respectively; red and blue symbols represent the transient early shading treatments and the controls, respectively. Solid line is the first bisector. Dashed line in A is the standardized major axis estimation with null intercept (not plotted in B because intercept was significantly not null).

Is the composition of one plant element a good proxy of the composition of other elements?

We have seen above that the compositional fractions of different plant elements showed parallel variations across time. Does it mean that the composition measured in a given plant element - or at whole plant level - is a good proxy of the concentration in any part of the plant? To address this question, we investigated if the composition of one plant element (x_i) was proportional to the composition of other elements (x_j) *i.e.* if the relation between x_i and x_j could be expressed without intercept ($x_i = a_{ij}\, x_j$, with a_{ij} a parameter unique across time and growth conditions).

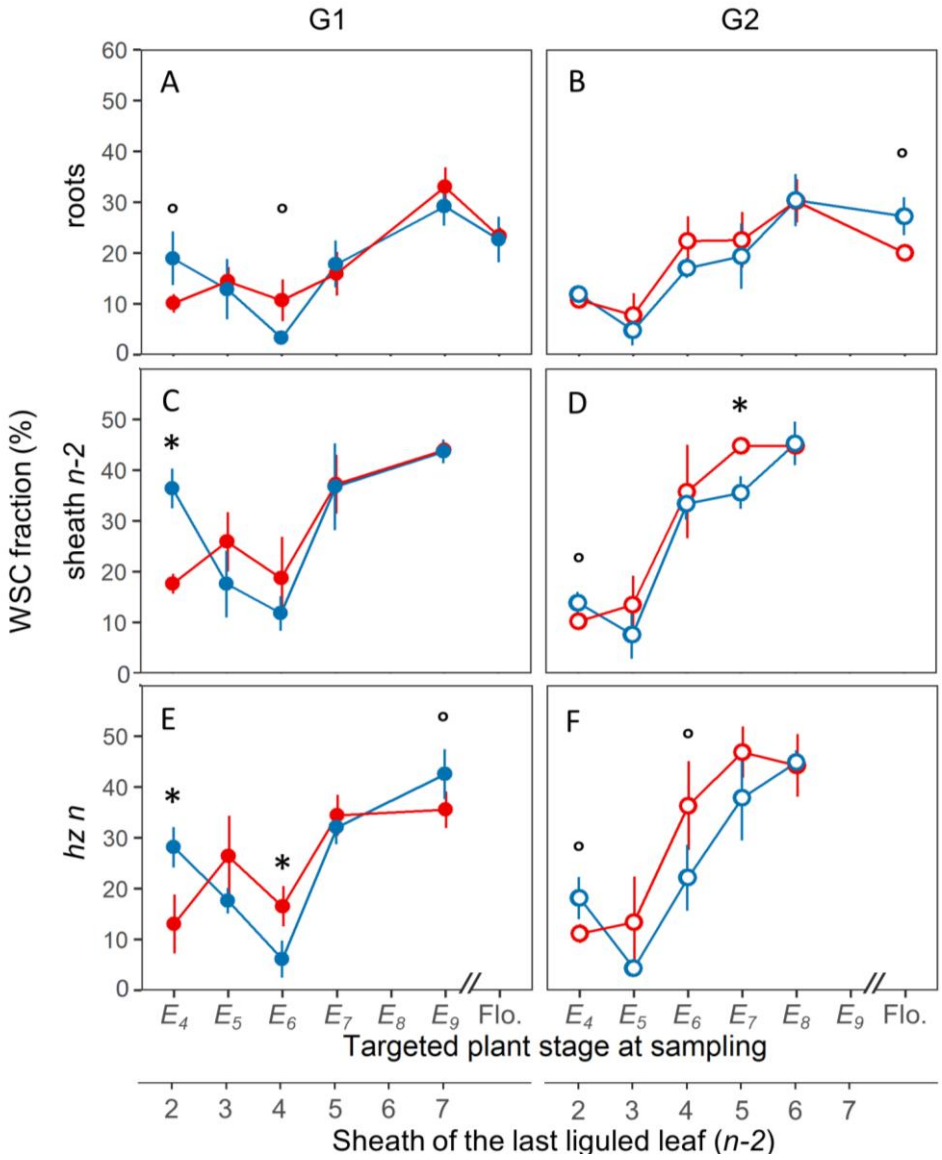

Figure 3.13 – Fraction of water-soluble carbohydrates (WSC) in the roots (A,B), the sheath of the last ligulated leaf (sheath *n-2*), and in the hidden part of the emerging leaf (*hz n*, E,F) on each sampling occasion for two sets of growth conditions (G1, G2), with (red) and without (blue) transient early shading of the stands. Samplings were performed at the time of emergence of a leaf *n* out of the pseudostem, which is denoted E_n. Vertical bars represent the 95 % confidence intervals. No vertical bar indicates that they are smaller than symbols. Star and circle above symbols indicate that the mean value of early shading treatment was significantly different (Student's t-test) from the mean value of the control with $p < 0.05$ and $0.05 < p < 0.1$, respectively.

We found that the relation between the WSC fractions of any pair of plant elements had a high coefficient of determination (R^2 in [0.69, 0.98]) for all pairs of plant elements (Table 3.2 A). In addition, the intercept of this relation was not significantly different from zero ($p>0.1$) in most pairs of plant elements (39 out of 56), except for some relations involving the sheath *n-2* (*vs.* plant, shoot, lamina *n-2* and *ez n-1*) and some relations involving *hz n-1* (*vs.* plant, shoot, lamina *n-2*, *ez n-1*, *hz n*). Thus, in most of the cases, the WSC fraction of one plant element was proportional to the WSC fraction of the other plant elements (*e.g.* Figure 3.12 A). For example, the WSC fraction of the roots was a good proxy of the WSC fraction of the whole plant, of the shoot and of the sampled

plant elements (Table 3.2 A). Overall, relations between the N fractions of a pair of plant elements were weaker than for WSC fractions (R^2 in [0.36, 0.94], Table 3.2 B) and the proportionality of N fractions between plant elements was observed in fewer cases than WSC fractions (33 out of 56). In particular, no proportionality (but correlation) was observed for the relations with the sheath *n-2* and for the relations with *hz n* (*e.g.* Figure 3.12 B).

When a proportionality was observed, plant elements did not have same concentrations, ie. the coefficient a_{ij} were not equal to 1. In contrast, we observed clear gradients of composition within the plant. WSC fraction of the shoot was 37 % higher than that of the roots (Table 3.2 A). Among the shoot elements, the highest WSC fractions were recorded in the elements that were (mostly) enclosed. The highest N fractions were measured in the hidden part of the growing leaves (Table 3.2 B).

Table 3.2 – Distribution of WSC and N fractions within the plant during the vegetative stages. A: WSC fractions within the plant relatively to the WSC fraction of the roots. B: N fractions within the plant relatively to the N fraction of the last ligulated lamina (lamina *n-2*). *r* is the Pearson correlation coefficient, and the related p-value is given in the following row. The ratio is, in A), the slope of the standardized major axis estimation of the WSC fraction of the plant element (see column name) *vs.* the WSC fraction of the roots with null intercept, and, in B) the slope of the standardized major axis estimation of the N fraction of the plant element (see column name) *vs.* the N fraction of lamina *n-2* with null intercept. Brackets indicate that the intercept was not significantly null (p>0.1). R^2 is the coefficient of determination of the related standardized major axis estimation (with intercept only if significantly not null). N is the number of observations. Leaf *n* was the leaf emerging at the time of sampling (E_n), leaf *n-1* was emerged and growing, and leaf *n-2* was recently ligulated. *ez* and *hz* refer to the exposed and hidden parts of a growing leaf, respectively. The data used were the mean WSC fraction per organ x treatment x sampling occasion for two or three replicates.

A)

WSC fraction (*vs.* roots)	**plant**	**shoot**	**lamina *n-2***	**sheath *n-2***	***ez n-1***	***hz n-1***	***hz n***
Correlation							
r	0.94	0.87	0.83	0.92	0.86	0.91	0.89
p	$4.0\ 10^{-6}$	$2.6\ 10^{-4}$	$7.7\ 10^{-4}$	$1.4\ 10^{-8}$	$1.5\ 10^{-4}$	$9.6\ 10^{-8}$	$3.4\ 10^{-7}$
Proportionality							
ratio	1.19	1.37	1.53	1.65	1.32	1.86	1.55
R^2	0.89	0.75	0.69	0.84	0.74	0.82	0.79
N	12	12	12	20	13	19	19

B)

N fraction (*vs.* lamina *n-2*)	**plant**	**shoot**	**roots**	**sheath *n-2***	***ez n-1***	***hz n-1***	***hz n***
Correlation							
r	0.83	0.83	0.74	0.97	0.94	0.94	0.72
p	$2.3\ 10^{-5}$	$1.3\ 10^{-4}$	$2.0\ 10^{-4}$	$3.5\ 10^{-7}$	$9.4\ 10^{-10}$	$1.5\ 10^{-6}$	$2.0\ 10^{-2}$
Proportionality							
ratio	0.64	0.85	(0.44)	0.61	1.13	1.21	(1.71)
R^2	0.68	0.69	0.54	0.93	0.88	0.89	0.51
N	18	15	20	12	20	13	10

Some results that contributed to the formalism and calibration of the leaf growth model

We focus here on two results about leaf composition that gave insights for developing our model. In this section, we present the experimental results. We will later argue, in the discussion, the importance of these results to the model calibration and to the definition of some formalism.

N fraction in the senesced laminae

When expressed in relation to the relative phytomer rank, the N fraction of the dry mass of the senesced laminae followed an ontogenic pattern common to all treatments (Figure 3.14): it decreased from ~2 % to 0.5 % for the laminae hold on short internodes, and was stable at 0.5 % for the laminae hold on elongated internodes.

Unpublished data from a field experiment (Bertheloot *et al.*, 2012) with the same wheat genotype cultivated on the same location under two N fertilizations presented a similar ontogenic gradient. More precisely, our results were almost perfectly aligned with the N stressed treatment of Bertheloot *et al.* (2012), while the usual N fertilization treatment of Bertheloot *et al.* (2012) was shifted positively by ~0.5 % (N fraction unit). Similar results were obtained on same experiment of Bertheloot *et al.* (2012) on another wheat cultivar (not shown). These results emphasized the N stress of our experiment. In addition, these results highlighted the impact of N fertilization on the N fraction of the dry mass of the senesced laminae.

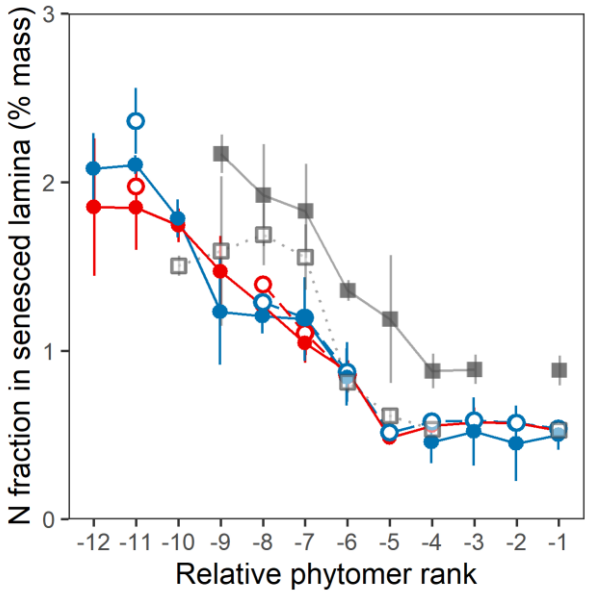

Figure 3.14 - Nitrogen fraction of the senesced lamina of the main stem *vs.* phytomer rank counted from the flag leaf, for two growth conditions (closed symbols: G1, open symbols: G2), with (red) and without (blue) transient early shading of the stands. For comparison, grey squares are experimental data for the same wheat cultivar, on the same location, under field conditions with two treatments of N fertilization (open symbols: No N fertilization during the crop cycle, closed symbols: usual N fertilization; 11 leaves at flowering) (Bertheloot *et al.*, 2012). Vertical bars represent the 95 % confidence intervals.

Dynamic of the N fraction of the leaf across contrasted developmental stages

The N fraction in the hidden part of the growing leaf and in the exposed part of the lamina is presented (Figure 3.15) in relation to the phyllochronic time that is the time relative to leaf emergence. At t=0, the leaf was about to emerge and fully hidden inside the pseudostem. At t=1, the leaf was emerged and was growing: its hidden part was made of the growing sheath, the elongation zone of the lamina and some mature tissues of the lamina; its exposed part was made of mature lamina (~80 % of the lamina final length was exposed). At t=2, the leaf was mature and recently ligulated.

When expressed relatively to phyllochronic time, the dynamics of the N fraction were similar in the phytomers 5 to 8 (Figure 3.15) and the few data available for the other phytomers suggested a similar dynamic (not shown). The N fraction of the hidden part of the growing leaf decreased from ~7 % at t=0 to 3-5 % at t=1, and the N fraction of the mature lamina decreased from 3-5 % at t=1 to 2.5-5 % at t=2. Surprisingly, at t=1, we did not observe a marked difference in N fraction between the hidden and the exposed parts of the growing leaf, despite the contrasting developmental states of the tissues.

The comparison with one simulation of CN-Wheat is done in the Discussion section.

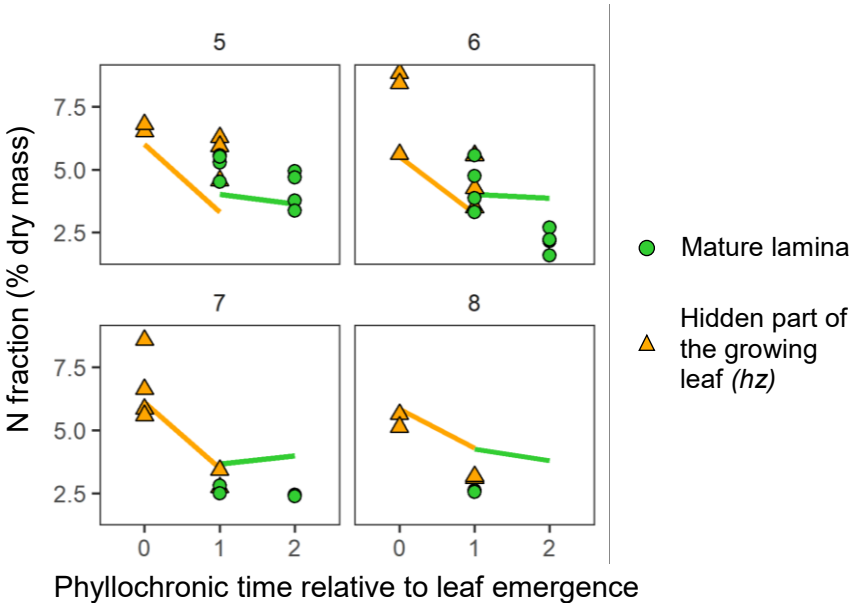

Figure 3.15 – N fraction of the leaf element *vs.* phyllochronic time relative to leaf emergence (0: emergence of the leaf, 1: emergence of the following leaf (*n+1*), 2: emergence of leaf *n+2*). Each panel is one phytomer rank (see panel title). Symbols and colours refer to the leaf element (see legend on the left). Each symbol is the mean of two to three measurements of one treatment. Lines are model simulation in Chapter 1.

3.4 - Discussion

On two growth conditions G1 and G2 contrasted by transplanting dates and plant densities, we applied a shade net that decreased by ~80 % the incident PAR from transplanting until E_4. From E_4 onward, the early shading treatment and the control grew under the same conditions. The whole experiment suffered from an uncontrolled N deficiency, which probably started before E_4, and resulted in plants with low tillering (Table 3.1) and small leaf dimensions (Figure 3.9). This early N deficiency departs from N deficiency that would occur under field conditions because the N needs of wheat fields are usually fulfilled by the soil residual N from the prior crop at least up to ~E_6. Despite such unusual growth conditions, our experiment revealed original results.

In both G1 and G2, early shading created, at E_4, plants that had significantly contrasted architecture and composition compared to the controls. Measurements revealed that the four treatments had contrasted architecture and composition up to E_8, and that, overall, no marked difference was visible at flowering between early shading treatment and control. First, we discuss the putative mechanisms of the lasting impact of the transient shading stress on plant architecture and composition, and compare with the CN-Wheat simulations of Chapter 2. Then, we demonstrate the originality of our results regarding plant composition, and why these results are of interest for developing a model that integrates shoot morphogenesis with the C and N metabolism of the whole-plant.

Early shading treatments had a lasting impact on plant architecture and composition.

At the end of shading (E_4), the shaded plants had lower dry mass, higher shoot:root dry mass ratio, longer sheath 1 and leaf 2, and lamina 2 was thinner, with higher N fraction and lower SLN. Lamina 2 was narrower in shaded plants compared to control in G1 only. In addition, the WSC fraction was lower in the shaded plants. These results are in line with the reported consequences of shading. In particular, thinner leaves were related to low WSC, as shown by Dale *et al.* (1972) and by Felippe and Dale (1973) on barley. In contrast, longer leaves could result from a photomorphogenetic response of leaf growth due to the low blue light irradiance induced by the PAR reduction (Gautier and Varlet-Grancher, 1996; Barillot *et al.*, 2020*a*). Remarkably, dimensions and mass of lamina 1 were unaffected by the shading in both growth conditions. Reasons might be that lamina 1 is largely developed in the seed (three to four leaves are already initiated in the wheat seed), and that the growth of lamina after germination 1 was probably fully fed by seed reserves as their exhaustion occurs after lamina 1 ligulation, around the emergence of leaf 3 (Williams, 1960). At least this shows that there was no direct impact of the light climate perceived by this lamina on its dimension and mass. The assumption in our model, that the structural properties of a lamina are defined prior to its emergence and do not depend on the light it perceives, is consistent with the behaviour observed in this case.

After removal of the shade net, differences were still visible between early shading treatment and control in both growth conditions. On one hand, some effects of early shading that were visible at E_4 lasted after the removal of the net: the higher shoot:root ratio lasted up to ~ E_8/E_9 and longer leaves up to lamina 4 in G1 and sheath 7 in G2. On the other hand, early shading had other later impacts that were opposite to those observed at E_4: early

shading treatments had higher WSC fractions (up to E_7 in G1 and E_8 in G2) and lower N fractions (still observed at flowering with a smaller magnitude than during the vegetative stages) compared to the control. Interestingly, the impact of early shading was more marked in G1 than in G2 at E_4, but was more marked in G2 than in G1 on the following sampling occasions (except for the shoot:root ratio). In addition, differences between early shading treatment and control were observed later in plant development in G2 than in G1. The reason for the differences in behaviour between G1 and G2 are not known, they might originate from different weather conditions due to different sowing dates and/or different final number of leaves and/or different planting intensity. The underlying mechanisms that could have led to differences between the early shading treatment and the control are discussed below.

Early shading increased the final length of some of the leaves (but not all) that had not yet emerged at the time of the shading but that were already initiated. Length differences between early shading treatment and control were maximum for leaves ~2-3 and then decreased along the axis, until the treatments became similar at leaf 5 in G1, and leaf 8 in G2. To our knowledge, the present experiment reports for the first time a case of propagation of leaf lengthening along the axis following transient abiotic stress. In contrast, Louarn *et al.* (2010) reported a case of propagation of maize leaf shortening following a transient chilling stress that resulted in a decreased leaf elongation rate. They found that the following the chilling stress leaf elongation duration increased along the axis so that the higher elongation duration compensated the lower elongation rate for the uppermost leaves. The present experiment did not allow studying if the lengthening of leaves 4-7 were due to a direct impact of shading prior E_4, and/or to the lengthening of leaves 1-3 that increased pseudostem length (Volenec and Nelson, 1983; Wilson and Laidlaw, 1985; Casey *et al.*, 1999). In addition, the present experiment did not allow studying the mechanisms leading to a compensation of leaf lengths between early shading treatment and control. In addition, while we expected that the differences of shoot:root ratio did not vanish as soon as the removal of the net, the reasons for amplification in G1 were unknown. The higher WSC fractions and lower N fractions in the early shading treatment could be consequences of the higher shoot:root ratio.

In Chapter 2, we simulated the growth of wheat monoculms with contrasting initial dimensions, from E_4 to ~E_{15} (plants were kept vegetative), under contrasting growth conditions. As in the present experiment, at E_4 (model initialization), leaves 1 and 2 of the simulated plants were liguled, leaf 3 was emerged and growing, and leaves 4-10 were initiated and growing inside the pseudostem (whereas only 9 leaves were initiated in the present experiment). Specifically, simulations were performed for plants that had, at E_4, longer leaves 1 to 4 (+ 10 %, + 25 %, + 50 %) than a control. The simulated effect of the lengthening of leaves 1-4 was highly dependent on growth conditions (Figure 2.18 A,B,C). Overall, CN-Wheat simulated that the lengthening of leaves 1-4 propagated to upper leaves up to ~leaf 12 (Figure 2.18 A,C) with same magnitude as the change made on leaves 1 to 4. Leaves above 12 were not affected as their elongation were already limited with the control initial dimensions. Contrary to the present experiment, the model did not simulate a decrease in the magnitude of the effect along the axis, nor a compensation of differences of leaf length between treatments for leaves above leaf 7. We propose three hypotheses to explain the absence of compensation of length differences in the simulations of Chapter 2. A first reason might be that the simulated system differed from the present experiment (different

growth conditions, and no stem elongation in the simulations). A second reason could be that some formalisms of CN-Wheat might not allow simulating a compensation of length differences between treatments. In particular, CN-Wheat assumes that (i) leaf elongation follows a two-phase kinetic with the transition being triggered be the emergence of the previous leaf (leaf *n-1*) outside the pseudostem, (ii) from the emergence of leaf *n-1*, leaf *n* enters a sigmoidal elongation, which has a fixed time-duration. One dedicated experiment, in which the kinetic of successive leaves is followed, could be performed to test if these two mechanisms are maintained in the case of the delayed impact of an early abiotic stress. A third reason might be that, in the simulations in Chapter 2, only the initial plant architecture was modified whereas, in the present experiment, both the architecture and the trophic status of the plant were impacted at E_4.

Insights on plant composition

The four contrasted plant populations allowed quantifying the distribution of WSC and N fractions inside the plant during the vegetative stages.

We must note that the upper range values of observed WSC fractions were high [5-55 %] compared to the highest WSC fractions reported in the literature on grass species: ~50 % in the sheath of winter wheat (Savitch *et al.*, 2000) and ryegrass (Robson and Deacon, 1978), 20 % in the laminae of ryegrass (Robson and Deacon, 1978) and rice (Fabre *et al.*, 2019), and 10 % in the roots of perennial grass (J.-L. Durand, unpublished experiment). However, the WSC fractions of this experiment seem realistic for two reasons. First, data from literature mostly correspond to plant cultivated at higher temperatures, whereas the present experiment was carried under low temperature (Figure 3.3) and high PTQ (Figure 3.11B). It has been shown that wheat accumulates fructans at low temperature (Bancal and Gaudillère, 1989). Second, plants of the present experiment suffered from N deficiency (Figure 3.4), which is expected to increase the WSC fraction (Robson and Deacon, 1978; Wilman, 1980; Volenec and Nelson, 1984).

Literature rarely presents compositional data (i) on plants cultivated outdoor during the vegetative stages, (ii) for the plant elements sampled that have been sampled in this experiment. In particular, we quantified the composition of the hidden part of the growing leaf, which is a compartment of CN-Wheat for which we did not have composition data from the literature. Thus, our results consisted in an original dataset of WSC and N fractions of the dry mass. One of the key results here are the strong correlations between the compositions of different plant elements, and for most of them, they were even proportional. Such a result is useful for future experimental studies because it implies that the WSC and N fractions of various elements can be estimated from a plant element easily measurable such as the lamina of the last ligulated leaf.

The parallel dynamics of composition in between plant elements is compatible with the strong hypothesis of CN-Wheat that all compartments share a common metabolic pool (that is called the *phloem* in CN-Wheat). However, comparison with CN-Wheat formalism should be nuanced for two reasons. First, in CN-Wheat, the *phloem* only considers “mobile” metabolites (sucrose and amino acids) whereas, in the present experiment, we measured WSC and total N, for which large proportions were probably made of fructans and proteins. Second, concentrations in CN-Wheat are expressed in unit of structural mass instead of unit of dry mass.

Taking the simulation results obtained in Chapter 1 (for different weather conditions but same cultivar and location as in our experiment), we can see that CN-Wheat also simulates parallel dynamics of WSC fractions between the plant elements that were observed in the present experiment (Figure 3.16 A). However, the ratios of WSC fractions in the last ligulated leaf (*n-2*) and the hidden part of the emerging leaf (*hz n-1*) were lower in the model than observed in the experiment. Figure 3.17 Distribution differences between simulations and observations might originate from the different growth conditions. Therefore, our results indicate that further investigations should be performed to test the ability of CN-Wheat to simulate the repartition of WSC within the plant. The simulated range of variations across time was much narrower than the observed range probably because of different growth conditions. Thus, we did not observe parallel dynamics of N fractions between plant elements (Figure 3.16 B) expect for the hidden part of the growing leaves *n* and *n-1* that were correlated (r=0.9, p=0.013).

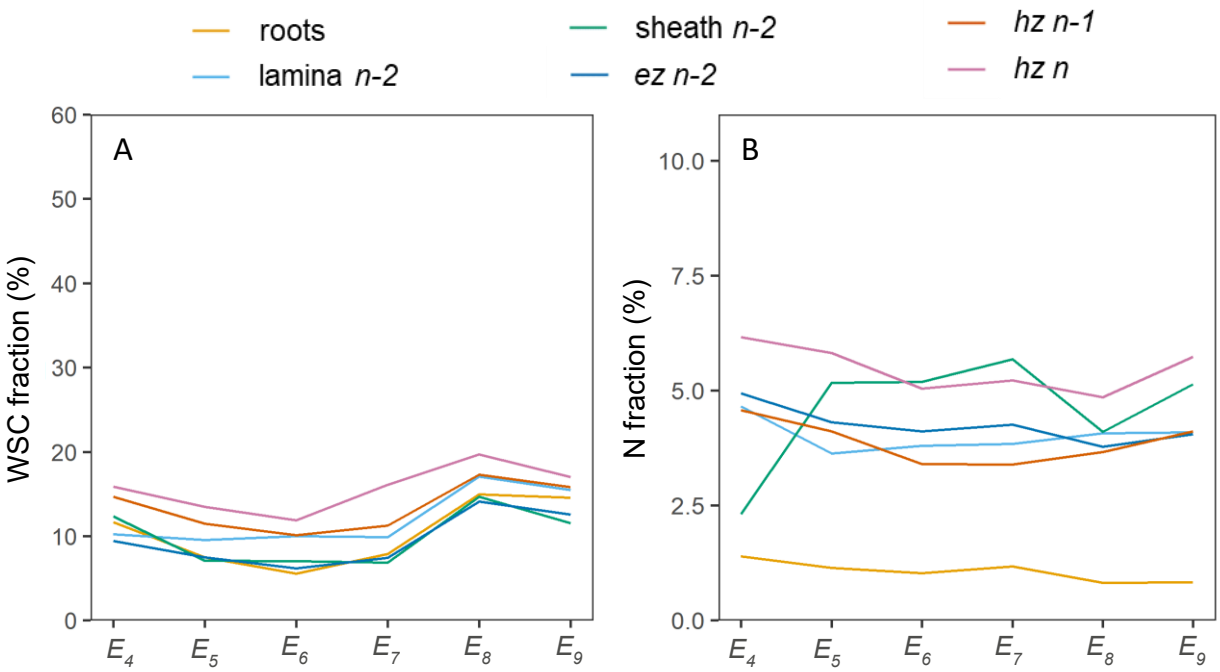

Figure 3.16 – Dynamic of WSC fraction (A) and N fraction (B) of the dry mass of several plant elements (see legend at the top of the figure) during the vegetative stages, as simulated by CN-Wheat in Chapter 1 for wheat cultivated in usual field conditions. Simulated values are taken at solar noon as soon as a new leaf (leaf *n*) emerged out of the pseudostem (E_n), which represent the measurements made in the present experiment. At this time, leaf *n-1* was emerged and growing, and leaf *n-2* was recently ligulated. *ez* and *hz* refer to the exposed and hidden parts of a growing leaf, respectively.

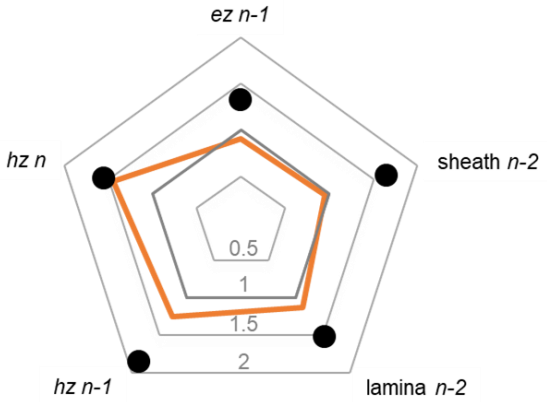

Figure 3.17 – Repartition of the WSC fractions within the plant during the vegetative stages. The figure represents the ratio of WSC fraction to the root WSC fraction. The black dots and the orange line represent the observed and simulated repartition, respectively. See Table 3.2 – Distribution of WSC and N fractions within the plant during the vegetative stages. A: WSC fractions within the plant relatively to the WSC fraction of the roots. B: N fractions within the plant relatively to the N fraction of the last ligulated lamina (lamina *n-2*). *r* is the Pearson correlation coefficient, and the related p-value is given in the following row. The ratio is, in A), the slope of the standardized major axis estimation of the WSC fraction of the plant element (see column name) *vs.* the WSC fraction of the roots with null intercept, and, in B) the slope of the standardized major axis estimation of the N fraction of the plant element (see column name) *vs.* the N fraction of lamina *n-2* with null intercept. Brackets indicate that the intercept was not significantly null ($p>0.1$). $R2$ is the coefficient of determination of the related standardized major axis estimation (with intercept only if significantly not null). N is the number of observations. Leaf *n* was the leaf emerging at the time of sampling (*En*), leaf *n-1* was emerged and growing, and leaf *n-2* was recently ligulated. *ez* and *hz* refer to the exposed and hidden parts of a growing leaf, respectively. The data used were the mean WSC fraction per organ x treatment x sampling occasion for two or three replicates. for details regarding the calculation of the repartition.

We demonstrated a gradient of N fraction of the senesced laminae along the axis.

The four treatments of the present experiment, and unpublished data from (Bertheloot *et al.*, 2012) representing two treatments contrasting by N fertilization, presented a marked gradient of N fraction of the fully senesced laminae along the axis (Figure 3.14): the N fraction decreased from 2 % to 0.5 %. These results are original considering the few data in the literature regarding the N fraction of senesced tissues (Aerts, 1996; Franklin and Ågren, 2002). To our knowledge, no gradient of N fraction of the senesced laminae along the axis has been reported in the literature. In addition, experimental results from Bertheloot *et al.* (2012) clearly showed that the N fraction of the senesced laminae was markedly higher in plants that received higher N fertilization, and that the steepness of the gradient along the axis was unaffected by N fertilization. Higher N fractions in senesced leaves of plants that received higher N fertilization have been reported for many tree species (Killingbeck, 1996; Wright and Westoby, 2003) and only studied in few perennial grasses such as ryegrass (Hunt, 1983), tall fescue (Gastal and Saugier, 1986) and Stipa capillata (Li *et al.*, 2020).

Senesced tissues are made of cellular structures such as cell walls (Penning de Vries *et al.*, 1989), and possibly residual metabolites that have not been recycled towards the rest of the plant during the senescing process (Kobe *et al.*, 2005). Most of the N mass of living laminae originates from proteins of the photosynthetic apparatus (Evans, 1989), which are degraded during the senescing process into mobile N and then translocated to younger

tissues (Hikosaka, 2005). It is commonly accepted that some of the N mass cannot be recycled because it is part of cellular structures (Evans, 1989), which is commonly named "structural N". However, the N fraction of the structural structures is unknown (Hikosaka, 2005). Some authors (Charles-Edwards *et al.*, 1987; Anten *et al.*, 1995) supported the idea that the structural N is represented by the X-intercept in the linear regression of photosynthetic capacity and nitrogen content, which is relatively constant regarding N fertilization, leaf age and phytomer rank. Nevertheless, there is no experimental evidence demonstrating this hypothesis. Thus, based on the literature, it is unclear if a higher N fraction of senesced tissues is due to a higher N fraction of the structural mass, or to a higher residual metabolic N mass due to incomplete remobilisation. Moreover, the mechanisms responsible for the effect of ontogeny on the N fraction of the senesced laminae might differ from those responsible for the effect of N fertilization.

We hypothesise that higher N fertilization resulted in higher residual metabolic N in the laminae at senescence but similar N fraction of the structural mass. Indeed, Bertheloot *et al.* (2012) compared treatments with the usual fertilization (N+) to treatments without any fertilization during plant development (N0); they found in N+ a higher N fraction of the senesced laminae for all phytomers above 2 (no data available for laminae 1 and 2). However, in that work, N0 and N+ plants were grown under same conditions from sowing to the first N application, which happened soon after leaf 5 ligulation. Because a lamina is considered as mature at ligulation (Kemp, 1980*a*; MacAdam and Nelson, 1987; Skinner and Nelson, 1994), we hypothesise that the structure of laminae 1-5 was identical for N0 and N+ and thus the impact of fertilization on the N fraction of senesced leaves 3-5 must have originated from a higher residual metabolic N.

Interestingly, the steepness of the gradient of N fractions of the senesced laminae along the axis was unaffected by N fertilization. It suggests that the mechanisms leading to the variations in N fraction of the senesced laminae with ontogeny are different from those leading to the variations with N fertilization. Thus, it may be that the gradient of the residual N fractions with ontogeny originates from a gradient of N fraction of the structural mass.

Our results are of interest for models of grass growth that account for the economy of N within the plan (*e.g.* CN-Wheat). Such models imply accurately quantifying the losses of N during plant development. Usually in models of grasses, the N mass that cannot be recycled during senescence is considered as the N fraction of the structural mass, and is estimated to be constant regarding ontogeny and fertilization, ~0.5 % (Martre *et al.*, 2006; Drouet and Pagès, 2007; Martre and Dambreville, 2018). In contrast, our results demonstrated that, for wheat, a much higher N mass may be lost with tissue death, especially for lower phytomers or for usual fertilization rate.

Based on these results, we implemented an ontogenic gradient of N fraction of the senesced laminae into CN-Wheat. The implemented mechanisms are a provisional choice since the real mechanisms are unknown. Although the effect of N fertilization on the N fraction of the senesced laminae is clear, the differences observed between N fertilization treatments represent a small amount of N compared to the total N budget of the plant. So, we did not implement an effect of N fertilization on the N fraction of the senesced laminae for parsimony reasons. Following most models, the structural mass is synthetized with a constant N fraction (0.5 %). At lamina

senescence, part of the amino acids of the lamina is not recycled towards the rest of the plant but is immobilised as residual metabolic N.

The existence of contrasting N fractions of the senesced laminae raised several questions of physiological interest. If there is some residual metabolic N in the senesced tissues, was this N available to the metabolism when tissues were alive? This question intends to better quantify the metabolic activity of the laminae, such as photosynthesis and protein turn-over. Another question is to know when the N of the senesced tissues arrived in the living tissues in order to know when happened the construction costs, and to investigate if the N fraction of the senesced laminae is linked to the N status of the lamina at the time of its construction. One dedicated experiment with different number of leaves and without floral transition would enable the hypothesis of an ontogenic gradient of N fraction of the structural mass to be tested, and so to further refine our model.

The strong trend of the N fraction of the leaf during leaf elongation implied considering an estimate of the size of the division zone.

Our experimental results showed that the N fraction of lamina tissues decreased during leaf growth (Figure 3.15). The decrease was more marked during the phyllochron that followed leaf emergence (from ~7 % at t=0 and 3-5 % at t=1) than during the next phyllochron (from 3-5 % at t=1 to 2.5-5 % at t=2).

The literature reported a trend of N fraction from the leaf base to the leaf tip. Gastal and Nelson (1994) observed, on emerged and growing leaves of tall fescue at high N, that the N fraction was high ~7 % at the leaf base in the zone of cell division, decreased across the zone of cell elongation up to 3-4 %, and then slightly rose along the mature zone up to 3-5 % at the leaf tip. Thus, the temporal trend of N fraction that we observed, might originate from the dynamics of the length of the different cell zones during leaf elongation (Durand *et al.*, 1999; Fournier *et al.*, 2005). However, we did not observe a marked spatial difference of N fraction when the lamina was emerged and growing (t=1). One reason might be that the leaf element that we sampled represented a wide diversity of the cell zones, so N fraction was measured at too large spatial scale. Indeed, we sampled the hidden part of the growing leaf, which encompasses, at t=1, the zones of cell division and elongation and part of the mature zone, which have highly contrasted N fraction.

In CN-Wheat, the concentration of amino acids in the hidden part of the growing leaf drives leaf elongation, mainly before the emergence of the previous leaf *i.e.* prior t=-1 in phyllochronic time. Thus, CN-Wheat must accurately simulate the N fraction of the hidden part of the growing leaf. In order to simulate the trend of N fraction during leaf elongation observed in the present experiment, we modulated the rate of protein synthesis by the length ratio representing the size of the division zone in the hidden part of the growing leaf. Our implementation was supported by the work of Gastal and Nelson (1994), who noted that protein deposition occurred mainly in the division zone. Figure 3.15 presents the simulations by CN-Wheat for wheat cultivated under usual field conditions (same cultivar and location as in our experiment, see Chapter 1 for details). Overall, CN-Wheat simulates the trend of N fraction during leaf elongation that was observed in the present experiment.

Acknowledgements

The authors gratefully acknowledge Pierre Bancal for his precious help in defining the experimental set-up and the protocols of the biochemical analyses. The authors acknowledge Josiane Jean-Jacques and Nicolas Boulard for their tremendous technical assistance.

Résumé du chapitre 3

Dans le contexte du changement climatique et des nouvelles pratiques agricoles, les modèles sont des outils utiles pour anticiper la réaction des plantes à de nouvelles conditions de croissance. Comme les modèles actuels sont limités dans leur capacité à simuler la plasticité phénotypique car la simulation de certaines variables clés de la morphogénèse reposent sur des formalismes empiriques. Aussi, nous avons développé un nouveau FSPM qui simule la croissance du blé en fonction de la disponibilité locale de carbone et d'azote. Une expérimentation a été menée avec deux objectifs. Le premier objectif était de caractériser les conséquences d'un stress précoce transitoire sur la croissance de blé pour ensuite discuter la capacité de notre modèle à simuler cet impact en comparant les résultats expérimentaux aux simulations du chapitre 2 pour différents états initiaux de plante. Le second objectif était de recueillir des données sur la composition biochimique des organes. Ces données sont nécessaires à la définition du modèle et à son évaluation.

L'expérience a révélé une propagation des déformations dues à l'ombrage précoce aux feuilles successives émises après l'ombrage. La propagation observée souligne la nature autorégulée de l'architecture du blé. Nous avons de plus mis en évidence des corrélations fortes et des proportionnalités entre la composition de plusieurs organes au cours des stades végétatifs. La capacité de notre modèle à simuler ces résultats a été discuté, en comparant les résultats expérimentaux aux simulations des chapitres 1 et 2.

De plus, nous avons trouvé (i) qu'il existe un gradient marqué de teneur en azote des limbes sénescents le long de l'axe, qui était reproductible pour des conditions expérimentales différentes (ii) que cette teneur augmente avec la fertilisation azotée. Nous avons aussi observé une évolution marquée de la teneur en azote de la feuille au cours de sa croissance. Ces résultats ont été utilisés pour la définition du modèle au chapitre 1.

Discussion générale

Dans un premier temps, nous rappelons les objectifs de l'étude et les principaux résultats. Ensuite, nous revenons sur la pertinence de nos principales hypothèses de modélisation. Enfin, nous abordons des perspectives de CN-Wheat.

1 - Résumé des objectifs et résultats principaux de l'étude

Rappel du contexte

Comprendre l'impact des conditions de croissance sur le comportement des plantes est nécessaire pour anticiper l'impact du changement climatique et des nouvelles pratiques culturales visant à augmenter les rendements tout en protégeant l'environnement. Les plantes adaptent leur architecture aux conditions de croissance par des variations de rythme de croissance, nombre d'organes, dimensions, masse et composition biochimique ; c'est la plasticité phénotypique.

De nombreux modèles ont été développés afin de simuler la plasticité phénotypique du blé (voir Introduction générale). Toutefois, les capacités prédictives de ces modèles sont limitées quand il s'agit de simuler la réponse de la plante à des conditions de croissance inexplorées par l'expérimentation (Poorter *et al.*, 2013), à des stress multiples (Muller and Martre, 2019) ou après un stress précoce (Louarn *et al.*, 2010). Une raison majeure à ces limitations est que plusieurs variables clés sont soit définies comme constantes (*e.g.* le phyllochrone), soit simulées de façon empirique (*e.g.* la masse surfacique des feuilles).

Hypothèse scientifique testée dans le cadre de l'étude

Dans le cadre de cette étude, nous avons voulu apporter une vision de la morphogénèse de la plante reposant sur un degré de mécanisme plus élevé que les modèles existants. Aussi, la thèse soutenue est que des règles de croissance définies à une échelle locale permettent de simuler, comme propriétés émergentes, l'architecture aérienne des plantes, la composition des organes, la répartition de la biomasse au sein de la plante et les équilibres source – puits, ainsi que les réponses de ces traits pour des conditions de croissance contrastées en lumière et en azote. Cette hypothèse scientifique s'est déclinée en deux hypothèses de modélisation : (i) les concentrations locales en métabolites carbonés et azotés pilotent les vitesses d'allongement des feuilles et certains traits foliaires majeurs, (ii) des règles de coordination entre les feuilles successives marquent la durée d'allongement des feuilles et les moments où sont définis certains traits foliaires majeurs.

Approche et étapes de l'étude

Nous avons développé un modèle structure-fonction du blé pour les stades végétatifs dans le but d'intégrer, à la l'échelle de la plante entière, le métabolisme C-N et la croissance. Pour cela, l'échelle choisie de représentation du métabolisme est intermédiaire à celle de la plupart des modèles : elle est plus fine que la plupart des modèles

de plante entière (*e.g.* les modèles de culture), mais plus large que les modèles « physiologiques » qui simulent le métabolisme des cellules individuelles voire des organites cellulaires. L'échelle choisie correspond à l'échelle « supra-cellulaire » plébiscitée par Poorter *et al.* (2013) pour l'intégration des boucles de rétroactions entre la croissance de la plante et son métabolisme.

Ce modèle est une extension du modèle CN-Wheat développé précédemment à cette étude pour simuler le métabolisme du carbone et de l'azote dans la plante durant le remplissage des grains (stades post-floraison). Dans le cadre cette étude, nous avons défini/implémenté/calibré des formalismes décrivant la croissance des feuilles en dimensions et en masse, ainsi que leur métabolisme du carbone et de l'azote (Chapitre 1). Nous avons aussi fait une première proposition de formalismes de la croissance des entre-nœuds, qui reposent sur les mêmes principes généraux que ceux choisis pour la croissance des feuilles (Chapitre 1). De plus, les phases de développement et de calibration du modèle ont soulevé la nécessité de prendre en compte des lois de réponses à la température. Un ensemble de lois de réponse des différents processus du modèle à la température a donc été proposé (Chapitre 1).

Les trois étapes de l'étude étaient de :

1) ***Intégrer*** le savoir existant sur la morphogénèse du blé au sein d'un modèle structure-fonction. Ceci a impliqué d'assembler et d'organiser des connaissances de la littérature. Ces connaissances portaient souvent sur des propriétés ou comportements observés soit à des échelles plus intégratives que l'échelle de description des processus dans le modèle, soit à des échelles plus fines. Il fallait donc proposer un ensemble de formalismes hypothétiques susceptibles de produire comme propriétés émergentes les comportements correspondant aux connaissances de la littérature (Chapitre 1).

2) ***Calibrer*** le modèle pour qu'il rende compte d'un comportement réaliste aux différentes échelles modélisées : organe, plante, couvert (Chapitres 1 et 2). Une revue de la littérature qui soit le plus exhaustive possible a été nécessaire pour identifier le comportement attendu des variables simulées par le modèle, d'un point de vue qualitatif et quantitatif (Chapitres 1 et 2). En complément, nous avons mis en œuvre une expérimentation dans le but d'acquérir des données utiles au modèle qui étaient manquantes dans la littérature (Chapitre 3). Cette étape de calibration a représenté un travail significatif de l'étude.

3) ***Evaluer*** la capacité du modèle à simuler de façon réaliste les traits foliaires et les traits de plante dans des conditions croissance usuelles au champ (Chapitre 1), et dans des conditions de croissances contrastées par la densité de plante, la lumière et la fertilisation azotée (Chapitre 2). Pour cela, les simulations du modèle ont été comparées à un jeu de données issu de trois expérimentations (Chapitre 1), ainsi qu'au comportement du blé tel que rapporté par la littérature. Au cours de cette étape d'évaluation du modèle, nous avons testé la pertinence de nos hypothèses de modélisation.

Principaux résultats

Intégration des interactions entre architecture et environnement

L'architecture aérienne de la plante définit la façon dont la plante perçoit son environnement. En retour, la plante adapte son architecture à cet environnement. CN-Wheat est, à notre connaissance, le modèle de plante entière le plus avancé dans la prise en compte mécaniste des interactions entre architecture aérienne et son environnement pour les raisons avancées ci-dessous.

D'une part, CN-Wheat est couplé avec un modèle de phylloclimat perçu par chaque organe (lumière, température de surface) ce qui permet de simuler le métabolisme à l'échelle de l'organe. Le modèle de phylloclimat utilisé a été développé précédemment à l'étude (Chelle and Andrieu, 1998). Si la prise en compte du phyllochlimat est originale par rapport aux modèles de culture, c'est un aspect « classique » pour les FSPM.

Ce travail a permis de progresser dans l'intégration des réponses de la morphogénèse aux conditions de croissance. CN-Wheat simule la croissance des organes à partir de leurs concentrations en métabolites carbonés et azotés, qui sont elles-mêmes modulées par la croissance. Nous avons montré, au chapitre 1, que CN-Wheat permet de simuler, comme propriétés émergentes, un grand nombre de variables qui sont forcées en entrée ou simulées de façon empiriques dans la plupart des modèles. Par exemple, le modèle simule l'émergence des feuilles successives à partir de règles de coordinations et des concentrations en métabolites carbonés et azotés dans la zone de croissance. On montre que la stabilité du phyllochrone est une propriété émergente des processus décrits dans CN-Wheat alors que la quasi-totalité des modèles pilotent l'émergence des feuilles à partir d'un phyllochrone défini en entrée du modèle. On peut aussi citer la RUE qui est simulée à partir du bilan entre l'acquisition du carbone par la photosynthèse, les activités de synthèse de composés carbonés et les pertes de carbone (respiration, exsudation, sénescence) de la plante. Au contraire, la majorité des modèles simulent la croissance en biomasse à partir d'une RUE donnée en entrée et du rayonnement intercepté. Nos simulations ont montré des variations de la RUE au cours du développement de la plante, ainsi que des variations suivant les conditions de croissance. Au chapitre 2, nous avons montré qu'une même calibration du modèle permettait de simuler de façon réaliste la plasticité phénotypique des dimensions, du phyllochrone, du SLA, des compositions d'organes, de la répartition de la biomasse au sein de la plante et de la RUE. De plus, nous avons monté au chapitre 2 que le modèle simule la propagation d'une déformation précoce, ouvrant la voie à la simulation des conséquences d'un stress précoce sur le développement ultérieur de la plante. Comme discuté au chapitre 3, cet aspect reste néanmoins à évaluer plus finement expérimentalement.

Intégration du métabolisme du carbone et de l'azote à l'échelle de la plante

Notre modèle est une approche intégrée qui simule les interactions carbone-azote dans la plante en croissance. Les interactions C-N sont impliquées dans de nombreux processus physiologiques représentés dans le modèle : l'absorption d'azote et son assimilation, la photosynthèse, le turn-over des protéines (qui est médié par les cytokinines dont la synthèse dépend de la concentration en saccharose dans les racines), les flux au sein de la plante. La simulation des interactions carbone-azote est possible parce que le modèle est un modèle de bilan

complet du carbone et de l'azote, c'est-à-dire qu'il comptabilise toutes les entrées de carbone et d'azote dans la plante, et les pertes de carbone et d'azote, notamment en simulant un rapport aérien/souterrain qui est cohérent avec la littérature.

Un modèle de bilan complet du carbone et de l'azote dans la plante en croissance

Comme détaillé dans la discussion du chapitre 2, notre modèle propose un bilan du carbone et de l'azote de la plante en croissance *i.e.* toutes les entrées (photosynthèse, absorption N) et pertes (sénescence, respiration, exsudation racinaire) majeures de carbone et d'azote sont comptabilisées. Cet aspect est original par rapport à la plupart des modèles qui calculent les entrées de carbone à partir de l'interception lumineuse et de la RUE, et/ou les entrées d'azote à partir de la biomasse aérienne et de la courbe de dilution critique de l'azote (Lemaire *et al.*, 2007). Dans notre approche, la RUE et la courbe de dilution critique de l'azote sont des sorties du modèle.

Grâce à l'expérimentation réalisée au chapitre 3, nous avons acquis des données sur la composition de la plante, nécessaires à la calibration du modèle, qui sont rares dans la littérature. Nous avons en particulier mis en évidence des corrélations fortes et des proportionnalités entre la composition de plusieurs organes au cours des stades végétatifs. Outre la modélisation, ce résultat fournit une piste très intéressante sur le plan expérimental puisqu'il suggère que la composition d'organes difficilement mesurables peut être estimée à partir de celle d'autres organes. De plus, nous avons trouvé (i) qu'il existe un gradient marqué de teneur en azote des limbes sénescents le long de l'axe, qui était reproductible pour des conditions expérimentales différentes (ii) que cette teneur augmente avec la fertilisation azotée. Ces résultats invitent à mieux prendre en compte, dans les modèles, l'allocation d'azote aux structures et la remobilisation à la sénescence des tissus ; ils fournissent aussi des pistes pour le faire.

Une preuve de concept

La présente étude ne démontre pas un caractère prédictif de notre modèle. En effet, CN-Wheat comprend ~160 paramètres. Parmi ces paramètres, ~100 paramètres ont été défini à partir de la littérature. Les autres (~60) n'ont pas pu être définis à partir de la littérature car nous n'avons pas trouvé de travaux ayant étudié les relations du modèle (*e.g.* la dépendance de la vitesse d'allongement des feuilles aux concentrations de leurs zones cachées). Ces paramètres ont alors été calibrés de sorte que les simulations reproduisent les observations des jeux de données d'évaluation ou les comportements attendus de la plante.

Toutefois, les résultats cités ci-dessus démontrent que règles définies à une échelle locale permettent de simuler, comme propriété émergente, les schémas d'organisation et de composition de la plante, leur cinétique et leurs réponses des conditions de croissance contrastées en lumière et en azote. Nos hypothèses de modélisation sont donc plausibles. Comme tout travail de modélisation, la présente étude n'a toutefois pas démontré que ces hypothèses étaient vraies. CN-Wheat est une proposition de représentation intégrée du blé en croissance. La présente étude a permis de démontrer que cette représentation était crédible dans une gamme de conditions relativement large. CN-Wheat est donc un outil utile pour explorer le comportement des plantes dans de nouvelles conditions de croissance.

2 - CN-Wheat pilote la croissance par de règles définies à l'échelle locale : fiabilité, limites et contraintes des hypothèses du modèle.

Dans cette section, nous discutons de la pertinence des deux principales hypothèses du modèle de croissance foliaire ainsi que de la représentation 3D du couvert, puis nous exposons leurs inconvénients liés à la complexité du modèle.

Hypothèse 1 : les concentrations locales en métabolites carbonés et azotés régulent la vitesse d'allongement des feuilles et certains traits foliaires majeurs.

Dans CN-Wheat, les concentrations en saccharose et en acides aminés des zones cachées des feuilles en croissance et des racines pilotent la croissance. Ce choix reflète l'idée selon laquelle la croissance répond à des disponibilités locales (Kroon *et al.*, 2005; Poorter *et al.*, 2013). Cette option de modélisation diffère par plusieurs aspects de ce qui est fait dans la plupart des modèles qui pilotent la croissance par la disponibilité en C-N : CN-Wheat considère (i) l'échelle de l'organe et non de la plante entière, (ii) les différents types de métabolites disponibles pour la croissance et non un pool global de carbone et d'azote, (iii) la quantité de métabolites est rapportée à la masse structurale (ce que nous définissons comme concentration) et non absolue ou rapportée à toute la biomasse. Cette hypothèse est satisfaisante intellectuellement mais la littérature ne propose pas de preuve directe de l'existence de ces régulations, ni de données pour calibrer les formalismes du modèle.

CN-Wheat fait l'hypothèse que les principales réponses de la plante à des conditions de croissance contrastées en lumière et an azote sont causées par des variations des concentrations locales en métabolites carbonés et azotés. Toutefois, d'autres facteurs co-varient avec les conditions de croissance telles que les teneurs en eau, la qualité de la lumière ou les hormones, qui sont d'autres facteurs majeurs impliqués dans la réponse morphogénétique des plantes. Les perspectives d'introduction de ces facteurs dans CN-Wheat sont discutées plus bas. Nous illustrons ci-dessous l'incertitude quant au moteur de la réponse morphogénétique en prenant le cas de la largeur maximum des limbes.

Il est montré dans la littérature que la largeur est fortement modulée par la lumière (PAR incident et densité de plantes). Pour simuler ces réponses à l'environnement lumineux, nous avons implémenté dans CN-Wheat une régulation du rapport entre la largeur et la longueur du limbe par la concentration en saccharose dans la zone cachée de la feuille en croissance. Toutefois, nous ne savons pas si les réponses observées de la largeur des limbes à la lumière résultent d'une réponse aux concentrations en sucres, au signal lumineux *per se*, ou aux deux (Fournier *et al.*, 2001). A partir des données concernant tous les étages foliaires de maïs cultivés au champ à plusieurs densités, Fournier *et al.* (2001) ont démontré que la largeur des limbes était très bien décrite par, uniquement, un facteur ontogénique et une fonction logarithmique du PAR absorbé entre l'émergence et la ligulation du limbe. Cette relation suggère que la réponse de la largeur des limbes à la lumière pourrait être uniquement le résultat de processus photo-morphogéniques.

De façon générale, les lois de réponse de la croissance aux concentrations locales implémentées dans CN-Wheat sont exploratoires.

Hypothèse 2 : les règles de coordination entre feuilles successives marquent la durée d'allongement des feuilles et les moments où sont définis certains traits foliaires majeurs.

Dans CN-Wheat, l'émergence d'une feuille (feuille *n*) hors de la pseudo-tige déclenche (i) le passage de la feuille suivante (feuille *n+1*) d'une cinétique d'allongement exponentielle à une cinétique d'allongement sigmoïdale prédéfinie et (ii) la définition de la largeur maximum du limbe et de la masse structurale spécifique de la feuille *n.*

Le point (i) repose sur les multiples observations de synchronismes dans le développement des phytomères successifs (Gallagher, 1979; Malvoisin, 1984*b*; Skinner and Nelson, 1995; Ljutovac, 2002; Fournier *et al.*, 2005). Ces synchronismes sont approximatifs et nombreux, si bien qu'un événement est ~synchronisé avec une multitude d'autres (Ljutovac, 2002). De plus, ces synchronismes semblent moins bien respectés pour les dernières feuilles (Figure 1.4). Enfin, les mécanismes à l'origine des synchronismes observés ne sont pas connus. Certains auteurs ont fait l'hypothèse que l'émergence d'une feuille entraine une transition dans la cinétique d'allongement de cette feuille ou d'une autre feuille (Begg and Wright, 1962; Fournier *et al.*, 2005). Williams (1974) propose que les coordinations émergent de contraintes mécaniques au sein du cornet. Toutefois, aucune de ces hypothèses n'a été démontrée. Ainsi, nous n'avons pas d'élément démontrant que l'allongement d'une feuille est piloté par l'émergence de la feuille précédente plutôt qu'une autre feuille, voire même qu'un autre facteur.

Dans le modèle, la feuille *n+1* débute, à partir de l'émergence de la feuille *n,* une cinétique d'allongement sigmoïdale dont la durée est fixe (en temps compensé des effets de la température) et dont la vitesse est légèrement modulée par les concentrations en métabolites carbonés et azotés. Ce choix de modélisation repose sur l'observation que la cinétique d'allongement des feuilles est commune à tous les phytomères, si le temps est exprimé en temps phyllochronique (et donc très proche en temps compensé des effets de la température puisque le phyllochrone est relativement stable dans cette unité). Ce résultat a initialement été observé par Fournier *et al.* (2005) sur des données issues du travail doctoral de Ljutovac (2002) correspondant à une expérimentation de blé cultivé au champ avec une densité de semis usuelle en France (210 plantes m^{-2}). Nous avons montré sur deux autres jeux de données (Malvoisin, 1984; un traitement à 70 plantes m^{-2} de l'expérimentation de Ljutovac, 2002) que la cinétique d'allongement et exprimée en temps phyllochronique est commune à tous les phytomères et commune aux trois jeux de données. Toutefois, par manque de données expérimentales, nous n'avons pas évaluer la capacité du modèle à simuler les cinétiques d'allongement individuel des feuilles dans des conditions de croissance contrastées (voir discussion chapitre 2).

Enfin, CN-Wheat définit la largeur maximum du limbe et de la masse structurale spécifique de la feuille dès son émergence (ii). Comme discuté au chapitre 2, cette définition est trop précoce dans la croissance dans la feuille

au vu des résultats expérimentaux. Toutefois, cette définition à l'émergence de la feuille a été contrainte par des raisons pratiques.

Dans quelle mesure notre représentation 3D de l'architecture aérienne des plantes est-elle représentative d'un couvert végétal ?

La modélisation FSPM vise à prendre en compte une architecture explicite de la plante pour mieux simuler les interactions plante-environnement. Aussi, la représentation de l'architecture doit être réalise. CN-Wheat propose une représentation de l'architecture aérienne uniquement. Nous discutons ici de sa pertinence.

Notre représentation 3D d'une plante et implications des simplifications réalisées.

Pour représenter la plante en 3D, un ensemble de simplifications ont été réalisées. Parmi celles-ci, nous allons discuter des simplifications découlant de l'échelle de représentation de la feuille, ainsi que les simplifications sur la géométrie des feuilles.

L'échelle de représentation des parties visibles des feuilles

Dans CN-Wheat, la feuille est représentée par un ensemble d'éléments visibles (limbe et partie visible de la gaine) et un élément caché. Chaque élément est un compartiment du modèle et est donc considéré comme homogène en termes d'environnement perçu, structure, composition et fonctionnement. Aussi, dans le cas de la photosynthèse, le modèle considère que les propriétés optiques, le PAR absorbé et la répartition de l'azote sont homogènes sur l'ensemble de la surface de l'élément. L'hypothèse selon laquelle la répartition de l'azote par unité de surface est uniforme le long du limbe et le long de la gaine semble réaliste pour les stades post-floraison. En effet, plusieurs auteurs n'ont pas noté de gradient d'azote par unité de surface pour des limbes et des gaines de blé (Bertheloot *et al.*, 2012), ni pour des limbes de maïs (Drouet and Bonhomme, 1999), malgré des gradients marqués de lumières le long de ces organes. Au contraire, un gradient positif de protéines photosynthétiques par unité de surface depuis la pointe vers la base des limbes a été observé, au cours des stades végétatifs, chez le blé (J. Bertheloot, communication personnelle), ray-grass italien (Prioul *et al.*, 1980) et le maïs (Drouet and Bonhomme, 1999). Au cours de la thèse, nous n'avons pas quantifié les erreurs potentielles d'estimation de la photosynthèse à l'échelle du limbe pour les stades végétatifs. Cependant, on a montré aux chapitres 1 et 2 que le modèle simulait des RUE réalistes.

La géométrie et propriétés optiques des feuilles

Le modèle considère une cinétique d'inclinaison et de courbure des feuilles qui dépend uniquement de l'âge de la feuille. Les cinétiques implémentées reposent sur des résultats expérimentaux (Abichou, 2016) qui montrent que la cinétique d'inclinaison des feuilles de blé est commune à différents génotypes de ports différents, et à différentes densités de semis. Toutefois, il est attendu que la géométrie des feuilles varie avec les conditions de croissance. Par exemple, il a été montré que l'angle d'insertion des feuilles varie avec la fertilisation azotée (Green, 1987), la densité et l'arrangement spatiale au sein du couvert (Abichou *et al.*, 2019). De plus, les caractéristiques des feuilles (*e.g.* épaisseur) pourraient aussi moduler la géométrie des feuilles. De la même façon, CN-Wheat ne considère pas de variations des propriétés optiques des feuilles, qui ont une grande

importance sur la répartition de la lumière dans le couvert (Chelle and Andrieu, 1999). Il a toutefois été montré qu'elles sont très variables, notamment en fonction des teneurs en azote foliaire (Jacquemoud and Baret, 1990). Ainsi, il serait intéressant d'étudier dans quelle mesure des variations de géométrie et de propriétés optiques des feuilles modifieraient l'interception de lumière et quelles seraient conséquences sur les simulations de CN-Wheat.

Notre représentation 3D du couvert végétal, limites et perspectives dans le contexte de la plasticité phénotypique.

En raison du temps de calcul élevé pour résoudre le système d'équations relatives au métabolisme du carbone et de l'azote, les simulations des chapitres 1 et 2 n'ont pas été faites pour un couvert représenté comme un ensemble de plantes individuelles. Néanmoins, pour les calculs d'interception lumineuse, le couvert a été représenté comme un ensemble de 50 (chapitre 2) ou 1000 (chapitre 1) plantes de même dimension et organisées en rangs. Afin de tenir compte d'une certaine hétérogénéité spatiale au sein du couvert, un aléa a été ajouté à (i) la position des plantes au sein du rang, (ii) l'inclinaison des feuilles, (iii) l'azimut des feuilles et (iv) à l'azimut de la tige. Le rayonnement absorbé par chaque élément de la plante a été calculé comme la moyenne du rayonnement absorbé par les éléments correspondants des 50 ou 1000 plantes. Les calculs d'acquisition et d'allocation du carbone et de l'azote ont ensuite été réalisés sur cette plante moyenne.

Dans le chapitre 2, CN-Wheat a simulé plusieurs situations de mort du couvert. La capacité du modèle à simuler la mortalité des plantes est en soi une originalité intéressante. La mort simultanée de l'ensemble des plantes est cependant irréaliste. En effet, le couvert est en réalité composé d'un ensemble de plantes individuelles plus ou moins hétérogènes. La compétition inter-plantes conduit une plante, précocement plus développée que sa voisine, à développer davantage de surface foliaire, augmentant alors l'ombrage de la plante voisine. Dans certains cas, les plantes les moins développées meurent, laissant alors plus de ressources lumineuses et azotées pour leurs voisines. On suppose qu'en cas de fort stress abiotique, l'hétérogénéité du couvert augmente au cours du temps ; il serait alors nécessaire d'évaluer le couvert simulé par CN-Wheat en cas de fort stress abiotique.

De façon générale, il est nécessaire de tester le réalisme de nos maquettes 3D dans des conditions de croissance contrastées. Pour cela, on pourrait évaluer la capacité du modèle à simuler, pour des conditions de croissance contrastées, des cinétiques d'indices usuellement utilisés pour décrire le couvert tels que le LAI, le taux de couverture du sol et l'indice d'extinction de la lumière par exemple. Cette validation n'a été réalisée que dans des conditions usuelles de culture (chapitre 1). De plus, une analyse de sensibilité permettrait de connaître le poids de nos simplifications sur les résultats du modèle, et peut-être d'identifier des facteurs qui mériteraient d'être mieux modélisés.

Limites du modèle liées à la complexité des processus représentés

CN-Wheat intègre, à l'échelle de la plante, des mécanismes complexes, simulant ainsi un grand nombre de variables. Toutefois, ces simulations sont réalisées au prix d'une grande complexité du modèle. Nous en détaillons les inconvénients ci-dessous.

Nombre de paramètres

Comme mentionné dans la section précédente, CN-Wheat comprend un grand nombre de paramètres ce qui demande un long travail pour en définir les valeurs. Notamment, ~60 paramètres n'ont pas pu être établis à partir de la littérature. Aussi, des erreurs éventuelles de valeurs de certains paramètres peuvent être compensées par des erreurs sur d'autres paramètres. Ce point a été soulevé dans la discussion du chapitre 2 à propos des paramètres en lien avec le métabolisme de l'azote. De plus, le nombre élevé de paramètres issus de la calibration soulève le risque d'un sur-ajustement aux jeux de données particuliers utilisés pour la calibration. Pour s'assurer de la validité des valeurs de paramètres choisies, il est nécessaire de valider toutes les variables simulées par le modèle, à l'échelle de l'organe et à l'échelle de la plante. Dans cette étude, nous avons évalué la capacité du modèle à simuler les dimensions finales de feuilles, leur composition proche de la ligulation (N total et sucres totaux), et des variables à l'échelle de la plante entière. Nous n'avons pas évalué la capacité du modèle à simuler les concentrations simulées en chacune des métabolites dans chaque organe, par manque de données expérimentales.

Temps de calcul et implémentation

Actuellement, le modèle a un temps de calcul élevé : ~1h30 pour la simulation présentée dans le chapitre 1, ~2h30 en moyenne pour une simulation du chapitre 2. Ce temps de calcul élevé est dû à la complexité du modèle : une moitié du temps de calcul est utilisée pour calculer la distribution du rayonnement au sein du couvert car celui-ci est représenté par un grand nombre d'éléments, l'autre moitié est utilisée pour résoudre le système d'équations différentielles relatives au métabolisme du carbone et de l'azote de chaque organe. Aussi, nous avons porté CN-Wheat sur un calculateur haute performance afin de réaliser de nombreuses simulations en parallèle. Néanmoins, le temps de calcul élevé limite le recourt à des techniques classiques de modélisation (analyse de sensibilité du modèle à ses paramètres, méthode d'ajustement automatique des paramètres).

Du fait du nombre élevé de processus pris en compte, le code de CN-Wheat est très long, ce qui rend difficile sa prise en main pour de nouveaux développements. Afin de faciliter la diffusion du modèle et sa réutilisabilité, le modèle a été implémenté selon une organisation modulaire *i.e.* le modèle est découpé en un ensemble de processus qui sont chacun implémentés sous forme d'un sous-modèle indépendant. Les sous-modèles échangent des données via une structure centrale qui stocke toutes les variables décrivant l'état de la plante (Multiscale Tree Graph). Ainsi, il est possible de réutiliser certains modules existants et de ne modifier que d'autres modules pour le transposer à une autre espèce. Toutefois, malgré la modularité, le couplage des sous-modèles de CN-Wheat à d'autres modèles (modèle de sol, maladies, transposition à d'autres espèces, *etc.*) demande un travail

d'implémentation important car les sous-modèles nécessitent un grand nombre de variables d'entrée qui sont très spécifiques.

3 - Perspectives d'utilisation et de développement de CN-Wheat

Une première partie présente les perspectives directes du modèle *i.e.* les utilisations possibles du modèle dans son état actuel. Nous présentons ensuite les perspectives d'extension du modèle pour simuler la totalité du cycle de développement de la plante. Puis, nous soulignons l'importance d'autres processus majeurs de la morphogénèse. Une ouverture à d'autres thématiques de recherche est alors proposée. Enfin, nous montrons comment CN-Wheat peut être facilement transposé à d'autres Poacées.

Perspectives directes

Un modèle pour explorer quantitativement le fonctionnement de la plante

CN-Wheat est un outil utile pour explorer le fonctionnement de la plante. En effet, CN-Wheat simule la cinétique des concentrations en métabolites carbonés et azotés dans la plante. Il est actuellement impossible d'acquérir expérimentalement cet ensemble de données avec des échelles spatiales et temporelles aussi fines que simulées par le modèle. Ainsi, au chapitre 1, nous avons utilisé les simulations de CN-Wheat pour analyser les relations source-puit au cours des stades végétatifs du blé.

De plus, CN-Wheat repose sur un certain nombre de lois de réponse aux concentrations locales. Comme mentionné plus haut, ces lois de réponses sont très exploratoires. Le modèle est donc un cadre pour tester des lois de réponses aux concentrations locales en métabolites carbonés et azotés, voir à d'autres facteurs. Il peut par exemple être utilisé pour proposer des hypothèses expérimentales.

Dans le cadre du changement climatique et des nouvelles pratiques culturales, le niveau original d'intégration de CN-Wheat en fait un bon outil pour explorer les réponses de la plante face à des stress multiples. Dans cette optique, CN-Wheat pourrait être utilisé pour tester des formalismes empiriques intégrés dans les modèles de culture, qui sont plus adaptés pour simuler le rendement.

Un modèle pour simuler des variations génotypiques

Théoriquement, les paramètres de notre modèle permettent de décrire des génotypes différents. Il n'est cependant pas démontré que les paramètres du modèle puissent être reliés à des informations génétiques telles que des allèles ou des QTL (Dingkuhn *et al.*, 2005; Muller and Martre, 2019), ou qu'ils puissent décrire précisément le comportement d'un génotype.

De nombreux travaux reposent sur l'hypothèse que les paramètres des modèles représentent bien des caractéristiques génotypiques (*e.g.* Dingkuhn *et al.*, 2005; Luquet *et al.*, 2012; Louarn *et al.*, 2020). Si on accepte cette hypothèse, CN-Wheat peut être utilisé pour explorer les conséquences de différences d'origine

génotypique sur la production. Ainsi, on peut identifier des idéotypes (Donald, 1968) qui maximisent la production pour des conditions de croissance données.

Perspectives d'extension du modèle à tout le cycle de développement de la plante

CN-Wheat permet actuellement de simuler de façon mécaniste la croissance du blé, depuis l'émergence de la feuille 4, jusqu'au début de l'allongement des entre-nœuds, puis les stades post-floraison. Un objectif est d'étendre le modèle à tout le cycle de développement de la plante.

Dans l'optique d'étudier la plasticité phénotypique du blé, il me semble que le premier processus à intégrer serait le tallage, puisque celui-ci varie fortement avec les conditions de croissances (Friend, 1965; Casal *et al.*, 1986; Longnecker *et al.*, 1993; Nelson, 2000; Evers *et al.*, 2006), impactant la cinétique d'interception de la lumière et l'allocation des ressources, et bien sur le nombre d'épis La façon d'aborder la modélisation du tallage a été développée dans la discussion du chapitre 2, à laquelle nous renvoyons pour plus de détails. En bref, le fonctionnement d'une talle peut être modélisé de la même façon que celui du maître-brin. Les processus à modéliser sont les déterminismes de l'émergence des talles, de l'arrêt du tallage et des flux entre talles. L'initialisation actuelle du modèle à l'émergence de la feuille 4 implique que le devenir des trois premières talles primaires est quasiment défini en entrée du modèle. Afin de simuler de façon mécaniste le déterminisme de l'émission des talles, il est donc nécessaire de modéliser aussi les phases précoces (germination, levée).

Une autre extension possible du modèle concerne la transition florale qui implique de nombreux changements : arrêt de production des feuilles, initiation de l'épi, allongement des entre-nœuds. Pour simuler la montaison, des formalismes de croissance des entre-nœuds ont déjà été proposé au chapitre 1. Ils sont largement inspirés des formalismes de la croissance des feuilles ; notamment, ils reposent sur des coordinations avec la ligulation des feuilles successives. Les formalismes proposés n'ont cependant pas été entièrement calibrés, ni validés. De plus, l'étude de trois jeux de données a montré que les coordinations et les cinétiques d'allongement retenues sont bien conservées pour les feuilles mais peu robustes pour les entre-nœuds. La prise en compte de la montaison nécessitera aussi de raffiner la description de la géométrie des plantes. En effet, au cours de la montaison, on observe que tous les axes d'une plante commencent à se redresser à l'arrêt du tallage pour attendre la position verticale à la ligulation de la feuille drapeau (Abichou, 2016). Ces résultats restent à implémenter afin de représenter de façon réaliste l'interception du rayonnement pendant la montaison.

La transition florale du méristème apical caulinaire détermine le nombre final de feuille et le début de la montaison. Les facteurs environnementaux impliqués dans la transition florale sont bien identifiés (température et photopériode) mais les lois de réponses permettant de quantifier la progression de la transition florale en conditions naturelles restent largement à déterminer (Robertson *et al.*, 1996; He *et al.*, 2011). La représentation fine des organes et de leur phylloclimat dans CN-Wheat fournit un cadre pertinent pour le couplage avec des modèles de transition florale existants (He *et al.*, 2011; Rouet *et al.*, 2020).

Le développement de l'appareil reproducteur représente un puit majeur pour les ressources au sein de la plante dès la montaison (allongement des entre-nœuds et développement de l'épi). Après la floraison (arrêt de

croissance des parties végétatives), la version initiale de CN-Wheat considère un épi photosynthétique (représenté en 3D par un cylindre), ainsi que des grains qui sont un compartiment du modèle avec une masse structurale, des protéines et de l'amidon. Dans ce cadre, modéliser le développement de l'épi nécessite de définir les formalismes de croissance en masse et en dimensions de l'épi jusqu'à la floraison. Une revue de la littérature à ce sujet est nécessaire pour synthétiser les connaissances et les données existantes. Les données à ce sujet sont nombreuses car la mise en place du rendement du blé est à forts enjeux.

D'autres facteurs clés de la morphogénèse pouvant être intégrés dans CN-Wheat

Pour le moment, la morphogénèse est pilotée dans CN-Wheat par les concentrations CN et par des règles de coordinations. Il existe cependant d'autres facteurs majeurs régulant la croissance ; nous citons ici le rôle de l'eau, la qualité de la lumière et des hormones.

Eau

L'eau est un des principaux facteurs limitant la croissance (Durand *et al.*, 1995; Pantin *et al.*, 2012). La croissance foliaire *per se*, c'est-à-dire l'expansion du volume cellulaire, est principalement due à l'augmentation de la teneur en eau des cellules (Schnyder and Nelson, 1988; Boyer and Silk, 2004). L'entrée d'eau dans les cellules en croissance implique que le potentiel hydrique de celles-ci soit plus faible que celui des tissus environnants. Il est donc nécessaire de représenter la topologie de la plante afin d'estimer l'entrée d'eau dans les zones de croissance, ce que propose CN-Wheat. De plus, il existe dans la plante de nombreuses interactions entre l'eau, le carbone et l'azote, notamment (i) au niveau des stomates qui régulent à la fois les entrées de CO_2 pour la photosynthèse et les pertes d'eau par transpiration ce qui a un impact direct sur le gradient de potentiel hydrique dans la plante ainsi que sur les températures d'organes, et (ii) via les concentrations en métabolites carbonés et azotés qui modulent le potentiel osmotique et donc l'influx d'eau dans les tissus (Fricke, 2019; Coussement *et al.*, 2020; Araus *et al.*, 2020). Une extension directe de CN-Wheat serait donc d'y introduire l'architecture hydraulique de la plante afin de rendre compte des interactions eau-carbone-azote sur la croissance foliaire. Le couplage entre CN-Wheat et l'eau est actuellement en cours (Barillot *et al.*, 2020*b*) dans le but d'étudier les effets du changement climatique (variations simultanées de la température, de l'eau et des concentrations atmosphériques en CO_2) sur la physiologie des prairies.

Qualité de la lumière

De par leurs propriétés optiques et leur géométrie (Chelle *et al.*, 2007), les feuilles absorbent et transmettent préférentiellement certaines longueurs d'onde, entrainant des gradients de composition spectrale au sein du couvert. Depuis le haut vers le bas du couvert, la fraction de rayonnement bleu et le rapport entre rouge clair et rouge sombre (RC/RS) diminuent (Varlet-Grancher *et al.*, 1993). Les variations de qualité de la lumière sont perçues par les plantes au niveau de photorécepteurs non-photosynthétiques, tels que les phytochromes, cryptochromes et phototropines (Ballaré and Casal, 2000), et entrainent des réponses spécifiques de la morphogénèse (photomorphogénèse) telle qu'une augmentation de la vitesse d'allongement des entre-nœuds ou encore de fortes variations du niveau de ramification (Ballaré and Pierik, 2017). Il a été en particulier montré

qu'une diminution du bleu entraine une augmentation de la vitesse d'allongement des feuilles de rye-gras et de fétuque (Gautier and Varlet-Grancher, 1996), et une augmentation du phyllochrone chez le blé (Barnes and Bugbee, 1992). De plus, une diminution du RC/RS réduit le nombre de talles de nombreuses espèces de Poacées (Gautier *et al.*, 1999; Evers *et al.*, 2006). La qualité de la lumière est donc un facteur important de la morphogénèse.

Des modèles simulant la distribution du bleu et du RC/RS au sein de couvert 3D (*e.g.* Chelle *et al.*, 2007) ont été développés dans le but d'étudier les réponses de la plante à la qualité de la lumière. Toutefois, en conditions naturelles, les variations de qualité de lumière sont concomitantes à des variations d'accès aux ressources carbonées et azotées. CN-Wheat serait donc un outil utile pour intégrer les interactions entre la photomorphogénèse et l'état trophique de la plante.

Hormones

Une extension possible de CN-Wheat serait d'introduire le métabolisme secondaire pour piloter la croissance par des hormones afin d'améliorer la simulation de certains processus tels que l'allongement des entre-nœuds.

Peu de modèles à l'échelle de la plante intègrent le métabolisme d'hormones et leur rôle sur la morphogénèse. On peut citer les travaux de Buck-Sorlin *et al.* (2005) qui ont simulé la variabilité génotypique d'allongement des entre-nœuds chez l'orge à partir de la production et de la répartition d'hormones dans la plante ; toutefois, le rôle des disponibilités en carbone et en azote n'est ici pas intégré. On peut aussi citer le modèle de Schneider (2020) qui simule le débourrement des bourgeons de rosiers en fonction des teneurs locales en sucres et en hormones. Il est jusqu'à présent difficile d'intégrer les hormones dans des approches quantitatives (en particulier dans des approches couplées au métabolisme primaire) puisque les connaissances sur le métabolisme des hormones ainsi que sur les mécanismes par lesquels les hormones régulent la morphogenèse sont beaucoup plus limitées que les connaissances sur les métabolites secondaires. Dans ce contexte, notre modèle est utile pour tester les formalismes présumés et l'impact potentiel quantifié des hormones sur la croissance et la plasticité phénotypique.

Actuellement, CN-Wheat considère l'action des cytokinines qui ont été introduites dans la version initiale du modèle (Barillot *et al.*, 2016*a*) pour simuler de façon réaliste la dynamique de sénescence des feuilles. Cependant, on pourrait vouloir étendre leurs actions dans le modèle puisque les cytokinines sont impliquées dans d'autres processus de la morphogénèse tels que les divisions cellulaires (Werner *et al.*, 2001; Farnsworth, 2004) et la croissance racinaire (Werner *et al.*, 2010). De plus, d'autres hormones avec un rôle dans la morphogénèse ont été identifiées, par exemple les gibbérellines (Botwright *et al.*, 2005; Buck-Sorlin *et al.*, 2005).

Avec les cytokinines, CN-Wheat propose un cadre pour introduire les régulations hormonales, en interaction avec les régulations trophiques. CN-Wheat intègre de façon très simplifiée le métabolisme des cytokinines et leur action sur le métabolisme primaire. Les formalismes choisis dans CN-Wheat sont très simplifiés (pas de diversité de forme de cytokinines notamment) mais représentent un cadre général possible pour le couplage entre le métabolisme primaire et le métabolisme secondaire (régulateur de croissance, composés de défense, COV, *etc.*).

Les objectifs d'un tel couplage sont de mieux prédire la production des métabolites secondaires (et donc leurs actions), et, en retour, de prendre en compte le coût de leur production en termes de carbone et d'azote. Ainsi, on propose que les hormones soient représentées dans le modèle de la même façon que les métabolites carbonés et azotés (synthèse, dégradation, flux). Leurs interactions avec le métabolisme primaire sont modélisées par (i) la régulation de leur production par les concentrations en métabolites carbonés et azotés, et (ii) la régulation des paramètres de synthèse/dégradation des métabolites carbonés et azotés par la concentration en hormones. Une perspective de modélisation est de réguler des paramètres de croissance des organes (*e.g.* les entre-nœuds) par la concentration d'hormone(s).

D'autres thématiques de recherche pouvant bénéficier de notre modèle

Dans cette partie, nous illustrons brièvement des applications potentielles de CN-Wheat à d'autres thématiques de recherche.

Cultures associées

Les cultures associées (peuplements plurispécifiques ou plurivariétaux) sont un thème de recherche relativement récent qui s'inscrit dans la transition agroécologique (Gaba *et al.*, 2015; Gaudio *et al.*, 2019). Il est attendu que les cultures associées soient plus résilientes et durables. La mise en place de culture associées soulève les questions des espèces/variétés à associer, des dates et densité de semis et de leur arrangement spatial. Un des enjeux consiste à assurer la coexistence des cultures et donc comprendre la compétition au sein du couvert. Dans ce contexte, CN-Wheat semble être outil utile pour explorer le fonctionnement du couvert et identifier des traits de plantes favorables aux associations.

Communication entre plantes

Les plantes émettent des Composés Organiques Volatiles (COV) qui peuvent être perçus par les plantes voisines comme un signal entrainant alors une réponse physiologique de défense, d'évitement ou de croissance préférentielle, face à un stress biotique ou abiotique (Ninkovic *et al.*, 2020). Par exemple, (Ninkovic, 2003) a montré qu'un cultivar d'orge exposé à des COV provenant d'un autre cultivar d'orge allouait plus de biomasse à ses racines. Une question est de savoir comment les plantes intègrent les différents signaux COV et trophiques, notamment pour trouver un compromis entre croissance et défense face aux stress. La modélisation peut permettre d'aborder cette question (*e.g.* Douma *et al.*, 2017). Puisque CN-Wheat simule avec un haut degré de mécanisme la plasticité phénotypique de la plante, notre modèle semble être un cadre intéressant pour aborder cette question.

Interactions plante – microorganismes du sol

La plante apporte du carbone et de l'azote au sol via les tissus sénescents (litière) et la rhizodéposition, dont fait partie l'exsudation racinaire. Les microorganismes du sol se nourrissent de ces apports. Certains microorganismes du sol (symbiotes) s'associent aux racines des céréales et améliorent leur acquisition de l'azote (Courty *et al.*, 2015; Wang *et al.*, 2020). Il existe donc des interactions entre la plante et ses symbiotes. La

compréhension des liens trophiques entre racines et symbiotes peut être appréhendée par une approche de modélisation intégrant les interactions plante – symbiotes. Dans ce contexte, CN-Wheat apparaît être un outil utile puisqu'il simule le métabolisme du carbone et de l'azote de la plante sans règle *a priori* de répartition de la biomasse au sein de la plante. CN-Wheat simule notamment que l'exsudation racinaire représente une perte importante de carbone (~10 % du carbone fixé par photosynthèse ; Figure 1.15A). Toutefois, comme discuté au chapitre 2, des développements du modèle sont nécessaires pour prendre en compte une architecture racinaire explicite et formaliser les processus de sénescence racinaire. Dans l'optique d'étudier les interactions plante – microorganismes du sol, Rees *et al.* (2020*b*) ont proposé un couplage entre CN-Wheat, un modèle architecturé de l'appareil racinaire, et un modèle de répartition spatiale de l'exsudation racinaire (Rees *et al.*, 2020*a*).

CN-Wheat peut être facilement transposé à la plupart des Poacées

Pour transposer CN-Wheat à d'autres Poacées, les hypothèses sous-jacentes du modèle doivent être valides sur les espèces considérées. L'hypothèse selon laquelle la croissance dépend des concentrations locales en métabolites carbonés et azotés est valide pour toutes les plantes car ce sont les principaux constituants de la biomasse. L'hypothèse selon laquelle le timing de croissance est défini par des règles de coordinations entre les feuilles successives semblent être valide pour un grand nombre de Poacées, malgré la large diversité d'habitats, de traits architecturaux et de fonctionnement. En effet, les règles de coordination reposent sur le fait que les feuilles poussent à l'intérieur d'une pseudo-tige constituée des gaines des feuilles précédentes, ce qui est une caractéristique commune à de nombreuses Poacées. Des modèles qui simulent l'allongement des feuilles sur la base des règles de coordination dépendantes de l'émergence des organes ont déjà été construits sur le ray-grass (Verdenal *et al.*, 2008) et le maïs (Zhu *et al.*, 2014; Vidal and Andrieu, 2020). En outre, des synchronismes entre l'émergence d'une feuille et l'allongement d'autres feuilles ont également été relevés pour d'autres Poacées telles que la fétuque élevée (Skinner and Nelson, 1995) et le sorgho (Nakamura *et al.*, 2011). Par conséquent, notre modèle apparaît comme générique à la plupart des espèces de Poacées telles que le maïs, le sorgho et les Poacées pérennes. Toutefois, en raison de la grande diversité de structures et de fonctions des espèces de Poacées, certains aspects clés doivent être pris en compte lors de l'adaptation du CN-Wheat ; nous abordons ci-dessous deux aspects principaux.

Un premier aspect concerne les différences de structure de pseudo-tige qui impliquent des difficultés expérimentales pour définir les règles de coordination reposant sur l'émergence des organes. Le blé a une pseudo-tige étroite ce qui implique que l'émergence d'une feuille, *i.e.* lorsque sa pointe dépasse la plus haute ligule, est synchrone à son apparition, *i.e.* lorsqu'elle est visible par l'expérimentateur sans dissection. Au contraire, la pseudo-tige du maïs est large, et est surplombée par un tube (cornet) formé par les limbes des feuilles en croissance qui se déroulent progressivement au cours de leur allongement. Les feuilles apparaissent alors après un délai variable suivant leur émergence (Fournier and Andrieu, 2000; Vidal and Andrieu, 2020).

Un autre aspect essential concerne les différences de structure et de fonctionnement racinaire entre les Poacées pérennes et les annuelles. Il est admis que les Poacées annuelles sont caractérisées par des traits aériens et racinaires typiques des espèces à croissance rapide, qui tendent à maximiser l'acquisition de ressources, à savoir

des feuilles fines et riches en N, des racines peu denses et riches en N. Les Poacées annuelles sont quant à elles caractérisées par des traits typiques des espèces à croissance lente, qui tendent à maximiser la conservation des ressources (Roumet *et al.*, 2006). Puisque CN-Wheat considère une architecture aérienne explicite, l'adaptation du modèle à d'autres traits foliaires consiste à calibrer les paramètres impliqués dans la formation de ces traits, qui ont un sens biologique précis. Au contraire, CN-Wheat ne considère pas d'architecture racinaire explicite ; l'adaptation du modèle à des traits racinaires de Poacées pérennes peut donc être plus complexes voire nécessiter de modifier les formalismes existants.

Conclusion générale

La présente étude a principalement permis de progresser dans l'intégration mécaniste des réponses de la morphogénèse aux conditions de croissance. Le modèle développé au cours de l'étude intègre, à l'échelle de la plante entière, les interactions entre l'architecture et l'environnement grâce à deux principaux moteurs (i) les concentrations locales en métabolites carbonés et azotés qui pilotent les vitesses d'allongement et de traits foliaires clés, (ii) des règles de coordinations entre les feuilles successives qui déterminent les durées de croissance des feuilles et le moment de définition de traits foliaires clé.

Les prochains travaux à mener sont de trois ordres : (i) réaliser des expérimentations pour calibrer plus finement le modèle (voire l'améliorer) et le valider, (ii) développer le modèle pour inclure de nouveaux processus et (iii) explorer le comportement du modèle. Il serait intéressant d'explorer le comportement du modèle pour démontrer de façon concrète son utilité. Toutefois, un prérequis nécessaire est, selon moi, une validation plus poussée du modèle, notamment en confrontant les simulations à des observations dans des conditions de croissance contrastées. Cette validation expérimentale est aujourd'hui limitée, d'un part par le manque de données expérimentales, d'autre part, par l'absence dans le modèle d'un module décrivant le tallage. De ce fait, les simulations ne peuvent être comparées à des expérimentations que pour des conditions de croissance très particulières, dans lesquelles le tallage est inhibé. Aussi, il me semble que la perspective prioritaire est de formaliser les déterminismes du tallage (et donc de la germination), conjointement à la réalisation d'expérimentations dédiées à l'évaluation du modèle.

Références

Abichou M. 2016. Modélisation de l'architecture 4D du blé : Identification des patterns dans la morphologie, la sénescence et le positionnement spatial des organes pour une large gamme de situations de croissance. PhD thesis, Université Paris-Saclay, Paris, France.

Abichou M, Fournier C, Dornbusch T, Chambon C, Baccar R, Bertheloot J, Vidal T, Robert C, Gouache D, Andrieu B. 2013. Reparametrisation of Adel-wheat allows reducing the experimental effort to simulate the 3D development of winter wheat. FSPM2013 Proceedings. Finland, 304–306.

Abichou M, Fournier C, Dornbusch T, Chambon C, de Solan B, Gouache D, Andrieu B. 2018. Parameterising wheat leaf and tiller dynamics for faithful reconstruction of wheat plants by structural plant models. Field Crops Research **218**, 213–230.

Abichou M, de Solan B, Andrieu B. 2019. Architectural Response of Wheat Cultivars to Row Spacing Reveals Altered Perception of Plant Density. Frontiers in Plant Science **10**.

Aerts R. 1996. Nutrient Resorption from Senescing Leaves of Perennials: Are there General Patterns? Journal of Ecology **84**, 597–608.

Akmal M, Janssens MJJ. 2004. Productivity and light use efficiency of perennial ryegrass with contrasting water and nitrogen supplies. Field Crops Research **88**, 143–155.

Albasha R, Fournier C, Pradal C, Chelle M, Prieto JA, Louarn G, Simonneau T, Lebon E. 2019. HydroShoot: a functional-structural plant model for simulating hydraulic structure, gas and energy exchange dynamics of complex plant canopies under water deficit—application to grapevine (*Vitis vinifera*). in silico Plants **1**, diz007.

Allard G, Nelson CJ, Pallardy SG. 1991. Shade Effects on Growth of Tall Fescue: I. Leaf Anatomy and Dry Matter Partitioning. Crop Science **31**, 163–167.

Altieri MA, Nicholls CI, Henao A, Lana MA. 2015. Agroecology and the design of climate change-resilient farming systems. Agronomy for sustainable development **35**, 869–890.

Anderson LS, Dale JE. 1983. The Sources of Carbon for Developing Leaves of Barley. Journal of Experimental Botany **34**, 405–414.

Andrieu B, Hillier J, Birch C. 2006. Onset of sheath extension and duration of lamina extension are major determinants of the response of maize lamina length to plant density. Annals of Botany **98**, 1005–1016.

Anten NPR, Schieving F, Werger MJA. 1995. Patterns of light and nitrogen distribution in relation to whole canopy carbon gain in C3 and C4 mono- and dicotyledonous species. Oecologia **101**, 504–513.

Araus V, Swift J, Alvarez JM, Henry A, Coruzzi GM. 2020. A balancing act: how plants integrate nitrogen and water signals. Journal of Experimental Botany **71**, 4442–4451.

Asseng S, Richter C, Wessolek G. 1997. Modelling root growth of wheat as the linkage between crop and soil. Plant and Soil **190**, 267–277.

Asseng S, Zhu Y, Wang E, Zhang W. 2015. Crop modeling for climate change impact and adaptation. In: Sadras VO,, In: Calderini DF, eds. Crop Physiology (Second Edition). San Diego: Academic Press, 505–546.

Atkin OK, Millar AH, Gardeström P, Day DA. 2000. Photosynthesis, Carbohydrate Metabolism and Respiration in Leaves of Higher Plants. In: Leegood RC,, In: Sharkey TD,, In: Caemmerer S von, eds. Photosynthesis. Netherlands: Springer, 153–175.

Azcón-Bieto J. 1983. Inhibition of Photosynthesis by Carbohydrates in Wheat Leaves. Plant Physiology **73**, 681–686.

Baccar R. 2011. Plasticité de l'architecture du blé d'hiver modulée par la densité et la date de semis et son effet sur les épidémies de *Septoria tritici*. PhD thesis, AgroParisTech, Paris, France.

Ball JT, Woodrow IE, Berry JA. 1987. A model predicting stomatal conductance and its contribution to the control of photosynthesis under different environmental conditions. In: Biggins J, ed. Proceedings of the 7th International congress on photosynthesis. Providence, Rhode Island, USA: Springer Netherlands, 221–224.

Ballaré CL, Casal JJ. 2000. Light signals perceived by crop and weed plants. Field Crops Research **67**, 149–160.

Ballaré CL, Pierik R. 2017. The shade-avoidance syndrome: multiple signals and ecological

consequences. Plant, Cell & Environment **40**, 2530–2543.

Bancal P, Gaudillère JP. 1989. Rate of accumulation of fructan oligomers in wheat seedlings (*Triticum aestivum* L.) during the early stages of chilling treatment. New Phytologist **112**, 459–463.

Barillot R, Chambon C, Andrieu B. 2016*a*. CN-Wheat, a functional–structural model of carbon and nitrogen metabolism in wheat culms after anthesis. I. Model description. Annals of Botany **118**, 997–1013.

Barillot R, Chambon C, Andrieu B. 2016*b*. CN-Wheat, a functional–structural model of carbon and nitrogen metabolism in wheat culms after anthesis. II. Model evaluation. Annals of Botany **118**, 1015–1031.

Barillot R, Chambon C, Fournier C, Combes D, Pradal C, Andrieu B. 2019. Investigation of complex canopies with a functional–structural plant model as exemplified by leaf inclination effect on the functioning of pure and mixed stands of wheat during grain filling. Annals of Botany **123**, 727–742.

Barillot R, De Swaef T, Combes D, Durand J-L, Escobar-Gutierrez AJ, Martre P, Perrot C, Roy E, Frak E. 2020*a*. Leaf elongation response to blue light is mediated by stomatal-induced variations in plant transpiration in *Festuca arundinacea*. Journal of Experimental Botany ***in press***.

Barillot R, Escobar-Gutiérrez AJ, Fournier C, Huynh P, Combes D. 2014. Assessing the effects of architectural variations on light partitioning within virtual wheat–pea mixtures. Annals of Botany **114**, 725–737.

Barillot R, Gauthier M, Andrieu B, Durand J-L, Roldán-Ruiz I, Swaef T. 2020*b*. Integrating the complex regulation of leaf growth by water and trophic dynamics in a functional-structural plant model of grass. Virtual: Katrin Kahlen, Tsu-Wei Chen, Andreas Fricke & Hartmut Stützel, 174.

Barnes C, Bugbee B. 1992. Morphological responses of wheat to blue light. Journal of Plant Physiology **139**, 339–342.

Basso B, Sartori L, Cammarano D, Fiorentino C, Grace PR, Fountas S, Sorensen CA. 2012. Environmental and economic evaluation of N fertilizer rates in a maize crop in Italy: A spatial and temporal analysis using crop models. Biosystems Engineering **113**, 103–111.

Baumont M, Parent B, Manceau L, Brown H, Driever SM, Muller B, Martre P. 2019. Experimental and modeling evidence of carbon limitation of leaf appearance rate for spring and winter wheat. Journal of Experimental Botany **70**, 2449–2462.

Beemster GTS, Masle J. 1996. Effects of soil resistance to root penetration on leaf expansion in wheat (*Triticum aestivum* L.): composition, number and size of epidermal cells in mature blades. Journal of Experimental Botany **47**, 1651–1662.

Begg JE, Wright MJ. 1962. Growth and Development of Leaves from Intercalary Meristems in *Phalaris arundinacea* L. Nature **194**, 1097.

Bélanger G, Gastal F, Lemaire G. 1992. Growth Analysis of a Tall Fescue Sward Fertilized with Different Rates of Nitrogen. Crop Science **32**, 1371–1376.

Bergmeyer HU, Bernt E, Schmidt F, Stork H. 1974. D-glucose. Determination with hexokinase and glucose-6-phosphate dehydrogenase. Methods for enzymatic analysis. Vol. 3. Academic Press, New York: H. U. Bergmeyer, 1166–1201.

Bertheloot J. 2009. Distribution de l'azote chez le blé (*Triticum aestivum* L.) après la floraison : un modèle dynamique fondé sur une approche structure-fonction. PhD thesis, AgroParisTech, Paris, France.

Bertheloot J, Andrieu B, Martre P. 2012. Light–nitrogen relationships within reproductive wheat canopy are modulated by plant modular organization. European Journal of Agronomy **42**, 11–21.

Bertheloot J, Cournède P-H, Andrieu B. 2011. NEMA, a functional–structural model of nitrogen economy within wheat culms after flowering. I. Model description. Annals of Botany **108**, 1085–1096.

Bertin N, Gary C. 1998. Short and long term fluctuations of the leaf mass per area of tomato plants—implications for growth models. Annals of Botany **82**, 71–81.

Bloom AJ, Chapin III FS, Mooney HA. 1985. Resource limitation in plants-an economic analogy. Annual review of Ecology and Systematics **16**, 363–392.

Boone MYL, Whisler FD, Rickman RW. 1990. Leaf appearance rates of two winter wheat cultivars

under high carbon dioxide conditions. Agronomy Journal **82**, 718–724.

Boote KJ, Jones JW, White JW, Asseng S, Lizaso JI. 2013. Putting mechanisms into crop production models. Plant, Cell & Environment **36**, 1658–1672.

Bos HJ, Neuteboom JH. 1998. Growth of Individual Leaves of Spring Wheat (*Triticum aestivum* L.) as Influenced by Temperature and Light Intensity. Annals of Botany **81**, 141–149.

Bos HJ, Tijani-Eniola H, Struik PC. 2000. Morphological analysis of leaf growth of maize: responses to temperature and light intensity. NJAS wageningen journal of life sciences **48**, 181–198.

Botwright TL, Rebetzke GJ, Condon AG, Richards RA. 2005. Influence of the gibberellin-sensitive Rht8 dwarfing gene on leaf epidermal cell dimensions and early vigour in wheat (*Triticum aestivum* L.). Annals of Botany **95**, 631–639.

Boyer JS, Silk WK. 2004. Hydraulics of plant growth. Functional plant biology **31**, 761–773.

Braune H, Müller J, Diepenbrock W. 2009. Integrating effects of leaf nitrogen, age, rank, and growth temperature into the photosynthesis-stomatal conductance model LEAFC3-N parameterised for barley (*Hordeum vulgare* L.). Ecological Modelling **220**, 1599–1612.

Bregard A, Allard G. 1999. Sink to source transition in developing leaf blades of tall fescue. New Phytologist **141**, 45–50.

Buck-Sorlin GH, Kniemeyer O, Kurth W. 2005. Barley morphology, genetics and hormonal regulation of internode elongation modelled by a relational growth grammar. New Phytologist **166**, 859–867.

Burnett AC, Rogers A, Rees M, Osborne CP. 2016. Carbon source–sink limitations differ between two species with contrasting growth strategies. Plant, Cell & Environment **39**, 2460–2472.

Caemmerer SV. 2000. *Biochemical Models of Leaf Photosynthesis*. Csiro Publishing.

Cai C, Yin X, He S, *et al.* 2016. Responses of wheat and rice to factorial combinations of ambient and elevated CO2 and temperature in FACE experiments. Global Change Biology **22**, 856–874.

Calderini DF, Dreccer MF, Slafer GA. 1997. Consequences of breeding on biomass, radiation interception and radiation-use efficiency in wheat. Field Crops Research **52**, 271–281.

Casal JJ, Sanchez RA, Deregibus VA. 1986. The effect of plant density on tillering: The involvement of R/FR ratio and the proportion of radiation intercepted per plant. Environmental and Experimental Botany **26**, 365–371.

Casey IA, Brereton AJ, Laidlaw AS, McGilloway DA. 1999. Effects of sheath tube length on leaf development in perennial ryegrass (*Lolium perenne* L.). Annals of Applied Biology **134**, 251–257.

Chang T-G, Zhu X-G. 2017. Source–sink interaction: a century old concept under the light of modern molecular systems biology (C Raines, Ed.). Journal of Experimental Botany **68**, 4417–4431.

Charles-Edwards DA, Stutzel H, Ferraris R, Beech DF. 1987. An analysis of spatial variation in the nitrogen content of leaves from different horizons within a canopy. Annals of Botany **60**, 421–426.

Chelle M. 2005. Phylloclimate or the climate perceived by individual plant organs: What is it? How to model it? What for? New Phytologist **166**, 781–790.

Chelle M, Andrieu B. 1998. The nested radiosity model for the distribution of light within plant canopies. Ecological Modelling **111**, 75–91.

Chelle M, Andrieu B. 1999. Radiative models for architectural modeling. Agronomie **19**, 225–240.

Chelle M, Evers JB, Combes D, Varlet-Grancher C, Vos J, Andrieu B. 2007. Simulation of the three-dimensional distribution of the red:far-red ratio within crop canopies. New Phytologist **176**, 223–234.

Christophe A, Moulia B, Varlet-Grancher C. 2006. Quantitative contributions of blue light and PAR to the photocontrol of plant morphogenesis in *Trifolium repens* (L.). Journal of Experimental Botany **57**, 2379–2390.

Coucheney E, Buis S, Launay M, *et al.* 2015. Accuracy, robustness and behavior of the STICS soil–crop model for plant, water and nitrogen outputs: Evaluation over a wide range of agro-environmental conditions in France. Environmental Modelling & Software **64**, 177–190.

Courty PE, Smith P, Koegel S, Redecker D, Wipf D. 2015. Inorganic nitrogen uptake and transport in beneficial plant root-microbe interactions. Critical Reviews in Plant Sciences **34**, 4–16.

Coussement JR, De Swaef T, Lootens P, Roldán-Ruiz I, Steppe K. 2018. Introducing turgor-driven growth dynamics into functional–structural plant models. Annals of botany **121**, 849–861.

Coussement JR, De Swaef T, Lootens P, Steppe K. 2020. Turgor-driven plant growth applied in a soybean functional–structural plant model. Annals of Botany **126**, 729–744.

Cutforth HW, Jame YW, Jefferson PG. 1992. Effect of temperature, vernalization and water stress on phyllochron and final main-stem leaf number of HY320 and Neepawa spring wheats. Canadian Journal of Plant Science **72**, 1141–1151.

Dale JE. 1982. Some Effects of Temperature and Irradiance on Growth of the First Four Leaves of Wheat, *Triticum aestivum*. Annals of Botany **50**, 851–858.

Dale JE. 1985. The carbon relations of the developing leaf. Control of Leaf Growth. Baker NR, Davies WJ, Ong CK, 135–153.

Dale JE, Felippe GM, Fletcher GM. 1972. Effects of Shading the First Leaf on Growth of Barley PlantsI. Long-term Experiments. Annals of Botany **36**, 385–395.

De Reffye P, Hu B-G. 2003. Relevant qualitative and quantitative choices for building an efficient dynamic plant growth model: GreenLab case. International Symposium on Plant Growth Modeling, Simulation, Visualization and their Applications-PMA'03. Springer and Tsinghua University Press, 87–107.

Deacon JW, Mitchell RT. 1985. Comparison of rates of natural senescence of the root cortex of wheat (with and without mildew infection), barley, oats and rye. Plant and Soil **84**, 129–131.

DeJong TM, Da Silva D, Vos J, Escobar-Gutiérrez AJ. 2011. Using functional–structural plant models to study, understand and integrate plant development and ecophysiology. Annals of Botany **108**, 987–989.

Delhon P, Gojon A, Tillard P, Passama L. 1996. Diurnal regulation of NO- 3 uptake in soybean plants IV. Dependence on current photosynthesis and sugar availability to the roots. Journal of Experimental Botany **47**, 893–900.

Devienne F, Mary B, Lamaze T. 1994. Nitrate transport in intact wheat roots: II. Long-term effects of NO3− concentration in the nutrient solution on NO3− unidirectional fluxes and distribution within the tissues. Journal of Experimental Botany **45**, 677–684.

Devienne-Barret F, Justes E, Machet JM, Mary B. 2000. Integrated Control of Nitrate Uptake by Crop Growth Rate and Soil Nitrate Availability under Field Conditions. Annals of Botany **86**, 995–1005.

Díaz-Francés E, Rubio FJ. 2013. On the existence of a normal approximation to the distribution of the ratio of two independent normal random variables. Statistical Papers **54**, 309–323.

Dingkuhn M, Luquet D, Fabre D, Muller B, Yin X, Paul MJ. 2020. The case for improving crop carbon sink strength or plasticity for a CO2-rich future. Current Opinion in Plant Biology **56**, 259–272.

Dingkuhn M, Luquet D, Quilot B, de Reffye P. 2005. Environmental and genetic control of morphogenesis in crops: towards models simulating phenotypic plasticity. Australian Journal of Agricultural Research **56**, 1289–1302.

Doddema H, Telkamp GP. 1979. Uptake of Nitrate by Mutants of Arabidopsis thaliana, Disturbed in Uptake or Reduction of Nitrate. Physiologia Plantarum **45**, 332–338.

Donald C t. 1968. The breeding of crop ideotypes. euphytica **17**, 385–403.

Dornbusch T, Andrieu B. 2010. Lamina2Shape--An image processing tool for an explicit description of lamina shape tested on winter wheat (*Triticum aestivum* L.). Computers and Electronics in Agriculture **70**, 217–224.

Dornbusch T, Baccar R, Watt J, Hillier J, Bertheloot J, Fournier C, Andrieu B. 2011. Plasticity of winter wheat modulated by sowing date, plant population density and nitrogen fertilisation: Dimensions and size of leaf blades, sheaths and internodes in relation to their position on a stem. Field Crops Research **121**, 116–124.

Douma JC, Vermeulen PJ, Poelman EH, Dicke M, Anten NPR. 2017. When does it pay off to prime for defense? A modeling analysis. New Phytologist **216**, 782–797.

Dreccer MF, van Oijen M, Schapendonk AHCM, Pot CS, Rabbinge R. 2000. Dynamics of Vertical Leaf Nitrogen Distribution in a Vegetative Wheat Canopy. Impact on Canopy Photosynthesis. Annals of Botany **86**, 821–831.

Drouet J-L, Bonhomme R. 1999. Do variations in local leaf irradiance explain changes to leaf nitrogen within row maize canopies? Annals of Botany **84**, 61–69.

Drouet J-L, Duretz S, Fiorelli J-L, Gabrielle B, Blanfort V, Cellier P, Capitaine M, Soussana J-F. 2008. A farm level tool coupling farm, cropland and grassland models to assess the effect of farming practices on reactive nitrogen emissions and greenhouse gas balance and to define mitigation strategies. Reactive Nitrogen and the European Greenhouse Gas Balance. NitroEurope IP Open Science Conference. Ghent, Belgium, np.

Drouet J-L, Pagès L. 2007. GRAAL-CN: A model of GRowth, Architecture and ALlocation for Carbon and Nitrogen dynamics within whole plants formalised at the organ level. Ecological Modelling **206**, 231–249.

Dumas JBA. 1831. Procédés de l'analyse organique. Ann. Chem. Phys. **47**, 198–213.

Duncan WG, Shaver DL, Williams WA. 1973. Insolation and Temperature Effects on Maize Growth and Yield. Crop Science **13**, 187–191.

Durand J-L, Onillon B, Schnyder H, Rademacher I. 1995. Drought effects on cellular and spatial parameters of leaf growth in tall fescue. Journal of Experimental Botany, 1147–1155.

Durand JL, Schäufele R, Gastal F. 1998. Modeling the elongation of successive leaves on grass tillers. Effect of temperature, cutting height and cutting frequency.141–142.

Durand J-L, Schäufele R, Gastal F. 1999. Grass leaf elongation rate as a function of developmental stage and temperature: morphological analysis and modelling. Annals of Botany **83**, 577–588.

Ellen J, Van Oene H. 1989. Effects of light intensity on nitrogen economy of spring barley (*Hordeum distichum* L.). Netherlands Journal of Agricultural Science **37**, 205–211.

Evans JR. 1983. Nitrogen and photosynthesis in the flag leaf of wheat (*Triticum aestivum* L.). Plant physiology **72**, 297–302.

Evans JR. 1989. Photosynthesis and nitrogen relationships in leaves of C3 plants. Oecologia **78**, 9–19.

Evers JB, Vos J, Andrieu B, Struik PC. 2006. Cessation of tillering in spring wheat in relation to light interception and red: far-red ratio. Annals of Botany **97**, 649–658.

Evers JB, Vos J, Fournier C, Andrieu B, Chelle M, Struik PC. 2005. Towards a generic architectural model of tillering in Gramineae, as exemplified by spring wheat (*Triticum aestivum*). New Phytologist **166**, 801–812.

Evers JB, Vos J, Fournier C, Andrieu B, Chelle M, Struik PC. 2007. An architectural model of spring wheat: Evaluation of the effects of population density and shading on model parameterization and performance. Ecological Modelling **200**, 308–320.

Evers JB, Vos J, Yin X, Romero P, van der Putten PEL, Struik PC. 2010. Simulation of wheat growth and development based on organ-level photosynthesis and assimilate allocation. Journal of Experimental Botany **61**, 2203–2216.

Fabre D, Yin X, Dingkuhn M, Clément-Vidal A, Roques S, Rouan L, Soutiras A, Luquet D, Lawson T. 2019. Is triose phosphate utilization involved in the feedback inhibition of photosynthesis in rice under conditions of sink limitation. Journal of Experimental Botany **70**, 5773–5785.

Farnsworth E. 2004. Hormones and shiftlng ecology throughout plant development. Ecology **85**, 5–15.

Farquhar GD, Caemmerer S von, Berry JA. 1980. A biochemical model of photosynthetic CO2 assimilation in leaves of C3 species. Planta **149**, 78–90.

Faverjon L, Escobar-Gutiérrez A, Litrico I, Julier B, Louarn G. 2019. A generic individual-based model can predict yield, nitrogen content, and species abundance in experimental grassland communities. Journal of experimental botany **70**, 2491–2504.

Felippe GM, Dale JE. 1973. Effects of Shading the First Leaf of Barley Plants on Growth and Carbon Nutrition of the Stem Apex. Annals of Botany **37**, 45–56.

Fournier C. 2000. Modélisation des interactions entre plantes au sein des peuplements. Application à la simulation des régulations de la morphogenèse aérienne du maïs (*Zea mays* L.) par la compétition

pour la lumière. PhD thesis, Institut National Agronomique Paris-Grignon, Paris, France.

Fournier C, Andrieu B. 2000. Dynamics of the elongation of internodes in maize (*Zea mays* L.): analysis of phases of elongation and their relationships to phytomer development. Annals of Botany **86**, 551–563.

Fournier C, Andrieu B, Ljutovac S, Saint-Jean S. 2003. ADEL-Wheat: a 3D Architectural Model of wheat development. , 54–63.

Fournier C, Andrieu B, Sohbi Y. 2001. Virtual plant models for studying interactions between crops and environment. Proceedings of the 13th European Simulation Symposium. Simulation in Industry. Marseilles, France: Giambiasi, N., Frydman, C., 476–480.

Fournier C, Durand JL, Ljutovac S, Schäufele R, Gastal F, Andrieu B. 2005. A functional–structural model of elongation of the grass leaf and its relationships with the phyllochron. New Phytologist **166**, 881–894.

Fournier C, Pradal C, Louarn G, Combes D, Soulié J-C, Luquet D, Boudon F, Chelle M. 2010. Building modular FSPM under OpenAlea: concepts and applications

Foyer CH, Ferrario-Méry S, Huber SC. 2000. Regulation of Carbon Fluxes in the Cytosol: Coordination of Sucrose Synthesis, Nitrate Reduction and Organic Acid and Amino Acid Biosynthesis. In: Leegood RC,, In: Sharkey TD,, In: Caemmerer S von, eds. Photosynthesis. Springer Netherlands, 177–203.

Franklin O, Ågren GI. 2002. Leaf senescence and resorption as mechanisms of maximizing photosynthetic production during canopy development at N limitation. Functional Ecology, 727–733.

Fricke W. 2002. Biophysical limitation of leaf cell elongation in source-reduced barley. Planta **215**, 327–338.

Fricke W. 2019. Night-Time Transpiration – Favouring Growth? Trends in Plant Science **24**, 311–317.

Fricke W, Flowers TJ. 1998. Control of leaf cell elongation in barley. Generation rates of osmotic pressure and turgor, and growth-associated water potential gradients. Planta **206**, 53–65.

Fricke W, McDonald AJS, Mattson-Djos L. 1997. Why do leaves and leaf cells of N-limited barley elongate at reduced rates? Planta **202**, 522–530.

Friedli CN, Abiven S, Fossati D, Hund A. 2019. Modern wheat semi-dwarfs root deep on demand: response of rooting depth to drought in a set of Swiss era wheats covering 100 years of breeding. Euphytica **215**, 85.

Friend DJC. 1965. Tillering and leaf production in wheat as affacted by temperature and light intensity. Canadian Journal of Botany **43**, 1063–1076.

Friend DJC, Helson VA, Fisher JE. 1962. Leaf growth in Marquis wheat, as regulated by temperature, light intensity, and daylength. Canadian Journal of Botany **40**, 1299–1311.

Gaba S, Lescourret F, Boudsocq S, Enjalbert J, Hinsinger P, Journet E-P, Navas M-L, Wery J, Louarn G, Malézieux E. 2015. Multiple cropping systems as drivers for providing multiple ecosystem services: from concepts to design. Agronomy for sustainable development **35**, 607–623.

Gallagher JN. 1979. Field Studies of Cereal Leaf Growth I. Initiation and expansion in relation to temperature and ontogeny. Journal of Experimental Botany **30**, 625–636.

Gallagher JN, Biscoe PV. 1978. Radiation absorption, growth and yield of cereals. The Journal of Agricultural Science **91**, 47–60.

Garin G, Fournier C, Andrieu B, Houlès V, Robert C, Pradal C. 2014. A modelling framework to simulate foliar fungal epidemics using functional–structural plant models. Annals of Botany **114**, 795–812.

Garin G, Fournier C, Pradal C, Houlès V, Robert C. 2016. Using combined virtual plant - pathogen models to compare the influence of wheat architecture on epidemics of two contrasted foliar fungi. FSPMA 2016, np.

Gastal F. 1984. Echanges de CO2 et croissance de la fétuque élevée en interaction avec l'alimentation azotée. PhD thesis, Université Paris 11, Paris, France.

Gastal F, Belanger G, Lemaire G. 1992. A Model of the Leaf Extension Rate of Tall Fescue in Response to Nitrogen and Temperature. Annals of Botany **70**, 437–442.

Gastal F, Nelson CJ. 1994. Nitrogen Use within the Growing Leaf Blade of Tall Fescue. Plant Physiology **105**, 191–197.

Gastal F, Saugier B. 1986. Alimentation azotée et croissance de la fétuque élevée. II.-Absorption de l'azote et distribution dans la plante. Agronomie **6**, 363–370.

Gate P. 1995. *Ecophysiologie du blé*. Paris, France: Lavoisier.

Gaudio N, Escobar-Gutiérrez AJ, Casadebaig P, Evers JB, Gérard F, Louarn G, Colbach N, Munz S, Launay M, Marrou H. 2019. Current knowledge and future research opportunities for modeling annual crop mixtures. A review. Agronomy for Sustainable Development **39**, 20.

Gauthier M, Barillot R, Schneider A, Chambon C, Fournier C, Pradal C, Robert C, Andrieu B. 2020. A functional structural model of grass development based on metabolic regulation and coordination rules. Journal of Experimental Botany **71**, 5454–5468.

Gautier H, Varlet - Grancher C, Hazard L. 1999. Tillering Responses to the Light Environment and to Defoliation in Populations of Perennial Ryegrass (*Lolium perenne* L.) Selected for Contrasting Leaf Length. Annals of Botany **83**, 423–429.

Gautier H, Varlet-Grancher C. 1996. Regulation of leaf growth of grass by blue light. Physiologia Plantarum **98**, 424–430.

Godin C, Sinoquet H. 2005. Functional-structural plant modelling. New Phytologist **166**, 705–708.

Green CF. 1987. Nitrogen nutrition and wheat growth in relation to absorbed solar radiation. Agricultural and Forest Meteorology **41**, 207–248.

Grindlay DJC. 1997. Towards an explanation of crop nitrogen demand based on the optimization of leaf nitrogen per unit leaf area. The Journal of Agricultural Science **128**, 377–396.

Hammer G, Messina C, Wu A, Cooper M. 2019. Biological reality and parsimony in crop models—why we need both in crop improvement! in silico Plants **1**, diz010.

Haun JR. 1973. Visual quantification of wheat development. Agronomy Journal **65**, 116–119.

He J, Le Gouis J, Stratonovitch P, *et al.* 2011. Simulation of environmental and genotypic variations of final leaf number and anthesis date for wheat. European Journal of Agronomy **42**.

Hellebust JA, Bidwell RGS. 1963. Sources of Carbon for the Synthesis of Protein Amino Acids in Attached Photosynthesizing Wheat Leaves. Canadian Journal of Botany **41**, 985–994.

Hendriks PW, Kirkegaard JA, Lilley JM, Gregory PJ, Rebetzke GJ. 2016. A tillering inhibition gene influences root–shoot carbon partitioning and pattern of water use to improve wheat productivity in rainfed environments. Journal of Experimental Botany **67**, 327–340.

Hikosaka K. 2005. Leaf canopy as a dynamic system: ecophysiology and optimality in leaf turnover. Annals of Botany **95**, 521–533.

Huber SC, Huber JL. 1992. Role of sucrose-phosphate synthase in sucrose metabolism in leaves. Plant Physiology **99**, 1275–1278.

Hunt R. 1975. Further observations on root—shoot equilibria in perennial ryegrass (*Lolium perenne* L.). Annals of Botany **39**, 745–755.

Hunt WF. 1983. Nitrogen cycling through senescent leaves and litter in swards of Ruanui and Nui ryegrass with high and low nitrogen inputs. New Zealand journal of agricultural research **26**, 461–471.

Iglesias DJ, Lliso I, Tadeo FR, Talon M. 2002. Regulation of photosynthesis through source: sink imbalance in citrus is mediated by carbohydrate content in leaves. Physiologia Plantarum **116**, 563–572.

Jacquemoud S, Baret F. 1990. PROSPECT: A model of leaf optical properties spectra. Remote sensing of environment **34**, 75–91.

Jamieson PD, Brooking IR, Porter JR, Wilson DR. 1995. Prediction of leaf appearance in wheat: a question of temperature. Field crops research **41**, 35–44.

Jamieson P, Brooking I, Zyskowski R, Munro C. 2008. The vexatious problem of the variation of the phyllochron in wheat. Field Crops Research **108**, 163–168.

Jamieson PD, Semenov MA, Brooking IR, Francis GS. 1998. Sirius: a mechanistic model of wheat

response to environmental variation. European Journal of Agronomy **8**, 161–179.

Johnson IR, Thornley JHM. 1985. Dynamic model of the response of a vegetative grass crop to light, temperature and nitrogen. Plant, Cell & Environment **8**, 485–499.

Jones DL, Nguyen C, Finlay RD. 2009. Carbon flow in the rhizosphere: carbon trading at the soil–root interface. Plant and Soil **321**, 5–33.

Justes E, Mary B, Meynard J-M, Machet J-M, Thelier-Huché L. 1994. Determination of a critical nitrogen dilution curve for winter wheat crops. Annals of botany **74**, 397–407.

Kang M, Evers JB, Vos J, De Reffye P. 2008. The derivation of sink functions of wheat organs using the GREENLAB model. Annals of Botany **101**, 1099–1108.

Kasai M. 2008. Regulation of leaf photosynthetic rate correlating with leaf carbohydrate status and activation state of Rubisco under a variety of photosynthetic source/sink balances. Physiologia Plantarum **134**, 216–226.

Keith H, Oades JM, Martin JK. 1986. Input of carbon to soil from wheat plants. Soil Biology and Biochemistry **18**, 445–449.

Kemp DR. 1980*a*. The Growth Rate of Successive Leaves of Wheat Plants in Relation to Sugar and Protein Concentrations in the Extension Zone. Journal of Experimental Botany **31**, 1399–1411.

Kemp DR. 1980*b*. The location and size of the extension zone of emerging wheat leaves. New Phytologist **84**, 729–737.

Kemp DR. 1981. The growth rate of wheat leaves in relation to the extension zone sugar concentration manipulated by shading. Journal of Experimental Botany **32**, 141–150.

Killingbeck KT. 1996. Nutrients in Senesced Leaves: Keys to the Search for Potential Resorption and Resorption Proficiency. Ecology **77**, 1716–1727.

Kirby EJM, Appleyard M, Fellowes G. 1985. Leaf emergence and tillering in barley and wheat. Agronomie **5**, 193–199.

Kirby EJM, Appleyard M, Simpson NA. 1994. Co-ordination of stem elongation and Zadoks growth stages with leaf emergence in wheat and barley. The Journal of Agricultural Science **122**, 21–29.

Kirby EJM, Faris DG. 1970. Plant population induced growth correlations in the barley plant main shoot and possible hormonal mechanisms. Journal of Experimental Botany **21**, 787–798.

Klepper B, Rickman RW, Belford RK. 1983. Leaf and Tiller Identification on Wheat Plants. Crop Science **23**, 1002–1004.

Klepper B, Rickman RW, Peterson CM. 1982. Quantitative Characterization of Vegetative Development in Small Cereal Grains1. Agronomy Journal **74**, 789.

Kobe RK, Lepczyk CA, Iyer M. 2005. Resorption efficiency decreases with increasing green leaf nutrients in a global data set. Ecology **86**, 2780–2792.

Kroon HD, Huber H, Stuefer JF, Groenendael JMV. 2005. A modular concept of phenotypic plasticity in plants. New Phytologist **166**, 73–82.

Lawlor DW, Boyle FA, Kendall AC, Keys AJ. 1987. Nitrate Nutrition and Temperature Effects on Wheat: Enzyme Composition, Nitrate and Total Amino Acid Content of Leaves. Journal of Experimental Botany **38**, 378–392.

Lawlor DW, Lemaire G, Gastal F. 2001. Nitrogen, Plant Growth and Crop Yield. In: Lea PJ,, In: Morot-Gaudry J-F, eds. Plant Nitrogen. Berlin, Heidelberg: Springer, 343–367.

Lazof DB, Rufty TW, Redinbaugh MG. 1992. Localization of Nitrate Absorption and Translocation within Morphological Regions of the Corn Root. Plant Physiology **100**, 1251–1258.

Legendre P, Legendre L. 2012. *Numerical Ecology*. Elsevier.

Lemaire G, Millard P. 1999. An ecophysiological approach to modelling resource fluxes in competing plants. Journal of Experimental Botany **50**, 15–28.

Lemaire G, Oosterom E van, Sheehy J, Jeuffroy MH, Massignam A, Rossato L. 2007. Is crop N demand more closely related to dry matter accumulation or leaf area expansion during vegetative growth? Field Crops Research **100**, 91–106.

Lemaire G, Salette J. 1984. Relation entre dynamique de croissance et dynamique de

prélèvement d'azote pour un peuplement de graminées fourragères. I. — Etude de l'effet du milieu. Agronomie **4**, 423–430.

Lestienne F, Gastal F, Moulia B, Thornton B. 2002. Pattern of leaf and tiller development of perennial ryegrass plants. Grassland Science in Europe **7**, 332–333.

Li L, Li X, Liu B, Lei J, Yue Z, Li C. 2020. Imbalanced stoichiometric patterns in foliar nutrient resorption response to N and P addition in grazing alpine grassland. Acta Oecologica **102**, 103505.

Ljutovac S. 2002. Coordination dans l'extension des organes aériens et conséquence pour les relations entre les dimensions finales des organes chez le blé. PhD thesis, Institut National Agronomique Paris-Grignon, Paris, France.

Lobet G, Pages L, Draye X. 2014. A modeling approach to determine the importance of dynamic regulation of plant hydraulic conductivities on the water uptake dynamics in the soil-plant-atmosphere system. Ecological modelling **290**, 65–75.

Lockhart JA. 1965. An analysis of irreversible plant cell elongation. Journal of Theoretical Biology **8**, 264–275.

Longnecker N, Kirby EJM, Robson A. 1993. Leaf Emergence, Tiller Growth, and Apical Development of Nitrogen-Deficient Spring Wheat. Crop Sci. **33**, 154–160.

Longnecker N, Robson A. 1994. Leaf Emergence of Spring Wheat Receiving Varying Nitrogen Supply at Different Stages of Development. Annals of Botany **74**, 1–7.

Louarn G, Andrieu B, Giauffret C. 2010. A size-mediated effect can compensate for transient chilling stress affecting maize (*Zea mays*) leaf extension. New Phytologist **187**, 106–118.

Louarn G, Barillot R, Combes D, Escobar-Gutiérrez A. 2020. Towards intercrop ideotypes: non-random trait assembly can promote overyielding and stability of species proportion in simulated legume-based mixtures. Annals of Botany.

Louarn G, Faverjon L. 2018. A generic individual-based model to simulate morphogenesis, C–N acquisition and population dynamics in contrasting forage legumes. Annals of Botany **121**, 875–896.

Louarn G, Song Y. 2020. Two decades of functional-structural plant modelling: now addressing fundamental questions in systems biology and predictive ecology. Annals of Botany **126**, 501–509.

Lupton FGH, Oliver RH, Ellis FB, Barnes BT, Howse KR, Welbank PJ, Taylor PJ. 1974. Root and shoot growth of semi-dwarf and taller winter wheats. Annals of Applied Biology **77**, 129–144.

Luquet D, Dingkuhn M, Kim H, Tambour L, Clement-Vidal A. 2006. EcoMeristem, a model of morphogenesis and competition among sinks in rice. 1. Concept, validation and sensitivity analysis. Functional Plant Biology **33**, 309–323.

Luquet D, Soulie JC, Rebolledo MC, Rouan L, Clement-Vidal A, Dingkuhn M. 2012. Developmental Dynamics and Early Growth Vigour in Rice 2. Modelling Genetic Diversity Using Ecomeristem. Journal of Agronomy and Crop Science-Zeitschrift Fur Acker Und Pflanzenbau **198**, 385–398.

Luxmoore RJ, Millington RJ. 1971. Growth of perennial ryegrass (*Lolium perenne* L.) in relation to water, nitrogen, and light intensity. Plant and Soil **34**, 561–574.

MacAdam JW, Nelson CJ. 1987. Specific leaf weight in zones of cell division, elongation and maturation in tall fescue leaf blades. Annals of Botany **59**, 369–376.

Macadam JW, Nelson CJ. 2002. Secondary Cell Wall Deposition Causes Radial Growth of Fibre Cells in the Maturation Zone of Elongating Tall Fescue Leaf Blades. Annals of Botany **89**, 89–96.

Malvoisin P. 1984*a*. Organogenèse et croissance du maître-brin du blé tendre (*Triticum aestivum*) du semis à la floraison. I. — Relations observées entre la croissance foliaire et la différenciation des ébauches foliaires ou florales. Agronomie **4**, 557–564.

Malvoisin P. 1984*b*. Organogenèse et croissance du maître-brin du blé tendre (*Triticum aestivum*) du semis à la floraison. II. - Contrôle des relations entre la croissance et la vascularisation de la tige et des feuilles. Essai de modélisation. Agronomie **4**, 587–596.

Manderscheid R, Burkart S, Bramm A, Weigel H-J. 2003. Effect of CO2 enrichment on growth and daily radiation use efficiency of wheat in relation to

temperature and growth stage. European Journal of Agronomy **19**, 411–425.

Martre P, Dambreville A. 2018. A model of leaf coordination to scale-up leaf expansion from the organ to the canopy. Plant physiology **176**, 704–716.

Martre P, Jamieson PD, Semenov MA, Zyskowski RF, Porter JR, Triboi E. 2006. Modelling protein content and composition in relation to crop nitrogen dynamics for wheat. European Journal of Agronomy **25**, 138–154.

McCormack ML, Dickie IA, Eissenstat DM, *et al.* 2015. Redefining fine roots improves understanding of below-ground contributions to terrestrial biosphere processes. New Phytologist **207**, 505–518.

McIntyre GI. 2001. Control of plant development by limiting factors: a nutritional perspective. Physiologia Plantarum **113**, 165–175.

McMaster GS. 2005. Phytomers, phyllochrons, phenology and temperate cereal development. Journal of Agricultural Science **143**, 137–150.

Mitchell CE, Tilman D, Groth JV. 2002. Effects of grassland plant species diversity, abundance, and composition on foliar fungal disease. Ecology **83**, 1713–1726.

Monteith JL. 1977. Climate and the efficiency of crop production in Britain. Philosophical Transactions of the Royal Society of London. B, Biological Sciences.

Moore KJ, Moser LE. 1995. Quantifying Developmental Morphology of Perennial Grasses. Crop Sci. **35**, 37–43.

Muller B, Martre P. 2019. Plant and crop simulation models: powerful tools to link physiology, genetics, and phenomics. Journal of Experimental Botany **70**, 2339–2344.

Nada RM, Abogadallah GM. 2016. Restricting the above ground sink corrects the root/shoot ratio and substantially boosts the yield potential per panicle in field-grown rice (*Oryza sativa* L.). Physiologia Plantarum **156**, 371–386.

Nakamura S, Nakajima N, Nitta Y, Goto Y. 2011. Analysis of Successive Internode Growth in Sweet Sorghum Using Leaf Number as a Plant Age Indicator. Plant Production Science **14**, 299—306.

Nelson CJ. 2000. Shoot morphological plasticity of grasses: leaf growth vs. tillering. Grassland Ecophysiology and Grazing Ecology. Wallingford, UK, 101–126.

Niinemets Ü. 1999. Components of leaf dry mass per area – thickness and density – alter leaf photosynthetic capacity in reverse directions in woody plants. New Phytologist **144**, 35–47.

Ninkovic V. 2003. Volatile communication between barley plants affects biomass allocation. Journal of Experimental Botany **54**, 1931–1939.

Ninkovic V, Markovic D, Rensing M. 2020. Plant volatiles as cues and signals in plant communication. Plant, Cell & Environment ***early online publication***.

Nix HA. 1976. Climate and crop productivity in Australia. Climate and rice. IRRI, Los Baños, The Philippines, 495–507.

Pace GM, McClure PR. 1986. Comparison of nitrate uptake kinetic parameters across maize inbred lines. Journal of Plant Nutrition **9**, 1095–1111.

Paciullo DSC, Gomide C de M, Castro CRT, Maurício RM, Fernandes PB, Morenz MJF. 2017. Morphogenesis, biomass and nutritive value of *Panicum maximum* under different shade levels and fertilizer nitrogen rates. Grass and Forage Science **72**, 590–600.

Pagès L, Vercambre G, Drouet J-L, Lecompte F, Collet C, Le Bot J. 2004. Root Typ: a generic model to depict and analyse the root system architecture. Plant and Soil **258**, 103–119.

Pantin F, Simonneau T, Muller B. 2012. Coming of leaf age: control of growth by hydraulics and metabolics during leaf ontogeny. New Phytologist **196**, 349–366.

Parry MA, Reynolds M, Salvucci ME, Raines C, Andralojc PJ, Zhu X-G, Price GD, Condon AG, Furbank RT. 2011. Raising yield potential of wheat. II. Increasing photosynthetic capacity and efficiency. Journal of experimental botany **62**, 453–467.

Patrick J. 1972. Distribution of Assimilate During Stem Elongation in Wheat. Australian Journal of Biological Sciences **25**, 455–468.

Paul MJ, Pellny TK. 2003. Carbon metabolite feedback regulation of leaf photosynthesis and

development. Journal of experimental botany **54**, 539–547.

Penning de Vries FWT, Jansen DM, Berger HFM. 1989. *Simulation of Ecophysiological Processes of Growth in Several Annual Crops*. Wageningen, Netherlands: Pudoc.

Poorter H, Anten NP, Marcelis LF. 2013. Physiological mechanisms in plant growth models: do we need a supra-cellular systems biology approach? Plant, cell & environment **36**, 1673–1690.

Poorter H, Niinemets Ü, Ntagkas N, Siebenkäs A, Mäenpää M, Matsubara S, Pons T. 2019. A meta-analysis of plant responses to light intensity for 70 traits ranging from molecules to whole plant performance. New Phytologist **223**, 1073–1105.

Poorter H, Niinemets Ü, Poorter L, Wright IJ, Villar R. 2009. Causes and consequences of variation in leaf mass per area (LMA): a meta-analysis. New Phytologist **182**, 565–588.

Poorter H, Niklas KJ, Reich PB, Oleksyn J, Poot P, Mommer L. 2012. Biomass allocation to leaves, stems and roots: meta-analyses of interspecific variation and environmental control. New Phytologist **193**, 30–50.

Pregitzer KS, DeForest JL, Burton AJ, Allen MF, Ruess RW, Hendrick RL. 2002. Fine Root Architecture of Nine North American Trees. Ecological Monographs **72**, 293–309.

Prioul J-L, Brangeon J, Reyss A. 1980. Interaction between external and internal conditions in the development of photosynthetic features in a grass leaf: II. Reversibility of light-induced responses as a function of developmental stages. Plant physiology **66**, 770–774.

Prusinkiewicz P. 1998. Modeling of spatial structure and development of plants: a review. Scientia Horticulturae **74**, 113–149.

R Core Team. 2020. *R: A Language and Environment for Statistical Computing*. Vienna, Austria: R Foundation for Statistical Computing.

Raseduzzaman MD, Jensen ES. 2017. Does intercropping enhance yield stability in arable crop production? A meta-analysis. European Journal of Agronomy **91**, 25–33.

Ratjen AM, Lemaire G, Kage H, Plénet D, Justes E. 2018. Key variables for simulating leaf area and N status: Biomass based relations versus phenology driven approaches. European Journal of Agronomy **100**, 110–117.

Rawson H, Gardner P, Long M. 1987. Sources of Variation in Specific Leaf Area in Wheat Grown at High Temperature. Functional Plant Biology **14**, 287.

Rees F, Andrieu B, Pages L, Barillot R, Richard-Molard C, Chenu C, Pradal C. 2020*a*. RhizoDep - A 3D root functional model to simulate rhizodeposition processes. iCROPM 2020 - Side event 'Phenotyping and modeling of plant anchorage and physiology'. Montpellier, France., .

Rees F, Barillot R, Gauthier M, Pagès L, Pradal C, Andrieu B. 2020*b*. Simulating rhizodeposition as a function of shoot and root interactions within a new 3D Functional-Structural PlantModel. 9th International Conference on functional-structural plant models. Virtual, 174.

Reyes F, Pallas B, Pradal C, Vaggi F, Zanotelli D, Tagliavini M, Gianelle D, Costes E. 2020. MuSCA: a multi-scale source–sink carbon allocation model to explore carbon allocation in plants. An application to static apple tree structures. Annals of botany **126**, 571–585.

Reynolds M, Foulkes J, Furbank R, Griffiths S, King J, Murchie E, Parry M, Slafer G. 2012. Achieving yield gains in wheat. Plant, cell & environment **35**, 1799–1823.

Rickman RW, Klepper BL. 1995. The Phyllochron: Where Do we Go in the Future? Crop Science **35**, 44–49.

Robertson MJ, Brooking IR, Ritchie JT. 1996. Temperature response of vernalization in wheat: modelling the effect on the final number of mainstem leaves. Annals of Botany **78**, 371–381.

Robson MJ, Deacon MJ. 1978. Nitrogen deficiency in small closed communities of S24 ryegrass. II. Changes in the weight and chemical composition of single leaves during their growth and death. Annals of Botany **42**, 1199–1213.

Robson MJ, Parsons AJ. 1978. Nitrogen deficiency in small closed communities of S24 ryegrass. I. Photosynthesis, respiration, dry matter production and partition. Annals of Botany **42**, 1185–1197.

Rogan PG, Smith DL. 1975. Rates of leaf initiation and leaf growth in *Agropyron repens* (L.) Beauv. Journal of Experimental Botany **26**, 70–78.

Rouet S, Denis L, Bernicot M-H, Combes D, Barillot R, Durand J-L. 2020. Phenology of grasslands: a new model. ICROPM2020: Second International Crop Modelling Symposium. Montpellier, France, .

Roumet C, Urcelay C, Díaz S. 2006. Suites of root traits differ between annual and perennial species growing in the field. New Phytologist **170**, 357–368.

Savitch LV, Harney T, Huner NPA. 2000. Sucrose metabolism in spring and winter wheat in response to high irradiance, cold stress and cold acclimation. Physiologia Plantarum **108**, 270–278.

Schneider A. 2020. Etude du rôle des sucres, en interaction avec les hormones, dans la régulation du débourrement des bourgeons axillaires par l'intensité lumineuse. Une démarche aliiant expériences et modélisation. PhD thesis, Agrocampus - Centre d'Angers, Angers, France.

Schnyder H, Nelson CJ. 1987. Growth Rates and Carbohydrate Fluxes within the Elongation Zone of Tall Fescue Leaf Blades. Plant Physiology **85**, 548–553.

Schnyder H, Nelson CJ. 1988. Diurnal growth of tall fescue leaf blades: I. Spatial distribution of growth, deposition of water, and assimilate import in the elongation zone. Plant Physiology **86**, 1070–1076.

Schnyder H, Nelson CJ. 1989. Growth Rates and Assimilate Partitioning in the Elongation Zone of Tall Fescue Leaf Blades at High and Low Irradiance. Plant Physiology **90**, 1201–1206.

Schnyder H, Nelson CJ, Coutts JH. 1987. Assessment of spatial distribution of growth in the elongation zone of grass leaf blades. Plant Physiology **85**, 290–293.

Schnyder H, Seo S, Rademacher IF, Kühbauch W. 1990. Spatial distribution of growth rates and of epidermal cell lengths in the elongation zone during leaf development in *Lolium perenne* L. Planta **181**, 423–431.

Sharkey TD. 2019. Is triose phosphate utilization important for understanding photosynthesis? Journal of Experimental Botany **70**, 5521–5525.

Siddiqi MY, Glass ADM, Ruth TJ, Fernando M. 1989. Studies of the Regulation of Nitrate Influx by Barley Seedlings Using 13NO3−. Plant Physiology **90**, 806–813.

Siddiqi MY, Glass ADM, Ruth TJ, Rufty TW. 1990. Studies of the Uptake of Nitrate in Barley I. Kinetics of 13NO3− Influx. Plant Physiology **93**, 1426–1432.

Sievänen R, Godin C, DeJong TM, Nikinmaa E. 2014. Functional–structural plant models: a growing paradigm for plant studies. Annals of botany **114**, 599–603.

Silvy A. 1982. La première feuille des plantules d'orge. I. Morphogenèse, les épidermes. Canadian Journal of Botany **60**, 2864–2876.

Sinclair TR, Amir J. 1992. A model to assess nitrogen limitations on the growth and yield of spring wheat. Field Crops Research **30**, 63–78.

Sinclair TR, Horie T. 1989. Leaf nitrogen, photosynthesis, and crop radiation use efficiency: a review. Crop science **29**, 90–98.

Skinner RH, Nelson CJ. 1994. Epidermal cell division and the coordination of leaf and tiller development. Annals of Botany **74**, 9–16.

Skinner RH, Nelson CJ. 1995. Elongation of the Grass Leaf and its Relationship to the Phyllochron. Crop Science **35**, 4.

Slattery RA, Ort DR. 2015. Photosynthetic energy conversion efficiency: setting a baseline for gauging future improvements in important food and biofuel crops. Plant physiology **168**, 383–392.

Smith H. 2013. *Light and plant development*.

Spollen WG, Nelson CJ. 1988. Characterization of fructan from mature leaf blades and elongation zones of developing leaf blades of wheat, tall fescue, and timothy. Plant Physiology **88**, 1349–1353.

Stockle CO, Debaeke P. 1997. Modeling crop nitrogen requirements: a critical analysis. European Journal of Agronomy **7**, 161–169.

Swinnen J, Van Veen JA, Merckx R. 1995. Carbon fluxes in the rhizosphere of winter wheat and spring barley with conventional vs integrated farming. Soil Biology and Biochemistry **27**, 811–820.

Tardieu F, Granier C, Muller B. 1999. Modelling leaf expansion in a fluctuating environment: are changes in specific leaf area a consequence of

changes in expansion rate? New Phytologist **143**, 33–43.

Tesařová J, Seidlová F, Nätr L. 1992. Relationships between the blade and sheath growth in the same leaf and in successive leaves of winter barley. Biologia Plantarum **34**, 325–333.

Thornley JHM, Cannell MGR. 2000. Modelling the Components of Plant Respiration: Representation and Realism. Annals of Botany **85**, 55–67.

Triboï E, Ntonga J. 1993. Effet de l'azote et du rayonnement sur le développement des feuilles et de l'épi chez le blé d'hiver : mise en place de l'appareil foliaire et de la structure de l'épi. Agronomie **13**, 253–265.

Varlet-Grancher C, Moulia B, Sinoquet H, Russell G. 1993. Spectral Modification Of Light Within Plant Canopies - How To Quantify Its Effects On The Architecture Of The Plant Stand. In: Varlet-Grancher C,, In: Moulia B,, In: Sinoquet H, eds. Crop Structure And Light Microclimate. Characterization and applications. Versailles: INRA, 427–452.

Verdenal A. 2009. De la simulation de la morphogénèse de l'appareil aérien du ray-grass anglais (*Lolium perenne* L.). Exploration d'un schéma cybernétique inspiré du concept d'auto-organisation et applications. PhD thesis, Université de Poitiers, Poitiers, France.

Verdenal A, Combes D, Escobar-Gutiérrez AJ. 2008. A study of ryegrass architecture as a self-regulated system, using functional-structural plant modelling. Functional Plant Biology **35**, 911–924.

Vidal T, Andrieu B. 2020. Contrasting phenotypes emerging from stable rules: A model based on self-regulated control loops captures the dynamics of shoot extension in contrasting maize phenotypes. Annals of Botany **126**, 615–633.

Volenec JJ, Nelson CJ. 1983. Responses of Tall Fescue Leaf Meristems to N Fertilization and Harvest Frequency 1. Crop Science **23**, 720–724.

Volenec JJ, Nelson CJ. 1984. Carbohydrate metabolism in leaf meristems of tall fescue II. Relationship to leaf elongation rates modified by nitrogen fertilization. Plant physiology **74**, 595–600.

Vos J, Evers JB, Buck-Sorlin GH, Andrieu B, Chelle M, de Visser PHB. 2010. Functional-structural plant modelling: a new versatile tool in crop science. Journal of Experimental Botany **61**, 2101–2115.

Wang S, Chen A, Xie K, Yang X, Luo Z, Chen J, Zeng D, Ren Y, Yang C, Wang L. 2020. Functional analysis of the OsNPF4. 5 nitrate transporter reveals a conserved mycorrhizal pathway of nitrogen acquisition in plants. Proceedings of the National Academy of Sciences **117**, 16649–16659.

Warton DI, Duursma RA, Falster DS, Taskinen S. 2012. smatr 3 - an R package for estimation and inference about allometric lines. Methods in Ecology and Evolution **3**, 257–259.

Werner T, Motyka V, Strnad M, Schmulling T. 2001. Regulation of plant growth by cytokinin. Proceedings of the National Academy of Sciences of the United States of America **98**, 10487–10492.

Werner T, Nehnevajova E, Köllmer I, Novák O, Strnad M, Krämer U, Schmülling T. 2010. Root-specific reduction of cytokinin causes enhanced root growth, drought tolerance, and leaf mineral enrichment in *Arabidopsis* and tobacco. The Plant Cell **22**, 3905–3920.

Williams R. 1960. The Physiology of Growth in the Wheat Plant I. Seedling Growth and the Pattern of Growth at the Shoot Apex. Australian Journal of Biological Sciences **13**, 401–428.

Williams RF. 1975. *Shoot Apex and Leaf Growth*. Cambridge University Press.

Williams RF, Rijven AHG. 1965. The physiology of growth in the wheat plant. II. The dynamics of leaf growth. Australian Journal of Biological Sciences **18**, 721–743.

Williams RF, Williams CN. 1968. Physiology of Growth in the Wheat Plant IV. Effects of Day Length And Light Energy Level. Australian Journal of Biological Sciences **21**, 835–854.

Wilman D. 1980. Early spring and late autumn response to applied nitrogen in four grasses. 1. Yield, number of tillers and chemical composition. Journal of Agricultural Science, UK **94**, 425–442.

Wilman D, Mohamed AA. 1980. Early spring and late autumn response to applied nitrogen in four grasses: 2. Leaf Development. The Journal of Agricultural Science **94**, 443–453.

Wilson R, Laidlaw A. 1985. The Role of the Sheath Tube in the Development of Expanding Leaves in Perennial Ryegrass. Annals of Applied Biology **106**, 385–391.

Wright IJ, Reich PB, Westoby M, *et al.* 2004. The worldwide leaf economics spectrum. Nature **428**, 821.

Wright IJ, Westoby M. 2003. Nutrient concentration, resorption and lifespan: leaf traits of Australian sclerophyll species. Functional Ecology **17**, 10–19.

Yang JT, Preiser AL, Li Z, Weise SE, Sharkey TD. 2016. Triose phosphate use limitation of photosynthesis: short-term and long-term effects. Planta **243**, 687–698.

Yu O, Gintzburger G, Gounot M. 1975. Modèle de fonctionnement d'un peuplement de Dactyle (*Dactylis glomerata* L.) en phase végétative Approche morphogénétique. Oecologia Plantarum **10**, 107–39.

Zhao Z, Wang E, Wang Z, Zang H, Liu Y, Angus JF. 2014. A reappraisal of the critical nitrogen concentration of wheat and its implications on crop modeling. Field Crops Research **164**, 65–73.

Zhen RG, Leigh RA. 1990. Nitrate accumulation by wheat (*Triticum aestivum*) in relation to growth and tissue N concentrations. Plant and Soil **124**, 157–160.

Zhu J, Andrieu B, Vos J, van der Werf W, Fournier C, Evers JB. 2014. Towards modelling the flexible timing of shoot development: simulation of maize organogenesis based on coordination within and between phytomers. Annals of Botany **114**, 753–762.

Annexe

Travaux publiés lors de la thèse

Article dans des revues internationales avec comité de relecture

Gauthier M, Barillot R, Schneider A, Chambon C, Fournier C, Pradal C, Robert C, Andrieu B. 2020*b*. A functional structural model of grass development based on metabolic regulation and coordination rules. Journal of Experimental Botany **71**, 5454–5468.

Communications orales avec actes dans des congrès internationaux

Gauthier M, Barillot R, Schneider A, Fournier C, Pradal C, Pinet A, Andrieu B. 2018. Towards a model of wheat leaf morphogenesis at plant scale driven by organ-level metabolites. In 6th International Symposium on Plant Growth Modeling, Simulation, Visualization and Applications – PMA2018, November 4-8, 2018. Hefei, China.

Barillot R, Gauthier M, Andrieu B, Durand J-L, Roldan-Ruiz I, Swaef T de. 2019. Integrating the complex regulation of leaf growth by water and trophic dynamics in a functional-structural plant model of grass. In Society of Experimental Biology Annual Main Meeting, July 2-5, 2019. Sevilla, Spain.

Gauthier M, Barillot R, Schneider A, Fournier C, Pradal C, Pinet A, Andrieu B. 2019. A model of Grass shoot morphogenesis at plant scale driven by organ-level metabolites. In Society of Experimental Biology Annual Main Meeting, July 2-5, 2019. Sevilla, Spain.

Barillot R, Gauthier M, Andrieu B, Durand J-L, Roldán-Ruiz I, Swaef T. 2020. Integrating the complex regulation of leaf growth by water and trophic dynamics in a functional-structural plant model of grass. In 9th International Conference on functional-structural plant models, October 5-9, 2020. Virtual.

Gauthier M, Barillot R, Schneider A, Chambon C, Fournier C, Pradal C, Andrieu B. 2020*a*. A 3D architectural model of grass shoot morphogenesis and plasticity, driven by organ metabolite concentrations and coordination rules. In 9th International Conference on functional-structural plant models, October 5-9, 2020. Virtual.

Rees F, Barillot R, Gauthier M, Pagès L, Pradal C, Andrieu B. 2020. Simulating rhizodeposition as a function of shoot and root interactions within a new 3D Functional-Structural PlantModel. In 9th International Conference on functional-structural plant models, October 5-9, 2020. Virtual.

université PARIS-SACLAY
ÉCOLE DOCTORALE
Agriculture, alimentation, biologie, environnement, santé (ABIES)

Titre : Simuler la plasticité phénotypique des Poacées comme propriété émergente de processus locaux : Un modèle structure-fonction couplant la morphogénèse et le métabolisme du carbone et de l'azote

Mots clés : Modélisation structure-fonction, morphogénèse, Poacées, métabolisme, plasticité, blé

Résumé : La plasticité phénotypique, la capacité d'un génotype à adapter son phénotype à ses conditions de croissance, est un aspect essentiel des interactions plante-environnement. Les modèles sont des outils permettant d'intégrer ces interactions, en particulier les modèles structure-fonction (FSPM) car ils proposent une description explicite de l'architecture de la plante. À ce jour, les FSPM traitant du couplage entre la disponibilité des ressources et la croissance sont limités car ils reposent largement sur des formalismes empiriques. L'objectif est de construire un FSPM de morphogenèse aérienne de Poacées qui considère le fonctionnement de la plante entière et qui simule l'acquisition de traits comme propriétés résultant des interactions entre la morphogenèse, les facteurs environnementaux et les activités source-puits au sein de la plante. Le modèle est piloté par le métabolisme du carbone et de l'azote dans chaque organe et par des règles de coordinations entre feuilles successives. Parallèlement au développement du modèle, une expérimentation a été menée pour recueillir des données nécessaires à la calibration et à l'évaluation du modèle. Le modèle a été calibré pour le blé et a simulé des traits foliaires et de plante réalistes, et la réponse de ces traits aux conditions de croissance était cohérente avec la bibliographie. En particulier, le modèle a simulé, comme propriétés émergentes, des caractéristiques clés qui sont fixes ou simulées empiriquement dans la plupart des modèles : profil de dimensions finales des feuilles, stabilité du phyllochrone, rapport aérien/souterrain, dilution du N, *etc.*

Title : Simulating the phenotypic plasticity of grasses as property emerging from local processes : A functional-structural model that couples morphogenesis with the carbon and nitrogen metabolism

Keywords : Functional-Structural Plant Modeling, morphogenesis, grass, metabolism, plasticity, wheat

Abstract : Phenotypic plasticity - the ability of one genotype to produce different phenotypes depending on growth conditions - is a core aspect of the interactions between the plants and their environment. Models are useful tools allowing integrating these feedback loops between shoot architecture and growth conditions so simulating their outputs, especially functional-structural plant models (FSPM) as they account for an explicit description of individual plant architecture. To date, the existing crop FSPM that address the coupling between resource availability and growth are hampered by their lack of capacity to simulate shoot morphogenesis as they lack processed-based formalism. This work aims to build a FSPM that includes morphogenesis, which simulates mechanistically the whole plant functioning and trait acquisition as properties arising from the feedback between morphogenesis, environmental factors and source–sink activities within the plant. The model is driven by carbon and nitrogen metabolism in each organ and coordination rules between successive leaves. In parallel with the development of the model, an experiment was performed to collect useful data for the model calibration and evaluation. The model was calibrated for wheat. It simulated realistic patterns of leaf traits and the variation of leaf traits with growth conditions was coherent with the bibliography. Interestingly, the model simulated, as emergent properties, key traits at organ and plant scales that are taken as inputs in most models: pattern of mature leaf dimensions along the culm, phyllochron stability, realistic shoot/roots ratio, *etc.*